Nottingham Geospatial Institute

Heading Drift Mitigation for Low-Cost Inertial Pedestrian Navigation

By
Khairi Abdul Rahim BEng, MEng

Thesis submitted to the University of Nottingham for
the degree of Doctor of Philosophy

March 2012

ABSTRACT

The concept of autonomous pedestrian navigation is often adopted for indoor pedestrian navigation. For outdoors, a Global Positioning System (GPS) is often used for navigation by utilizing GPS signals for position computation but indoors, its signals are often unavailable. Therefore, autonomous pedestrian navigation for indoors can be realized with the use of independent sensors, such as low-cost inertial sensors, and these sensors are often known as Inertial Measurement Unit (IMU) where they do not rely on the reception of external information such as GPS signals. Using these sensors, a relative positioning concept from initialized position and attitude is used for navigation. The sensors sense the change in velocity and after integration, it is added to the previous position to obtain the current position.

Such low-cost systems, however, are prone to errors that can result in a large position drift. This problem can be minimized by mounting the sensors on the pedestrian's foot. During walking, the foot is briefly stationary while it is on the ground, sometimes called the zero-velocity period. If a non-zero velocity is then measured by the inertial sensors during this period, it is considered as an error and thus can be corrected. These repeated corrections to the inertial sensor's velocity measurements can, therefore, be used to control the error growth and minimize the position drift. Nonetheless, it is still inadequate, mainly due to the remaining errors on the inertial sensor's heading when the velocity corrections are used alone. Apart from the initialization issue, therefore, the heading drift problem still remains in such low-cost systems.

In this research, two novel methods are developed and investigated to mitigate the heading drift problem when used with the velocity updates. The first method is termed Cardinal Heading Aided Inertial Navigation (CHAIN), where an algorithm is developed to use building 'heading' to aid the heading measurement in the

Kalman Filter. The second method is termed the Rotated IMU (RIMU), where the foot-mounted inertial sensor is rotated about a single axis to increase the observability of the sensor's heading.

For the CHAIN, the method proposed has been investigated with real field trials using the low-cost Microstrain 3DM-GX3-25 inertial sensor. It shows a clear improvement in mitigating the heading drift error. It offers significant improvement in navigation accuracy for a long period, allowing autonomous pedestrian navigation for as long as 40 minutes with below 5 meters position error between start and end position. It does not require any extra heading sensors, such as a magnetometer or visual sensors such as a camera nor an extensive position or map database, and thus offers a cost-effective solution. Furthermore, its simplicity makes it feasible for it to be implemented in real-time, as very little computing capability is needed. For the RIMU, the method was tested with Nottingham Geospatial Institute (NGI) inertial data simulation software. Field trials were also undertaken using the same low-cost inertial sensor, mounted on a rotated platform prototype. This method improves the observability of the inertial sensor's errors, resulting also in a decrease in the heading drift error at the expense of requiring extra components.

Acknowledgement

The research undertaken for this thesis was conducted at the Nottingham Geospatial Institute (NGI) at the University of Nottingham,UK. I would like to express my sincere gratitude to my academic supervisors Professor Terry Moore, Dr Chris Hill and Dr Chris Hide for their infinite support and guidance throughout this research.

My special thanks also go to my financial sponsor, the Ministry of Higher Education of Malaysia (MOHE) and the Universiti Sains Islam Malaysia (USIM).

For staffs and students of NGI, who have made my time in NGI an unforgettable moment, I cherish it always.

From far, I would like to say thank you to my family, in particular my beloved mother, Hjh. Rosnah binti Kamis, and my beloved father, Hj. Abdul Rahim bin Abdul Rahaman, for their continuous support, motivation and prayer for me. Not to forget my mother-in-law, Hjh. Siti Zaleha binti Mat Din and my father-in-law, Hj. Abd Rahman bin Din.

Finally, and most importantly, I would like to thank my wife, Mashitoh, my son, Muhammad Naufal, and my daughter, Nuha Nafeesa, who have given delight to my life.

Contents

List of Publications

[1] Abdulrahim, K., Hide, C., Moore, T., Hill, C. (2012). Using constraints for shoe mounted indoor pedestrian navigation. *The Journal of Navigation*, 65, 15-28.

[2] Abdulrahim, K., Hide, C., Moore, T., Hill, C. (2011). Aiding low cost inertial navigation with building heading for pedestrian navigation. *The Journal of Navigation,* 64, 219-233.

[3] Abdulrahim, K., Hide, C., Moore, T., Hill, C. (2011). Integrating low cost IMU with building heading in indoor pedestrian navigation. *Journal of Global Positioning Systems,* 10(1), 30-38.

[4] Pinchin, J., Hide, C., Abdulrahim, K., Moore, T., Hill, C. (2011). Integration of heading-aided MEMS IMU with GPS for pedestrian navigation. In *Proceedings of ION GNSS 2011.* Oregon, USA, 19-23 September 2011.

[5] Hide, C., Hill, C., Abdulrahim, K., Moore, T. (2010). Positioning System. *International PCT Patent Application,* PCT/GB2011/051959, filed 11 October 2011.

[6] Abdulrahim, K., Hide, C., Moore, T., Hill, C. (2010). Investigating the effect of rotating MEMS IMU for pedestrian navigation. In *Proceedings of ENC-GNSS 2010.* Braunschweig, Germany, 19-21 October 2010.

[7] Abdulrahim, K., Hide, C., Moore, T., Hill, C. (2010). Aiding MEMS IMU with building heading for indoor pedestrian navigation. In *Proceedings of Ubiquitous Positioning Indoor Navigation and Location Based Service (UPINLBS) 2010.* Helsinki, Finland, 14-15 October 2010.

[8] Abdulrahim, K., Hide, C., Moore, T., Hill, C. (2010). Pedestrian navigation with heading drift correction. In *Proceedings of Royal Institute of Navigation NAV10*. London, UK, 30 November – 2 December 2010.

[9] Hide, C., Moore, T., Hill, C., Abdulrahim, K., and Pourabdollah, A. (2010). Rapid Wi-Fi fingerprint mapping for indoor navigation. In *Proceedings of Royal Institute of Navigation NAV10*. London, UK, 30 November – 2 December 2010.

[10] Abdulrahim, K., Hide, C., Moore, T., Hill, C. (2010). Low-cost, high accuracy positioning for indoor navigation. In *Digital Future 2010 Conference.* Nottingham, UK, 11-12 October 2010. [online] Available at:<https://www.horizon.ac.uk/images/stories/p31-Abdulrahim.pdf>

[11] Abdulrahim, K., Hide, C., Moore, T., Hill, C. (2010). Aiding indoor pedestrian navigation with building heading. *GPS World Tech Talk*, *GPS World.* [online] Available at: <http://www.gpsworld.com/tech-talk-blog/aiding-indoor-pedestrian- navigation-<with-building-heading-11384-0>

[12] Abdulrahim, K. (2010). Improving algorithm for inertial pedestrian navigation. In *Wearable Personal Sensing Workshop*. The University of Nottingham. [online] Available at: <http://cgs.nottingham.ac.uk/~wearable/AK.pdf>

[13] Abdulrahim, K. (2010). Low-cost non-GPS navigation using foot mounted IMU. *Horizon Ubiquitous Navigation Workshop*. Nottingham. 16 July 2010.

List of Figures

Fig. 6.15: Comparison of Horizontal Position Error (HPE) between three cases; no magnetometer used (green), magnetometer used but infrequent updates (red) and magnetometer used with frequent updates (blue). · · · · · · · · · · · · · · · · · · 128

Fig. 7.1: The concept of the RIMU for a low-cost PNS · · · · · · · · · · · · · · 131

Fig. 7.2: RIMU accelerations in its b-frame · 138

Fig. 7.3: RIMU angular rates in its b-frame · 139

Fig. 7.5: Comparison of z-axis gyro bias when different rotation schemes were used · 141

Fig. 7.6: Accelerometer bias for (a) x-axis, (b) y-axis and (c) z-axis, and gyro bias for (d) x-axis, (e) y-axis and (f) z-axis. · 143

Fig. 7.7: A walking trajectory as a reference. · 145

Fig. 7.8: Sample velocity for walking pedestrian (left) true, and (right) simulated. · 145

Fig. 7.9: Simulated inertial sensor output for (left) acceleration, and (right) angular rate · 146

Fig. 7.10: Comparison of heading angle for RIMU and non-RIMU. · · · · · · · 147

Fig. 7.11: Magnified heading angle from Fig. 7.10 · · · · · · · · · · · · · · · · · 148

Fig. 7.12: The RIMU initial heading · 149

Fig. 7.13: The RIMU heading after resolving the error in Down axis · · · · · · 149

Fig. 7.14: The comparison of the RIMU position with the reference and without-RIMU · 152

Fig. 7.15: The drifting in the initial RIMU heading · · · · · · · · · · · · · · · · 152

Fig. 7.16: RIMU prototype with (left) IMU mounted on a rotating platform, and (right) the RIMU controller · 153

Fig. 7.17: The visualization of the RIMU trajectory · · · · · · · · · · · · · · · · 154

Fig. 7.18: The actual raw IMU acceleration data · · · · · · · · · · · · · · · · · · 155

Fig. 7.19: An example of ZUPT detection for the trial. · · · · · · · · · · · · · · 155

Fig. 7.20: A comparison of *z*-gyro bias estimation with different approaches · · 159

Fig. 8.16: Areas of irregular walking in QMC hospital. · · · · · · · · · · · · · · · 187

Fig. 8.17: Description of each stages [A], [B], [C], and [D] as depicted in Fig. 8.16. · 188

Fig. 8.18: Irregular walking trajectory using CHAIN algorithm. · · · · · · · · · · 189

Fig. 8.19: From left top corner (clockwise) - Trajectory [A],[B],[C] and [D]. · · · 190

Fig. 8.20: Heading errors using ZUPT only and ZUPT with ZIHR. · · · · · · · · 198

Fig. 8.21: Heading errors of INS/ZUPT with ZIHR. · · · · · · · · · · · · · · · · · · 198

Fig. 8.22: Comparison of attitude error standard deviation on the Down axis for the ZIHR case and 'fixing yaw' case. · 199

Fig. 8.23: Four constructed polygon areas for the trial. · · · · · · · · · · · · · · · 202

Fig. 8.24: The position solutions of HSGPS (red), low-cost PNS + ZUPT (blue), low-cost PNS + ZUPT + CHAIN (green) · 203

Fig. 8.25: Low-cost PNS/ZUPT solution without MPA trajectory solution · · · 204

Fig. 8.26: Low-cost PNS/ZUPT with MPA trajectory solution · · · · · · · · · · 205

Fig. 8.27: Extreme scenario when MPA causes problem to the overall PNS solution · 207

Fig. 8.28: IMU height output with and without Heuristic Height · · · · · · · · 211

Fig. 8.29: Height constraint is being updated · 211

Fig. 8.30: Comparison of position error for CHAIN-aided and magnetometer-aided for the low-cost PNS · 212

Fig. 8.31: (clockwise from bottom left): Example of position output from trial 8, trial 4 and trial 2 tabulated in Table 1. · 214

List of Tables

Chapter 1

Introduction

This chapter begins with a short background on pedestrian navigation systems. A general review of the limitations of such a system in an indoor environment is given, followed by a section on the research aims and objectives of the study. Finally, the thesis structure is outlined briefly, along with the chapter summary.

1.1 Background

People spend about 70% of their time indoors. The National Human Activity Pattern Survey (NHAPS) showed that people in the United States of America and Canada spent an average of 87% of their time in enclosed buildings (Klepeis et al., 2001), whilst Ezzati et al. (2000) and Bruce et al. (2004) found that the average proportion of time spent indoors for women in Kenya and Mexico is 70% and 75% respectively. In the far East, Korean people were also found to spent more than 87% (21 hours) of their times indoors (Choi et al., 2010). Recently, Diffey (2011) analyzed that on average, people spend only about 2 of 24 hours outdoors, which means more than 22 hours are spent indoors daily. These, therefore, indicate that most of the daily activities are indoors and highlight the significance of indoor navigation systems for pedestrians.

Pedestrian navigation can be defined as "the process of determining and maintaining positional information for a person travelling on foot" (Stirling et al., 2005). Whilst the growth of interest in pedestrian navigation may be associated with the amount of time spent indoors, it might also be partly due to the technological advances in mobile computing. This is represented by the growing use of smart phones and computer tablets, which makes them possible to become more than just a phone; for example it becomes a navigation device. Some of the pedestrian navigation applications that may benefit from this include systems to guide people with visual difficulties, virtual gaming, walking routes for tourism and so forth.

In recent years, the Global Positioning System (GPS) has become one of the primary methods for outdoor pedestrian navigation and has many benefits for civilian daily use. For example, it was reported that 1.05 million Japanese people use GPS-based pedestrian navigation applications (Arikawa et al., 2007). In ideal conditions, often in an outdoor environment in which there is a clear line of sight to at least four GPS satellites, GPS provides accuracy ranging from tens of metres to tens of centimetres, depending on the GPS receiver grade and methodology.

Typically, for civilian applications such as pedestrian navigation, sub-metre level accuracy can be achievable in a good outdoor environment.

The use of GPS technology to navigate in an indoor environment, however, proves to be a complicated navigation problem, and therefore remains a challenge (Karimi et al., 2011). Indeed there are many improvements made to date to ease such complications. This includes the use of assistance to GPS (A-GPS) data via a cellular network (Zandbergen and Barbeau, 2011), additional signal transmission channels (GPS modernization) (Fernández-Prades et al., 2011, Alkan et al., 2005), and augmentation with cellular network positioning (Lin et al., 2011, Sun et al., 2005). Nevertheless, GPS still operates at a relatively low power, even with the modernized GPS signals. For example, the minimum received signal strength for GPS Block III L1 C/A signal is only -158.5 dBW, or merely 1.4×10^{-16} W (GPS, 2010). This fundamental issue with the GPS signals means that they are vulnerable to the surrounding environment. As a result, GPS signals will always become attenuated due to signal reflection and refraction. Indoors, the amount of signal attenuation can be much higher, such that the signal can no longer be used reliably anymore for position computation. This is because of the additional effect that the indoor infrastructure has on signal attenuation. This infrastructure, comprising different types of materials; such as concrete walls, furniture, and electrical appliances, will significantly weaken the received GPS signals (Kjærgaard et al., 2010).

Alternatively, High Sensitivity (HS) GPS receivers can be used to operate even with the weakened GPS signals. In many cases, however, they are more likely to struggle to produce continuous positioning with good accuracy indoors, and often the signals are not reliable enough to produce good position solutions (Lachapelle et al., 2006). This is partly due to the difficulty of separating errors, such as multipath error, from good GPS signals. Multipath error occurs when duplicated GPS signals are received by the GPS antenna; one comes along a direct path from the GPS satellite and the other one arrives at a slight delay due to reflection from nearby objects or surfaces. This results in a long-period deformation in the range

measurements that degrade the position solutions (Kijewski-Correa and Kochly, 2007). Even if this problem can be overcome, in many situations, there are simply too few GPS satellites in view to be used. A logical approach then would be to increase satellite availability. This was investigated for example with the use of a combined GPS/GLONASS high sensitivity receiver (O'Driscoll et al., 2011) and (simulated) GPS/GLONASS/Galileo high sensitivity receiver (Ji et al., 2010), in an urban canyon. Unfortunately, it was found that although the number of detectable satellites increased, the multipath error remains a major problem in an indoor environment.

This leads to a different approach to indoor positioning and navigation in the form of non-GPS systems (Fischer and Gellersen, 2010). Using infrastructure, either dedicated or non-dedicated for positioning, a form of non-GPS positioning systems are implemented. Dedicated infrastructure means that the infrastructure is purposely installed to aid navigation. Conversely, a non-dedicated infrastructure means the use of existing infrastructure that is not meant for navigation, but can be used to aid navigation. Radio Frequency IDentification (RFID), Wireless Local Area Network (WLAN/WIFI) and Ultra Wide Band (UWB) are examples of systems that do not use GPS signals, but can be used to compute position. RFID can use absolute position information embedded in it to aid navigation (Fu and Retscher, 2009; Ting et al., 2011). WLAN or WIFI provides absolute position information either by 'fingerprinting' or by using Received Signal Strength (RSS) (Kealy et al., 2010a; Biswas and Veloso, 2010). UWB also uses a similar approach to GPS positioning by making use of signal signatures such as Time of Arrival (ToA) and Angle of Arrival (AoA) to compute position (Tan and Law, 2007; Pittet et al., 2008; Chiu, 2009). A further explanation of these systems will be described in Chapter 3.

All of these, however, do require some form of infrastructure, either dedicated or non-dedicated, which relate directly to an increase in cost. For example in a typical building, there are often lots of small rooms. Therefore, it is very costly to add some form of dedicated infrastructure in each room to aid navigation. Although one could argue that the cost, after installation, will be one off,

maintaining this infrastructure is another potentially expensive task. In some cases, for example in emergency situations, both dedicated and non-dedicated infrastructure might not be available at all to aid navigation. Therefore, in order to have a low-cost navigation system, a reasonable option is to resort to another technology that does not rely on external infrastructure.

A common approach would be to use inertial sensors, commonly configured as an Inertial Measurement Unit (IMU), which has the advantage of not relying on external infrastructure. The sensors (normally three accelerometers and three gyroscopes) are small, of low power, and inexpensive due to advances in Micro-Electro-Mechanical Sensors (MEMS) technology. They provide the change in position information, and, once initialized, the system is totally autonomous. Unfortunately, the performance of low-cost MEMS inertial sensors is still relatively low. For example, within 1 minute of operation, a 1-sigma horizontal position error for typical high grade IMU is only 3 m but the typical low-cost grade IMU has a remarkable error of 102 m (Moore et al., 2008). As a result, their use for positioning applications is relatively limited, unless frequent measurement updates from external sensors or technologies are available to correct the low-cost IMU error.

One recent idea that has advanced the use of MEMS IMUs for pedestrian navigation is the notion of attaching the IMU to the pedestrian's foot/shoe (Stirling et al., 2003, Foxlin, 2005, Beauregard, 2007, Godha and Lachapelle, 2008, M. Jadaliha et al., 2008, Rajagopal, 2008, Hide et al., 2009, Feliz et al., 2009, Robertson et al., 2009). This results in the substantial advantage that the foot has to be briefly stationary while it is on the ground. During this period, Zero Velocity Updates (ZVU or ZUPT), for example shown in (Grejner-Brzezinska et al., 2001), can be used to correct the user's velocity. Furthermore, if the ZUPT measurements are used in the Kalman Filter (KF), they can be used not only to correct the user's velocity, but also help to restrict the growth of the position and attitude errors and estimate the sensor bias errors (Foxlin, 2005, Godha and Lachapelle, 2008). The frequent use of ZUPT measurements consistently overcomes many of the errors and,

as a result, even relatively low-cost sensors can provide useful navigation performance.

There remain, however, two significant problems with the low-cost MEMS IMU pedestrian navigation. Firstly, the initial position, velocity and attitude have to be obtained. For a stationary IMU, the velocity, roll and pitch can be set, where roll and pitch are obtained by comparing the accelerometer output to the local gravity vector. An initial estimate of the gyro biases can be initialised if the IMU is non-rotating. The main problem, though, is that position and heading need to be obtained from external sensors. Typically, position is initialised using GPS, although the ability to do this will depend on whether the user is located in an area in which GPS is available, and if so, whether it can provide an accurate location. Heading also needs to be initialised since low-cost gyros are unable to measure the rotation of the Earth, which is used to initialise heading for higher grade sensors (Section 2.3.3.1). For example, Earth rotation rate is approximately 15 $^{0}/hr$, or $\frac{1}{240}$ $^{0}/s$, whilst typical low-cost gyro has a bigger bias specification of $\frac{1}{6}$ $^{0}/s$ (see Table 2.1 in Chapter 2). This means that the low-cost gyro would not be able to provide accurate initial heading because its bias is bigger than the value to be measured, which is the Earth rotation rate. Therefore, heading must be obtained from an external sensor, such as a magnetometer, which is, however, undesirable since magnetic disturbances can cause significant errors (analyzed in Chapter 6).

The second significant problem that remains is the heading drift in the measured period of navigation, which ultimately will cause position drift error. Heading drift still remains, despite the use of ZUPT measurements in the KF, because the heading error is unobservable. Observability is the ability to determine a state from a given sequence of measurements and, with the use of ZUPTs to aid a low-cost IMU, it is not possible to estimate the heading error using these measurements alone. This causes a significant issue since there then becomes a requirement to use heading measurements from external sensors. Typically, magnetometers are used; however, their measurements are often unreliable when navigating in environments such as indoors, where there are significant magnetic disturbances. Instead, it is desirable to use innovative methods and algorithms, and

measurements from other systems in order to control heading drift. This second significant problem has, therefore, become the basis of this research.

1.2 Research Aims and Objectives

The aim of the research presented in this thesis is to propose a low-cost inertial pedestrian navigation system, capable of navigating autonomously in an indoor environment. The term 'low-cost' is used to represent an MEMS grade IMU sensor that incorporates only accelerometers and gyros. The system will subsequently be considered as a low-cost Pedestrian Navigation System (low-cost PNS), where applicable, in this thesis.

The originality of this research, therefore, lies in investigating innovative methods of using only a low-cost IMU for positioning. This leads to the main research problem – the heading drift error – which is addressed specifically in this thesis. A novel approach to low-cost PNS is proposed by developing a new, effective, yet simple algorithm, using only a low-cost IMU. Previously, in order to investigate the problem, a low-cost IMU would have either been integrated with other sensors such as a camera, electronic tag and/or magnetometer (Hide et al., 2009, Storms et al., 2010, Seco et al., 2010), or with an extensive map database (Woodman and Harle, 2008, Robertson et al., 2009).

The broad aims of the research are therefore summarized as follows:

1. Undertake research into improving the system performance of a low-cost, autonomous inertial pedestrian navigation system.
2. Investigate the performance of the methods proposed within the research.

More specifically, the objectives of this research are:

1. To investigate the performance of a conventional approach (magnetometer) to address the research problem in a low-cost PNS.

2. To propose a 'mechanically rotating IMU mounted on a shoe' as an alternative to the magnetometer to investigate the research problem.

3. To undertake simulation and practical field trials for the proposed approach in (2).

4. To develop a new algorithm to combat the drift problem without the existence of mechanical moving parts as in (2) and (3).

5. To undertake practical field trials with the low-cost PNS using the developed algorithms.

The research undertaken, which is presented in this thesis, demonstrates two significant findings:

- A single axis rotation of the IMU for indoor pedestrian navigation can be used to address the poor observability of the heading, at the expense of needing mechanically moving parts. This results in two important outcomes. First, the approach improves the heading observability during walking, which results in a significant reduction in position drift error without the need for extra sensors and aids. Second, it also improves the observability of most of the IMU errors and the cancellation of the constant IMU errors. This improvement is quite pronounced during stationary alignment, which is potentially very useful during the period of alignment and initialization of the IMU.

- A new proposed building-heading aided algorithm can also be used to address the poor observability of the heading for an inertial pedestrian navigation system, which subsequently reduces position drift error. With this approach, measurements from GPS, a compass or other sensors are not needed, once the system has been initialized. The approach, therefore, eliminates the dependence of the inertial pedestrian navigation system on extra sensors, which should directly result in a reduction in cost. It also

facilitates a significant reduction in position drift error for a long period of low-cost IMU-only navigation, which was previously very difficult to achieve.

1.3 Thesis Outline

This thesis is arranged into nine chapters which are now outlined.

Following this chapter, Chapter 2 describes the theoretical knowledge used throughout the thesis. The fundamental principles for Strapdown Inertial Navigation System (SINS) will be explained. This includes the mechanization process, which forms the basis of inertial navigation. Then, a brief overview of the fundamentals of the Kalman Filter will be given.

In Chapter 3, a literature search of pedestrian navigation systems will be reviewed. This chapter will explain some of the current system approaches to the matter of indoor pedestrian navigation. The use of GPS as the state-of-the-art navigation technology will be explained first, followed by a consideration of the alternative technologies available, including Inertial Navigation System (INS). This chapter finishes with a review of the possibility for a low-cost PNS, using a 'foot-mounted INS' approach.

This leads to Chapter 4, which will discuss the problems of indoor navigation using a foot-mounted INS. A specific emphasis will be given to a discussion of the primary errors of such a system, particularly the heading drift error. The performance and limitations of different approaches to aid a low-cost PNS will be explained. The chapter finishes by detailing the need for an additional research in this field.

In Chapter 5, the tools used in this research will be described. The processing software and the data simulation software will be covered in terms of their architecture and algorithms, linking directly with Chapter 2. The selection of hardware used in the field trials will also be explained.

Chapter 6 details how a magnetometer may be used as one means of solving the research problem. The chapter will describe magnetometer performance using a

filtering method. This chapter will show that the occasional reliable heading measurements, which can sometimes be obtained after filtering a high magnetic disturbance environment, such as found when indoors, are still not sufficient to reduce the heading drift error.

Following on from the findings of the previous chapter, Chapter 7 describes a new approach. This was proposed to make the INS heading measurement observable, to effectively reduce the heading drift. This will initially be done by proposing the rotation of the IMU mechanically on a single axis, on a platform mounted on a pedestrian's shoe. The simulation results and real field trial results will be discussed. The chapter will show how the approach can improve the observability of the modelled IMU errors, subsequently reducing the heading drift error. Conversely, the existence of mechanical moving parts using this approach motivates Chapters 8 to find a much simpler and inexpensive way of tackling the heading drift problem.

Chapter 8 describes a new approach to mitigate the heading drift problem, termed Cardinal Heading Aided Inertial Navigation (CHAIN). A new algorithm will be developed and explained in detail, followed by results from several field trials. A comprehensive discussion follows, presenting possible limitations and weaknesses of the new algorithm. The CHAIN algorithm is extended by adding a number of sub-algorithms to address properly its operation in different scenarios. The sub-algorithms include Multiple Polygon Areas (MPA) approach, Zero Integrated Heading Rate (ZIHR) and Heuristic Height (HH). The performance of the full CHAIN algorithm will be tested and evaluated by presenting the results from a series of field trials.

Finally, Chapter 9 concludes the thesis by summarizing the major findings. Based on the results achieved during the research, conclusions will be drawn. The summary of contributions will be detailed again, and the continuity of the research will be suggested by recommending further research.

1.4 Thesis Structure

To improve the understanding of the structure and layout of the thesis, each chapter in the thesis is structured to have three distinct features; the preface, the content and the summary. The preface, which appears at the first page of each chapter, briefly summarizes the content that the chapter intends to deliver, and optionally the significance made by the chapter. The summary, which appears at the last page of each chapter, summarizes the content that the chapter has delivered to the reader. To visualize the whole thesis flow, a thesis flowchart is drawn in Fig. 1.1:

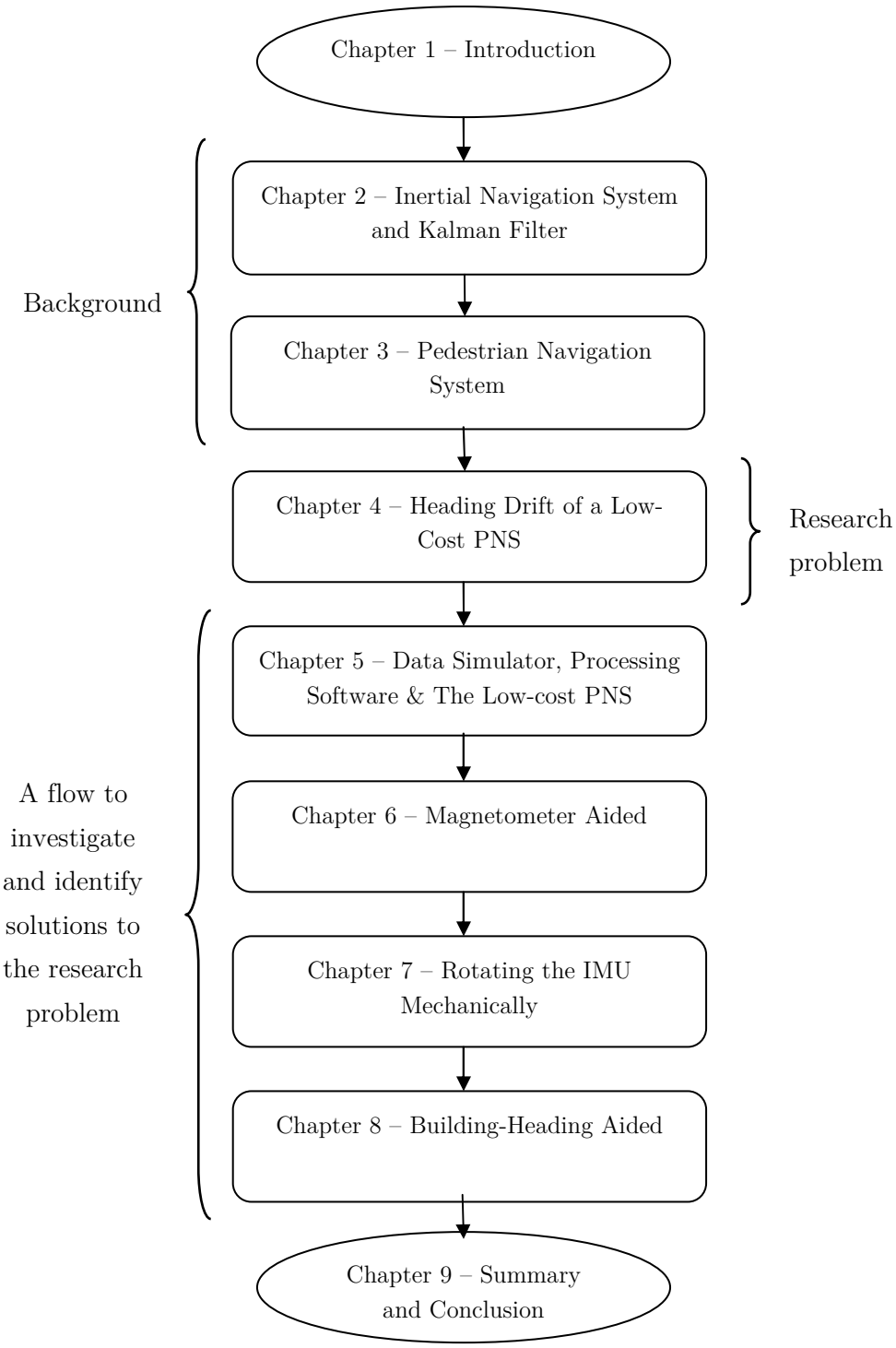

Fig. 1.1: Thesis flowchart

1.5 Summary

The opening chapter of this thesis has provided the relevant background to support the research into low-cost inertial Pedestrian Navigation Systems (low-cost PNSs). It has been pointed out that the current systems suffer limitations that might be overcome by suitable assistance. A set of research aims and objectives were then presented to address the issues. A brief overview of the thesis is provided, describing each chapter in turn and, finally, the contributions to knowledge made by the research are summarized.

Chapter 2

Inertial Navigation System and Kalman Filter

The main technology that was researched is inertial navigation technology. Therefore, before going into the literature of the research in the next chapter, this chapter is presented first to familiarize the reader with the technical background. It begins with an overview of the background theory behind the Strapdown Inertial Navigation System (SINS) technology. Following this, a section explaining the fundamentals of the Kalman Filter (KF) is introduced, followed finally by a chapter summary.

2.1 Introduction

The low-cost inertial Pedestrian Navigation System (low-cost PNS) presented in the thesis uses an inertial navigation technology. Therefore, this chapter will attempt to describe briefly the inertial sensors and how they can be used to navigate, using a technology known as an inertial navigation. First, Section 2.2 will introduce the inertial navigation, before focussing next on the low-cost MEMS inertial sensor technology in Section 2.3. This is followed by Section 2.4, where it will describe the strapdown inertial navigation technology that was used in the research. This involves describing the inertial sensor mechanization process to produce position solutions from inertial sensor data. Finally, Section 2.5 briefly explains the fundamentals of the Kalman Filter (KF) as an estimation filter, as it was used in the research to estimate the low-cost inertial sensors' errors.

2.2 Inertial Navigation

Inertial navigation can be said as an autonomous navigation technique that uses the concept of 'dead-reckoning'. This implies that it navigates on its own, based on the information produced by its sensors, without requiring external information. In reality, however, it does require *a priori* information, which consists of an initial position, velocity and attitude of the system. In order to navigate, current displacement and attitude are computed through a set of mathematical navigation equations and added to the previous position and attitude information.

The combination of Inertial Measurement Unit (IMU) and a navigation processor to do the computation can be collectively known as Inertial Navigation System (INS). An IMU typically contains three orthogonal accelerometers and three orthogonal gyroscopes (gyros). The accelerometers measure specific force, which is the acceleration due to all forces, whilst gyros measure angular rate. The term navigation processor refers to the computer used to 'mechanize', or process these measurements using mathematically formulated navigation equations.

Through mechanization, the IMU measurements are processed, or computed, to get the current position, velocity and attitude information. The mechanization process will be explained in detail in Section 2.4.

INS can be generally divided into two categories; one is known as a stable platform INS or Gimballed INS (GINS), and another one is known as a Strapdown INS (SINS). In the stable platform INS (Woodman, 2007), the IMU is mounted on a stable platform and aligned with the global frame of reference. In order to keep the platform stable and free from any external rotation, gimbals are used. If there is a rotation, the amount of rotation or attitude rate will be picked up by the gyros on the platform. Thus, any platform rotation will be neutralized by subtracting it with the attitude rate obtained from gyros. A stabled-platform permits the accelerometers to be used correctly because forces due to gravity can be deducted directly from the accelerometer measurements. The position is then acquired by 'integrating' the accelerometers measurements twice. The second configuration, SINS, is used in the research because of its convenience for pedestrian navigation. As the name implies, strapdown inertial navigation is defined when an IMU is 'strapped' to the body of a system or onto a device where the IMU is installed. SINS will be covered in detail, including its mechanization, in Section 2.4.

2.2.1 IMU Grades

There are generally four categories of IMU, often defined to describe the four different grades of inertial sensors used. The lowest grade is commonly known as the consumer grade and the second lowest grade is known as the low-cost grade. The medium grade is known as the tactical grade, whilst the highest grade is known as the navigation grade. The categorization of different grades is mainly based on the IMU price and specifications. This means that usually the lowest grade is the cheapest and has the lowest specifications (for example in terms of error specifications). Because of this, it is commonly found in consumer devices such as smart phones, laptops and motion-enabled games controller. Table 2.1 shows a typical performance comparison for different grades of IMU. The difference

between error terms which appeared in the table (bias, scale factor and noise) will be explained in Section 2.3.1.

The research presented in this thesis uses low-cost grade IMU with strapdown INS technology. Although it is tempting to use current consumer grade inertial sensors as they are the 'lowest-cost', it is considered to be not convenient for the research. This is because typically they have extremely high and varying error specifications, which means they must be estimated and modelled correctly within a very short period of time. If not, when the inertial navigation technology is used, the errors that are not properly estimated (for example because of the inaccurate dynamic model used – dynamic model will be described in Section 2.5.2) will grow rapidly within this short period. This will finally corrupt the computed position solution. In the case of pedestrian navigation, this poses a daunting task in the estimation process because then it needs a very high rate of measurement updates to help the estimation process and possibly a very precise dynamic model, which often are not available. In contrast, these consumer grade inertial sensors are commonly used in consumer devices because they can be used for non-positioning tasks. For example, they can detect sudden/abrupt change of acceleration and orientation to activate certain simple task (O'Reilly and Weinberg, 2010) such as changing screen orientation from landscape to portrait for smart phones.

The next Section 2.3 will focus on Micro-Electro-Mechanical System (MEMS) IMU (the type of inertial sensor used in this research), which falls under the low-cost grade IMU. For further descriptions of navigation and tactical grades IMU, readers are directed to texts such as (Groves, 2008).

Table 2.1: IMU grades: performance and cost data (MicroStrain, 2011a; Blake, 2008; Lukianto et al., 2010; Invense, 2010; STMicroElectronics, 2010; Farnell, 2010; SparkFun, 2010)

IMU Grade	**Navigation**	**Tactical**	**Low-cost**	**Consumer**
Example	Honeywell CIMU	Honeywell HG1700	Microstrain 3DM-GX3-25	Invensense ITG-3200 (gyros) STMicroelectronics LIS3LV02DL (acc)
Dim.(mm)	204x204x168	94 dia, 74 ht	44x25x11	Gyro (4x4x0.9) Acc(4.4x7.5x1.0)
Cost	~£60,000	~£14,000	~£1700	Gyro (~£17/unit, ~£38/board), Acc (~£14/unit, ~£31/board)
Gyro	Ring Laser	Fibre Optic	MEMS	MEMS
Bias(^{0}/hr)	0.0035	1-10	0.2 ^{0}/s	4 ^{0}/s
Scale Factor Error	5 ppm	150 ppm	$<$ 2000 ppm	-
Noise ($^0/\sqrt{hr}$)	0.0025	0.125 - 0.5	3.5	22.8
Accelerometer	Silicon	Silicon	Silicon	Silicon
Bias (mg)	0.05	1-2	$<$ 10	$<$100
Scale Factor Error	100 ppm	300 ppm	$<$ 2000 ppm	-
Noise (mg/$\sqrt{Hz}$)	-	-	-	-

2.3 MEMS Inertial Sensor Technology

The low-cost IMU used in this research features an off-the-shelf Micro Electro Mechanical System (MEMS) type IMU. Because of its attractive specification such as low-power consumption, no-moving parts, cheapness, compact size, enhanced durability and mass production capability, these sensors are becoming more popular in consumer-grade navigation systems. In 2007, the MEMS-based systems was reported to have generated $47 billion in revenue, and estimated to grow to a massive $103 billion by the end of year 2012 (Boucher and Lensch, 2010).

MEMS uses micro-fabrication technology to mini-fabricate quartz and silicon sensors in a large volume, on a common single wafer (Kourepenis et al., 1998). The use of quartz and silicon, as proven in semiconductor electronics industry for inertial sensing elements, is therefore very significant for cost reduction especially when they are mass produced. An IMU typically consists of three orthogonal accelerometers and gyros. A simple construction of a MEMS accelerometer is shown in Fig. 2.1, where it contains proof mass, usually held by a flexural support (ibid.). It works by measuring the displacement of the proof mass, due to acceleration, using a pickup sensor. Alternatively, the force required to maintain its position can also be measured.

Another typical MEMS gyro contains a vibrating proof mass held by a flexural support, operating on a slightly different principle. It uses Coriolis acceleration effect on the vibrating proof mass to detect inertial angular rate (Leondes and Apostolyuk, 2006). Fig. 2.2 shows the basic principle of Coriolis acceleration (Titterton and Weston, 2004) and Fig. 2.3 shows its principle in MEMS gyros (Chang et al., 2006). In Fig. 2.3, the proof mass is made to vibrate with certain velocity by a drive motor. This velocity vector axis (x-axis) is perpendicular with the angular rate input axis (z-axis, out of the plane). When angular rate is applied on its input axis (gyro rotates), a Coriolis force is produced, which induces an oscillation of the proof mass in y-axis. Angular rate can then be estimated by measuring the amplitude of the oscillation in y-axis (Coriolis acceleration), which is proportional to the applied input rate.

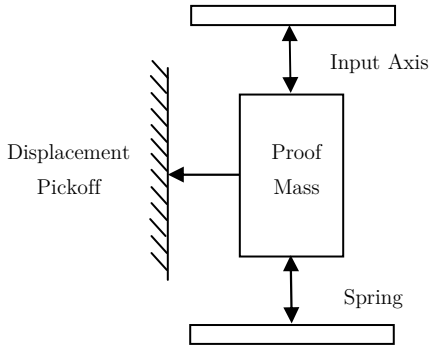

Fig. 2.1: Basic principle of MEMS accelerometer

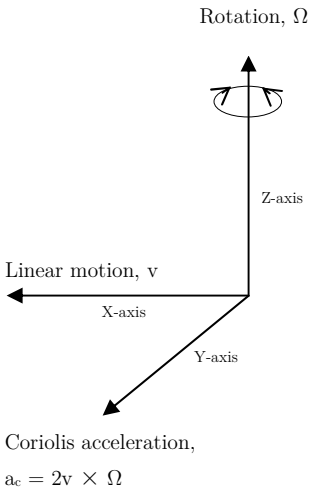

Fig. 2.2: Coriolis force generation

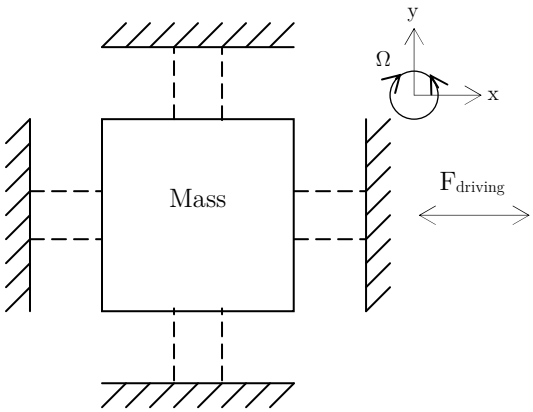

Fig. 2.3: Simple principle MEMS vibrating gyroscope

2.3.1 Error Characteristics

According to Groves (2008), each MEMS IMU error has some or all of these components: a fixed contribution, a temperature-dependent variation, a run-to-run variation, and an in-run variation. A fixed contribution error and a temperature dependent variation error can be corrected using a suitable factory calibration (Aggarwal et al., 2008, Skog and Handel, 2006). A run-to-run variation error, although different each time the sensor is used, remains constant within any run. It can be addressed during system alignment (which will be explained in Section 2.3.3.1), although typically not for all errors because of an observability problem (observability will be explained in Section 4.4). The fourth component, which is an in-run variation error that slowly changes during its operation, cannot be corrected during system alignment. Nonetheless, although there are still some residual errors from the first three components, it is this fourth component that can affect the performance of MEMS IMU the most.

In the case of MEMS gyro, for example, the measurement equation for the most common significant errors can be written as (Mezentsev, 2005):

$$G_w = \omega + b_\omega + S.\omega + \varepsilon\left(\omega\right) \tag{2.1}$$

where G_w is the gyro measurement, ω is the true angular velocity, b_ω is the gyro bias, S is the gyro scale factor error, and $\varepsilon\left(\omega\right)$ is the gyro noise. Theoretically, all errors in this equation can be estimated, provided good quality measurements with sufficient dynamics are available to observe each errors. Otherwise, MEMS gyro errors cannot be observed separately and often, they are modelled simply as gyro bias with noises that includes all of the above errors. A similar situation is also often assumed for MEMS accelerometer type errors (ibid.), where all the accelerometer errors are modelled simply as accelerometer bias error.

The next Section 2.3.1.1, 2.3.1.2 & 2.3.1.3 will discuss the MEMS IMU dominant error sources that appeared in Table 2.1 (bias, scale factor error and random noise), which may fall under the fourth error component that affect both accelerometers

and gyros performance. For a detailed explanation on other IMU error sources such as cross-axis sensitivity, temperature dependence and axis misalignment errors, please refer to texts such as Groves (2008).

2.3.1.1 Bias

Bias can be defined as the offset of the output signal from the true value. It can be split into two terms, static bias and dynamic bias (ibid.). It is usually specified in milli-g, (mg), for accelerometers (b_a) and degrees per hour, ($^0/h$), for gyros (b_g).

$$b_a = b_{as} + b_{ad}; b_g = b_{gs} + b_{gd}, \tag{2.2}$$

Static bias (b_{as}, b_{gs}) is a constant bias throughout the IMU operation, but differs from every IMU run. For example, it is possible to estimate gyro bias by taking an average measurement for a certain time when the IMU is stationary. Dynamic bias (b_{ad}, b_{gd}) which is sometimes called bias instability, is a varying bias that may change over a specified period of time. For example, if the gyro bias instability is quoted as 10 $^0/h$ for 60 s and the known bias at time t is $b_a(t)$, it means that the bias at $(t + 60)$ is a random variable with an expected value of $b_a(t)$ and a standard deviation of 10 $^0/h$.

An uncompensated bias can introduce error in the computed velocity and position. Eq. (2.3) shows that an uncompensated accelerometer bias introduces error proportional to time (t) in velocity and proportional to (t^2) in position (Aggarwal et al., 2010):

$$v = \int b_f \, dt = b_f \, t \Leftrightarrow p = \int v \, dt = \int b_f \, t \, dt = \frac{1}{2} b_f \, t^2 \tag{2.3}$$

where b_f is accelerometer bias, p is the position and v is the velocity.

Likewise, an uncompensated gyro bias introduces an angle error, $\delta\theta$ proportional to time, t as:

$$\delta\theta = \int b_w \, dt = b_w \, t \tag{2.4}$$

where b_w is the gyroscope bias.

The small tilt angle error will cause a misalignment of the INS, and therefore project the acceleration vector in the wrong direction. This results in a proportional acceleration to $\delta\theta$ ($a = g\ \sin(\delta\theta) \approx g\ \delta\theta = g\ b_w t$) in one of the horizontal axes. Position and velocity errors, as a result of this angle, are given by:

$$v = \int a\ dt = \int g b_w t\ dt = \frac{1}{2} g b_w\ t^2 \tag{2.5}$$

$$p = \int v\ dt = \int \frac{1}{2} g b_w\ t^2\ dt = \frac{1}{3} g b_w\ t^3. \tag{2.6}$$

For example, suppose accelerometer bias is $1\ ms^{-2}$ and gyro bias is $1\ ^0/s$ (approximately $0.02\ rad/s$). If these biases are not compensated in the measurements, accelerometer bias will generate a $50\ m$ error in position after only $10\ s$, and $5\ km$ error after $100\ s$. In contrast, gyro bias will generate a $27.8\ m$ error in position after $10\ s$, but then grow to $27.8\ km$ after $100\ s$. This shows that over time, the effect of gyro bias on position error is more pronounced than accelerometer bias as it introduces cubic error growth in position error.

2.3.1.2 Scale Factor Error

Scale factor is the ratio of the sensor input and sensor output. A scale factor error is the error in this ratio after unit conversion, which means a zero scale factor error produces a unity ratio. It can be caused by, for example, the imperfection in the pick-off sensor inside IMU assembly (Weinberg and Kourepenis, 2006). It is often expressed in units of parts-per-million (ppm). For MEMS IMU, as tabulated in Table 2.1, the scale factor error can be as high as 2000 ppm ($0.2\ \times 10^{-2}$) or 0.2 percent from the true output.

2.3.1.3 Noise

The MEMS IMU outputs are perturbed by various sources of noise, such as thermal noise and electrical noise (Woodman, 2007). Gyro noise is integrated to

produce Angular Random Walk (ARW), and accelerometer noise is integrated to produce Random Walk (RW) on its velocity solution. Usually manufacturers specify noise in terms of ARW with units in degrees per hour ($^0/\sqrt{hr}$). Some specify it as Power Spectral Density $(^0/hr)^2/Hz$) or FFT ($^0/hr/\sqrt{Hz}$) noise density, in which case the conversion between them can be made using formula described in Stockwell, (n.d). For example in Table 2.1, the Honeywell HG1700 has gyro noise specification of $0.5^0/\sqrt{hr}$, which means after 1 hour the standard deviation of attitude error will be 0.5^0; after 2 hours about $0.5^0.\sqrt{2} = 0.71^0$, and after 3 hours about $0.5^0.\sqrt{3} = 0.87^0$.

2.4 Strapdown Inertial Navigation System

This research used a low-cost MEMS IMU with a Strapdown Inertial Navigation System (SINS) configuration. The discussion afterwards will use the term IMU to represent the low-cost MEMS IMU.

The heart of SINS is the navigation processor, which uses the IMU measurements using a process called mechanization. Fig. 2.4 shows the mechanization process in general. The IMU measurements are measured in its own body frame with respect to an inertial frame (frame definition will be covered in Section 2.4.1). The process starts by integrating the rate gyroscope measurements to get the orientation (or attitude) of the system. This orientation is then used to transform accelerometer measurements from the body frame to the resolving frame. This research uses navigation frame as the resolving frame (Section 2.4.1.3), where resolving frame is defined as a set of axes in which the motion is represented (Groves, 2008). Next, after subtracting gravity, the transformed accelerometer measurements are integrated to yield velocity, and the velocity is integrated again to yield displacement. The displacement is then added to the previous position solution to produce the current position solution.

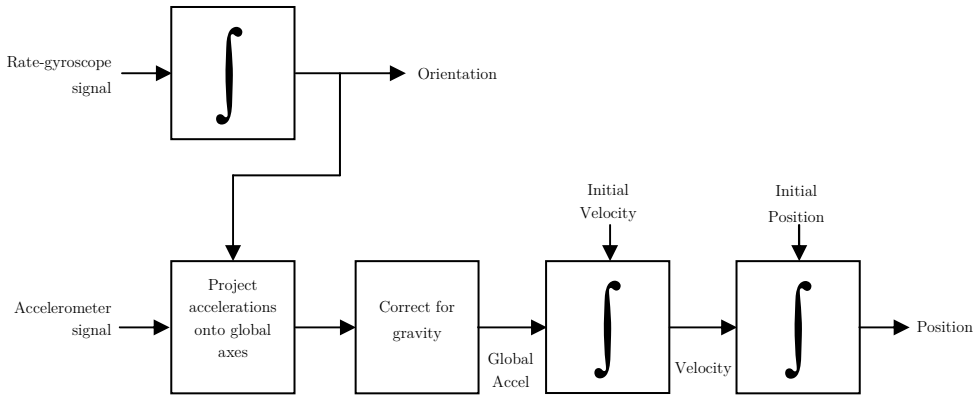

Fig. 2.4: Strapdown inertial navigation algorithm (Woodman, 2007)

2.4.1 Coordinate Frames

There are four types of coordinate frame typically used in inertial navigation (Shin, 2005): the inertial frame, the earth frame, the navigation frame and the body frame. These coordinate frames are used because the INS mechanised outputs, which comprise position, velocity and attitude, need to be transferred to meaningful navigation information to user.

2.4.1.1 The Inertial Frame

The inertial frame (*i*-frame) is an ideal reference frame where it does not rotate nor accelerate. In practice, however, a more practical approach is adopted as it is difficult to define the true *i*-frame. Distant fixed stars are, therefore, used as a point of reference for a generic *i*-frame, where the coordinate frame does not accelerate and does not rotate with respect to this point. In other words, the coordinate frame does not rotate along with the earth. It is commonly known as Earth-Centred Inertial (ECI) frame, where earth-centred simply means that the frame's origin is at the Earth's centre of mass. The *x*-axis and *y*-axis lie along the equatorial plane such that *x*-axis always points toward the mean vernal equinox and *y*-axis always lies 90^0 ahead of *x*-axis in the direction of Earth's rotation. The *z*-axis always points along the mean rotation axis of the Earth.

2.4.1.2 The Earth Frame

The earth frame (*e*-frame) more commonly known as Earth-Centred Earth-Fixed (ECEF) frame is also an earth-centred coordinate frame. As opposed to ECI, however, where the axes do not move together with the Earth, ECEF axes moves together with the Earth (remains fixed with respect to the Earth). The *x*-axis points from the Earth's centre of mass towards the equator, which intersects with 0^0 longitude and 0^0 latitude (Greenwich Meridian). The *y*-axis completes the right-handed orthogonal system, whilst the *z*-axis points from the centre towards the North Pole (true, not magnetic).

The *e*-frame rotates about the *z*-axis at a rate known as Earth rate. This rotation rate vector with respect to *i*-frame resolved to the *e*-frame is given as (Farrell and Barth, 2008):

$$\omega_{ie}^{e} \approx \begin{pmatrix} 0 & 0 & \omega_e \end{pmatrix}^T \tag{2.7}$$

where ω_e is the magnitude of Earth rate ($7.292115 \times 10^{-5}\ rad/s$). This value, however, can be considered an approximation because it depends on the approximation of earth's geoid to an ellipsoid. Apart from Cartesian coordinates, the position vector, r_e can also be expressed in geodetic latitude (φ), longitude (λ), height (h) in *e*-frame relative to an ellipsoid (most commonly the WGS-84 ellipsoid) as follows (ibid.):

$$r_e = \begin{pmatrix} x \\ y \\ z \end{pmatrix} = \begin{pmatrix} (R_N + h)\, cos\varphi\, cos\lambda \\ (R_N + h)\, cos\varphi\, sin\lambda \\ (R_N(1 - e^2) + h)\, sin\varphi \end{pmatrix} \tag{2.8}$$

where e is the eccentricity of the reference ellipsoid and R_N is the meridian radius of curvature. Eccentricity describes how elliptical the ellipsoid, where $e = 0$ means the ellipsoid is perfectly sphere.

2.4.1.3 The Navigation Frame

The navigation frame (n-frame) is a local geodetic coordinate frame that has its x-axis points towards geodetic North. The y-axis completes the right-handed orthogonal system, thus pointing towards geodetic East. The z-axis is normal (makes 90^0 angle) to the surface of reference ellipsoid, pointing roughly towards the centre of the Earth. Thus, the n-frame is also commonly known as North-East-Down (NED) system. The frame's origin overlaps with body frame's origin (this will be explained in Section 2.4.1.4). The n-frame is often used (as in this research) because users want to know their attitude relative to North, East and Down direction. The n-frame is subjected to a rotation with respect to the e-frame referred to as a transport rate (ω_{en}^{n}). The navigation frame's rotation to keep North axis aligned is done on a rotating earth, causes Coriolis acceleration, which, therefore, needs to be accounted for during IMU mechanization.

2.4.1.4 The Body Frame

The body frame (b-frame) is a coordinate frame that remains fixed with respect to the IMU. Its origin coincides with the n-frame's origin. The x-axis points forward, which represents the typical direction of travel. The y-axis completes the right-handed orthogonal system, whilst z-axis points downwards, which is the typical direction of gravity. For angular motion, x-axis, y-axis and z-axis are often known as roll-, pitch- and yaw-axis respectively. All measurements in inertial sensors are, therefore, described in b-frame, with respect to i-frame.

2.4.2 Rotation of Coordinate Frames

In a case of INS, its output, measured in b-frame, needs to be represented in more meaningful information for user interpretation. This can be done by transforming, for example, the INS b-frame output to n-frame representation as used in this research. To do this, coordinate frames rotation is done by rotating each coordinate axis in successive rotations. The rotation can be represented in inertial navigation

using Euler angles or quaternions (ibid.). The next section describes the coordinate transformation matrix using Euler angle from *b*-frame to *n*-frame.

2.4.2.1 Earth to Navigation Frame

In order to transform measurements in *e*-frame, such as from Global Positioning System (GPS) data, to the *n*-frame, the rotation is performed in two steps. Firstly, the coordinate axes are rotated about the ECEF *z*-axis such that the rotated *y*-axis is aligned with the East axis of *n*-frame. Secondly, the axes are rotated about the new *y*-axis to align the new *z*-axis with the Down axis of *n*-frame. This results in the rotation matrix (Shin, 2005, Hide, 2003):

$$C_e^n = \begin{pmatrix} -sin\varphi cos\lambda & -sin\varphi sin\lambda & cos\varphi \\ -sin\lambda & cos\lambda & 0 \\ -cos\varphi cos\lambda & -cos\varphi sin\lambda & -sin\varphi \end{pmatrix} \tag{2.9}$$

Similarly, transformation from the *n*-frame to the *e*-frame can be obtained via its transpose matrix because Eq. (2.9) is orthogonal. The transpose is denoted by the superscript T, $C_n^e = (C_e^n)^T$.

2.4.2.2 Body to Navigation Frame

In order to make IMU measurements constructive to the user, it is resolved into *n*-frame such that the user is able to recognize their position in relation with North, East and Down directions on Earth. To do this, a series of Euler Angles rotations: roll (ϕ), pitch (θ) and yaw (ψ) angles, are rotated in order. Each corresponding rotation matrix is multiplied in its corresponding order to produce the coordinate transformation matrix. The rotation order is therefore critical because of the non-commutative behaviour of matrix multiplication. This means that if the rotations are performed in different order, the orientation of the axes after transformation will be different. The coordinate transformation matrix, commonly called Direction

Cosine Matrix (DCM), from *n*-frame to *b*-frame can be written as (Farrell and Barth, 2008; Groves, 2008),

$$C_n^b = C_3 C_2 C_1$$

$$= \begin{pmatrix} 1 & 0 & 0 \\ 0 & cos\phi & sin\phi \\ 0 & -sin\phi & cos\phi \end{pmatrix} \begin{pmatrix} cos\theta & 0 & -sin\theta \\ 0 & 1 & 0 \\ sin\theta & 0 & cos\theta \end{pmatrix} \begin{pmatrix} cos\psi & sin\psi & 0 \\ -sin\psi & cos\psi & 0 \\ 0 & 0 & 1 \end{pmatrix} \quad \textbf{(2.10)}$$

Therefore, because of its orthogonality, the DCM from the *b*-frame to *n*-frame can be found via its transpose matrix,

$$C_b^n = (C_n^b)^T = C_1^T C_2^T C_3^T$$

$$= \begin{pmatrix} c\theta c\psi & -c\phi s\psi + s\phi s\theta c\psi & s\phi s\psi + c\phi s\theta c\psi \\ c\theta s\psi & c\phi c\psi + s\phi s\theta s\psi & -s\phi c\psi + c\phi s\theta s\psi \\ -s\theta & s\phi c\theta & c\phi c\theta \end{pmatrix} \quad \textbf{(2.11)}$$

where *sin* and *cos* are denoted as s and c respectively.

The Euler angles can then be extracted from the DCM using the following equations:

$$\phi = tan^{-1}(\frac{C_{32}}{C_{33}}) \quad \textbf{(2.12)}$$

$$\theta = sin^{-1}(C_{31}) \quad \textbf{(2.13)}$$

$$\psi = tan^{-1}(\frac{C_{21}}{C_{11}}) \quad \textbf{(2.14)}$$

where C_{mn} refers to row (m) and column (n) of elements in Eq. (2.11).

The coordinate frame transformation can also use a quaternion. The quaternion, q, is a vector that has four components:

$$q = \begin{pmatrix} q_0 & q_1 & q_2 & q_3 \end{pmatrix}^T \tag{2.15}$$

where q_0 represents the magnitude of the rotation, and the other three components represent the three axes where the rotation takes place. It is often used for coordinate transformations because of its efficient computation such as lack of trigonometric functions and the fact that only four parameters are involved (ibid.). If Euler Angles are used, the transformation from *b*frame to *n*-frame can be computed as (Shin, 2005):

$$q_b^n = \begin{pmatrix} cos\frac{\phi}{2}cos\frac{\theta}{2}cos\frac{\psi}{2} + sin\frac{\phi}{2}sin\frac{\theta}{2}sin\frac{\psi}{2} \\ sin\frac{\phi}{2}cos\frac{\theta}{2}cos\frac{\psi}{2} - cos\frac{\phi}{2}sin\frac{\theta}{2}sin\frac{\psi}{2} \\ cos\frac{\phi}{2}sin\frac{\theta}{2}cos\frac{\psi}{2} + sin\frac{\phi}{2}cos\frac{\theta}{2}sin\frac{\psi}{2} \\ cos\frac{\phi}{2}cos\frac{\theta}{2}sin\frac{\psi}{2} - sin\frac{\phi}{2}sin\frac{\theta}{2}cos\frac{\psi}{2} \end{pmatrix} \tag{2.16}$$

2.4.3 Navigation Frame Mechanization

In inertial navigation, the mechanization can be defined as the process of producing navigation solutions from a set of raw measurements obtained from inertial sensors. The mechanization approach is comprehensively described in main texts such as Groves (2008), Farrell and Barth (2008), Titterton and Weston (2004), Hide (2003) and Shin (2005), so is briefly described in this section. Only the navigation frame mechanization will be covered although different coordinate frames can also be used. It starts with the initialization and alignment of the system, followed by the use of differential equations to produce navigation solutions.

2.4.3.1 Initialization and Alignment

The INS mechanization process starts with initialization and alignment of the system. Initialization is often defined as the process of obtaining the initial position

and velocity of the system, whilst alignment is usually referring to the process of obtaining the initial attitude parameters of the system (Hide, 2003).

Because of its inertial behaviour, an INS must be initialized from external measurements. In a case of an integrated INS/GPS system, for example, INS is normally initialized with the position and velocity information obtained from GPS. This obviously depends on how well and reliable the GPS measurements are. Alternatively, manual initialization can also be performed, for example by using a pre-surveyed coordinates and known velocity (zero velocity in a case of stationary INS).

For IMU alignment, the process is often divided into two. First is the horizontal alignment, sometimes known as levelling, which is used to obtain initial roll and pitch estimates. Second is the heading alignment, sometimes known as gyrocompassing; which is used to obtain the initial yaw estimates.

In horizontal alignment, accelerometer measurements are often used for stationary IMU. This is because while the IMU is stationary, the only specific force sensed by the accelerometers is the reaction to gravity, which is in the negative direction of the navigation frame Down axis. Therefore, the raw measurements in body frame, f^b can be compared with the known (or modelled) gravity vector,

$$f^b = \begin{pmatrix} f_x \\ f_y \\ f_z \end{pmatrix} = -C_n^b \begin{pmatrix} 0 \\ 0 \\ g^n \end{pmatrix} = \begin{pmatrix} sin\theta \\ -sin\phi cos\theta \\ -cos\phi cos\theta \end{pmatrix} g \qquad \textbf{(2.17)}$$

which can then be solved for initial roll, ϕ, and pitch, θ, as follows,

$$\begin{pmatrix} \phi \\ \theta \end{pmatrix} = \begin{pmatrix} atan2(-f_y, -f_z) \\ atan2(f_x, \sqrt{f_y^2 + f_z^2}) \end{pmatrix} \qquad \textbf{(2.18)}$$

For heading alignment, the underlying principle is that while stationary, the only rotation sensed by the gyros is the Earth rotation, which rotates about the z-direction of the ECEF frame in Eq. (2.7). Since the East component of Earth rotation is zero, the initial yaw measurement can be found by rotating the IMU about its z-axis such that the East gyro component will be zero. Through this process, the x-axis of IMU will be aligned to North, thus providing the initial heading for the system. The process of horizontal and heading alignment is sometimes known together as coarse alignment process.

After position, velocity and attitude of the INS have been initialised and coarsely aligned, a fine alignment is often made using an estimation algorithm such as the Kalman Filter (Kalman, 1960, Maybeck, 1979). This is because after a few seconds of coarse alignment, there are still residual attitude errors between the estimated and the true attitude that could be resulting from the systematic errors in the IMU outputs. Using stationary IMU, the observations can be defined as

$$\delta f^n = f^n - \hat{f}^n \tag{2.19}$$

$$\delta \omega^n = \omega^n - \hat{\omega}^n \tag{2.20}$$

where f^n and ω^n are the known gravity vectors and Earth rotation, and $\hat{f}^n$ and $\hat{\omega}^n$ are the current measurements from the IMU.

Both processes for heading alignment (coarse and fine alignment) require the gyro to be sensitive enough to measure Earth rotation rate. This therefore highlights the significance of heading alignment for the low-cost MEMS IMU because currently this is not possible. Other methods using external sensors such as GPS or magnetometer can be used for this purpose. GPS-based method, however, requires the system to be moving, which means a static heading alignment cannot be made. Furthermore, GPS measurements are likely to be perturbed by noise and multipath in harsh environments such as indoors and urban canyon, which means the GPS heading information may be noisy as well. Magnetometer can also be used for heading alignment using the horizontal component of the Earth's magnetic field

vector. Nevertheless, the accuracy depends on the quality of the measurements, which can be severely affected by magnetic disturbances that are likely indoors.

2.4.3.2 Navigation Frame Equation & Mechanization

Fig. 2.5, extended from Fig. 2.4, shows the mechanization process for SINS in the navigation frame. Several navigation equations are involved throughout the process. Attitude is referred to as the body-to-navigation-frame coordinate transformation matrix, C_b^n whilst position is referred to as latitude (φ), longitude (λ) and height (h). Notation for angular rate, for example ω_{ib}^n, is written as two subscripted letters and one superscript letter. Of the two subscripted letters, the first represents the frame which the rotation is in respect to, while the second represents the frame which the rotation is being measured. The superscript letter represents the frame whose rotation is being represented. Literally, ω_{ib}^n denotes the angular rate measured in body frame with respect to inertial frame, represented in navigation frame.

The next paragraph summarizes the forward mechanization process based on Fig. 2. It is largely influenced by the reference texts such as (Hide, 2003; Farrell and Barth, 2008; Titterton and Weston, 2004).

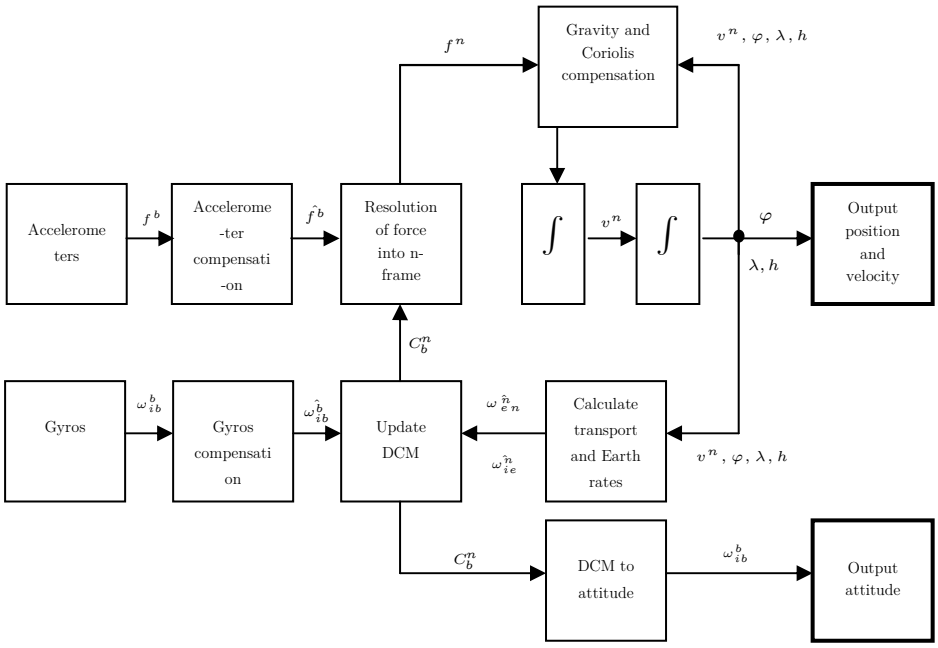

Fig. 2.5: INS mechanization process in navigation frame, adapted from Hide, (2003)

The iterative mechanization process is summarized as follows:

1. Sample the raw measurements from accelerometers and gyros in discrete time intervals. Accelerometers measure the specific force, denoted by f^b, and gyros measure the sensor rotation, denoted by ω_{ib}^b, with respect to inertial frame. An initial correction to the sensor measurements can be applied if the knowledge of the sensor errors is known, for example from laboratory tests, manufacturer specifications or an online calibration.

2. Compensate gyro measurements for the Earth's rotation, ω_{ie}^n, and the navigation frame transport rate, ω_{en}^n. This gives the turn rate of the body frame with respect to the navigation frame referenced in the body frame, ω_{nb}^b, given by:

$$\omega_{nb}^b = \omega_{ib}^b - C_n^b \left(\omega_{ie}^n + \omega_{en}^n \right) \tag{2.21}$$

where, using Eq. (2.7) and Eq. (2.9),

$$\omega_{ie}^{n} = C_{e}^{n}\omega_{ie}^{e} = \begin{pmatrix} \omega_e cos\varphi & 0 & -\omega_e sin\varphi \end{pmatrix}^{T} \tag{2.22}$$

and the transport rate, expressed in terms of the rate of change of latitude and longitude,

$$\omega_{en}^{n} = \begin{pmatrix} \dot{\lambda}\cos\varphi & -\dot{\varphi} & -\dot{\lambda}\sin\varphi \end{pmatrix}^{T} \tag{2.23}$$

Substituting $\dot{\varphi} = v_N/(R_N + h)$ and $\dot{\lambda} = v_E/(R_E + h)\cos\varphi$ into Eq. (2.23) yields:

$$\omega_{en}^{n} = \begin{pmatrix} \frac{v_E}{R_E+h} & -\frac{v_N}{R_N+h} & \frac{v_E \tan\lambda}{R_E+h} \end{pmatrix}^{T} \tag{2.24}$$

where v is the velocity in navigation frame, R_N is the meridian radius of curvature, and R_E is the transverse radius of curvature of the Earth.

3. Calculate the updated attitude from the rotation matrix, C_b^n .The attitude can be updated by propagating C_b^n in accordance with the equation:

$$\dot{C_b^n} = C_b^n \Omega_{nb}^b \tag{2.25}$$

where

$$\Omega_{nb}^{b} = \begin{pmatrix} 0 & -\omega_z & \omega_y \\ \omega_z & 0 & -\omega_x \\ -\omega_y & \omega_x & 0 \end{pmatrix} = \omega_{nb}^{b}\times \tag{2.26}$$

Thus, Eq. (2.25) can be rewritten, using Eq. (2.21), as:

$$\dot{C}_b^n = C_b^n(\omega_{ib}^b\times) - (\omega_{in}^n\times)C_b^n \quad \textbf{(2.27)}$$

where $\omega_{in}^n = \omega_{ie}^n + \omega_{en}^n$.

4. Resolve the specific force measurements from body to navigation frame using the updated attitude. Then, compensate the measurement for the local gravity vector (g^n) and Coriolis acceleration using:

$$\dot{v}^n = C_b^n f_b + g^n - (2\omega_{ie}^n + \omega_{en}^n)\times v^n \quad \textbf{(2.28)}$$

Integrate Eq. (2.28) to get velocity (in terms of latitude rate and longitude rate), and integrate again to get position in the navigation frame (where height is given by $\dot{h} = -v_D$).

5. Repeat process 1-4, where the current computed measurements are used in the next iteration.

2.4.3.3 INS Error Model

Shin (2005) explained in detail the difference between several types of inertial sensor error models: phi-angle model, psi-angle model, modified error model and large heading uncertainty model. The first two models perturb the navigation parameters with respect to different resolving frames: navigation frame and computer frame respectively. The third model modifies the first two models, whilst the last one addresses a case where the initial heading uncertainty may be large.

The phi-angle error model was used in this research to propagate error states that were being estimated. It perturbs the navigation parameters appeared in Eq. (2.27) & (2.28) with respect to the navigation frame, and can be written as (Hide, 2003; Titterton and Weston, 2004):

$$\delta\dot{r}^n = F_{rr}\delta r^n + F_{vr}\delta v^n \quad \textbf{(2.29)}$$

$$\delta\dot{v}^n = C_b^n\delta f^b + C_b^n f^b \times \epsilon + \delta g^n - (2\omega_{ie}^n + \omega_{en}^n)\times\delta v^n - (2\delta\omega_{ie}^n + \delta\omega_{en}^n)\times v^n \quad \textbf{(2.30)}$$

$$\dot{\epsilon} = -\omega_{in}^n \times \epsilon + \delta\omega_{in}^n - C_b^n\delta\omega_{ib}^b \quad \textbf{(2.31)}$$

where δr , δv and ϵ are the vectors of position, velocity and attitude errors respectively, $\times$ is the cross product operator, C_b^n is the rotation matrix that transform from body frame to local navigation frame, ω_{en}^n is the navigation frame transport rate, ω_{ie}^n is the Earth's rotation, δg^n is the gravity vector error and $\delta(\cdot)$ represents the error of specific vectors. F_{rr} and F_{rv} is the partial derivatives with respect to position and velocity (full expression of the matrices in Chapter 5). The middle terms in brackets in Eq. (2.30) that contain Earth rotation and gravity error can be ignored since low cost IMUs are not capable of measuring Earth rotation and also navigation is done with a small velocity in a small area (thus assumed insignificant gravity error). These error equations represent the system dynamic model, which are used to form the dynamic matrix, F in the Kalman Filter (this will be explained in Chapter 5).

An error model is used to describe the temporal behaviour of inertial sensor errors because of the uncertainties in the sensors and the gravity field. These uncertainties cause the navigation parameters computed from INS mechanization to have errors. Thus, using the knowledge from the error model, an estimation filter can be used to estimate the inertial sensor errors over time, and subsequently can be used to correct the navigation parameters. In this research, along with the error model, an error-state Kalman Filter was used as the estimation filter, which will be explained in Chapter 5. The next Section 2.5 therefore explains on the fundamentals of the Kalman Filter.

2.5 The Kalman Filter

One of the most common methods in estimation theory applications is the use of the Kalman Filter (KF). The KF is not actually a physical filter with electronics, but rather a series of mathematical equations. For an exhaustive explanation and derivation of KF and its sub-algorithms, including its limitations, readers are directed to more prominent texts such as Grewal and Andrews (2008).

This research used a traditional error-state KF to estimate INS errors, and, together with all the states that were modelled, will be covered in detail in Section 5.3. The KF was used because: (1) optimal estimation at the current epoch by the KF contains all previous statistical history of the system, (2) only estimations at the current epoch are required to predict the future states, and primarily (3) propagation of INS errors over time can be acquired, monitored and evaluated. Point (1) and (2) can be important for future development, where a real-time system might be possible because of the low computational load, whilst point (3) is significant for this research as the knowledge of the behavior of INS errors over time can be evaluated and solutions can be proposed.

The error-state KF that was used falls under an Extended KF (EKF), which is a linearized-type of KF that has an INS error control loop (feedback) control system (Shin, 2005), where it linearizes the system dynamic model and the measurement model. This means that the low-cost IMU errors are assumed to be propagated linearly, and the use of EKF with this assumption is deemed reliable for this research. This is because, in the case of an approach investigated in this research (which will be covered in the subsequent chapters), the time between measurement updates is typically very short (about ~1s). Within this short period, therefore, the assumption of linearization should be adequate to model the low-cost IMU errors. It might be possible, for example, if consumer grade IMU is used, this assumption might not be valid anymore. This results from its high error variations within a short period of time.

The next subsequent sections explain the fundamentals of KF, and are largely based on the references mentioned above.

2.5.1 Principle of the Kalman Filter

The Kalman Filter (KF) is a linear estimation technique that comprises a set of algorithms in a recursive configuration. The algorithms are made from a set of mathematical equations that describe the states of the system, and how these

states evolve over time using the system dynamics model. States are the quantities that are to be estimated and can be defined as a set of parameters that can sufficiently model the movement of a system, whilst a system dynamic model is defined as the change in the parameters of the state vectors with respect to time (Hide, 2003).

Using the algorithm and the statistical properties of the system measurement errors, the KF is able to estimate the current states and predict the future states of the system. This is done by updating the states with weighted measurements recursively, based on their statistical information. The system measurement error is defined as the error between the measured value and its predicted value from the KF (ibid.). KF is occasionally called a discrete KF because it is discreet in the time domain, where it is updated at some measureable time interval.

Often in navigation applications, many measurements are available from different sensors. For example in GPS/INS integrated applications, there are two position solutions from GPS and INS. The KF has the capability to weigh these two measurements statistically, in order to give the best estimate of position state. Apart from this, the KF is therefore a very useful tool because it uses every measurement available, based on its statistical information, to estimate the states of the system.

2.5.2 The Kalman Filter Models

In order to estimate the states, x, of the system, the KF uses two models known as dynamic model and measurement model. The dynamic model is represented in continuous time as

$$\dot{x} = Fx + Gu \tag{2.32}$$

Similarly, in discreet form, it is represented as

$$x_{k+1} = \Phi x_k + w_k \tag{2.33}$$

where x is the system state vectors, F is the system dynamic matrix, G relates the disturbing forces to the state vectors, u is the disturbing force vectors, Φ is the state transition matrix that relates the state vector from epoch (k) to epoch $(k+1)$ and w_k is the process noise vector.

A discrete measurement model is represented as,

$$z_k = H_k x_k + v_k \tag{2.34}$$

where z_k is the measurement vectors at time epoch k , H_k is the measurement model matrix (or design matrix), which linearly relates states to the measurements and v_k is the measurement noise vector.

Both noise vectors (w_k, v_k) are assumed to be uncorrelated with each other. They are also assumed to be zero mean Gaussian white, normally distributed and mutually independent, with their covariance written as,

$$P_w = E[w_a w_b^T] = \begin{cases} Q & a = b \\ 0 & a \neq b \end{cases} \tag{2.35}$$

$$P_v = E[v_a v_b^T] = \begin{cases} R & a = b \\ 0 & a \neq b \end{cases} \tag{2.36}$$

More details about how the processing software, which was used in the research, approximates these parameters for INS error estimation are given in Section 5.3.

2.5.3 The Kalman Filter Algorithm

The KF algorithm involves three stages: initialization, prediction and measurement update. The last two stages make the KF a recursive filter because it is done recursively. This means that after initialization, the KF predicts the states at epoch (k) using the previous epoch $(k-1)$, corrects it using new measurements, and then predicts again using the corrected states at the next epoch $(k+1)$, using epoch (k).

The minus (-) and plus (+) are used to describe *before* and *after* in the KF algorithm. For example, suppose x_k represents the state with epoch (k). This means that there exists a *before* and *after* error estimate, e_k at epoch (k), denoted by (-) and (+),

$$e_k^{(-)} = x_k - x_k^{(-)} \tag{2.37}$$

$$e_k^{(+)} = x_k - x_k^{(+)} \tag{2.38}$$

which produce a *before* and *after* error covariance estimates,

$$P_k^{(-)} = E\left[\ e_k^{(-)} . e_k^{(-)T}\ \right] \tag{2.39}$$

$$P_k^{(+)} = E\left[\ e_k^{(+)} . e_k^{(+)T}\ \right] \tag{2.40}$$

2.5.3.1 Initialization

The initialization stage starts by estimating the initial state vectors, $\hat{x}_0^{(+)}$, and its corresponding error covariance matrix, $\hat{P}_0^{(+)}$. The covariance matrix represents the uncertainty in the state vectors and in Kalman filter context, these two values are often known as a *priori.*

2.5.3.2 Prediction

There are two steps involved in prediction stage:

1. First, to estimate the state at epoch (k), $\hat{x}_k^{(-)}$, the previous best estimate at epoch ($k-1$), $\hat{x}_{k-1}^{(+)}$ is used,

   $$\hat{x}_k^{(-)} = \Phi \hat{x}_{k-1}^{(+)} \tag{2.41}$$

   where Φ is the state transition matrix.

2. Then, similar to step (1), the corresponding covariance at epoch (k), given by Eq.(2.39), is estimated using the previous best estimate at epoch ($k-1$), $P_{k-1}^{(+)}$,

   $$P_k^{(-)} = \Phi P_{k-1}^{(+)} \Phi^T + Q_{k-1} \tag{2.42}$$

where Q is the covariance of process noise vector from Eq.(2.35).

For the first iteration, these two values in Eq. (2.41) and Eq. (2.42) are obtained from the initialization stage (Section 2.5.3.1).

2.5.3.3 Measurement Update

There are essentially four steps involved in measurement update stage:

1. First, the innovation vector, $v_k^{(-)}$, is computed. It is the difference between the measurement, z_k , and the predicted estimate of the state (predicted measurement). It represents how far off the estimate was from the measurement and is computed using,

$$v_k^{(-)} = z_k - H_k \hat{x}_k^{(-)} \tag{2.43}$$

2. Next, the filter gain (Kalman gain), K_k, is computed. The Kalman gain is the weight between the predicted states and the innovation and is given as,

$$K_k = P_k^{(-)} H_k^T [H P_k^{(-)} H_k^T + R_k]^{-1} \tag{2.44}$$

3. Then, the filtered estimate of the states, $\hat{x}_k^{(+)}$, is finally updated using the innovation in Eq.(2.43), weighted by the Kalman gain in Eq.(2.44),

$$\hat{x}_k^{(+)} = \hat{x}_k^{(-)} + K_k [z_k - H_k \hat{x}_k^{(-)}] \tag{2.45}$$

4. Similarly, corresponding measurement update covariance matrix, $P_k^{(+)}$, is computed using,

$$P_k^{(+)} = (I - K_k H_k) P_k^{(-)} \tag{2.46}$$

It is common to use Joseph form for Eq.(2.46) because it improves numerical stability and has natural symmetry (Grewal and Andrews, 2008),

$$P_k^{(+)} = (I - K_k H_k) P_k^{(-)} (I - K_k H_k)^T + K_k R_k K_k^T \tag{2.47}$$

2.6 Summary

Several subjects relevant to the low-cost inertial pedestrian navigation system presented in this thesis have been reviewed. First, the basic principles of inertial navigation, in particular the Strapdown Inertial Navigation System with its low-cost MEMS IMU technology, was covered. It was then followed by an introduction to the Kalman Filter. These subjects now form the basis of the theoretical knowledge used in the research. Moving on to the next chapter, it will discuss the background literatures of the research application.

Chapter 3

Pedestrian Navigation System

This chapter begins by briefly reviewing the Global Positioning System (GPS)-based pedestrian navigation systems. Following this, aided pedestrian navigation systems are introduced for indoor navigation. They comprise different kinds of sensors and technology used to aid pedestrian navigation systems indoors. There then follows a section explaining the concept of an autonomous indoor pedestrian navigation system using foot-mounted-low-cost-IMU approach. This is then followed by a brief chapter summary at the end.

3.1 Introduction

An ideal Pedestrian Navigation System (PNS) should be able to navigate everywhere. Often the term *ubiquitous* is used in the research community to describe this capability. In general, pedestrian navigation can be divided into two categories: outdoor and indoor navigation. Outdoor navigation can be defined when navigation is done outside a building, whilst indoor navigation can be defined when navigation is performed inside a building.

Outdoor PNSs often utilize the Global Positioning System (GPS) as a means to help navigation. Extensive literature can be found on GPS technology and how it can be used to navigate (GPS, 2010; Groves, 2008; Titterton and Weston, 2004; Ahmed, 2006; Farrell and Barth, 1998). GPS is very useful as it provides continuous positioning and timing information anywhere in the world in any weather. Furthermore, GPS is available freely for civilian uses such as vehicle navigation, which typically requires only a few meters of position accuracy. As it is a passive-ranging (one way) system, it can serve an unlimited number of users, which is thus very convenient from a user's point of view. Some of the many commercial consumer navigation applications available today which use GPS are from widely known manufacturers such as, for example, TomTom, Navman, Garmin, Trimble, and Apple (Grejner-Brzezinska et al., 2008).

In the case of indoor PNSs, however, using GPS alone can be very problematic (Januszewski, 2010). This is because GPS performs best in an environment where there is a clear view of satellite signals and good satellite availability. This is not the case for indoor pedestrian navigation, as it is performed inside buildings, considered by many as a GPS-challenging environment (Lachapelle, 2004). To make thing worse, signal disturbance, such as because of jamming and spoofing, are always possible (Pozzobon, 2011). Furthermore, the GPS signals are transmitted such that the minimum received power for GPS signals is relatively low and thus very fragile to the transmission medium (will be discussed in Section 3.2.1). As a result, GPS signals will always get attenuated resulting from, for example

multipath. This is much worse inside buildings, where the level of attenuation is significantly higher because of variations in indoor infrastructures. For example, Lachapelle et al. (2004) recorded a maximum GPS signal attenuation of up to 30 dB when inside a building. Therefore, an aided system is often adopted for indoor PNSs (Fuchs, 2010, Fischer and Gellersen, 2010, Skog and Handel, 2009, Liu et al., 2007, Legat and Lechner, 2000). This is realized by using available infrastructure, sensors or information, to aid positioning for indoor pedestrian navigation.

Section 3.2 will describe various technologies that have been used to augment indoor PNSs. Following this, Section 3.3 will describe the low-cost autonomous PNS, which has been used throughout the research.

3.2 Aided PNS for Indoors

As explained in Section 3.1, an absolute positioning system, such as GPS, is quite useful and reliable in outdoor environments with a clear view of GPS signals, but using this technology indoors remains a complicated task. Therefore, an aided system (or an integrated system) is often adopted. Nevertheless, aided PNSs also face some challenges, as previously reported by for example Mather et al. (2006), Godha et al. (2006), Hide et al. (2009), Chen et al. (2009), Retscher (2007) and Grejner-Brzezinska et al. (2009). These challenges (or limitations) of some of the existing positioning systems for indoor pedestrian navigation are compared and tabulated in Table 3.1. Liu et al. (2007) and Fuchs (2010) have completed a survey on these indoor positioning systems, including their limitations. Thus, the next section will review the systems tabulated in Table 1 concisely. After considering the limitations of each system based on this review, an autonomous positioning system is proposed and explained in Section 3.3, which then becomes the basis of the research presented in this thesis.

Table 3.1: Comparison of indoor positioning system, adapted from Renaudin et al., (2007)

TECHNOLOGY	PROCESS	ACCURACY	ADVANTAGES	LIMITS
Network Based/Infrastructured-Systems				
GPS-based	Massive correlations, network-assisted ranging	5-50m	Improve signal tracking sensitivity and time-to-first fix	Multipath, not working in deep indoors
WiFi	Angle Of Arrival (AOA)	Up to 100m	2 Transmitter (Tx) provide a position	Multipath, range to Base Station (BS), antenna quality
	Time Of Arrival (TOA)	1-50m	High accuracy	Multipath, clock offset between Tx and Receiver (Rx)
	Time Difference Of Arrival (TDOA)	1-50m	High accuracy	Multipath
	Received Signal Strength (RSS)	Propagation models ~10m, fingerprinting 1-5m	High accuracy, compatible with existing hardware	Creation of RSS database/propagation models
RFID	Cell identity	Relative to cell size	Simple & compatible with existing handset	Number & size of the cells, multipath
UWB	AOA	Few decimetres	2 Tx provide a position	Range to Tx, antenna quality
	TDOA	Few decimetres	High accuracy	Low emission power, high Tx density
Visual sensor	Image matching,	~10-15 m	Compatible with existing handset	Blurry image, low-light, processing power, database
Map-matching	Advance filtering, fingerprinting	~1-2 m	High accuracy	Processing power, database quality, building geometry, map accuracy
Independent Positioning/Infrastructureless-System				
Inertial sensor	Dead reckoning, INS	~5% distance travelled	Autonomous system, position always available	Drifts affect the accuracy

3.2.1 GPS-Based

There are two types of GPS-based systems that can be possibly used for indoor pedestrian navigation. One is the High Sensitivity (HS)-GPS system and the other is the Aided (A)-GPS system, which will be explained next.

3.2.1.1 High Sensitivity GPS

As the name implies, High Sensitivity (HS) GPS is a system that is capable (or sensitive enough) to track weak GPS signals that are often found indoors (Watson

et al., 2006; Schon and Bielenberg, 2008; Schwieger, 2007; Zhang et al., 2010; van Diggelen and Abraham, 2001a). Typically, the direct received GPS L1 C/A-code signal power is specified to be at least -160 *dBW* (GPS, 2010). For example, Lachapelle et al. (2004) showed that in an indoor environment such as a residential garage and a concrete (or steel) building, the received signal power varied between -175 *dBW* to -190 *dBW*. Mezentsev et al. (2003) also demonstrated that a commercial HSGPS receiver (SiRF XTrac LP) was capable of tracking weak signals, as low as -185 *dBW*. This, therefore, implies that the HSGPS receiver can be used indoors because it has a high tracking sensitivity.

Traditionally, to acquire the GPS signal, a GPS receiver must search sequentially through the total 'search space' (or 'bins'), defined by the possible frequency offsets bins multiplied by the possible code-delay. The total search time is therefore the time taken to search the entire space, which means a sequential search is performed over possible code delays at each different frequency bins. Therefore, the high tracking sensitivity of the HSGPS receiver is made possible by enabling a longer search time (or dwell time) in each frequency bins. This increases the signal-to-ratio gain to up to 10 dB gain if a 10 *ms* increase in the dwell time can be afforded (Dedes and Dempster, 2005; van Diggelen and Abraham, 2001b) using the equation (van Diggelen and Abraham, 2001a):

$$20log_{10}(\sqrt{N}) \tag{3.1}$$

where N is the search time (in *ms*). This means that instead of searching sequentially over the possible code delays, a parallel search is performed by far more correlations in the receiver. With enough correlators, all possible code delays can be calculated at the same time. Therefore, because the total search time over the entire search space is still the same, the parallel correlation increases the search time in each frequency bin. This ultimately increases the sensitivity gain of the receiver.

The real problem, however, lies in the reliability of the received GPS signals indoors (Lachapelle, 2007). This is partly because of the inability to separate signal

interference errors, such as multipath, from good GPS signals. Multipath error occurs when duplicate GPS signals are received by the GPS antenna; one comes along a direct path from the GPS satellite and the other one arrives at a slight delay resulting from the reflection from nearby objects or surfaces. Thus, multipath is considered to be the largest error for HSGPS because it is extremely difficult to estimate and truly unpredictable (Mezentsev, 2005). For example, using a low-cost handheld HSGPS unit (Trimble Juno ST), it was demonstrated by Zandbergen and Barbeau (2011) that in a 2-hour static indoor test, although the solutions availability is close to 100%, the maximum horizontal error was still high at 18.94 *m*.

Even if the problem of multipath can be overcome, in many situations, there are simply too few GPS satellites in view to be used that have detectable reliable GPS signals and good geometry. In a worst case scenario, GPS satellites might not be in view at all such as in deep indoors (or underground). A logical approach would be to increase the availability of the satellites by combining different constellation as well. For example, O'Driscoll et al. (2011) investigated this using a combined GPS–GLONASS HSGPS receiver in an urban canyon. GLONASS is a GPS-like navigation satellite system owned and operated by Russia. Nonetheless, although the percentage of position solutions' availability and redundancy increased, their performance was found to be still limited by the effect of multipath. Until now, multipath investigation therefore attracts a major interest in GNSS research community (Soloviev and Dickman, 2011; Yi et al., 2011; Seung-Hyun, 2011; Dragunas and Borre, 2011).

3.2.1.2 Assisted GPS

The second GPS-based system that might possibly be used for indoor pedestrian navigation is Assisted (A)-GPS. It can be defined as a system that relays satellite data to GPS-receivers or HSGPS-receivers more quickly than it could be gathered autonomously from the satellite signals, using a telecommunication network-based approach (Brown and Olson, 2006; Dovis et al., 2008; Zandbergen and Barbeau,

2011). A-GPS normally involves a GPS receiver (for example a mobile phone) that is capable of receiving assistance data from a telecommunication network that has an assistance server. The assistance server can access information about GPS satellites from its reference network and can relay the information to the GPS receiver.

One of the benefits of A-GPS for indoor navigation is the improved acquisition sensitivity. The network can provide the GPS receiver with information from the server that reduces necessary search space. This increases the search time in the narrowed frequency offset bins, which then increases the sensitivity gain as in Eq. (3.1). For example, this can be done by providing the current ephemeris of the expected satellites in view to the GPS receiver. The GPS receiver can then use this information to estimate the satellite Doppler ahead of time, thus reducing the required frequency offset bins that must be searched during the acquisition period.

The same problem of multipath and satellite availability indoors faced by the HSGPS (discussed in the previous section) is also faced by the A-GPS. Additionally, A-GPS still require the GPS receiver always to have a link with the network (a good wireless link), and in some indoor areas might still pose a problem. Furthermore, time synchronization is an issue when relaying the information from the assistance server to the GPS receivers. First, the time of the assistance server must be in GPS time to ensure good synchronization when receiving the data from its reference stations. Second, it must be in a good synchronization with the GPS receivers indoors. This is so that the partial navigation message from the server can be accurately combined and decoded by the GPS receivers.

3.2.2 WiFi

WiFi, which stands for Wireless Fidelity, refers to any systems that use 802.11 IEEE standard. It is a system that allows computers that are equipped with a network card to connect to the internet wirelessly using a wireless router. According to the 802.11 standard, WiFi signals coverage typically range from 0 to 100 m in indoors. Thanks to its convenience to provide internet connection

wirelessly to multiple users, it has become the dominant local wireless networking standard and is very popular in houses, hotels, offices and public areas.

Although WiFi is not intended to be used for positioning, the pervasiveness of existing WiFi infrastructures has resulted in several commercial WiFi indoor positioning systems such as Ekahau (Ekahau, 2011) and SkyHook (SkyHook, 2011). Ekahau is a commercial positioning system intended primarily for positioning in public places such as hospitals. Signal strength information from tags (worn by users) are sent over the WiFi network, and processed by a central controller for accurate location determination and visualisation. Ekahau claims position accuracy is between 1 and 3 m. Similar with Ekahau, SkyHook uses the correlation between WiFi signal strength information with locations to calculate accurate locations. Whilst Ekahau is intended for certain defined and controllable areas such as hospitals (hence higher accuracy), SkyHook operates over larger areas. The coverage is claimed to cover most metro areas in North America, Europe, Asia and Australia, with position accuracy of between 10 and 20 m accuracy.

Generally, WiFi positioning technology can be divided into three (Vossiek et al., 2003): lateration (measurement of distance), angulation (measurement of angle) and fingerprinting (pattern matching). Fig. 3.1 and 3.2 show the lateration and angulation principles to determine one position. The black dots represent the transmitters and the red dots represent the position of the computed position.

In the lateration-based method, the time it takes for a signal to travel from a transmitter to a receiver is recorded (thus known as Time of Arrival, TOA). Based on the speed of signal propagation, the distance between the transmitter and the receiver can then be computed. For a proper localization in the lateration method, the distances to at least three reference points (transmitters) with known positions are required. Similarly, a variant of this method is using the round trip time of the signals. The transmitter sends the signal and waits for the signal to be reflected back. The distance between the transmitter and the receiver is computed as half the distance travelled by the signal. This can be quite costly and inconvenient because transceivers must be used at both ends. The major issue, though, with the

time based approach such as TOA (in fact with any other systems that depends on accurate timing) is the time synchronization concern. The time must be synchronized for all the transmitters and the receivers to ensure good accuracy. This means, if a 3 m accuracy is required, the time must be accurate to within 0.1 ns. This therefore leads either to a very expensive system, or to a less accurate system.

In the angulation-based method, the location of an object is determined from the measured angles to fixed reference points (with known locations). The direction (or angle) of the received signals from at least two references (transmitters) is captured (thus known as Angle of Arrival, AOA). However, the angulation using radio signals for example requires directive antenna and strongly affected by interferences and multipath propagation arriving from misleading directions within buildings (ibid.).

In the fingerprinting-based approach, the Received Signal Strength Indicator (RSSI) is used. It can be based either on the propagation-loss equation, or surveying the signal strength information and its correlated positions beforehand. A simple equation of propagation-loss says that the free-space signal transmission loss is proportional to the square of the distance between a transmitter and a receiver. Therefore, the distance can be calculated by knowing the difference between the transmitted and received power. More advance and complex signal propagation model may be required, however, to account for unpredictable transmission losses such as those resulting from multipath. In reality, this can still introduce errors because of the uncertainty of the propagation model. If the 'fingerprinted' method is used, where a survey of positions is made in advance, reliable and accurate matching must still be performed. This is not trivial because two readers (mobile users) separated by a few metres can possibly have the same signal strength readings. Incorrect matching of the captured signal strength with the database is more likely to happen, which in turn will cause errors in position computation.

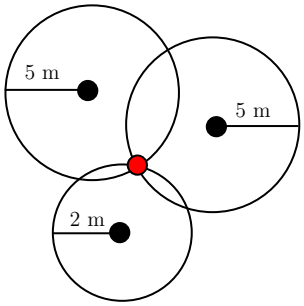

Fig. 3.1: Time based trilateration method

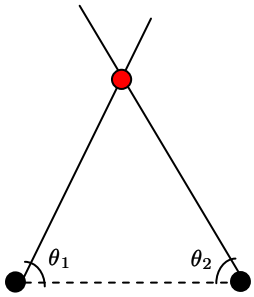

Fig. 3.2: Angulation method

3.2.3 RFID

Radio Frequency Identification (RFID) system is a system used to identify and track an object using radio signals (Seco et al., 2010; Ting et al., 2011). It usually consists of three main components: RFID tags, RFID readers and data processing system. The RFID tags can send out messages (for example the tag ID) actively and consistently (active mode) or when triggered (passive mode). The RFID readers can then read the data from the tags using a defined protocol for transmitting and receiving data. Finally the data processing subsystem can use the data from the readers to execute its positioning algorithm and can send out the positioning results to other users (or applications). RFID tags can be further divided into two: passive and active. Passive RFID tags have a limited read range of approximately 1 m from the reader. Active RFID tags powered by a battery (which can sometimes last for more than 7 years) can have a read range of up to 300 m (less if there is no line of sight)(ibid.).

RFID-based positioning technology can be divided into four categories: tag-based, reader-based, transceiver-free and hybrid. Only the first two will be explained as they are the most commonly used. Please refer to Ni et al. (2011) for further explanation on the remaining two categories.

To explain the tag-based approach, consider this example. Assume an object in a room has an RFID tracking tag and needs to be tracked. Many RFID reference

tags were also already deployed in that room in several known locations. To track this object, a reader at a fixed location will receive a Received Signal Strength Indicator (RSSI) from both the object RFID tracking tag and the RFID reference tags. Because of the correlation of the radio propagation, the generated RSSI from the object will be similar to the nearby reference tag. Therefore, the location of the object can be estimated from the correlation of the RSSI with distance and location of the reference tags. The accuracy nonetheless depends on the distribution of the reference tags, where a denser distribution attributes to a higher positioning accuracy. On the other hand, in the reader-based approach, the roles of tags and readers are swapped. Therefore, a reader is no longer at a fixed location, but is carried by a mobile user, and the RFID tracking tag is place at a fixed known location (much like the RFID reference tag). The location of the mobile-reader can then be estimated from the tag IDs (and possibly the RSSI values) detected by the portable reader.

Although the cost and the accuracy for this technology are of concern, the major limitation of the technology actually comes primarily from the limitation when using the RF signals. This is because a single passive RFID tag is quite cheap at a cost less than £1. Assuming a reader-based approach in a fixed navigation area, the total cost would only be proportional to the number of tags used to ensure adequate accuracy for the target application (assuming the reader cost is absorbed by the user). If only a lower accuracy is required (for example a few metres), fewer tags can be deployed at a lower cost.

Therefore, cost aside, the first limitation when using RF signals is the multipath, which is common for a positioning system that uses radio frequency signals. Theoretically, signal strength is a function of a distance, which means the signal strength reduces as the distance increases. Indoors, however, where multipath is commonly observed, the relationship between signal strength and distance cannot be used reliably anymore. Thus, for an RFID system that uses the signal strength, accuracy might be severely affected. Secondly, a problem might arise when multiple objects (or users) that are very close to each other need to be

tracked. This is because the RF signals (which gives the RSSI) from multiple tags (users) might interfere with each other, which then might cause problems in the positioning (localization) algorithm. Thirdly, the limitation due to the assumption that there are no variations in the signals emitted from the RFID tags. Generally, all tags are assumed to be transmitting with approximately the same signal strength, which is not always true. If this is not true, error in the position estimation will occur.

3.2.4 UWB

Ultra Wide Band (UWB) technology was developed in 1960 for radar application (Renaudin et al., 2007), but has been explored to be used for positioning indoors (Kietlinski-Zaleski et al., 2010; Pittet et al., 2008). The process involves transmitting a series of signals as narrow pulses, where the pulse duration is very short, varying between nanoseconds and picoseconds. This ensures a very high positioning accuracy of less than 1 m. Because short pulses are used, UWB occupy a very wide bandwidth (> 500 MHz) and thus very low power density. The Federal Communication Commission (FCC), in 2002, authorized unlicensed use of UWB in $3.1 - 10.6$ GHz frequency spectrum.

As with the WiFi positioning method, UWB also uses either TOA, AOA or RSSI. Generally there are two types of UWB signal structures: the impulse UWB and the multicarrier UWB (Chiu, 2009). Impulse UWB does not use a modulated carrier to transmit information; instead information is sent through a series of narrow pulses. On the other hand, multicarrier UWB uses a set of subcarriers. It is able to minimize interference with other signals because the subcarriers can be chosen to avoid interfering with bands used by other systems that share the spectrum.

One of the advantages of UWB is a very precise distance measurement because of the fine time resolution used. Its low power density also gives minimal interference to the other systems in the same frequency spectrum. There are also minimal multipath cancellation effects. Multipath cancellation occurs when an

indirect signal reaches the receiver partially or totally out of phase with the direct signal, which reduces the amplitude response of the direct signal. With short duration pulses used in UWB technology, the signals may come and go before the indirect signals arrive; therefore minimal multipath cancellation is noticed. Nonetheless, UWB also suffers the drawbacks when using RF signals, similar to when using WiFi and RFID technology.

3.2.5 Visual Sensors

So far, it has been discussed that using different ways to navigate indoors requires the navigation system to either rely on the RF signals or the (non-dedicated) infrastructures. When radio signals are used as part of the positioning technology, the issue of signals interference and its reliability will always be a concern. Additionally, if infrastructures-based systems are used, there will always be the issue of cost (for example in terms of prices of equipment, installations and maintenances). In some cases, for example during earthquake and emergency situations, infrastructures might not be available at all to aid navigation systems and most likely, there will be no electricity to power up the infrastructures. This means that resorting to another technology that does not rely on external infrastructures is a reasonable option to decrease the cost and eliminate environment disturbances.

Therefore, using visual-based approach for indoor pedestrian navigation can be one of the viable ways, as adopted by robotic navigations and unmanned aerial vehicles (Lobo and Dias, 2007). As humans perceive their surrounding environments using their eyes, the same principle can be applied in this approach. The advantage of this approach is because more and more affordable visual sensors are available on the market that can be used to acquire visual information (Ruotsalainen et al., 2011), such as the recent advancement in mobile phones that incorporates cameras and video recorders. Users can therefore use their mobile phones to gather visual information easily at no extra (or significant) cost. Whilst this helps the visual aspect of the visual-based approach for navigation, the main

issue is really about how reliable the visual information in relation to the positioning information is. Many different methods are therefore being researched on how to effectively integrate the visual information with accurate (or at least usable) positioning information (Hide et al., 2009; Jones and Soatto, 2011).

One of the methods is to use a 'fingerprinting' method (Walther-Franks and Malaka, 2008). In this method, images captured from the visual sensors are compared with the database. This database can be made available beforehand from a survey of the navigation area by capturing thousands of images of the area and embedding the images with known position information. During navigation, the images are continuously captured and compared with the database. If any of the images can be matched (or closely matched) with the images in the database, then position information can be relayed to the user.

Nonetheless, there are some disadvantages when using the visual-based approach for indoor pedestrian navigation. First, a massive database needs to be prepared before navigation can be done. This procedure is considered laborious and is sometimes restricted to a pre-defined area. The surveyed position also needs to be as accurate as possible. Furthermore, this needs to be monitored as often as possible because of the 'always changing' indoor environment that can create an outdated database. With an outdated database, users cannot use reliably the information contained in the database for navigation. Second, processing the captured images and comparing them with thousand of images in the database requires huge computing power. Moreover, if a real-time navigation is sought, data latency and processing time might be an issue. Third, visual defects on the captured images can possibly cause the loss of discriminative power when processing and matching the images with the database. For example, in a low light environment such as during smoky condition or simply in a dark night, the images can be sometimes blurry, shadowy or not visible at all. The movement of the camera sensor in practice, for example when holding a mobile phone to capture an image, can also cause the blurry effect of the images. This will burden the image processing and matching algorithm, to the possible extent where no matching can

be performed. Finally, the problem with the status of the images (captured or surveyed) which can be sometimes related to privacy-sensitive information and thus not available for visual-based approach navigation (Lane et al., 2010).

3.2.6 Map Matching

Conventionally, maps are used for navigation by determining one direction using magnetic compass and relying on information available (landmark) on maps such as streets, signage, river and so forth. Based on the classical approach of navigating using maps, people therefore can navigate from one place to another.

A 'generic map' (or a database) can be constructed using any available information that can be embedded with the position information such as the 'fingerprinting' approach (discussed in the previous section). This approach can be adopted for indoor pedestrian navigation and can be also categorized within a map matching approach as discussed in this section. Examples include using magnetic maps (Storms and Raquet, 2009), magnetic anomaly maps (Kemppi et al., 2010) and WiFi signal strength maps (Biswas and Veloso, 2010).

On the other hand, a different approach of not using the generic maps can also be adopted for indoor pedestrian navigation. This means, instead of generating maps based on the available information and using the maps to navigate as described before, 'true' indoor maps that are often available are instead used, such as the building blueprints or floor plans (Nam, 2011; Aggarwal et al., 2011). To do this, one of the technologies described in the previous sections may still be used to give positional information. Together with the indoor maps, the location of the user can be estimated and/or corrected relative to the maps. This can be performed using probabilistic filtering approach such as Particle Filter (PF) (Ascher et al., 2010; Krach and Robertson, 2008; Robertson et al., 2009; Woodman and Harle; 2008; Widyawan and Beauregard, 2008). To define the best estimated position, a group of particles (or probable positions) are generated based on its uncertainty distribution. Then the particles are propagated based on the next positional information, but are constrained to only exist in a constrained layout (the indoor

maps). It makes a logical assumption that the particles cannot penetrate the floor plan layout such as building walls or room walls. To further enhance the accuracy, more information from the indoor maps such as furniture and desks can also be used (if available) to constrain the particles. Another approach includes the use of Simultaneous Localization And Mapping (SLAM) (Robertson et al., 2010), where navigating and environment mapping are done simultaneously.

However, there are also some disadvantages at relying on map matching method for indoor pedestrian navigation (from literatures). Firstly, the method still needs to use other positioning technologies (described in the previous sections) to give the positional information to be used with the maps. Secondly, for example for SLAM and PF, intensive computations need to be performed that may require huge processing power. Each particle, which represents a probable position of the user, needs to be checked individually for the initial localisation by a probabilistic computation. The computation cost is further increased if the area of navigation is huge because then more particles need to be checked. Thirdly, huge resources are still required to store massive information about the indoor maps. For example, accurate coordinates such as wall coordinates still need to be embedded in the map to constrain the particles' position. Fourthly, the accuracy and the scalability of the indoor maps need to be taken into account. High accuracy maps may be needed to constrain the particles accurately. Furthermore, the particles need to be scaled to match the scale of the maps used and this increases computing cost when scaling is performed for each particles. If an inaccurate map is generated when using the SLAM method, position accuracy will be degraded. Finally, indoor maps may also require legislative action specifying building information to be submitted to authorities before they can be used by the public (or users).

3.2.7 Inertial Sensors

In Chapter 2, the inertial navigation technology and inertial sensors' principles were introduced. This section thus introduces the use of inertial sensors for pedestrian navigation system. From the discussion presented so far on the existing indoor PNSs and their limitations, a potential alternative is to resort to different types of navigation technology that do not use RF signals, which are independent of infrastructures and are a lower cost (price, computation, parts). Inertial sensors satisfy the first two of these criteria because they do not receive or transmit any RF signals and operate autonomously without infrastructures. For the third criterion, the advent of low-cost MEMS inertial sensors (Section 2.3) suits the requirement for a low-cost pedestrian navigation system. Two configurations are often used for the system using the low-cost inertial sensors: 'dead-reckoning' and Inertial Navigation System (INS) (Groves et al., 2007).

3.2.7.1 Dead Reckoning

In the Dead Reckoning (DR) configuration, accelerometers are often used as an odometer (Torres-Solis and Chau, 2010). Typically they are used to detect steps, and then, using a fixed-pre-determined step length, a relative position can be computed by adding the step length from the previous position. The absolute heading of the system is often determined by the use of a compass. Apart from the problems of compass measurements relating to magnetic disturbances, the position can be inaccurate because of the assumption of a fixed step length. Furthermore, walking backwards or side-stepping will cause a problem because DR assumes the user to be moving forward.

3.2.7.2 Inertial Navigation System

The principle of Inertial Navigation System (INS) has been explained in Chapter 2. In the INS, attitude parameters from the integrated gyro measurements are used to transform the acceleration measurements from the accelerometers into a desired

frame such as the navigation frame. From these, one can calculate the position of the system regardless of the walking directions (can be in any direction) and the way the pedestrian walks (such as backwards walking and running). This is the reason that INS was chosen for this research. However, if the low-cost inertial sensors were to be used, they are prone to errors because of their low-cost nature, such as a low precision in manufacturing, which eventually causes large position errors (Pang and Liu, 2001; Godha et al., 2006; Park and Gao, 2006).

3.3 Foot Mounted IMU System

An approach of using low-cost-foot-mounted inertial sensor with INS technology resolved to *n*-frame is adopted in this research, and is called low-cost Pedestrian Navigation System (low-cost PNS). The reason is that although the low-cost inertial sensors are known to have huge errors, an idea from for example Jiménez et al. (2010), Skog et al. (2010b), Glanzer and Walder (2010), Callmer et al. (2010) and Foxlin (2005) can be adopted to reduce the errors. Using this idea, the IMU is mounted (or strapped) on a user's foot or shoe, enabling Zero Velocity Updates (ZUPT) to be performed (this will be discussed in the next section). The IMU location on a shoe is not as critical as it may first seem as demonstrated by Wan and Foxlin (2010), where various locations were tested for ZUPT detection reliability. Different IMU locations, such as embedded in the sole, taped to a heel and taped to a toe, had resulted in insignificant performance difference.

3.3.1 Zero Velocity Update (ZUPT)

The name Zero Velocity Update (ZUPT or ZVU) is often used because the known zero-velocity measurements are used to update the velocity estimation of a specific system, such as the low-cost PNS. Thanks to the strap-down configuration in the low-cost PNS (using foot-mounted approach), it has the advantage of measuring the foot's velocity directly. It is therefore valid to assume that during the stance phase (zero velocity) of a walking gait, the IMU should produce zero velocity

measurements for the foot's velocity. In practice, however, this is not entirely true because of the inherent errors of the inertial sensors. Therefore, the non-zero velocity measurement from the strapped-down IMU during this period is considered as an error, and can be subsequently corrected. For example, this can be performed by feeding back this error to a control system (Jadaliha, 2007).

Furthermore, if this measurement update (zero-velocity measurement) is used in an estimation filter such as the Kalman Filter (KF) (as adopted in this research), they can be used not only to correct the user's walking velocity, but also to help to restrict the position and attitude errors, and estimate the sensor bias errors (see Section 4.3.3). For example, Grejner-Brzezinska et al. (2001) have demonstrated the significance of using velocity measurements (using ZUPT) for a standalone tactical grade INS. In a 140 s of navigation, the horizontal position error was shown to decrease from 0.30 m to 0.07 m when ZUPT was performed for 20s in the middle of the navigation. This is because the KF uses an inertial error model that can build up information on the correlation between the states modelled such as position, velocity, attitude and sensor biases (this will be explained more in Chapter 5).

For the low-cost PNS, ZUPT is applied during each detected stance phase of a walking pedestrian, which normally occurs repetitively. By applying ZUPT frequently, INS errors are therefore allowed to grow only in between these ZUPTs (assuming that all ZUPTs are detected correctly). To apply ZUPT correctly in the KF, reliable stance phase detection is thus needed, and is explained next.

3.3.1.1 Stance Phase Detection

In order to apply ZUPT measurements in the KF, it is paramount to recognize the periods during which the user's foot is stationary (stance phase). Correct stance phase detection is essential in a self-contained inertial navigation system that uses ZUPTs, such as the low-cost PNS, because it enables ZUPTs to be used correctly in the KF for error estimation.

Four detection methods to correctly detect stance phase have been investigated extensively by Skog et al. (2010b). They are acceleration Moving Variance (MV), acceleration MAGnitude (MAG), Angular Rate Energy (ARE) and Stance Hypothesis Optimal Estimation (SHOE). In essence, all four use the prior knowledge of the IMU signals, and are tested using a binary hypothesis problem (Skog et al., 2010b). This means if certain conditions are met, the stance phase can be declared (stationary) or else, no declarations are made (moving).

In the research presented in this thesis, the detection based on angular rates was used, similar to the ARE approach. The angular rates detection was used mainly because it was shown in Amendolare et al. (2008), Feliz et al. (2009) and Skog et al. (2010a) during which the ARE provided the highest position accuracies and was the most robust to the change in walking speed. As a result, this method gives a satisfactory result with regards to step misdetection and works fairly reliably, at least for the trials presented in this thesis. Fig. 3.3 shows an example of the detected ZUPT events for one of the trials presented in Chapter 6. It shows that 2 misdetections occurred within a period of 7 s when using accelerometer-based detection (MAG), but works well when gyro-based detection (angular rate) was used (ARE).

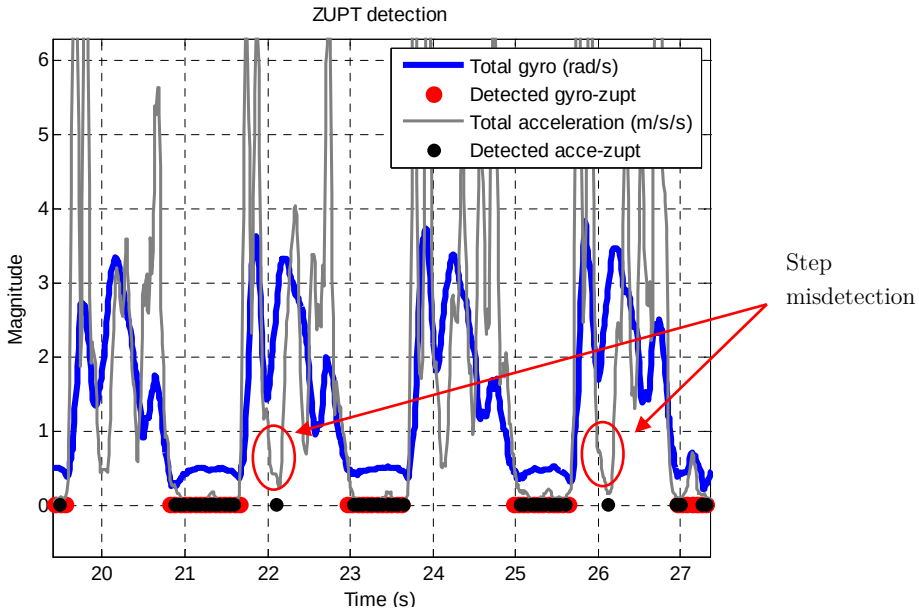

Fig. 3.3: An example of ZUPT detection

For the stance phase (or step) detection method used in this research, first, a simple moving average filter was used (with a sliding window = 7) to smooth out some of the short term angular rate measurement fluctuations. Then an empirically determined threshold is applied to the magnitude of angular rates to detect a stance phase condition (zero velocity condition). The measurements are then decimated from 100 *Hz* (the INS measurement rate) to 20 *Hz* (chosen empirically) to reduce the KF computational load before being used in the filter. Another integrity check is then applied to ensure ZUPT is detected correctly. This is done by ensuring that only two consecutive filtered measurements fall below the set threshold, before ZUPT can be declared and used during the stance phases.

3.3.1.2 ZUPT in the Kalman Filter

The fundamental of the Kalman Filter (KF) has been explained in Chapter 2. Its use as an optimal state estimation is widely recognized and extensively reported in literatures such as in Grewal and Andrews (2008) and Hide et al. (2007a). Configuration of the KF used in the research will be further described in Chapter 5. For discussion purpose, however, the KF error states used in the research are introduced in this chapter as:

$$\delta x = \begin{pmatrix} \delta r^n & \delta v^n & \epsilon^n & b_g & b_a \end{pmatrix}^T \qquad \textbf{(5.1)}$$

where δr^n is the vector of latitude, longitude and height errors, δv^n is the vector of navigation frame velocity errors, ϵ^n is the vector of attitude errors, b_g is the vector of gyro bias errors and b_a is the vector of accelerometer bias errors.

In this research, the knowledge of the errors during ZUPT is used as a measurement update to the KF to better estimate IMU errors (the IMU dynamic error equations are reserved for discussion in later chapters). During ZUPT epoch, differences between inertial measurements and ZUPT condition are entered into the KF for errors estimation. Effectively all type of observations or measurements that are known during stance phases can potentially be used in the measurement update

equation, depending on how a system is designed and what kind of state space is being used. The design matrix used, which uses velocity update (ZUPT) to update the KF is shown below:

$$H = \begin{pmatrix} 0_{3\times3} & I_{3\times3} & 0_{3\times3} & 0_{3\times3} & 0_{3\times3} \end{pmatrix} \tag{5.2}$$

with observation $z_k = \delta v^n$ and covariance matrix $P_k = E[n_k n_k^T]$ from Eq. (2.35), where δv^n is the difference between the INS velocity and zero, n_k is a constant measurement noise and k is the current epoch. When a ZUPT is applied, it is usually the case that the user's foot is not perfectly stationary. This uncertainty is modelled in the measurement covariance matrix, which was empirically determined (0.005 m/s) to give good performance.

3.4 Summary

A review of the current state-of-the-art in aided pedestrian navigation systems for indoor navigation has been presented. The inertial sensor based approach with INS technology was then chosen to be used in this research; mainly because it does not require infrastructures, as opposed to the other approaches. Following this, a low-cost autonomous inertial Pedestrian Navigation System using foot-mounted approach (low-cost PNS) has been proposed and presented, and now will be the focussed subject in the subsequent chapters.

Chapter 4

Heading Drift of a Low-Cost PNS

This chapter begins with an introduction of the drift problem faced by the low-cost PNS. This sets the scene for a focussed review of the current state-of-the-art research concerning the drift problem. This includes an integration of low-cost PNS with other aiding sensors such as a magnetometer. There then follows a section discussing the knowledge gap in research highlighting the drift problem that motivated this research, followed by a brief chapter summary.

4.1 Introduction

This chapter looks in detail at the current practices in providing heading drift correction for a low-cost indoor inertial system. There then follows a strong focus on the heading drift for the low-cost PNS and the review of the current methods used within the research community. The problems with the current heading drift correction methods, highlighted in this chapter, are exactly those which the research presented in this thesis has substantially mitigated.

Mitigating heading drift has a direct correlation with the improvement in the position accuracy for the low-cost PNS. As a result, improving position accuracy for such a low-cost system can benefit many potential applications. For example, the military or rescue sectors usually have a mobile workforce such as armies, fire fighters and police. In this sector, apart from navigating, it is important to, for example, track fallen personnel in a certain mission. For example, the tragic loss of 343 fire fighters from the Fire Department of New York City (FDNY) and 23 officers from the New York City Police Department (NYPD) in the collapse of the World Trade Center on 9/11 because they could not be tracked (Reissman and Howard, 2008) indicates the importance of such capability.

Although finding and rescuing applications in hazardous environments are the major motivation, there are many other possible applications as well. For example, in a survey community, coarse and rapid indoor mapping can be made possible without the need for expensive survey equipment. This can be further extended to account for many users in a collaborative way, where an infinite number of users can contribute to create an indoor open map database, such as those initiated by the OpenStreetMap community for open street map database (OSM, 2012).

There are also other potential applications for social use such as in tourism industry, health care and social responsibility sectors. For example, in a hospital environment, the mobility of patients can be tracked to ensure their safety (Molina et al., 2011). Guiding blind or visually impaired persons can also be a potentially useful application, where they can have guidance from the system for a better

navigation experience. Indeed there are many more possible applications that can be thought of, as a result of reducing the heading drift error for such a low-cost pedestrian navigation system.

In this chapter, Section 4.2 will explain the terms used to describe the drift problem for the foot-mounted low-cost PNS (low-cost PNS). Then, Section 4.3 will demonstrate the drift problem and several field trials are presented to support the discussion. Section 4.4 will then discuss specifically the primary cause for the drift problem and finally, Section 4.5 will describe the current method used to overcome the drift problem and their limitations.

4.2 Terms Used In the Thesis

It is possible that there will be confusion when different drift terms are used for the same context, for example between heading drift, position drift and yaw drift. Therefore, a clear distinction between each term should be made. In this thesis, heading drift (used interchangeably with yaw drift) refers to the drift on the IMU gyro z-axis measurement (b-frame) that is caused by the accumulation of small errors perturbing the axis. On the other hand, position drift term is used to indicate an event where the position trajectory no longer agrees with the true trajectory.

4.3 Position Drift Error

For the low-cost PNS (using only foot-mounted IMU), the position drift error can be caused by two factors. First is the unavailability of ZUPTs (ZUPT-unaided) and second is, if ZUPTs are available (ZUPT-aided), the unobservability of rotational errors primarily on INS Down axis (when levelled). When ZUPTs are unavailable, no other measurements are updated to the estimation filter. This results in a huge position drift error because of the huge errors of the low-cost IMU used (was

discussed in Section 3.3). On the other hand, the position error can be reduced when ZUPTs are available (was discussed in Section 3.3.1). Nonetheless, there remains the unobservable heading error that causes the remaining position drift (will be discussed in Section 4.4). To illustrate the impact of these two factors, practical trials were performed first when the low-cost PNS was aided and unaided with ZUPTs, and the results are presented next.

4.3.1 Evaluation

Walking trials were performed using the low-cost PNS to demonstrate the significance of the two factors mentioned before on the drift in position for the low-cost PNS. Details about the low-cost PNS hardware is reserved for explanation later in Section 5.4 but essentially, the system contains a foot-mounted IMU that connected to a data logger, which is housed in a user backpack. During the trials, the data was logged by the data logger and was post-processed for evaluation using in-house processing software (reserved for explanation in Section 5.3). Note that in a practical deployment, the low-cost PNS system could be replaced by a much cheaper/smaller data logger and a micro-processor that could possibly be embedded into the IMU package on the user's foot. For the trials, the low-cost PNS initial position and attitudes (roll and pitch) were initialized during an alignment period as explained in Section 2.4.3.1. The initial heading however was manually set by processing the trial data multiple times with different heading values. The value that gave the best estimated trajectory was then selected. Initial accelerometer biases were set to zero, whilst the gyro biases were set by taking their average obtained during the alignment period.

Because of a lack of a more accurate ground truth in which the low-cost PNS solution can be evaluated with, it was not possible to determine the absolute heading drift error in each individual step event for all the trials. Even if a high grade inertial sensor can be used as the ground truth, it still needs frequent ZUPTs measurements because of the drift. However, it is not practical to mount the high grade inertial sensor on foot to perform ZUPTs because of its size and weight.

Therefore, a simple evaluation method to assess the heading drift is performed by using the knowledge that walking in a square trajectory should result in four distinctive heading values, offset by 90^0 between each other. If the heading drift is apparent, it will be reflected on the drift in these values. For the position drift error, another simple evaluation method is performed by processing the trials data and visualizing it using Google Earth imagery. Therefore, an approximation of the trajectory can be seen clearly by overlapping the knowledge of the true trajectory performed during the trial with the image in Google Earth (where the trial was actually performed). Although these evaluations are only coarse estimations of the errors, they are considered adequate when visualizing the heading drift and the growth in position error for the low-cost PNS because the errors can be seen clearly.

4.3.2 ZUPT Unavailable Trials

This section presents the result when the low-cost PNS was not aided by measurements from ZUPTs. When the low-cost PNS is said to be unaided, it literally means no forms of measurement are available to correct the error in the estimation filter (Section 3.2). For an autonomous system like the low-cost PNS, this means the velocity measurements generated from a zero velocity condition when taking a step are not applied to the low-cost PNS.

The result obtained from a 2-round walking around a football pitch is plotted in Fig. 4.1. In Fig. 4.1(a), the approximation of the trial's trajectory is drawn manually on the image represented by the blue line, and in Fig. 4.1(b), the unaided low-cost PNS solution is plotted, represented by the red line. As expected from Section 2.2.1, Fig. 4.1(b) shows that the position estimated from unaided low-cost PNS diverged rapidly from the true user's position, relative to Fig. 4.1(a) that is overlaid on top of its trajectory. After a period of just under 18 minutes, walking a distance of approximately 1.3 *km*, the estimated position has drifted more than 50 *km* (approximated using line distance measurement tool in Google Earth).

(a) (b)

Fig. 4.1: (a) Estimated true trajectory, (b) a section of unaided low-cost PNS trajectory

4.3.3 ZUPT Available Trials

To see the impact of ZUPTs in reducing position drift error, the same trial data was reprocessed, but this time zero velocity measurements were updated to the Kalman Filter (KF). More about the KF and the processing software are explained in Chapter 5. Fig. 4.2(a) is the estimated trajectory, manually drawn and overlaid on the image of the trial area, whilst the result of aiding the low-cost PNS with ZUPTs measurement is plotted in Fig 4.2(b). From Fig. 4.2(b), it clearly shows when ZUPT was available, the low-cost PNS shows far better performance than when ZUPT was unavailable (not applied) as in the previous section. It is observed that the position drift error has reduced significantly, although still inaccurate, when compared with previous Fig. 4.1(b). Four more walking trials were further undertaken and plotted in Fig. 4.3. Similar results of improved position solutions are observed, although the positions are still drifting over time.

To further quantify the significance of using ZUPTs for low-cost PNS in reducing position drift error, Fig. 4.4 is plotted. The figure shows a comparison of the Horizontal Position Error (HPE) growth when the low-cost PNS was aided and unaided with ZUPT, taken from the outdoor trial data presented in Chapter 6. In this trial, the user walked around the same football pitch for about 10 minutes. Instead of only visualizing the estimated trajectory on an image as in the previous section, a reference system was used. The ground reference system was taken from

a Network Real Time Kinematic (NRTK) GPS solution, which has a typical accuracy of a few cm. Full details of the trial will be reserved for Chapter 6.

(a)

(b)

Fig. 4.2: (a) Estimated true trajectory, (b) ZUPT-aided low-cost PNS trajectory

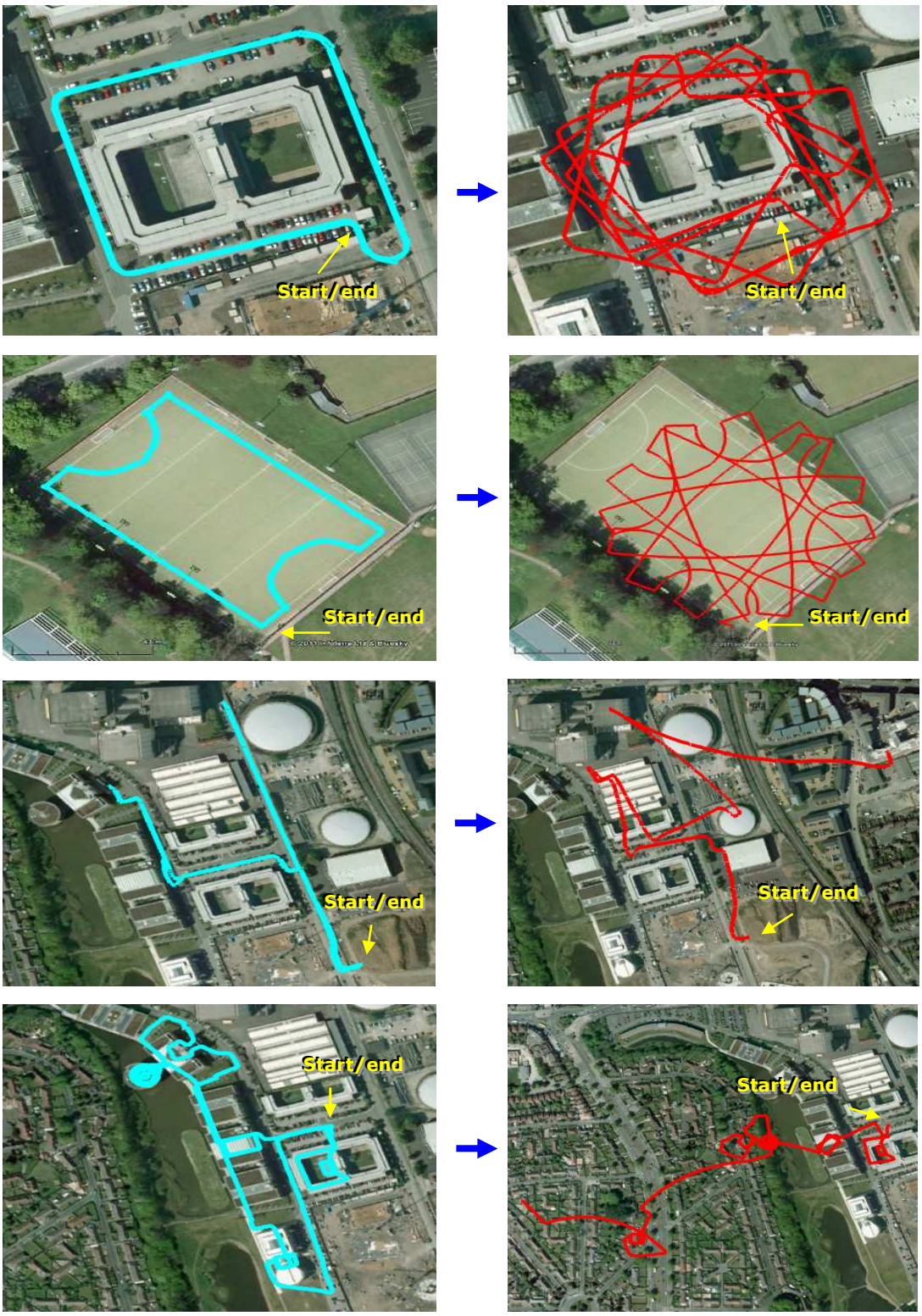

(a) (b)

Fig. 4.3: (a) Estimated true trajectory, (b) Heading drift for ZUPT-aided low-cost PNS trajectory

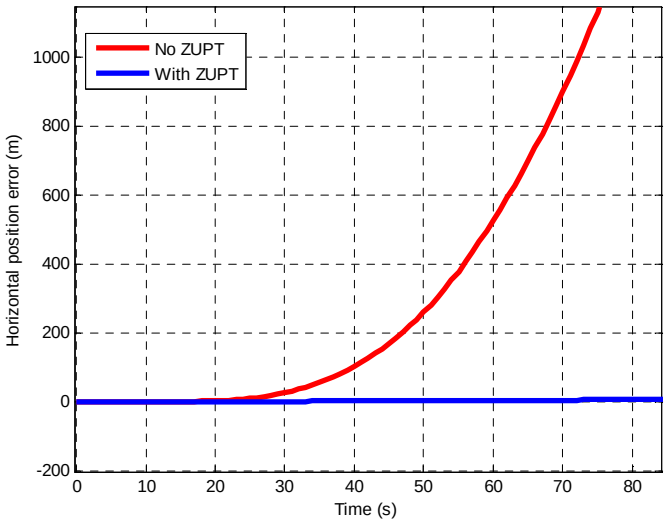

Fig. 4.4: Horizontal position error comparison when low-cost PNS is aided with ZUPT and when is not aided with ZUPT.

It is observed from Fig. 4.4 that applying ZUPT measurements to the estimation filter such as the KF reduces the position error growth significantly (as expected and discussed in Section 3.3). Within 1 minute, unaided low-cost PNS has drifted by more than 500 m, but ZUPT-aided low-cost PNS has a considerably lower position error (less than 100 m). In the case of the low-cost PNS, ZUPTs have, therefore, become an important method to reduce the position drift error (Petovello et al., 2003; Stirling and Edmonton, 2003; Foxlin, 2005; Cho and Park, 2005; Groves et al., 2007; Godha and Lachapelle, 2008; Feliz et al., 2009; Bebek et al., 2010; Bird and Arden, 2011).

However, when Fig. 4.4 is extended in time from approximately 80 s to 600 s and is plotted as Fig. 4.5, it can be clearly seen that the Horizontal Position Error (HPE) still grows. This happened even when frequent ZUPTs are available, although the error is still significantly reduced compared to when ZUPTs were not applied (Section 4.3.2). In this figure, after about 10 minutes, HPE has reached a significant 60 m.

Section 2.3.1.1 has discussed that the position drift can be caused by small errors perturbing the gyroscope signals, which can cause 'tilt' errors (attitude errors in the horizontal axes) in the INS orientation. A small tilt error causes a

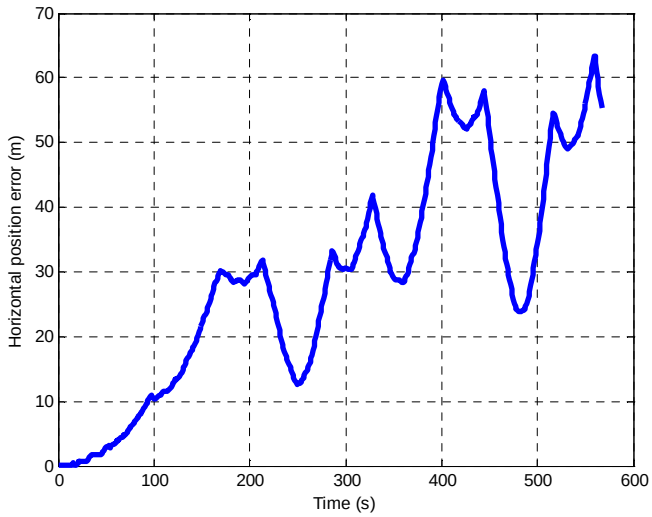

Fig. 4.5: Horizontal position error when low-cost PNS is aided with ZUPT only

component of acceleration due to gravity to be projected onto the horizontal axes. It will then be double integrated during position computation, which ultimately causes an error in the position that grows cubically in time.

In the case of the low-cost PNS, however, the 'tilt' error can be observed through the availability of ZUPTs. The remaining error that is not observable through ZUPTs therefore can be identified as the heading error, which grows over time (drift) (this will be explained next in Section 4.4). This therefore subsequently resulted in huge position error, as shown for example in the previous Fig. 4.4. To illustrate this, the INS heading from the same trial that was used to plot Fig. 4.5 is plotted in Fig. 4.6. The blue lines represent the true headings, which are offset by 90^0 from each other resulting from walking in a rectangular trajectory. It can be observed clearly that over time, the INS heading is drifting, from about 180^0 at $t = 0\ s$ to about 140^0 at $t = 500s$.

The heading drift error is mainly caused by the inertial sensor gyro errors such as bias, scale factor error and gyro noise that perturbs subsequently the attitude measurements about the INS Down-axis. As discussed in Section 2.3.1, they are often modelled simply as the gyro bias with noises during the estimation process. It needs to be estimated because the bias changes over time. If it is not properly estimated, over time, this error will cause a significant position drift error.

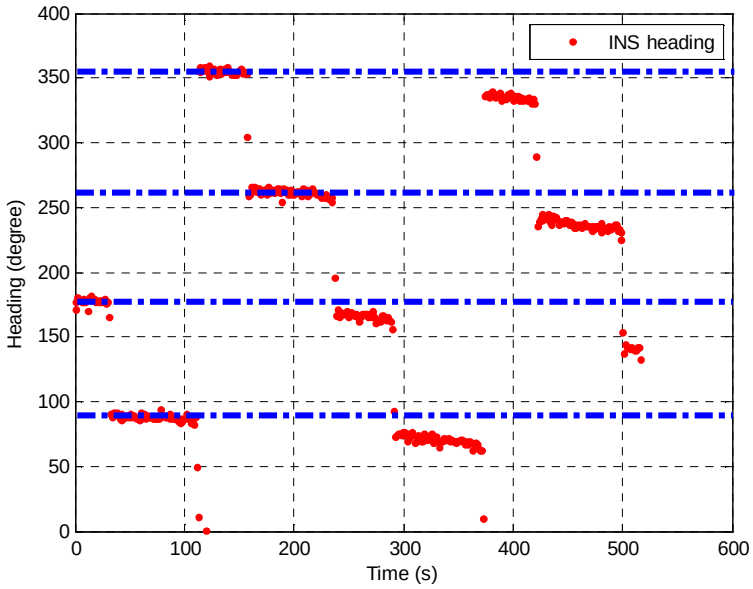

Fig. 4.6: INS heading when low-cost PNS was aided with ZUPTs only

Unfortunately, these errors are not well observed (cannot be estimated) when using zero velocity updates alone in the low-cost PNS, as demonstrated in this section. This problem is known as the observability problem (which becomes the basis of this research) and is explained next.

4.4 Heading Observability

As mentioned in the previous section, the position drift error for the low-cost PNS is primarily the result of the poor observability of errors about the INS Down-axis, when ZUPTs are the only measurements available to update the Kalman Filter (KF). Hide (2003) described the INS error observability using velocity error dynamic equations (the dynamic model used in this research is explained more in Section 5.3.3). The equations can therefore be written as:

$$\dot{\delta v_N} = -f_D \epsilon_E + f_E \epsilon_D \tag{4.1}$$

$$\dot{\delta v_E} = f_D \epsilon_N - f_N \epsilon_D \tag{4.2}$$

$$\dot{\delta v_D} = -f_E \epsilon_N + f_N \epsilon_E \tag{4.3}$$

Eq. (4.1), (4.2) and (4.3) model the velocity errors relationship with the forces terms and attitude errors terms in the navigation frame. These equations show that when the external attitude updates are not available, the INS attitude errors (ϵ) are observable through the velocity error measurements ($\delta\dot{v}$) . These equations show that the attitude errors about the North and East axes (ϵ_N, ϵ_E) result in the velocity errors through the North, East and Down force terms (f_N, f_E, f_D). Likewise, in Eq. (4.1) and (4.2), the North and East attitude errors (ϵ_N, ϵ_E) are always observable through velocity updates because the force in the Down direction is always large as a result of the gravity force. For the low-cost PNS, these horizontal attitude errors are observable because velocity updates can be performed through ZUPTs during momentary stationary condition when the user takes a step.

On the other hand, Eq. (4.1) and (4.2) show that the attitude error about the Down axis (ϵ_D) is only observable through the horizontal acceleration terms (f_N, f_E). This means that in order to observe ϵ_D, the horizontal acceleration must not be zero, which is not the case for the low-cost PNS during stationary condition when ZUPTs are performed (Section 3.3). Therefore, the attitude error about the Down axis for the low-cost PNS is not observable because there is no horizontal acceleration observed during ZUPTs. This error thus becomes the crucial factor contributing to the position drift error for the low-cost PNS.

Eq. (4.4), (4.5) and (4.6) further shows the relationship between roll, pitch and heading errors with the attitude errors in North, East and Down axes (ibid.):

$$\delta\varphi = \epsilon_E \frac{\sin\psi}{\cos\theta} + \epsilon_N \frac{\cos\psi}{\cos\theta} \tag{4.4}$$

$$\delta\theta = \epsilon_E \cos\psi - \epsilon_N \sin\psi \tag{4.5}$$

$$\delta\psi = \epsilon_E \sin\psi \tan\theta + \epsilon_N \cos\psi \tan\theta + \epsilon_D \tag{4.6}$$

It shows that the roll and pitch errors ($\delta\varphi, \delta\theta$) are correlated with the attitude error about North and East axes, and the heading error ($\delta\psi$) when levelled is correlated mainly with the attitude error about the Down axis (ϵ_D).

Whilst the discussion so far relates directly to the low-cost PNS measurements update using ZUPTs when stationary (stance phase), it does not discuss the observability of errors during a swing phase. The swing phase is the phase when the foot is swung when taking a step. Because the IMU is likely to undergo very high accelerations during the swing phase, the velocity error dynamic equations presented above may not model these dynamics accurately (for example the values in the force terms may be wrong). If this is not accurately modelled, the attitude errors may be wrongly estimated by the filter as well, which subsequently will affect the estimation of other error states because of their correlation. One theoretical possibility is to use the true values of the dynamic terms from other reference systems (if available). By using these values, the true heading error can be observed. This theoretical result can then be compared with the values estimated from the chosen dynamic model. Using this comparison, a more accurate dynamic model can possibly be modelled. As a result, the heading drift can possibly be mitigated significantly because the heading error can now be estimated correctly during the swing phase. In other words, the heading error can be made observable during this phase, thanks to the availability of the correct horizontal acceleration terms in Eq. (4.1) and (4.2).

When the velocity update is applied using ZUPTs during stationary (stance phase), the velocity error information during the swing phase just before the IMU comes to stationary is very significant. This is because the velocity error information contains all the information about the accumulated errors. If the dynamic model used accurately models the propagation of these errors, this velocity error information truly represents all the accumulated errors. As a result, more accurate estimation of the modelled states can be performed through ZUPTs by the estimation filter. Furthermore, the update rate of ZUPT measurements might not have significant impact to the overall estimation process when an accurate dynamic model is available (and used). This is because during velocity updates through ZUPTs, the error growth is modelled perfectly and there will be no difference theoretically if either a higher rate or a lower rate is used. Nonetheless, in reality,

the dynamic model used may not correctly model the system and thus resulting in inaccurate velocity error estimations. This in turns affects the estimation of other correlated states as well and may result in suboptimal solutions.

4.5 Heading Drift Mitigation and Limitation

This section reviews some of the current methods used to address the heading drift problem for a low-cost indoor inertial pedestrian navigation system. Section 3.2 has presented several technologies to aid GPS-based pedestrian navigation systems. For clarity, this section therefore differs slightly from Section 3.2, as it focuses directly on the limitations of such methods in mitigating heading drift.

4.5.1 High Grade IMU

A high grade IMU can be used to mitigate the heading drift problem because of its high performance. For example, Collin et al. (2003) and Mezentsev et al. (2005) used a tactical grade IMU for their indoor positioning system to provide a very high accuracy heading sensor. The IMU used was a HG1700 from Honeywell, a typical ring-laser gyro type that has a small bias of only 1^0/h.

There are, however, two obvious drawbacks of using this approach. First is the cost of the high grade IMU (shown in Table 2.1), in terms of weight, size and price, which limits its application to the wider community. For example, it is not practical for a typical pedestrian to carry a high grade inertial sensor with a weight of more than a few kilograms. Moreover, if a foot-mounted IMU approach is used as in this research, it is practically impossible. Secondly is that inertial navigation is a relative position technique where ultimately position will drift because of the accumulation of IMU errors. Therefore, even high grade inertial sensors still need velocity updates such as ZUPTs to control some of its errors. If not, these errors might still accumulate over time and corrupt the position solutions. Unfortunately, as discussed in the previous section, even with ZUPTs, the heading error is still not observable. Therefore, heading drift error is still the main cause for the drift in

positions, although the drift rate will now be much slower than the low-cost inertial sensors because of its high performance.

4.5.2 Magnetometer

In a standalone low-cost inertial pedestrian navigation system (or a low-cost PNS), a magnetometer is identified to be the most practically used sensor for heading error mitigation. This is because low-cost IMUs, such as from Xsens™ (Xsens, 2011), Microstrain™ (MicroStrain, 2011b) and Intersense™ (Intersense, 2011), are often manufactured and cased together with a 3-axis MEMS magnetometer. This, therefore, makes the use of magnetometer quite appealing as additional sensors are no longer needed.

There are generally two methods that magnetometers are often used to address the heading drift problem for a low-cost PNS. One is by getting the heading measurement directly from the magnetometer (Sabatini, 2008; Bird and Arden; 2011; Stirling et al., 2005) and two is by integrating the magnetometer heading measurements with the gyro yaw measurements due to its complementary effect (Mather et al., 2006; Faulkner et al., 2010). In the first approach, locally levelled horizontal magnetometer measurement vectors are used to work out the magnetic heading, and this heading is used directly in the navigation system. In the second approach, an absolute heading measurement from the magnetometer is used to compensate the relative gyro yaw measurement that contains substantial error. The magnetometer measurement can be used, for example in the Kalman Filter, to estimate yaw attitude errors, resulting in the best estimate of heading. A different method is by 'fingerprinting' magnetometer measurements with surveyed positions, which will be reserved for discussion in Section 4.5.4.

Nonetheless in both methods, the magnetometer is still used to provide heading measurements, which is quite useful only in an environment clear from magnetic disturbances. In a magnetically-disturbed environment such as in buildings, the magnetometer measurements are easily corrupted. This problem motivates current research relating to low-cost PNS, by looking in a way to solve

the uncertainties in the magnetic measurements, for example in Wei et al. (2010), Bird and Arden (2011), Faulkner et al. (2010) and Renaudin et al. (2010). This can be done by identifying measurements that are free from disturbance using a filter. For instance, Bird and Arden (2011) filtered these measurements using a single 3-axis magnetometer, whilst Afzal et al. (2010) used a multiple magnetometers. Further explanation on these follows in Chapter 6, as Chapter 6 is dedicated to assess the performance of a 3-axis magnetometer using a similar method to provide heading measurements to the low-cost PNS.

4.5.3 Drift reduced MEMS IMU

It is also possible to use an improved MEMS IMU in a low-cost PNS to reduce heading drift error. The improvement in design was made, in particular, to the gyro, stating performance values that approach the specification of tactical grade IMU specified in Table 2.1. For example, Wan and Foxlin (2010) have introduced the newest drift-reduced MEMS IMU engineering sample (NavChip™), manufactured by Intersense. The developer kit is now available for purchase from August 2011 (Intersense, 2011). Peshekhonov et al. (2011) and Peshekhonov (2011) also reported a prototype MEMS gyro that approached tactical grade specifications. However, while its benefit cannot be denied in standalone IMU navigation, using it without any aiding will still result in a gradual drift in position over time because, again, heading is not observable. Its advantage is, obviously, on the slow rate of the drift, similar to when using high grade IMUs (discussed in Section 4.3.1), and is appealing to the mass market as it is small, lightweight and has a low power consumption.

4.5.4 Position Updates

If a low-cost PNS can be updated with reliable position information frequently, most of the accumulated heading drift can be eliminated. This includes using a tagging approach such as RFID (Section 3.2.4); a matching approach such as image

matching (Section 3.2.5); a fingerprinting approach such as fingerprinted-magnetometer measurements; or getting the position information directly such as with HSGPS (Section 3.2.1). In the magnetometer fingerprinting approach, it is used differently when the magnetometer was discussed in Section 4.2.1. It can be achieved by creating a database of magnetic field environment, embedded or 'fingerprinted' with position information (Storms et al., 2010). There is also an effort (Kemppi et al., 2010) in creating the position database using magnetic anomaly.

As described in Chapter 2, the gyros attitude information can be used to transform the specific force measured by the accelerometers in a body frame to the desired navigation frame. Through INS mechanization, the position can then be calculated. Therefore, thanks to this correlation, the heading error can be made observable through a sequence of frequent position updates. This is because the difference between a sequence of position measurements and the computed INS position is largely resulting from the heading error (demonstrated in Section 4.3). The heading error can therefore be estimated in the KF because of the availability of these frequent sequences of position measurements. This indicates that if only few position measurements are available to update the estimation filter and they are not frequent, then the heading error will be weakly observable.

Nonetheless, in terms of position error, even if there are only a few position measurements available to update the filter, the position error can still be corrected with these updates. The only uncorrected position error remains is therefore the position drift that has been accumulated up to the update. Imagine a position trajectory that is drifting in one direction, but whenever there is a position measurement update; it jumps to the correct reference trajectory, before drifting again until the next position update is available to correct the position drift.

Therefore, although position updates can be useful to mitigate the heading drift error that affects the position drift error, frequent position measurements must always be available to update the estimation filter. For low-cost inertial sensors based systems such as the low-cost PNS, this should occur as frequent as

possible because the drift can happen very quickly because of its low performance. The possible systems discussed here that can provide position updates such as RFID and HSGPS have their own limitations, which were discussed previously in Chapter 3. Therefore unfortunately for indoors, providing frequent position updates from the available systems to mitigate heading drift are not always possible.

4.6 Summary

A review of the heading drift problem for the foot-mounted low-cost inertial Pedestrian Navigation System (low-cost PNS) has been highlighted. Current approaches to mitigate this error, together with its limitation, have also been reviewed. The work in the research is therefore based on this motivation, where the possibility of resolving the heading drift problem with the use of only low-cost inertial sensors (accelerometers and gyros) on its own is explored in the remaining chapters.

Chapter 5

Data Simulator, Processing Software & the Low-Cost PNS

This chapter presents the tools that were used in the research. This includes Inertial measurement Data Simulator (IDS) software for inertial data simulation and Position and Orientation Integration (POINT) software for data processing. For the low-cost PNS, a MicroStrain low-cost MEMS IMU was used as the only source of inertial sensor, and the Precise Time Data Logger (PTDL) was used as a data recorder. These software and hardware form the low-cost PNS used throughout the research.

5.1 Introduction

This chapter is devoted to a brief description of the software and hardware that were used for the research. A brief overview of Inertial measurement Data Simulator (IDS) will be explained first in Section 5.2, where it was used to simulate inertial sensor data for the work presented in Chapter 7. Simulated data is first used because it provides an early opportunity to analyze the new method for the low-cost PNS presented in the chapter, where the method can be assessed with controlled error budgets. In Section 5.3, the processing software will be explained, where it was used to process the simulated data and real field trials data presented in Chapter 6, 7 and 8. The software is called Position and Orientation INTegration (POINT) software. Then finally in Section 5.4, a description on the low-cost PNS hardware will be given, where the system was used for all the real field trials presented in this thesis.

5.2 Inertial Data Simulator (IDS)

Inertial measurement Data Simulator (IDS) is a part of Navigation Sensor Simulator (NSS) software, used to simulate inertial sensor measurements. NSS is an in-house GPS–INS simulator, first developed in the Institute of Engineering Surveying and Space Geodesy (IESSG) (Smith et al., 2003), currently known as the Nottingham Geospatial Institute (NGI). The NSS comprises a GPS data simulator, which was extended later to include an Inertial measurement Data Simulator (IDS). It was used in many projects in the NGI, most notably the European Space Agency (ESA)-funded 'Low-cost Navigator' project and the development of the Adaptive Kalman Filter (Hide et al., 2003). The following sections give a brief description of the IDS only, as it was used to provide test data with full truth information for the development and investigation of the method presented in Chapter 7.

5.2.1 IDS Overview

The Inertial Data Simulator (IDS) simulates measurements for a 3-axis Inertial Measurement Unit (IMU) that consists of three orthogonally mounted gyros and accelerometers. Using user-specified error models, the truth information about the errors on IMU measurements can be simulated. This is very important for the method proposed for the low-cost PNS presented in Chapter 7 because error observability can be analyzed accurately when the method is attempted. The next section will describe the IDS architecture in terms of the way the inertial sensor measurement is simulated for later processing.

5.2.1.1 The Algorithm Flow

The explanation herein is based on Fig. 5.1, which shows the algorithm flow for IDS.

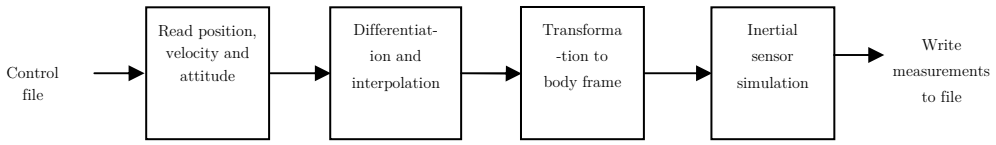

Fig. 5.1: The algorithm flow for inertial measurement simulation

IDS starts by reading a user-defined control file, which contains all the information required for the simulation. Most importantly for the work in Chapter 7, the control file contains the following information:

- Definition of trajectory.
- Selection of the error models to be used and their associated parameters.
- Selection of inertial sensors.
- Simulation period.

These four parameters describe: 1) what kind of trajectory is going to be simulated, 2) with what kind of errors to be simulated, 3) for which inertial sensor (gyros or accelerometers or both), and 4) for how long (period of the simulated trajectory).

Please refer to Appendix A for the specific parameters with its corresponding values.

The specific simulated trajectory file is created externally before the simulation begins. The trajectory file (please refer to Appendix B) is based on the previous GPS-only simulator trajectory file used in the previous version of NSS, where it requires only position and velocity information. Therefore, in order to simulate inertial sensor measurements in IDS, the same trajectory file is extended to include the attitude information of the IMU (Hide et al., 2003). The simulator thus provides interpolation of inertial sensor measurements so that data can be simulated at higher data rates than those entered in the trajectory file. Then, the double differentiation of position and single differentiation of attitude are performed in the IDS based on the equations fitted in between points during the interpolation stage.

After reading the control file with specific parameters and doing the differentiation and interpolation, next, the interpolated angular rates and accelerations are transformed into the body frame coordinate system of the inertial sensor. The standard INS mechanisation process (described in Section 2.4) is reversed to produce body frame measurements. This is done using the direction cosine matrix from the interpolated attitude measurements. During this time, the rotation rate of the Earth is added to the body frame angular rate measurements, and the Coriolis and gravity accelerations are added to the body frame acceleration measurements. For more details on the reverse mechanisation process, readers are directed to Hide (2003).

Finally, after accelerations and angular rates had been resolved in the body frame, they were then simulated with typical accelerometer errors and gyro errors, specified in the input control file as explained before. The inertial sensor measurements are simulated using the following equation:

$$\hat{l} = l + e \qquad \textbf{(5.1)}$$

where,

$\hat{l}$ is the inertial sensor measurement in body frame

l is the actual measurement vector

e is the simulated inertial sensor error vectors

The output of the IDS is a file containing the measurement time and gyro and accelerometer measurements in the body frame. This file will then be used for analysis in the processing software (this will be described in Section 5.3).

5.2.1.2 Construction of Trajectories

The IDS requires trajectory data in the form of position, velocity, and attitude data. The epoch separation for the input trajectory can be in any value as long as it is constant. A low data rate was used in the input trajectory file, which was then further interpolated in the IDS to 200 *Hz* data to form the simulated inertial sensor measurements.

The IDS is used to investigate by simulation the method presented in Chapter 7. Two trajectories; static and kinematic (walking), were constructed using a simple C-language program. For the latter case, the walk is constructed along a straight trajectory, as it will be then much easier to analyze and identify the heading drift problem. The static trajectory is also constructed to investigate the IMU errors observability when the KF is updated during ZUPT periods when the method is applied.

The next section will discuss the processing software used to process the simulated data and the real field trials data.

5.3 Processing Software

All the datasets (simulated and real) in this research are processed using the in house NGI's POINT (Position and Orientation Integration) software. The software was designed specifically with the purpose of allowing easy integration with

measurements from external sensors, and has been successfully used for many projects at NGI. Author used this software to integrate measurements from the proposed methods presented in the thesis and processed them. The POINT software is essentially the Kalman Filter that models states, and accepts measurements to correct the states. For more details of POINT software, please refer to Hide et al. (2007a), Hide et al. (2007b) and Hide (2009).

5.3.1 The Kalman Filter

The Kalman Filter (KF) forms the basis of the algorithm in POINT. Section 2.5 has described the fundamentals of the KF in detail. Essentially it is an iterative filter, which starts with initialisation (Section 2.5.3.1) where the states and their covariances in the filter are initialised. The states are the quantities that are to be estimated, and the covariance is the estimate of the errors of the states (more details are discussed in the next section).

The states can be initialized ($\hat{x}_0^{(+)}$) from the prior knowledge of the system obtained either during the alignment period (Section 2.4.3.1), from the calibration data, or from the information obtained from external sensors (for example GPS). For example, the position can be initialized from a GPS position solution, or a known surveyed point, and roll and pitch can be initialized during alignment period (Section 2.4.3.1). Additionally, the initial estimation uncertainty standard deviations must be given first to initialize the system noise covariance matrix Q_k (given by Eq. (2.35)). These noise statistics represent the uncertainty of the states, for example the attitude uncertainty is dependent on the accelerometer and gyroscope errors. They may be empirically determined based on the performance of the filter, sometimes known as the KF tuning (Groves, 2008). If factory calibration data is available for these errors, it may also be used to determine the suitable values for initializing the system noise. The choice of which depends on the system designer, where the stability and the accuracy of the filter needs to be taken into account. Normally, a trial and error process in determining the optimal value is adopted by for example comparing the filter estimated output with a good

reference system. According to Groves (2008), a good tuning philosophy may be made by fixing $\hat{P}_0^{(+)}$ and Q_k, and varying measurement noise, R_k that gives the best estimates. This approach was adopted in this research.

After the initialisation step (Section 2.5.3.1), the filter goes into the iterative part of the algorithm, where it comprises a prediction step (Section 2.5.3.2) and an update step (Section 2.5.3.3). In the prediction step, the states are predicted forward until the next KF update. A dynamic model (Section 2.5.2), which describes the way the states vary with time, is used by the KF to carry out the prediction. The covariance is also predicted forward using the dynamics model and the modelled process noise (an estimate of the error in the model).

After the prediction step, the KF is updated with the new measurement (observation). In order to perform the update step, the KF also requires information about the expected noise in the new measurement, which is called the measurement noise. The KF then estimates the new state by combining the predicted states with the new measurement. The weight between the predicted state and the new measurement is formed using the predicted covariance and the measurement noise. The prediction step and update step then occur recursively until the end. Fig 5.2 shows the process in the KF. The next section will further describe the KF in POINT in details, such as the states and observations, which are used for the research presented in the thesis.

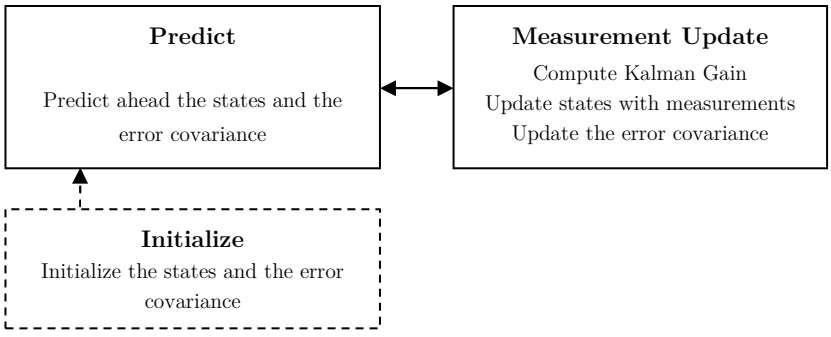

Fig. 5.2: High level diagram of the KF operation

5.3.2 States

There are 15 error states modelled in POINT for the research, although POINT is capable to model more states. They are:

$$\delta x = \begin{pmatrix} \delta r^n & \delta v^n & \epsilon^n & b_g & b_a \end{pmatrix}^T \tag{5.2}$$

where

δr^n	is the vector of n-frame latitude, longitude and height errors
δv^n	is the vector of n-frame velocity errors
ϵ^n	is the vector of n-frame attitude errors
b_g	is the vector of b-frame gyro bias
b_a	is the vector of b-frame accelerometer bias

Other IMU errors such as accelerometer and gyro scale factor error, cross-coupling error and gravity dependent errors were not modelled in this research. Therefore, the effects these unmodelled errors have towards the KF states were coarsely approximated by increasing accelerometer and gyro noise empirically so that the measurement noise impact is much greater than the unmodelled errors.

As discussed in Section 2.5, an error state KF was used for this research. For the initialisation phase, all the error states were initialized to zero, except the gyro bias where its value was initialized by averaging the gyro measurements during stationary alignment. This gyro bias value is used to correct the IMU gyro raw measurements, before using these measurements in the INS mechanization process (step 1 in Section 2.4.3.2).

It is important to mention that the KF in POINT is an error-state KF used in feedback form, which means that the estimated errors from the KF are feedback at every iteration, or at regular intervals, to correct the low-cost PNS solutions. This is sometimes known as a closed-loop configuration of the KF (Groves, 2008). Because of this, the KF states are kept small and thus maintaining the small error

assumption of the states. This ensures that the linearized error model assumption in the filter remains valid.

In Section 2.5.3.2, the KF predicts the state $\hat{x}_{(k)}^{(-)}$ using the knowledge of how the previous state $\hat{x}_{(k-1)}^{(+)}$ evolves over time based on its state transition matrix, where

$$\hat{x}_{(k)}^{(-)} = \Phi \hat{x}_{(k-1)}^{(+)} \tag{5.3}$$

In POINT, state transition matrix, Φ is formed using the approximation

$$\Phi = exp(F\,\Delta t_k) \approx I + F\,\Delta t_k + \frac{(F\,\Delta t_k)^2}{2!} \tag{5.4}$$

where the dynamic matrix F is formed using the error dynamics of the inertial system, explained in the next section, and Δt_k is the time separation. Eq. (5.3) is used under the assumption that either $\Delta t_k = t_k - t_{k-1}$ is very small or the dynamic matrix F is approximately constant over time interval Δt_k. As Eq. (2.35) shows, the covariance matrix associated with process noise vector, w_k is given by

$$E\begin{bmatrix} w_k & w_i^T \end{bmatrix} = \begin{cases} Q_k & \text{if } i = k \\ 0 & \text{if } i \neq k \end{cases} \tag{5.5}$$

In POINT, the process noise matrix, Q_k is approximated using the equation (Shin, 2005, Hide, 2003)

$$Q_k \approx \frac{1}{2}\left[\Phi G Q_s G^T + G Q_s G^T \Phi^T\right] \Delta t_k \tag{5.6}$$

where G is the noise mapping matrix (that relates the modelled states with their respected noises) and Q_s is a diagonal matrix formed from the standard deviations of the process noise (for example the accelerometer and gyro measurements).

5.3.3 Dynamic Model Representation

The derivation of the phi-angle error model equations in Eq. (2.29), (2.30) & (2.31) and its development into functions of position and velocity errors can be found in Shin (2001) and Farrell and Barth (2008), which can be rewritten as:

$$\delta \dot{r}^n = F_{rr}\delta r^n + F_{rv}\delta v^n \tag{5.7a}$$

$$\delta \dot{v}^n = F_{vr}\delta r^n + F_{vv}\delta v^n + f^n \times \epsilon^n + C_b^n \delta f^b \tag{5.7b}$$

$$\dot{\epsilon}^n = F_{er}\delta r^n + F_{ev}\delta v^n - \omega_{in}^n \times \epsilon^n - C_b^n \delta \omega_{ib}^b \tag{5.7c}$$

where $(\cdot)\times$ refers to a skew symmetric matrix form of function $(\cdot)$ and $F(\cdot)$ represents the partial derivatives with respect to the position and velocity terms (ibid.). The full form of these matrices can be found in Appendix C.

The last matrix terms in Eq. (5.7b) and (5.7c), specifically δf^b and $\delta \omega^b$, represent the errors in IMU measurements. Theoretically, these errors terms can be refined by modelling all possible IMU error terms such as temperature dependent errors and misalignment errors (Petovello, 2003). However, as discussed in (ibid.) and Section 2.3.1, the observability of all the error states, even if it is theoretically possible, is almost impossible because of operational conditions such as requiring sufficient dynamics and long data collection. Similar with (ibid.), in this research, both sensor error terms are therefore considered to only consist bias terms (b_a, b_g) and noise (w_a, w_g), with some temporal variability given to the bias states (τ), and can be written as:

$$\delta f^b = b_a + w_a \tag{5.8}$$

$$\delta \omega_{ib}^b = b_g + w_g \tag{5.9}$$

From Section 2.5.2, the system dynamics for the phi-angle error model used in POINT can be written in matrix form as

$$\dot{\delta x} = F\delta x + Gu \tag{5.10}$$

Using Eq. (5.8) & (5.9) in Eq. (5.7), the final system model in state space form used in the research can therefore be written as:

$$\begin{pmatrix} \delta\dot{r}^n \\ \delta\dot{v}^n \\ \dot{\epsilon}^n \\ \dot{b}_g^b \\ \dot{b}_a^b \end{pmatrix} = \begin{pmatrix} F_{rr} & F_{rv} & 0 & 0 & 0 \\ F_{vr} & F_{vv} & f^n\times & 0 & C_b^n \\ F_{er} & F_{ev} & -\omega_{in}^n\times & -C_b^n & 0 \\ 0 & 0 & 0 & \tau & 0 \\ 0 & 0 & 0 & 0 & \tau \end{pmatrix} \begin{pmatrix} \delta r^n \\ \delta v^n \\ \epsilon^n \\ b_g^b \\ b_a^b \end{pmatrix} + \begin{pmatrix} 0 & 0 & 0 & 0 \\ C_b^n & 0 & 0 & 0 \\ 0 & C_b^n & 0 & 0 \\ 0 & 0 & I & 0 \\ 0 & 0 & 0 & I \end{pmatrix} \begin{pmatrix} w_a \\ w_g \\ w_{bg} \\ w_{ba} \end{pmatrix} \tag{5.11}$$

where a more detailed form of Eq. (5.11) is included in Appendix C.

5.3.4 Observation Equations and Design Matrix

A number of measurement types are pre-determined in POINT for processing the INS measurements for the research, defined as:

- Position
- Velocity
- Attitude

In POINT, the linearized measurement, z_k in Eq. (2.34) is approximated using the following equation:

$$z_k = h(k)\delta x(k) \approx H_k \delta x_k = z_k^{observed} - z_k^{predicted} \tag{5.12}$$

where the observed value comes from an external sensor or measurement, whilst the predicted value comes from the KF's prediction or computation. For example, velocity updates from ZUPT measurements will be differenced with the computed velocity, producing an estimate velocity error as the measurement to the KF to update velocity error state, δv^n. Eq. (2.43) is then used to compute the innovation vector, $\boldsymbol{v_k^{(-)}}$, re-written as:

$$v_k^{(-)} = z_k - H_k \delta x_k^{(-)} \tag{5.13}$$

The design matrix, H (sometimes called measurement matrix) defines how the measurement vector varies with the error state vector, δx.

Therefore, using linearized measurement $z_k = H_k \delta x_k$, the formulation of measurement equations for position error can be written as (Farrell and Barth, 2008; Shin (2005):

$$z_k = H_k \delta x_k$$

$$\begin{pmatrix} \delta\varphi \\ \delta\lambda \\ \delta h \end{pmatrix} = \begin{pmatrix} R_N + h & 0 & 0 \\ 0 & (R_E + h)cos\varphi & 0 \\ 0 & 0 & -1 \end{pmatrix} \begin{pmatrix} \delta r_N \\ \delta r_E \\ \delta r_D \end{pmatrix} \tag{5.14}$$

For example, if the position from GPS is available as measurement, then the measurement in Eq. (5.14) is given as:

$$z_k = \begin{pmatrix} r_{INS}^n - r_{GPS}^n \end{pmatrix} = \begin{pmatrix} \varphi_{INS} - \varphi_{GPS} \\ \lambda_{INS} - \lambda_{GPS} \\ h_{INS} - h_{GPS} \end{pmatrix} \tag{5.15}$$

Likewise, the measurement equations for velocity error can be written as (ibid.):

$$\begin{pmatrix} \delta v_N \\ \delta v_E \\ \delta v_D \end{pmatrix} = \begin{pmatrix} 1 & 0 & 0 \\ 0 & 1 & 0 \\ 0 & 0 & 1 \end{pmatrix} \begin{pmatrix} \delta v_N \\ \delta v_E \\ \delta v_D \end{pmatrix} \tag{5.16}$$

And, for heading error, the linearized heading measurement equations can be written as (Shin, 2005):

$$\begin{pmatrix} \\ \delta\psi \\ \\ \end{pmatrix} = \begin{pmatrix} \frac{\partial\psi}{\partial\epsilon_N} & \frac{\partial\psi}{\partial\epsilon_E} & \frac{\partial\psi}{\partial\epsilon_D} \end{pmatrix} \begin{pmatrix} \epsilon_N \\ \epsilon_E \\ \epsilon_D \end{pmatrix} \tag{5.17}$$

where the partial derivative is formed from the elements of the estimated direction cosine matrix, $\hat{C_b^n}$. Assuming small angle misalignment, $\hat{C_b^n}$ can be written as (ibid.):

$$\hat{C_b^n} = [I - \epsilon\times]\, C_b^n \tag{5.18}$$

Let c_{ij} represents the ijth elements of C_b^n. By referring to Eq. (2.14), the computed heading can be written as follows:

$$\hat{\psi} = tan^{-1}(\hat{c_{21}}/\hat{c_{11}}) \tag{5.19}$$

where,

$$\hat{c_{11}} = c_{11} + c_{21}\epsilon_D - c_{31}\epsilon_E \tag{5.20}$$

$$\hat{c_{21}} = c_{21} + c_{31}\epsilon_N - c_{11}\epsilon_D \tag{5.21}$$

Therefore,

$$\frac{\partial\hat{\psi}}{\partial\epsilon_N} = \frac{\frac{\partial\hat{c_{21}}}{\partial\epsilon_N}\hat{c_{11}} - \hat{c_{21}}\frac{\partial\hat{c_{11}}}{\partial\epsilon_N}}{\hat{c_{11}}^2 + \hat{c_{21}}^2} \approx \frac{\hat{c_{11}}\hat{c_{31}}}{\hat{c_{11}}^2 + \hat{c_{21}}^2} \tag{5.22}$$

$$\frac{\partial\hat{\psi}}{\partial\epsilon_E} = \frac{\frac{\partial\hat{c_{21}}}{\partial\epsilon_E}\hat{c_{11}} - \hat{c_{21}}\frac{\partial\hat{c_{11}}}{\partial\epsilon_E}}{\hat{c_{11}}^2 + \hat{c_{21}}^2} \approx \frac{\hat{c_{21}}\hat{c_{31}}}{\hat{c_{11}}^2 + \hat{c_{21}}^2} \tag{5.23}$$

$$\frac{\partial\hat{\psi}}{\partial\epsilon_D} = \frac{\frac{\partial\hat{c_{21}}}{\partial\epsilon_D}\hat{c_{11}} - \hat{c_{21}}\frac{\partial\hat{c_{11}}}{\partial\epsilon_D}}{\hat{c_{11}}^2 + \hat{c_{21}}^2} \approx \frac{-\hat{c_{11}}\hat{c_{11}} - \hat{c_{21}}\hat{c_{21}}}{\hat{c_{11}}^2 + \hat{c_{21}}^2} \tag{5.24}$$

The estimation process then continues as described in Section 2.5.3.2 and 2.5.3.3. All the relationships and assumptions in this section are derived in Farrell and Barth (2008) and Shin (2005).

5.4 Low-cost PNS

Apart from the simulation and processing software used as described in the previous sections, the trials and investigations in this research were also performed using hardware. This is important because simulation may not be realistic and for more accurate analysis, undertaking real field trials using real equipment can provide the true outputs. The hardware used that makes up the low-cost PNS includes the inertial sensor and the data logger, and is explained next.

5.4.1 Inertial Sensor

A 3DM-GX3-25 IMU from MicroStrain® was the only sensor used for pedestrian navigation investigation in this research. When it was purchased two years ago, 3DM-GX3-25 was the latest available IMU from MicroStrain®. It has a dimension of 44mm x 25 mm x 11mm, weighing only 11.5 *grams,* making it the smallest and the lightest Attitude and Heading Reference System (AHRS) on the market. It was already factory-calibrated, and therefore was used in the research without any further calibration. Fig. 5.3 shows the IMU and when it is mounted on a shoe. Apart from being known as an IMU, it is also known as AHRS because it incorporates 3-axis MEMS magnetometer on board as well, along with 3-axis MEMS accelerometers and 3-axis MEMS gyros. It is fully temperature compensated over the entire -40^0 to +75^0 C operational range and is available with either RS-232 or USB connection for data communication, which might be convenient for different user requirements. It has a user adjustable data rate from 1 Hz to up to 1000 Hz and varieties of outputs such as Euler angles, rotation matrix, acceleration, angular rate and magnetic field. The full specification of the IMU can be further found in MicroStrain (2011a).

3DM-GX3-25 has a technical specification of a typical low-cost IMU grade. For this research, the IMU used has a limit of 16 g for acceleration and 1200 $^0/s$ for angular rotation, which is sufficient for walking trials. This is because an angular rate of a pedestrian foot is typically less than 600 $^0/s$, and acceleration is typically

Fig. 5.3: The 3DM-GX3-25 IMU from MicroStrain (left) and mounted on a shoe (right).

6 g (Huang et al., 2010). The accelerometer bias stability is quoted as ± 0.01 m/s^2 for the 16 g model, and the gyro bias is specified as ± 0.2 $^0/s$ for the 300 $^0/s$ model (higher gyro bias should be expected for the higher angular rate model used). More technical specification of the IMU can be found in Table 2.1 in Chapter 2.

MicroStrain® 3DM-GX3-25 has similar specifications to some of the low-cost IMUs currently on the market. Table 5.1 shows their comparison. In terms of performance, Kealy et al. (2010b) conducted comparative experiments involving all the low-cost MEMS IMU tabulated in Table 5.1 (except MicroStrain® 3DM-GX3-25) with Applanix navigation grade IMU. It was concluded that the low-cost IMU still contains substantial error in its absolute measurements (acceleration, angular rate) when compared with the navigation grade IMU (ibid.). Note that the 3DM-GX3-25 should also produce similar results because of the similar specifications. These significant errors had some interpretable values, however, where they are able to detect relative changes in the platform motion. For example, the change in the measurements can distinguish the operating environment, such as changing from stationary to moving motion. It is therefore sufficient to say that using a low-cost IMU-only for a good positioning system provides a huge challenge. As demonstrated in Section 4.3.2, if the low-cost IMU is used without any aiding measurements, it is practically impossible to get a good positioning solution.

Table 5.1: Comparison of different low-cost IMUs and navigation grade IMU, adapted from Kealy et al. (2010b)

Sensor		**Measurement**	**Bias Stability**	**Range**	**Sampling rate (Hz)**	**Size (cm)**	**Weight (g)**	**Cost (£)**
Low-Cost grade MEMS IMU	Crista IMU, *Cloudcap Technology*	3-axis acc.	0.5 ms^{-2}	$\pm$10g	100	5.2x3.9 x2.5	36.8	<1300
		3-axis gyros	0.6 ^{0}/s	$\pm$300 ^{0}/s				
	MTI *Xsens*	3-axis acc.	0.02 ms^{-2}	$\pm$5g	100	5.8x5.8 x2.2	50	<1300
		3-axis gyros	1.0 ^{0}/s	$\pm$300 ^{0}/s				
	Inertia Link *MicroStrain*	3-axis acc.	0.1 ms^{-2}	$\pm$5g	200	4.1x6.3 x2.4	39	<1000
		3-axis gyros	0.2 ^{0}/s	$\pm$300 ^{0}/s				
	IMU 400CC *Crossbow*	3-axis acc.	0.01 ms^{-2}	$\pm$2g	40	7.6x9.5 x8.1	64	<8000
		3-axis gyros	0.2 ^{0}/s	$\pm$300 ^{0}/s				
	3DM-GX3-25 *MicroStrain*	3-axis acc.	0.01 ms^{-2}	$\pm$16g	100	4.4x2.5 x1.1	11.5	<1700
		3-axis gyros	0.2 ^{0}/s	$\pm$300 ^{0}/s				
Navigation grade IMU	Honeywell CIMU *Applanix*	3-axis acc.	50×10^{-6} ms^{-2}	n/a	100	20.4x20.4 x16.8	4.5 kg	<60 000
		3-axis gyros	0.0035 ^{0}/s	n/a				

5.4.2 PTDL

The Geospatial Research Centre (GRC) New Zealand Precise Time Data Logger in Fig. 5.4 was used to record the IMU data. It incorporates a precise time GPS receiver, which has a time stamp accuracy of 0.1 *us*, and a high speed flash memory data logger. The data inputs, available through the back panel connectors, can be logged to the SD memory card with time tags aligned to GPS time. The GPS time stamp is only recorded for the purpose of synchronising the IMU with GPS so that a performance comparison can be made between the INS and GPS solutions. If there is no GPS satellite in view to provide accurate timing inside buildings, an internal IMU clock is used instead. This means that if autonomous navigation is sought only indoors, (assuming known initial position) the GPS time stamp might not be needed and the IMU internal clock can be used instead.

This however introduces an issue with the accuracy of the IMU clock. It is possible over a long period of usage that the clock accuracy might be degraded. This means that if the clock is not accurate, the IMU data will be recorded with errors in the time stamp. For example, if an inaccurate IMU clock is used (assuming delayed by 1 *s*) when recording the IMU data, a typical pedestrian step

that lasts for 1 s will appear to last for 2 s. This in turns will cause error in the estimation of position, where the position error will appear to be larger than it should be.

For this research, the accuracy of the IMU clock is assumed to be satisfactory for the data collection based on its specification sheet, where the IMU clock is specified to have an accuracy of +/- 0.01% (accumulate error of approximately 100 μs for every 1 s). For the longest trial recorded in this research (2400 s), the clock is thus accurate to within 0.24 s, which means the accumulated position error resulting from clock inaccuracy will be approximately less than the half-step distance of a typical pedestrian. This therefore is considered adequate for the research when analyzing the IMU performance. Note that to properly quantify the accuracy of the IMU clock for all the trials and the effect it has on the results is beyond the scope of this thesis. Therefore, all recorded data and the estimated solutions are assumed to be corrupted with this error, and are part of the final estimated solutions.

Fig. 5.4: The PTDL used to record data

5.5 Summary

Information about the software and hardware used for the research has been presented, including the modelled states, the observation matrix and the dynamic model used. The IDS software will be used in Chapter 7 for simulation purposes, and the POINT software will be used for integrating measurements and data processing in Chapters 6, 7 and 8. For the hardware, the low-cost MicroStrain MEMS IMU has been selected for use in the research as a representative of the low-cost MEMS IMU. In the next chapter, the performance of the low-cost magnetometer to deal with the problem described in Chapter 4 will be analyzed.

Chapter 6

Magnetometer Aided

This chapter discusses how a low-cost magnetometer may be used to aid a pedestrian navigation system. A background study of the low-cost magnetometer is first explained, describing specifically how the magnetometer may be used. The chapter leads on to describe a filter to extract good measurements from the magnetometer. Analysis from real field trial results will show that magnetometer measurements are insufficient to aid INS heading, unless it is reliable on every epoch. A discussion and a chapter summary follow at the end.

6.1 Introduction

As discussed in Section 4.5.2, a magnetometer may be useful to aid the drift in the low-cost IMU heading. This is because magnetometer heading measurements do not drift over time, as often happened with the low-cost IMUs. Furthermore, it is practically possible and easier to use the magnetometer for the low-cost PNS, as often it is already encapsulated together with the low-cost IMU used. Therefore additional sensors for the purpose of mitigating the heading drift may not be required. Mainly because of these two reasons, the magnetometer can be the most practical method to aid the low-cost PNS heading. Therefore it was chosen in this research to be an exemplary method to mitigate heading drift for the low-cost PNS. Additionally, in the case of the pedestrian navigation system, the magnetometer is often integrated to give the heading measurement (Haverinen and Kemppainen, 2009; Huang et al., 2010; Glanzer and Walder, 2010; Storms et al., 2010; Bird and Arden, 2011; Faulkner et al., 2010; Shin et al., 2010). In this chapter, the performance of the magnetometer to provide heading measurements is thus investigated. Unlike Section 4.5.2, this chapter will offer more detail in describing magnetometers as the aiding source of heading measurements for the low-cost PNS.

The investigation starts in Section 6.2 by familiarization with the current ideas in the literatures on integrating magnetometer heading measurements in the low-cost PNS. This is followed by introducing its principle of operation in Section 6.3. This includes how magnetometer readings can be used to compute the heading measurements, what kind of errors affect the measurements and how calibration can be made to reduce these errors. Next, Section 6.4 will use one of the ideas from Section 6.2 to aid the IMU heading in the low-cost PNS. To assess its performance in mitigating IMU heading drift, trials (outdoor and indoor) were performed and the results are presented in Section 6.5. Chapter summary follows.

6.2 Heading Measurements from Magnetometer

A 3-axis magnetometer senses magnetic field components in each of its axes that represent an electromagnetic environment of the earth. Using these measurements, the magnetic heading can be calculated (Caruso, 2000). These magnetic field components, however, change with respect to its environment. Steel is one of the materials known to affect the magnetic field. Thus the magnetic field sensed by magnetometers will be biased, ultimately giving a false magnetic heading measurement to the system. Bachmann et al. (2007) have done extensive tests on the effect that indoor environments have on magnetometer measurements. This includes steel cabinets, desktop computers and cable conduits inside bricks walls. These were shown to disturb significantly the magnetic field components sensed by the magnetometer, and subsequently corrupt the magnetometer heading measurements. This therefore provides a huge challenge in using the magnetometer for the low-cost PNS in indoors.

Nonetheless, there are two known approaches often attempted in the literatures to try overcoming this challenge: magnetometer-fingerprinting and magnetometer-filtering.

In the magnetometer-fingerprinting method (Chung et al., 2011, Storms et al., 2010, Haverinen and Kemppainen, 2009), magnetic field measurements for the area intended to perform navigation are pre-surveyed, tagged with position and stored in a database (similar to the methods described in Section 3.2.6 & 3.2.7). The user equipped with a magnetometer can then use the database to localize his position based on the magnetic field measurements. For example a probabilistic method (Storms and Raquet, 2009) can be used to estimate the user's position from the database using the matched magnetic measurements. The magnetometer-fingerprinting method does not use the computed magnetic heading measurements explicitly, but rather it uses the measured magnetic field components instead. There are some limitations of using the fingerprinting method and similar discussion from Section 3.2.6 & 3.2.7 are referred. The accuracy of the estimated

position can therefore be dependent on the quality of the magnetic map database, the quality of the measurements from the magnetometer, and how well these two can be reliably matched.

In the magnetometer-filtering method (Bird and Arden, 2011, Faulkner et al., 2010), a magnetometer filter is used to reject bad magnetometer measurements (or magnetometer outliers), characterized by a certain predetermined condition (this point will be explained later in Section 6.4). The accepted measurements (good measurements) are then integrated with the IMU heading measurements to give the best estimate of heading (thanks to their complementary effect). The integration can be done for example using the Kalman Filter (KF).

A similar filtering approach was also used by Renaudin et al. (2010) and Afzal et al. (2011) to provide good magnetometer heading measurements; but instead of only one magnetometer, six magnetometers were used. It was based on observation by Afzal et al. (2010), which concluded that if 3-axis magnetometers are placed close to each other but with different orientation, there exists information about the presence and absence of magnetic disturbances in the magnetic field vectors. Using a magnetometer filter and the magnetic field model (such as the International Geomagnetic Reference Field (IGRF) magnetic model (Finlay et al., 2010)), disturbed measurements can be detected. When magnetic disturbances are detected, the cleanest Earth's magnetic field components from the multi-magnetometer can be identified using the multi-magnetometer measurements. This can then be used to compute the magnetometer heading measurements. Examples from these two approaches (single magnetometer and multi-magnetometer) show that the magnetometer-filtering method can improve the position accuracy of the pedestrian navigation system. Therefore, the magnetometer-filtering method was considered useful in indoor environments that have significant magnetic disturbances.

Because of the challenges with the magnetometer-fingerprinting approach, the magnetometer-filtering approach is instead adopted for the investigation work presented in this chapter. Additionally, only single magnetometer approach is

attempted because only single 3-axis magnetometer is available with the low cost IMU used. The investigation carried out therefore seeks to address the following issues (which were not addressed properly in the literatures) with respect to the magnetometer-filtering method:

- What happens if only a few reliable filtered heading measurements are available (worst case scenario for indoors)?
- What effect does this have over a longer period of time on the low-cost PNS position solution?

6.3 Background on Magnetometer

Before presenting the investigation on the performance of the magnetometer, firstly the fundamentals of magnetic field and magnetometer are briefly reviewed in this section.

6.3.1 Earth Magnetic Field

Imagine an Earth magnetic field as a large dipole magnet, where two opposing poles are labelled geographically as North and South poles. This field is created by the "outer core region of the earth", which comprises "a hot and dense liquid of highly conductive nickel iron" and "the earth's spin and shape" (Campbell, 2001). The direction of the field is from the Earth's magnetic South pole towards the Earth's magnetic North pole (Fig. 6.1). The magnetic field strength, which varies with location, ranges between 50 μT to 60 μT (500 mG to 600 mG) and has components parallel to the Earth surface (Caruso, 1998).

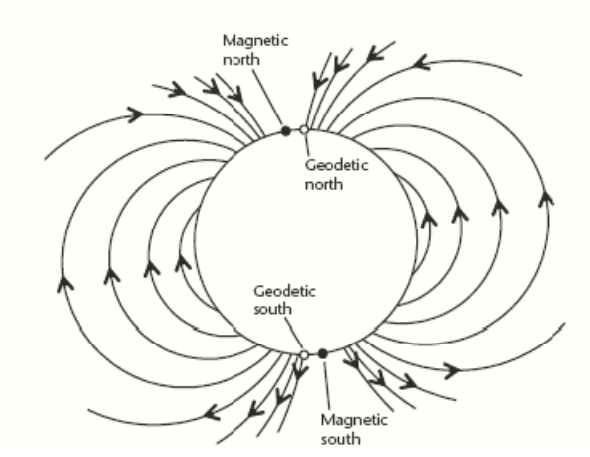

Fig. 6.1: Earth magnetic field (Groves, 2008)

The Earth's magnetic field varies with location and time. These changes can be characterized into two categories known as variation and perturbation. Variation is a slow change to the Earth's magnetic field, often in a large scale over a few kilometres, because of the nature of Earth's geology. Perturbation is a change in the Earth's magnetic field locally (such as indoors) and often varies significantly in terms of strength and durations, mostly because of man-made materials. Perturbation corrupts the magnetometer measurements and therefore is the main problem faced when using magnetometers indoors.

6.3.2 Magnetic Field Model

Earth's magnetic field can be mapped and modelled. Global magnetic models such as the International Geomagnetic Reference Field (IGRF) (Finlay et al., 2010) or the U.S./U.K. World Magnetic Model (WMM) (National Geophysical Data Centre. 2011), can be used to identify elements related to the Earth's magnetic field such as the total magnetic field intensity according to a specific location on Earth. This model is derived from observations all over the world by magnetic observatory groups, and often used for research such as space weather investigations and magnetic field anomaly investigations. Fig. 6.2 shows a screenshot of IGRF model parameters (BGS, 2011).

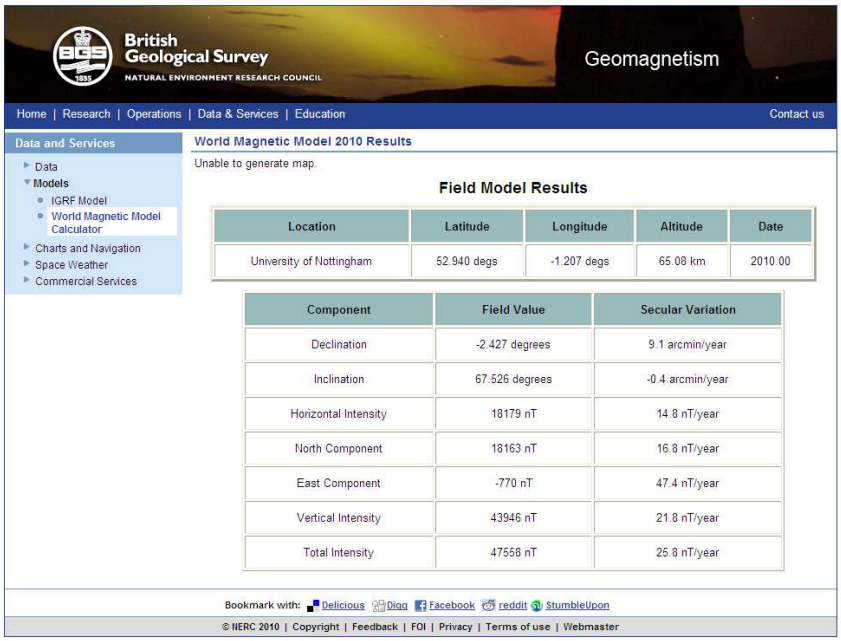

Fig. 6.2: IGRF2010 model parameter screenshot

6.3.3 Magnetometer Heading

A magnetometer measures the strength of the earth magnetic field. A 3-axis MEMS magnetometer is often cased together with accelerometers and gyros in an Inertial Measurement Unit (IMU) because of its smaller size and weight. In an ideal disturbance-free environment, a 3-axis magnetometer should measure the components of Earth magnetic field in its body-frame, $m_e = \begin{bmatrix} m_x^b & m_y^b & m_z^b \end{bmatrix}^T$. Magnetic heading in a Local-Levelled frame $(\varphi = 0, \theta = 0)$, ψ_m^{LL} can then be computed as (Kaniewski and Kazubek, 2009):

$$\psi_m^{LL} = -atan2\left(m_y^{LL}, m_x^{LL}\right) \tag{6.1}$$

6.3.4 Primary Source of Magnetometer Errors

There are several errors that can disturb magnetometer measurements. They can be categorized into two (Liu et al., 1989): instrumentation errors and compass deviation error. Instrumentation errors include sensor offset, scale factor mismatch,

non-orthogonality and sensor tilts. On the other hand, compass deviation error is caused by the perturbation, and generally is divided into two (Chen et al., 2010): hard iron and soft iron (which will be described in the next section).

Instrumentation errors can often be calibrated (or compensated), either at the user level (user-calibrated) or at the manufacturer level (factory-calibrated). Tilt error, for example, will cause an error in heading computation in Eq. (6.1) because the horizontal magnetic field is corrupted by components of the vertical magnetic field. For a low-cost PNS, this error can be calibrated at the user level using accelerometers and levelling approach (Section 2.4.3.1). However, compass deviation error is more significant for accurate magnetometer measurements. This is because the error, especially soft iron perturbation, is dependent on the magnetometer surrounding environment that cannot be controlled. Because of this, the perturbation appears to be varying spatially and temporally, and thus it is very difficult (and complicated) to model its effect on magnetometer measurements.

6.3.4.1 Hard Iron and Soft Iron.

Hard iron and soft iron (Guo et al., 2008) affect the magnetometer measurement in magnitude and/or direction. Hard iron distortions are caused by permanent magnets and magnetized iron or steel in a fixed location on the compass platform. These distortions are equivalent to a constant magnetic field vector observed by the 3-axis magnetometers in all direction. It will add a constant magnetic field component to the true magnetic field measurement in each axis of the magnetometer. Similarly, the soft iron comes from materials surrounding the magnetometer and also distorts the Earth's magnetic field lines. Unlike the hard iron, the difference is that the amount of distortion from the soft iron depends on the magnetometer orientation, which then appears to be varying in different direction.

Hard iron can be compensated during static calibration (more details are provided in the next section). On the other hand, compensation for soft iron is considered difficult as the soft iron varies in different directions. Therefore, soft

iron calibration is not attempted in this chapter and is beyond the scope of this thesis, and its disturbance effect on magnetometer measurements are reduced using a filtering approach (Section 6.4).

6.3.5 Magnetometer Calibration

As discussed in the previous section, calibration is important to compensate for the errors disturbing magnetometer measurements. It is very difficult, however, to compensate properly for the soft iron error continuously (sometimes known as online calibration). This is because a good calibration method requires a proper sampling method in all possible orientations to gather as much as possible magnetic perturbations information. Therefore, only static calibration is thought to be feasible for the low-cost PNS and is explained next.

6.3.5.1 Static Calibration

For a low-cost PNS indoors, ideally calibration should be performed continuously. However, when the user is walking, getting enough measurement samples for soft iron error calibration is not practical. This is because to gather as much perturbation information as possible, the magnetometer needs to rotate in all possible orientations throughout the walk. This is so inconvenient for the low-cost PNS. Even if this is possible, getting enough samples means the system will be time delayed, which is often not preferable for a real-time solution. Therefore, for the work presented in this chapter, only static calibration is adopted for the sole purpose of initializing the low-cost PNS heading for the trials. Stirling et al. (2003) tabulated possible methods for magnetometer calibration and are summarized in Table 6.1

Table 6.1: Comparison of magnetometer calibration techniques

Method	**Description**	**Advantage**	**Disadvantage**
1. Spot turn	User spins 360^0	Convenient	Few calibration points
2. Full circle	User walks around a circle of approximately 4m diameter	Calibration in pedestrian mode. Many calibration points.	Requires open level calibration area, more time consuming.
3. GPS calibration	Compass calibrated by GPS heading	Convenient, continuous	Requires GPS, user must be moving. Not the true heading as it is the direction of travel.
4. Gyroscope correction	Measures relative heading change	Removes effect of short term field disturbances	Added sensor expense, low-cost gyros have substantial drift.

A simpler method than Table 6.1 from Caruso (1998) was performed offline for the static calibration. A MicroStrain™ "3DM-GX3 Firmware Soft & Hard Iron Calibration" proprietary software was used (MicroStrain, 2011a). The IMU (Section 5.4.1), which contains a 3-axis MEMS magnetometer, was rotated manually about its axes in all possible orientations to collect magnetic field data. This lasted for about 1 minute, with 1000 points collected (maximum allowed in the software).

Assuming a 2-D case, when rotating a magnetic sensor 360^0 on a level horizontal plane without any magnetic error, the horizontal magnetic readings should form a circle centred at the origin (0, 0). In the presence of perturbation however, the hard iron will shift the centre of the circle, and the soft iron effect will distort the circle to an ellipse (Skvortzov et al., 2007). This is because hard iron causes constant bias on the magnetic measurements and therefore all the measurements appear to be biased (offset from the measurements' origin). Soft iron, on the other hand, causes the distortion because it varies the measurements.

To compensate for the hard iron, one simple way is to use offsets based on the maximum and minimum of the horizontal magnetometer readings, $m^{LL}_{xy,off}$ (ibid.):

$$m^{LL}_{x,off} = \frac{m^{LL}_{x,max} + m^{LL}_{x,min}}{2};\ m^{LL}_{y,off} = \frac{m^{LL}_{y,max} + m^{LL}_{y,min}}{2} \qquad \textbf{(6.1)}$$

The values from Eq. (6.1) are then used to subtract all the horizontal magnetometer measurements to produce hard iron-compensated measurements, $m_{X,Y}^{LL}$:

$$m_{X,i}^{LL} = m_{x,i}^{LL} - m_{x,off}^{LL} \mid_{i=1}^{n};\ m_{Y,i}^{LL} = m_{y,i}^{LL} - m_{y,off}^{LL} \mid_{i=1}^{n} \tag{6.2}$$

The effect of this method is illustrated in Fig. 6.3 for a 3-D case (similar methods as above applied for the third axis). Fig. 6.3 (a) shows the output of the magnetometer measurements in a 3-D before calibrated. Red dots are the magnitude of magnetic field vectors measured in all axes without calibration from Eq. (6.1) & (6.2) (in unit Gauss, G) and the green sphere shows what the calibrated data should look like (disturbance-free). The 'purple star' in the middle of the 'globe' represents the centre of the collected measurements (shifted measurements) and the 'green solid circle' in the middle of the 'globe' represents the centre of the compensated measurements. In Fig. 6.3 (a), hard iron disturbances, which cause constant bias in the magnetometer measurements (red dots), are compensated by shifting the red dots-sphere to its origin. This is done in the software by 'superimposing' the red dots sphere onto the green sphere (essentially applying Eq. (6.1) & (6.2) to the measurements).

With the hard iron subtracted out, the remaining soft iron can be represented by a tilted and elongated circle (or sphere for 3D cases), normally called ellipsoid. The tilted circle can be characterized by the angle of the major axis of the elongated circle from the origin. This can be compensated by rotating all the measurements by this angle. The elongated circle can be characterized by the ratio of the major axis and the minor axis of the elongated circle. The major axis can then be scaled and multiplied to the magnetometer measurements to transform the elongated circle back to a circle. The scale factor can be determined by:

$$x_{sf} = \begin{cases} b, & b = \frac{m_{y,max}^{LL} - m_{y,min}^{LL}}{m_{x,max}^{LL} - m_{x,min}^{LL}} \\ 1, & \text{if } b > 1 \end{cases} \tag{6.3}$$

$$y_{sf} = \begin{cases} b, & b = \frac{m_{x,max}^{LL} - m_{x,min}^{LL}}{m_{y,max}^{LL} - m_{y,min}^{LL}} \\ 1, & \text{if } b > 1 \end{cases} \tag{6.4}$$

Measurements from Eq. (6.2) are then multiplied with Eq. (6.3) & (6.4) to produce compensated hard iron and soft iron measurements during static calibration. Note that the methods discussed assumes a 2D-case, but the same method can be applied for the third axis in a 3D-case. Using the software, static soft iron perturbations are compensated by selecting 'sphere fit' in the software (essentially applying Eq. (6.3) & (6.4) to Eq. (6.2)).

After calibrating and saving the offset parameters for all three axes into the IMU firmware, the IMU was once again rotated in all possible orientations. The output is now shown in Fig. 6.3 (b), where the green-dots represent magnetometer readings taken after the static calibration. Now it fits the green sphere well, and the 'purple star' overlaps the 'green solid circle' in the middle.

Note that when the user starts to walk in the indoors environment, it is likely that the soft iron perturbations will come into effect again and corrupt the magnetometer measurements. As discussed before, online calibration (for soft iron) is no longer deemed an advantage and is not attempted. Therefore, the next section will address the magnetometer-filtering method used to filter out unreliable measurements during real walking trials, based on approach by Faulkner et al. (2010).

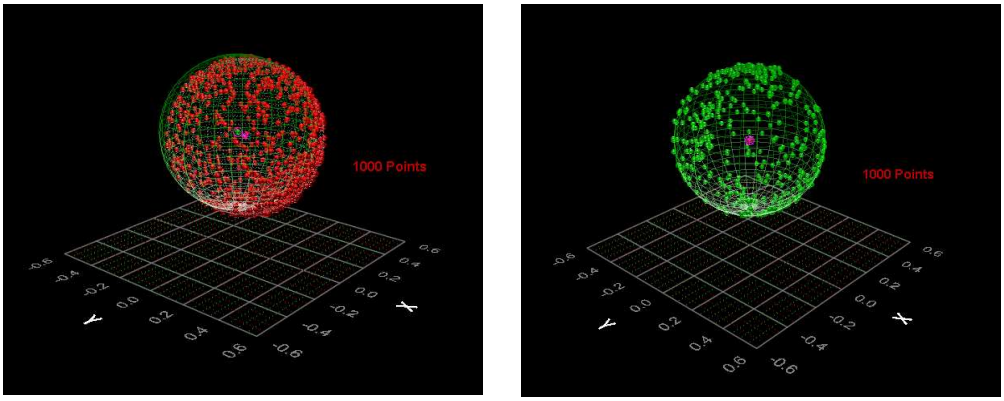

(a) (b)

Fig. 6.3: Magnetometer output (a) before calibration, (b) after calibration

6.4 Magnetometer Filtering

Because of the limitation of the magnetometer-fingerprinting approach as discussed in Section 6.2, the magnetometer-filtering method was chosen to address the perturbation issue on the magnetometer measurements. To do this, a filter proposed by for example Faulkner et al. (2010) and Bird and Arden (2011) can be used. The method from the former was selected for the investigation presented in this chapter because during the investigation, the latter was not available to the author. As the author was completing the thesis, the author became aware of the second reference. Nonetheless, the objective of this section is not to assess the performance differences between each of these filters, but rather to show only how filtering the magnetometer measurements can be performed to get reliable heading measurements. Table 6.2 summarizes the two methods. Using an empirically determined threshold, γ , Faulkner's filter accepts magnetometer heading measurements if they pass steps 1 and 2 (or 3). Bird's filter on the other hand accepts the measurements if they pass all steps. These filtered measurements are then used to update the Kalman Filter (KF).

Table 6.2: Comparison between two magnetometer-filtering approaches

Steps	Faulkner	Bird
1	RSS of the measurement magnetic strength vectors – predicted (from model) $< \gamma_1$ and,	Same, and
2	Change in magnetometer heading – change in KF estimated heading $(t_{current} - t_{previous}) < \gamma_2$ or,	Magnetometer heading – KF estimated heading $< \gamma_4$, and
3	Step 2 but with different time epoch, $(t_{current} - t_{next}) < \gamma_3$	Same with Faulkner step 2, and
4	n/a	Change in magnetometer-derived rotation rate – change in gyro measured rotation $< \gamma_5$

6.4.1 Magnetometer Filter

After describing the background of the magnetometer in the previous sections, the investigation now starts by describing the magnetometer filter proposed by Faulkner et al. (2010) below:

- *The first test compares the difference between the measured value of the total Magnetic Field Intensity (MFI) and the predicted value of the total MFI.* The measured value of total MFI is the Root Sum Squared (RSS) of the measurements from the 3-axis magnetometer. The predicted value of the total MFI makes use of Earth's total MFI measurement, taken from the International Geomagnetic Reference Model 2010 (BGS, 2011), based on the approximate position of the low-cost PNS. The measured total MFI is then compared against the IGRF model. The measurement is accepted for the next test if it does not exceed the empirically determined thresholds. Otherwise, the test aborts and restarts at the next measurement epoch.

This assumes that the Earth's magnetic field changes only slowly with position because the rate of the Earth's magnetic field change spans a few kilometres (Campbell, 2001). In the case of indoor pedestrian navigation, this is considered valid because of the small area of navigation. Therefore, if there are any rapid changes to the magnetic field, it can be considered as a result of the perturbations.

- *The second test compares the difference in the change of heading between the estimated navigation heading from the Kalman Filter (KF) and the measured magnetic heading from the magnetometer.* The estimated navigation heading from the KF is compared between the current epoch and the previous epoch to produce the change in the estimated navigation heading. The estimated navigation heading is an optimal estimate from all previous sensed rotations (via the strapdown INS) and the KF updates. Similarly, the measured magnetic heading is compared between the current epoch and the previous epoch to produce the change in the measured magnetic heading. These two changes in heading are then compared against each other and the result is tested against an empirically predetermined threshold.

- *Test 3 is similar to test 2, but with a different definition of calculation epoch.* Instead of using the current epoch and the previous epoch, the change in heading is computed between the current epoch and the future epoch (user-defined). The difference in the change in heading is again tested against an empirically predetermined threshold. This however requires the filter to be time delayed, which for real time purposes might not be suitable.

Tests 2 and 3 based on the assumption that magnetic perturbations tend to vary quickly over distance. On the other hand, the Kalman-Filtered INS heading errors are expected to change slowly with time, at a rate determined by the filter-estimated gyro bias.

For the low-cost PNS used during the research, an epoch is defined as when ZUPT is detected and the user has walked a step (reserved for discussion in Section 8.2.3.1). In other words, the current epoch and previous epoch refer to the current detected step and previously detected step. Magnetometer heading measurements are chosen if they pass test 1, and either test 2 or test 3. Otherwise no heading update to the KF is performed.

6.4.2 Trials

Two trials were performed: outdoor and indoor. The outdoor trial was performed to assess the performance of the magnetometer outdoors. Likewise, the indoor trial was also performed to assess its performance indoors, and also to investigate the issues with the magnetometer highlighted in Section 6.2. Each trial and its results will be described in the next two sections: outdoor trial (Section 6.4.2.1) and indoor trial (Section 6.4.2.2). Fig. 6.4 shows the setup used for the trials. The IMU is shown to be mounted on a shoe (strapped with a masking tape) while the backpack contains the PTDL, and a 12 V battery to power up the data logger and the shoe-mounted IMU. The data is then post-processed using POINT software (see Chapter 5).

Fig. 6.4: Example of the system setup

6.4.2.1 Outdoor trial

An outdoor walking trial was performed on a football pitch for approximately 40 minutes. The user walked for 10 rounds approximately on the pitch line throughout the trial. A similar system setup as Fig. 6.4 is used but with an additional Network Real Time Kinematic (NRTK) GPS system deployed as a reference system. The NRTK GPS system has a typical horizontal position accuracy of approximately 2 *cm* (Aponte et al., 2009). The NRTK antenna was carried on the backpack and its receiver held by the user's hand. The initialization of the low-cost PNS was done as described in Section 4.3.1, but now the heading was initialized using the static-calibrated magnetometer heading measurement. The magnetometer measurements (with a rate of 20 *Hz*) were processed using the magnetometer-filtering method (Section 6.5.1) on every detected footstep. The accepted measurements were then used to update the heading estimation in the KF.

6.4.2.1.1 Disjunction Error

During the trial, varying lever arm errors between the NRTK reference position and the IMU estimated position were created, which was called a disjunction error (Bancroft, 2010). This is because the NRTK antenna and the IMU were not co-located. The term was used in (ibid.) to describe an error between the system and its reference, caused by a varying lever arm during walking. During the trial, the reference was constructed from the NRTK solution, which has the antenna

mounted on top of the backpack carried by the user. In contrast, the IMU was mounted on the foot. This makes an exact comparison of the IMU solution with the NRTK solution impossible, because the reference solution is not the position estimated by the KF-filtered IMU solution.

In a standing stationary position, the lever arm can be fixed for direct comparison of the position solution with NRTK. The lever arm is the vector from the foot (where the IMU was mounted) to the antenna in the backpack. As the user walks, however, the lever arm varies because of the periodic change caused by the mechanics of walking. Although this error can be approximated, it is however considered negligible compared to the large errors of the low-cost IMU tested within this research. Analysis of the results, therefore, will include this error as part of the position errors.

6.4.2.1.2 Results

For simplicity, the results are presented only for the first two rounds of the walking trial (the result for the full trial is reserved for Section 6.4.2.2). First, the Total Magnetic Field Intensity (total MFI) is plotted in Fig. 6.5. It clearly shows a fairly stable measurement (blue line) with respect to the IGRF model measurement used (red line), indicating very low magnetic perturbations. The maximum value of the total MFI was recorded as 0.5367 G, a difference of only 0.0470 G from the reference model. The acceptance threshold for the magnetometer filter (step 1) is empirically determined (0.1 G). As a result, all magnetometer measurements passed step 1 of the magnetometer filter and were used for the next step in the filter.

Next, Fig. 6.6 shows the absolute differences between the estimated change of navigation heading from the KF (current epoch and previous epoch) and the change of measured magnetic heading from the magnetometer (current epoch and previous epoch). It shows only small variations between the headings, indicating also very low magnetic perturbations. Using empirically determined threshold of 1^0, most of the magnetometer heading measurements passed step 2 and were accepted to update the heading estimation in the KF. The result from step 3 of the

magnetometer filter is not presented because the filter algorithm (described in Section 6.4.1) chooses between step 2 and step 3. Because most of the measurements have passed step 2, step 3 is not needed.

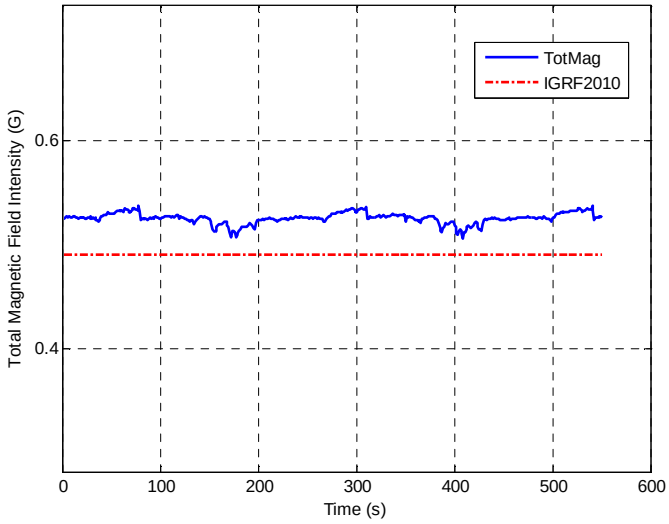

Fig. 6.5: The Total MFI measured by the magnetometer on every step for the outdoor trial.

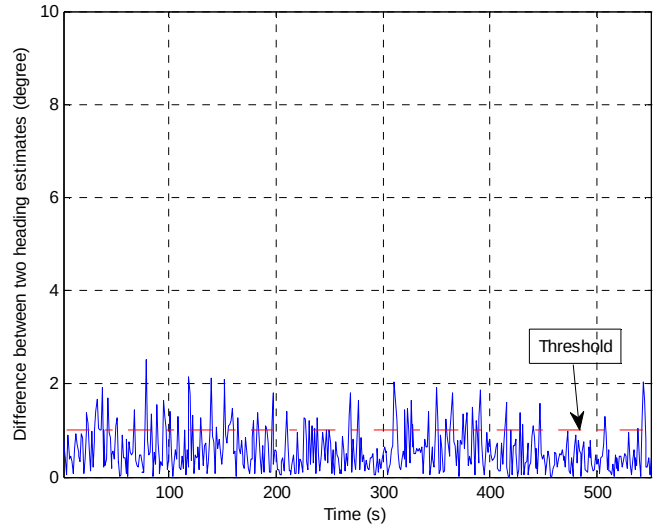

Fig. 6.6: The difference between the change of heading (current epoch and previous epoch) for magnetometer and KF estimated heading.

Fig. 6.7 shows the difference between the magnetometer-aided INS heading and the NRTK-aided INS heading (the reference). It can be observed that the error in the INS headings when aided with magnetometer heading measurements is relatively small ($< 5^0$). This indicates that most of the magnetometer-aided heading measurements for the outdoor trial are reliable to update the KF. Most of the magnetometer measurements were indeed accepted and this resulted in frequent updates to the KF.

To visualize the frequency of the updates, Fig. 6.8 is plotted. It shows the events when magnetometer heading measurements are accepted (green dots). It can be observed that because of the low magnetic perturbations (from Fig. 6.5 & 6.6), most of the measurements are accepted by the magnetometer filter. The interval of these accepted measurements can be identified at about $1s$ (shown in Fig. 6.9), which means that the accepted magnetometer heading measurements are updated to the KF at almost every step during the trial.

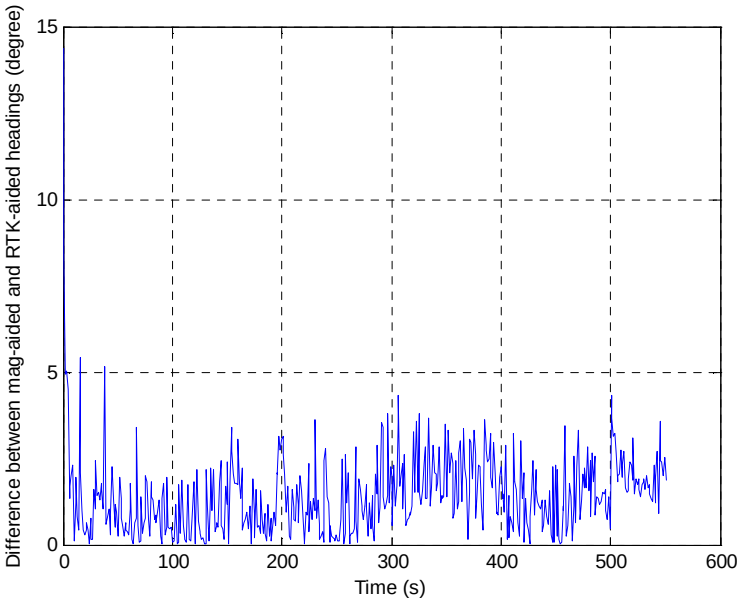

Fig. 6.7: INS heading error when aided with filtered-magnetometer heading measurements

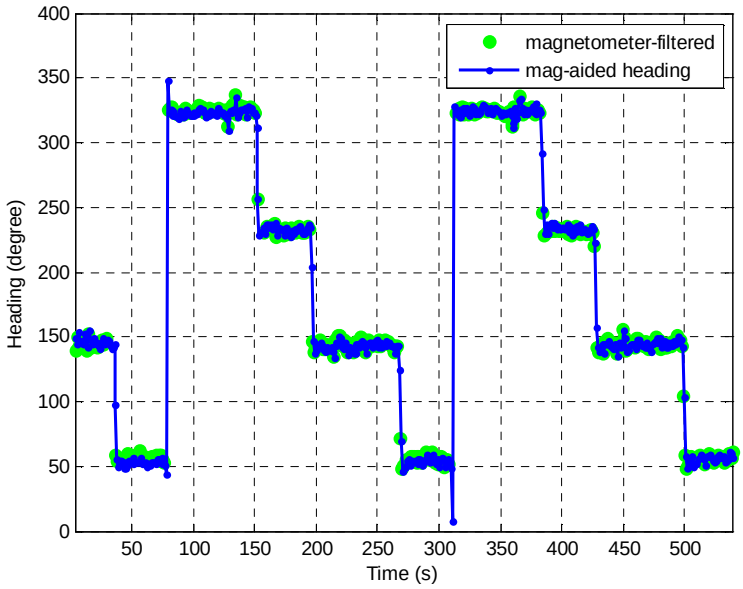

Fig. 6.8: Magnetometer-aided INS heading and the filtered measurements

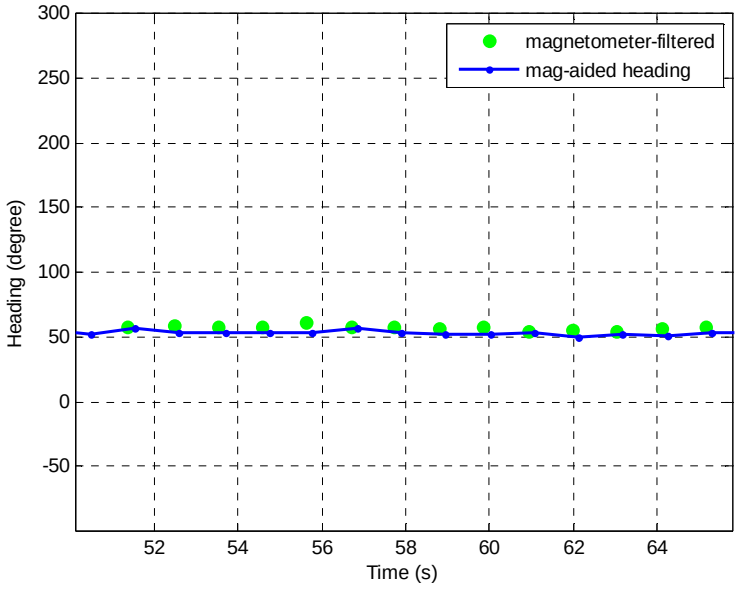

Fig. 6.9: The filtered-magnetometer heading measurements (frequently accepted in the filter)

As a result of using frequent filtered magnetometer heading measurements, the position error for the magnetometer-aided-low-cost PNS was reduced. Figure 6.10 shows a comparison of the Horizontal Position Error (HPE) for when the magnetometer was and was not used, for the low cost PNS. They are compared against the NRTK position. When the magnetometer was not used, the low-cost PNS were updated only by ZUPTs measurements. It is observed that when the magnetometer was not used, the maximum HPE was relatively large at 50 m after about 9 minutes of navigation. Conversely, when the magnetometer was used, the maximum HPE was reduced significantly to only about 14 m. This shows the importance of using the magnetometer because when reliable and frequent magnetometer heading measurements are available, they significantly reduce the position error for the low-cost PNS. Note that for the blue plot in the figure, the dips plotted at 200 s $<$ t $<$ 300 s and 500 s $<$ t $<$ 600 s are a result of returning to the same starting position.

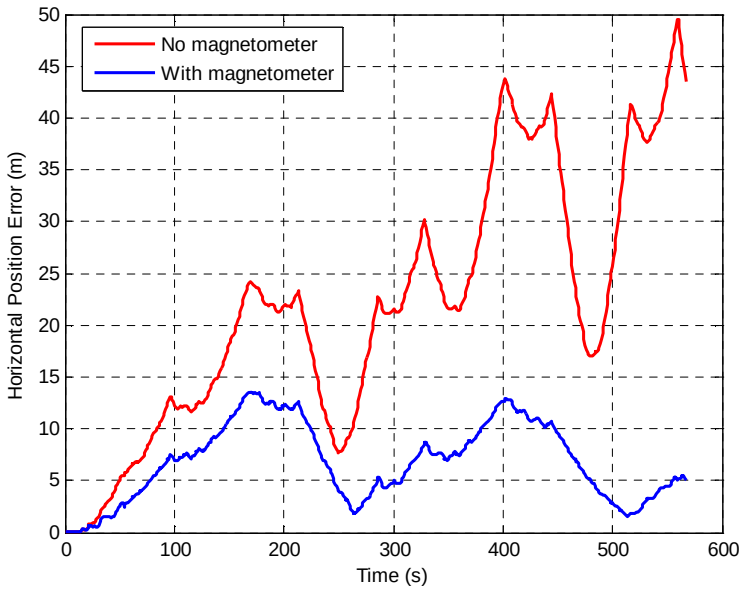

Fig. 6.10: Comparison of horizontal position error for the low-cost PNS when aided (blue) and unaided (red) with magnetometer.

6.4.2.2 Indoor Trial and Results

Next, an indoor walking trial was performed inside an office building in the Nottingham Geospatial Institute (NGI), shown in Fig. 6.11. The pedestrian walked approximately around the office twice. Notice that there are several elements that could perturb the magnetometer measurements such as steel cabinets (on the left), computers (on the right) and concrete pillars (on the left).

The total MFI was first plotted in Fig. 6.12. It can be observed that there are big variations in the total MFI readings, characterized by the magnetic perturbations caused by the elements described before. The highest total MFI was recorded as 1.034 G, a difference of 0.5441 G from the IGRF2010 reference model. Note that this is significantly higher than what was observed in Fig. 6.5 for outdoors, where more stable measurements were recorded.

For the purpose of investigation for this chapter (in particular in this section), two issues were addressed in Section 6.2 if magnetometer-filtering method were to be used: the effect of a long interval between heading updates and its impact on the low-cost PNS when longer trial duration is required. To investigate these correctly, therefore the same trial data (from the outdoor trial) should be re-analyzed so that a consistent observation can be made when emulating indoor environment. Furthermore, using the outdoor trial data enables a proper quantification of errors because there was a reference system available.

For the first issue, the result from the previous section has identified that frequent updates from reliable magnetometer headings were useful to reduce the low-cost PNS position error. In reality however, this can only be realized in an environment with very minimal magnetic perturbations. Therefore when indoors, it is very unlikely to have such minimal perturbations (as shown in Fig. 6.11 & 6.12). In order to investigate this issue, infrequent heading updates must therefore be shown. This is considered difficult using true measurements from the indoor trial because magnetic disturbances are uncontrollable in real indoor environments (for example reliable magnetometer headings may not be visible at all).

Fig. 6.11: The office environment with several man made material that could perturb magnetometer measurements.

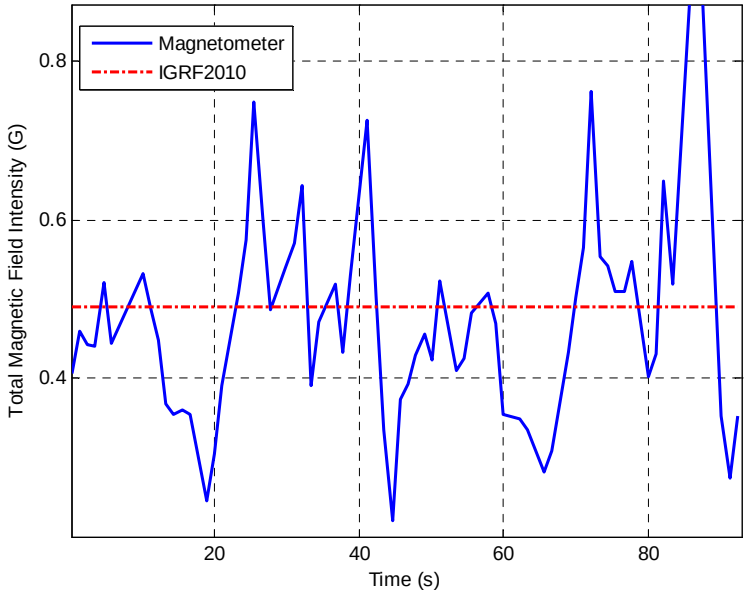

Fig. 6.12: The total MFI in the office of NGI building

Therefore, because of the reasons discussed in the previous paragraph, it was decided that the same data from the outdoor trial would be manipulated. This could be done by increasing the threshold used in the magnetometer filter so that stricter tests could be used to filter the magnetometer measurements. As a result, only few measurements would be accepted, thus would emulate the indoor environment where significant magnetic perturbations would cause significant errors in the magnetometer measurements (thus would not pass the magnetometer filter).

To achieve this, the threshold for step 2 in the magnetometer filter (in Section 6.4.1) was reduced from 1^0 to 0.1^0. The interval of the magnetometer heading is plotted again in Fig. 6.13, where the accepted magnetometer heading measurements are shown by the green dots. It is observed from the figure that the interval between accepted measurements is now increased to approximately 20 s from 1 s in Fig. 6.9. This therefore causes infrequent heading measurements to be updated to the KF.

Fig. 6.14 shows the Horizontal Position Error (HPE) of the low-cost PNS when frequent (blue) and infrequent (red) heading updates were performed. The plot is taken from the difference between the NRTK GPS position and the estimated magnetometer-aided-INS position. As a result of infrequent heading updates, the position error increases for the low-cost PNS. When there are many accepted magnetometer headings, the maximum HPE is about 14 m. In contrast, when there are only a few accepted magnetometer headings, the maximum HPE increases to 35 m.

Although the position error increased when the heading updates are not frequently available, it does highlight again the usefulness when using a magnetometer to reduce position error. When comparing Fig. 6.14 and Fig. 6.10 (where magnetometer was not used at all), an improvement of about 15 m in maximum HPE is noticed.

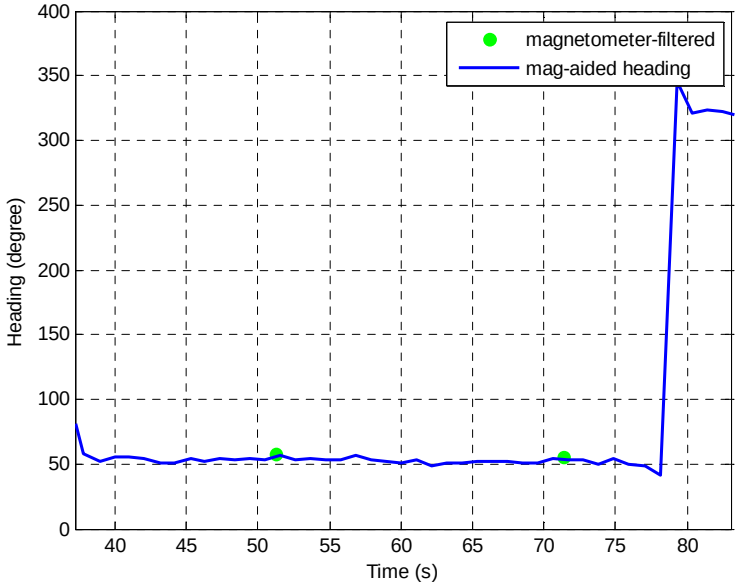

Fig. 6.13: The filtered-magnetometer heading measurements (infrequently accepted in the filter)

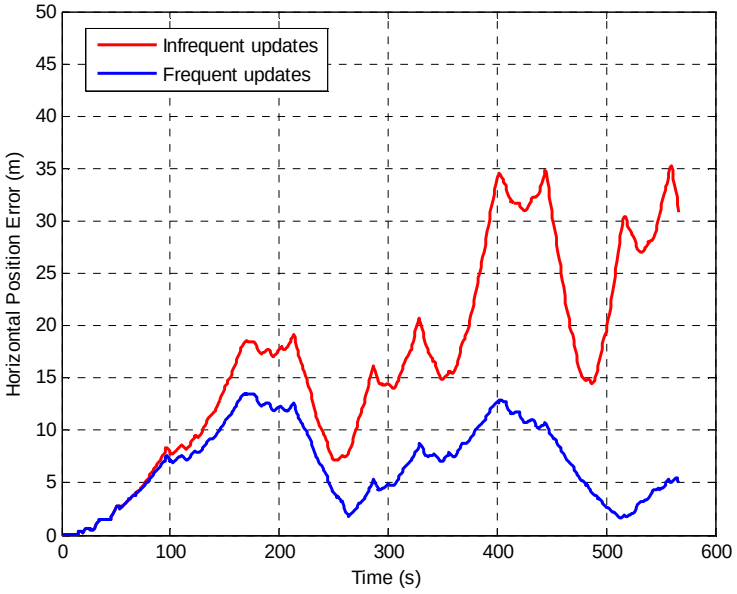

Fig. 6.14: Comparison of Horizontal Position Error (HPE) for the low-cost PNS when frequent updates (blue) and infrequent updates (red)

Next, the impact of longer trial duration (with infrequent heading updates) to the low-cost PNS solution is addressed by plotting the Horizontal Position Error (HPE) for the whole duration of the outdoor trial. Note that the actual outdoor trial was performed for 40 minutes and results so far are only presented for the shorter duration of 10 minutes. Therefore, the impact of this second issue can be seen by analyzing longer trial duration. Fig. 6.15 is plotted to show the HPE for three cases: (a) no magnetometer is used, thus heading updates are not available (green), (b) magnetometer-filtering is used with frequent magnetometer heading updates (blue) and (c) magnetometer-filtering is used with infrequent magnetometer heading updates (red). The maximum HPE for when there were no updates (green), infrequent updates (red) and frequent updates (blue) are found to be 114 m, 53 m and 14 m respectively. These once again show that using a magnetometer can indeed help in reducing position error for the low-cost PNS.

Furthermore, the interval between heading updates are also important in determining the accuracy of the solution. In a worst case scenario indoors where magnetic perturbations can be significantly high, frequent heading updates are very unlikely. This will result in significant position errors because the position error will still grow when there are no heading measurements available (in between heading updates). This is because of the correlation between heading error and position error. Moreover, when there are no heading measurements available, the position errors already accumulated are unrecoverable unless a good position update is also available during this period. Even if good heading measurements are available afterwards, the position errors already accumulated still cannot be corrected. This is because the heading measurement update only corrects the INS heading and does not correct the accumulated position error. Therefore, in the case of the low-cost PNS when longer indoor navigation is required, frequent heading updates are needed if a magnetometer were to be used as the only source of heading measurements.

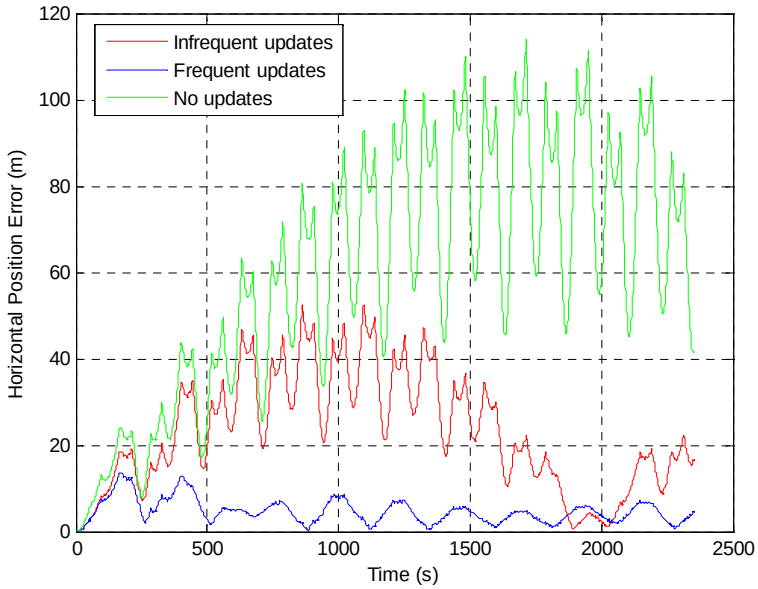

Fig. 6.15: Comparison of Horizontal Position Error (HPE) between three cases; no magnetometer used (green), magnetometer used but infrequent updates (red) and magnetometer used with frequent updates (blue).

6.5 Discussion

1. In an indoor environment, severe magnetic perturbations are often found. In order to identify and reject the corrupted heading measurements, different filtering methodologies on the magnetometer measurements can be adopted, such as the magnetometer filter presented in this chapter and the innovation filter in the KF. The innovation filter in the KF for example, can filter magnetic outliers in the magnetic measurements. However, although filtering magnetometer measurements can be achieved, it might not significantly reduce heading drift sufficiently to also reduce position errors. This is because of the unavailability of good magnetometer measurements which result from magnetic perturbations.

2. Using the magnetometer-filtering method, it was observed that the interval between heading updates from magnetometer heading measurements is important. Indoors, high magnetic perturbations cause significant error in magnetometer heading measurements. When the magnetometer-filtering

method is used, most of the measurements will be rejected. Only a few measurements are thus used to update the KF sparsely. Therefore a long interval between these updates was found to cause significant position errors. However, if the interval is short (frequent updates given to the KF), a magnetometer can be useful to aid the INS heading for the low-cost PNS. For a low-cost IMU, the heading update needs to be as often as possible (preferably in the space of a few seconds) to be able to control the heading drift error. Unfortunately, frequent heading updates from filtered magnetometer measurements are rarely available in typical indoor buildings, thus compromising its advantage in providing absolute heading measurements.

3. In the case of a longer navigation period, the impact of a long interval between heading updates is significant more in the low-cost PNS solution. This is because the accumulated error in position between heading updates is unrecoverable unless there are good position measurements available. This means that having occasional good heading updates from the magnetometer afterwards still cannot correct the position error. It worsens in a long run, where the position error will be so significant because of the accumulated position error.

6.6 Summary

This chapter has analyzed the significance of magnetometer measurements to aid heading in a low-cost PNS. Filtering the magnetometer measurements can be performed to give a reliable heading measurement to mitigate heading drift. It was, however, identified that frequent reliable heading measurements from a magnetometer were needed, which are often not available indoors. Because of this, a new strategy, which does not use the magnetometer as the additional heading sensor, is drawn in the next chapter to mitigate heading drift for the low-cost PNS.

Chapter 7

Rotating the IMU Mechanically

Following the findings in Chapter 6, this chapter moves on to propose mounting an IMU on a rotating platform and attaching it to a pedestrian's shoe. The analysis begins by simulating the Rotating IMU (RIMU), followed by performing a real walking trial using a RIMU prototype. The significance of the RIMU is analyzed and discussed using simulation and real field trial results. The RIMU will be shown to mitigate the heading drift error and improve the IMU error observability when used with ZUPTs. These therefore reduce the position drift error of the low-cost PNS. A chapter summary is then followed at the end. Part of the results and the discussions in this chapter have been published in (see List of Publications, pp. x).

7.1 Introduction

Chapter 6 has highlighted the fact that even when the low-cost Pedestrian Navigation System (low-cost PNS) was aided by a magnetometer, position drift was still inherent in an environment with high magnetic disturbances such as indoors. This is because it was shown that occasional heading updates from filtered magnetometer measurements to mitigate heading drift were still not enough. Although integrated gyro measurements can be used between these occasional heading updates in the Kalman Filter (KF), it is often only valid for several epochs because of high drifts in low-cost gyros over a short period of time.

In this chapter, an innovative approach to mitigate heading drift is proposed for the low-cost PNS by mounting a Rotating IMU (RIMU) on the shoe (or foot). The concept is depicted in Fig. 7.1. The low-cost IMU was mounted on a platform that rotated on a single axis, and the platform was attached to a pedestrian's shoe. The concept is that if it were possible to physically 'flip' the IMU at regular intervals about a certain axis (suppose y-axis) such that the other axes (suppose x-axis and z-axis) are 'flipped', errors on the x- and z-axis would cancel, as these errors would have a positive and negative effect along the path every time when the IMU is flipped. It is envisaged that as a result of RIMU, the heading observability will also be improved.

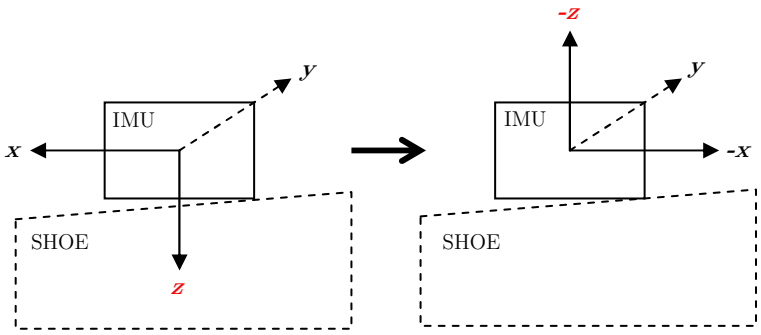

Fig. 7.1: The concept of the RIMU for a low-cost PNS

The concept of rotating IMU to reduce IMU errors was introduced by (Geller, 1968), where he described and computed the mathematical equations relating to rotating gyros about its azimuth axis. Two terminologies were proposed by (Curey et al., 2004) for this concept; carouselling and indexing. The former was defined as rotating the IMU with continuous rotation in multiple orientations, while the latter was defined as rotating the IMU with discrete known rotation. There are also many researchers exploring the same ideas (Zha et al., 2010, Ben et al., 2010, An et al., 2010, Zhao et al., 2009, Zhang et al., 2009, Lai et al., 2010, Feng et al., 2009, Waldmann, 2007, Syed et al., 2007, Ishibashi et al., 2007, Yang and Miao, 2004, Uliana et al., 1997, Qi et al., 2009). For clarity, however, the differences of all these approaches with the author's work are summarized below. This chapter therefore emphasizes:

- Pedestrian navigation application with a low-cost MEMS IMU,
- Performed in both simulation and real field environment with true walking trajectory,
- Rotating the IMU on a single axis (y-axis) continuously throughout the trajectory, and
- Neither carouselling – because of the single rotation axis – nor indexing because of the ambiguity of the rotation rate to the user.

The idea is, therefore, adopted for the low-cost PNS. Whilst this is undesirable in terms of increasing the size, power and weight requirements of the IMU, it is not unrealistic to do so considering the exceptionally small mass of MEMS sensors. Furthermore the reliability and precision requirements for the mechanical rotations are relatively low when considering a simple one-axis rotation, and there is no requirement for a constant or measurable rotation as position, not rotation, is the only output of concern.

The next Section 7.2 will give the mathematical equations describing the INS output after undergoing rotations because of the RIMU. The performance of the

RIMU is investigated first using simulation in Section 7.3, before presenting the real field trials results in Section 7.4.

7.2 The Effect of RIMU

This section describes the effect of the RIMU to the estimated INS solutions through errors modulation, which subsequently increase the observability for the error states. The INS output resulting from the RIMU will be concisely analyzed by presenting a series of INS error equations (Section 7.2.1 equations are derived mainly from Qi et al. (2009)).

7.2.1 INS Error Modulation

As described in Chapter 2, velocity error states and attitude error states can be propagated using a standard strapdown error navigation equation using the phi-angle error model (refer to Eq. (2.30) & (2.31)). In these two equations, $\delta\omega^b$ and δf^b are errors caused by the gyroscope and accelerometer sensor errors. When the IMU is rotated about its y-axis, C_b^n is made to change continuously. Therefore, multiplication of $\delta\omega^b$, δf^b and C_b^n in the equations affects the INS navigation accuracy. The idea of a RIMU therefore lies in the periodical change of the elements in C_b^n such that the average of $C_b^n\delta\omega^b$ and $C_b^n\delta f^b$ approximate to zero.

When the RIMU is rotated about its y-axis, angular rate error and specific force error can be represented as:

$$C_b^n\delta\omega_{ib}^b = \begin{pmatrix} \cos\omega_r t & 0 & \sin\omega_r t \\ 0 & 1 & 0 \\ -\sin\omega_r t & 0 & \cos\omega_r t \end{pmatrix} \begin{pmatrix} \varepsilon_x \\ \varepsilon_y \\ \varepsilon_z \end{pmatrix} = \begin{pmatrix} \varepsilon_x cos\left(\omega_r t\right) + \varepsilon_z sin\left(\omega_r t\right) \\ \varepsilon_y \\ -\varepsilon_x sin\left(\omega_r t\right) + \varepsilon_z cos\left(\omega_r t\right) \end{pmatrix} \quad \textbf{(7.1)}$$

$$C_b^n\delta f^b = \begin{pmatrix} \cos\omega_r t & 0 & \sin\omega_r t \\ 0 & 1 & 0 \\ -\sin\omega_r t & 0 & \cos\omega_r t \end{pmatrix} \begin{pmatrix} \Delta_x \\ \Delta_y \\ \Delta_z \end{pmatrix} = \begin{pmatrix} \Delta_x cos\left(\omega_r t\right) + \Delta_z sin\left(\omega_r t\right) \\ \Delta_y \\ -\Delta_x sin\left(\omega_r t\right) + \Delta_z cos\left(\omega_r t\right) \end{pmatrix} \quad \textbf{(7.2)}$$

where ω_r is the RIMU rotation rate, $\begin{pmatrix}\varepsilon_x & \varepsilon_y & \varepsilon_z\end{pmatrix}^T$ are the errors of gyros on the *x*-, *y*- and *z* axes, and $\begin{pmatrix}\Delta_x & \Delta_y & \Delta_z\end{pmatrix}^T$ are the errors of accelerometers on the *x*-, *y*- and *z*- axes.

From Eq. (7.1) and (7.2), it was shown that the IMU error terms for the *x*-axis and *z*-axis vary periodically due to cosine and sine functions. This however is not the case for the *y*-axis because it is the rotation axis, which does not have the cosine and sine functions. If the *x*- and *z*-axis errors are constantly positive or negative over the whole rotation, the errors will then reduce to zero after the whole rotation period of $(360^0/\omega_r)$. The RIMU is therefore very effective in eliminating the constant error terms on IMU axes that are perpendicular with the rotation axis.

7.2.2 INS Error Observability

The principle of the RIMU in improving the error states observability of the INS can be explained by assuming a simple case of a stationary and level IMU. The velocity error model from Eq. (4.1), (4.2) and (4.3) can be rewritten by including the errors in the accelerometer sensor force terms as (Godha and Lachapelle, 2008):

$$\delta\dot{v}^n = C_b^n f^b \times \epsilon + C_b^n \delta f^b \tag{7.3}$$

where it is similar with Eq. (2.30) (when ignoring the other terms in that equation as discussed in Section 2.4.3.3). It can be written in a matrix form as:

$$\begin{pmatrix}\delta\dot{v}_N\\ \delta\dot{v}_E\\ \delta\dot{v}_D\end{pmatrix} = \begin{pmatrix}0 & -f_D & f_E\\ f_D & 0 & -f_N\\ -f_E & f_N & 0\end{pmatrix}\begin{pmatrix}\epsilon_N\\ \epsilon_E\\ \epsilon_D\end{pmatrix} + C_b^n \begin{pmatrix}\delta f_x\\ \delta f_y\\ \delta f_z\end{pmatrix} \tag{7.4}$$

When the IMU is stationary and level, Eq. (7.4) becomes:

$$\begin{pmatrix}\delta\dot{v}_N\\ \delta\dot{v}_E\\ \delta\dot{v}_D\end{pmatrix} = \begin{pmatrix}0 & g & 0\\ -g & 0 & 0\\ 0 & 0 & 0\end{pmatrix}\begin{pmatrix}\epsilon_N\\ \epsilon_E\\ \epsilon_D\end{pmatrix} + \begin{pmatrix}\delta f_x & 0 & 0\\ 0 & \delta f_y & 0\\ 0 & 0 & \delta f_z\end{pmatrix} \tag{7.5}$$

where C_b^n is an identity matrix because of the small angle error approximation when stationary and level. When the IMU rotates 180^0 about its y-axis (still in a stationary and level mode), the C_b^n changes sign. Eq. (7.5) then becomes:

$$\begin{pmatrix} \dot{\delta v_N} \\ \dot{\delta v_E} \\ \dot{\delta v_D} \end{pmatrix} = \begin{pmatrix} 0 & g & 0 \\ -g & 0 & 0 \\ 0 & 0 & 0 \end{pmatrix} \begin{pmatrix} \epsilon_N \\ \epsilon_E \\ \epsilon_D \end{pmatrix} + \begin{pmatrix} -1 & 0 & 0 \\ 0 & 1 & 0 \\ 0 & 0 & -1 \end{pmatrix} \begin{pmatrix} \delta f_x & 0 & 0 \\ 0 & \delta f_y & 0 \\ 0 & 0 & \delta f_z \end{pmatrix} \quad \textbf{(7.6)}$$

Eq. (7.5) and (7.6) can be written as simultaneous equations (7.7) and (7.8):

$$\dot{\delta v_N} = (+g)\epsilon_E + \delta f_x \quad \textbf{(7.7a)}$$

$$\dot{\delta v_E} = (-g)\epsilon_N + \delta f_y \quad \textbf{(7.7b)}$$

$$\dot{\delta v_D} = \delta f_z \quad \textbf{(7.7c)}$$

$$\dot{\delta v_N} = (+g)\epsilon_E - \delta f_x \quad \textbf{(7.8a)}$$

$$\dot{\delta v_E} = (-g)\epsilon_N + \delta f_y \quad \textbf{(7.8b)}$$

$$\dot{\delta v_D} = -\delta f_z \quad \textbf{(7.8c)}$$

Eq. (7.7) shows when the RIMU is in a stationary and level condition; whilst Eq. (7.8) shows when the RIMU has rotated 180^0 about its *y*-axis (upside down). Eq. (7.7a) & (7.8a) and (7.7c) & (7.8c) can then be solved simultaneously to observe accelerometer errors in the *x*- and *z*-axis through velocity error updates. The accelerometer error in the *y*-axis cannot, however, be made observable because of the same Eq. (7.7b) & (7.8b) because it is the rotation axis for the RIMU.

For the attitude errors, the North and East attitude errors are observable through the velocity error updates because there is a large force in the Down axis resulting from the gravity heading when stationary (for example see Eq. (7.5)). The RIMU effect is therefore more appealing in making the attitude error in the Down axis more observable, where the error is not observable for the normal IMU when stationary (as discussed in Section 4.4). As in the previous discussion, the attitude error model from Eq. (2.31) for the low-cost IMU can be rewritten as:

$$\dot{\epsilon} = -(C_b^n)\delta\omega_{ib}^b \tag{7.9}$$

Note that the other terms in Eq. (2.31) can be ignored to come at Eq. (7.9) because of the low-cost IMU used (see Section 2.4.3.3). Again when stationary and level, Eq. (7.9) becomes:

$$\begin{pmatrix} \dot{\epsilon_N} \\ \dot{\epsilon_E} \\ \dot{\epsilon_D} \end{pmatrix} = - \begin{pmatrix} 1 & 0 & 0 \\ 0 & 1 & 0 \\ 0 & 0 & 1 \end{pmatrix} \begin{pmatrix} \delta\omega_x \\ \delta\omega_y \\ \delta\omega_z \end{pmatrix} \tag{7.10}$$

When the IMU rotates 90^0 about its y-axis, the C_b^n changes and Eq. (7.10) becomes:

$$\begin{pmatrix} \dot{\epsilon_N} \\ \dot{\epsilon_E} \\ \dot{\epsilon_D} \end{pmatrix} = - \begin{pmatrix} 0 & 0 & -1 \\ 0 & 1 & 0 \\ 1 & 0 & 0 \end{pmatrix} \begin{pmatrix} \delta\omega_x \\ \delta\omega_y \\ \delta\omega_z \end{pmatrix} \tag{7.11}$$

Eq. (7.11) shows that the gyro sensor error on the z-axis is now made observable through the North attitude error. Because the North attitude errors are already observable from Eq. (7.5), the correlated gyro sensor error on z-axis (i.e z-axis gyro bias) can therefore be observed as well.

Note that the discussion assumes a simple case of the IMU when it is stationary and level. Nevertheless, it does explain the principle of rotating the IMU in improving the observability of the error states. In reality, however, many terms during the modelling and estimation process in the KF may contain errors. For example, C_b^n and $(f^n\times)$ may contain errors and the state transition matrix, Φ may not correctly model the propagation of error. Nevertheless by also improving the observability of the error states, more information is updated to the KF. This will help during the estimation process as these errors may correlate with the other error states. Therefore, over time the KF can propagate more information about the uncertainty of all the error states for better estimation of the errors of the system.

7.3 RIMU Trials Using Simulation

This section presents the RIMU trials simulated for static and walking scenarios. These were performed to identify the impact of the RIMU to mitigate heading drift error for the low-cost PNS, based on the discussion from the previous section. The observability of the IMU errors will be also analyzed, where particular attention will be given to weakly observable states such as heading and z-axis gyro bias.

The simulated data for RIMU were generated using the in house Inertial Data Simulator (IDS) software. The IDS process flow was described in Section 5.2. The trajectory was first defined in a separate file containing the INS positions. Using a control file (see Appendix A and description in Section 5.2.1.1), the software simulated IMU gyro bias errors and noises and used them to perturb the simulated measurements. Noise was assumed to represent other unmodelled IMU errors such as scale factor errors, the quantization errors and the temperature dependent errors (see discussion in Section 2.3.1). The simulated data was aided with simulated ZUPT measurements and then processed and analyzed using the POINT software (described in Section 5.3). The initialization and alignment were performed as described in Section 2.4.3.1. The heading was initialized manually using the reference heading, and the accelerometer bias and gyro bias were initialized to zero.

It is worth mentioning that this section analyzes the performance comparison of the low-cost PNS with and without the RIMU used. Among the parameters that will be analyzed are the accelerometer biases, gyro biases, heading and position solution. The analysis thus ignored the sensitivity of *'a priori'* process noise covariance and measurement noise covariance towards the Kalman Filter (KF) convergence (Hide et al., 2003). This was done by giving the same initial uncertainties values for both the low-cost PNS (with and without the RIMU), so that their performance can be compared equally on both, and the advantage of adopting RIMU for the low-cost PNS could be clearly seen.

7.3.1 Simulation of Static RIMU Trial

The POINT software was used to process the simulated inertial sensor output, which was aided by a simulated ZUPT data. The impact of an RIMU to mitigate heading drift was first examined during a stationary scenario for 1000 *s*. As discussed in Chapter 4, the heading error for the low-cost PNS, which was mainly caused by the error on the IMU Down-axis, was not observable when stationary. This is because only ZUPTs measurements were available during the stationary period to update the KF, and this was not enough for all errors to be estimated. Because of this, in order to make the error more observable, the RIMU impact was investigated using stationary scenario.

Fig. 7.2 shows the proposed *y*-axis rotation scheme for the RIMU when 6 ^{0}/s RIMU rotation rate was used. The scheme was simulated such that the *y*-axis was rotated from 0^0 to 360^0 back and forth continually. Fig. 7.3 shows that the *x*-axis and *z*-axis were not rotated, represented by almost flat blue and red lines respectively in the figure. The *y*-axis was rotated at a rate of 6 ^{0}/s, represented by the green plot in the figure (has a mean of 6 ^{0}/s). The *y*-axis rotation scheme, thus, caused acceleration in *x* and *z*-axis to be modulated as shown in Fig. 7.2.

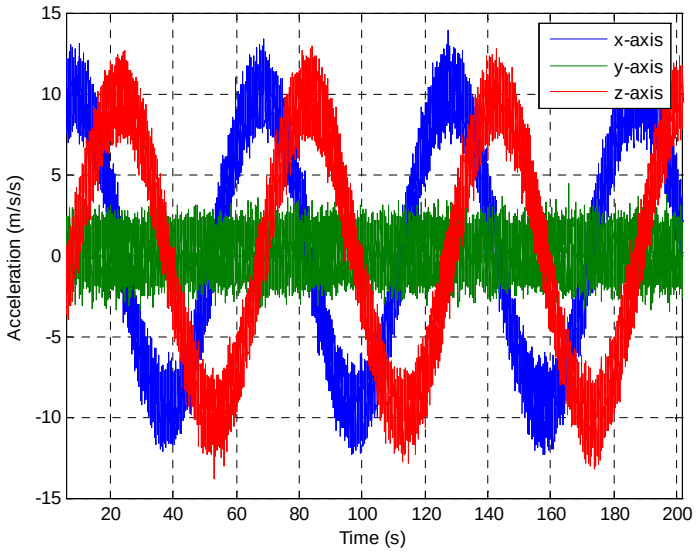

Fig. 7.2: RIMU accelerations in its b-frame

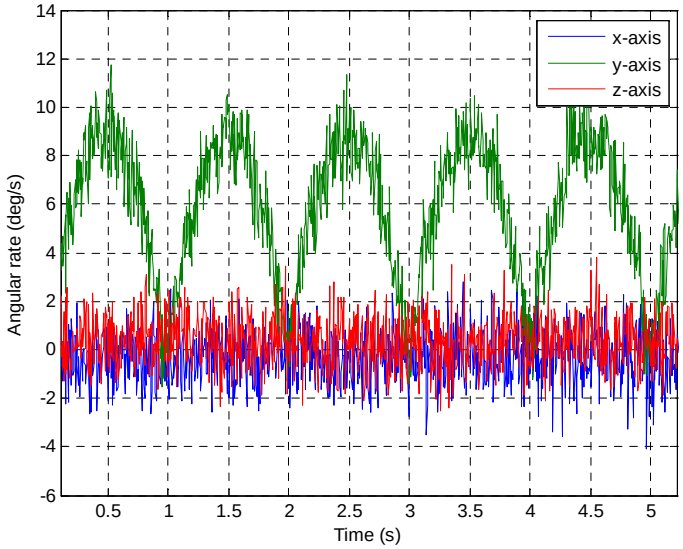

Fig. 7.3: RIMU angular rates in its b-frame

7.3.1.1 RIMU Rotation Rate

In order to simulate the RIMU in IDS, the attitude needed to be rotated at a certain rate in the trajectory data input file. Therefore, a test was first established to check the outcome of having different rates for platform rotation, where the IMU was to be mounted. This is shown in Fig. 7.4, in terms of the Time-To-Converge (TTC), for the z-axis gyro bias during stationary condition. Further analysis for the z-axis gyro bias estimation will be reserved for Section 7.5.3.

Fig. 7.4 shows the different rotation rates used, which were 0.6 $^{0}/s$, 1 $^{0}/s$ and 6 $^{0}/s$, when the RIMU was rotated continually. It is observed from the figure that a faster rotation rate resulted in a quicker convergence to the true simulated bias. Using the rotation rate of 6 $^{0}/s$ resulted in the z-axis gyro bias being resolved to within 0.1 $^{0}/s$ after approximately 100 s. Conversely, using slower rotation rates of 1 $^{0}/s$ and 0.6 $^{0}/s$ resulted in the z-axis gyro bias being resolved to within 0.1 $^{0}/s$ only after approximately 250 s and 750s respectively, approximately slower by 150s and 650 s from the former case. The faster rotation rate of more than 6 ^{0}/s, however, could not be simulated because of the unresolved problem with IDS at the moment, thus 6 ^{0}/s was chosen as the optimal rotation rate for RIMU. It is,

however, not considered a big issue here since the main goal of the approach was to show how the RIMU can be an advantage to mitigate heading drift error, and not to compare how quick the convergence rate for the estimation of errors can be.

7.3.1.2 Different Rotation Scheme

After the rotation rate had been chosen, the different types of RIMU schemes needed to be identified. The RIMU scheme is defined as to how the rotation is performed for the RIMU. This was done to see if there was any benefit in utilizing different schemes, and if it was, whether it was feasible practically.

Therefore, five different schemes of rotation about the y-axis have been tested with the chosen platform rotation rate of 6^0/s from Section 7.3.1.2. The schemes were named as schemes 1, 2, 3, 4, and 5; where scheme 1 = continuous IMU rotation; scheme 2 = 360^0 rotation back and forth; scheme 3 = 180^0 rotation back and forth; scheme 4 = 90^0 rotation back and forth and scheme 5 = 45^0 rotation back and forth. The result of using different schemes during the stationary condition is depicted in Fig. 7.5 in terms of Time-To-Converge (TTC) for the z-axis gyro bias estimates. As with Section 7.3.1.2, further analysis will be analyzed in detail in a later section.

From Fig. 7.5, it is observed that all schemes converged to the reference. Nevertheless, when the flipping effect of the IMU changed from scheme 1 (continuous rotation) to scheme 5 (45^0 rotation back and forth), the TTC increased from approximately 100 s to 1000 s. Scheme 1, 2 and 3 have a similar convergence rate, resolving to within $0.01^0/s$ after approximately 100 s, while schemes 4 and 5 converged slower at approximately 300 s and 1000 s respectively.

Although schemes 1, 2 and 3 showed similarity, scheme 2 was chosen for the RIMU because it was more practical when the RIMU platform was mounted on a shoe for the field trial. This was in order not to tangle the IMU data cables so much. If scheme 1 is selected, the data cable from the IMU to the data logger might become tangled. Nevertheless, it might be possible to use schemes 1 and 3 for future work if the IMU has the capability to operate wirelessly. Furthermore,

although smaller rotation (schemes 4 & 5) may be practically easier to perform without tangling the cables, it was not chosen because of the slow convergence rate. Again, further analysis on the error state will be analyzed in a later section.

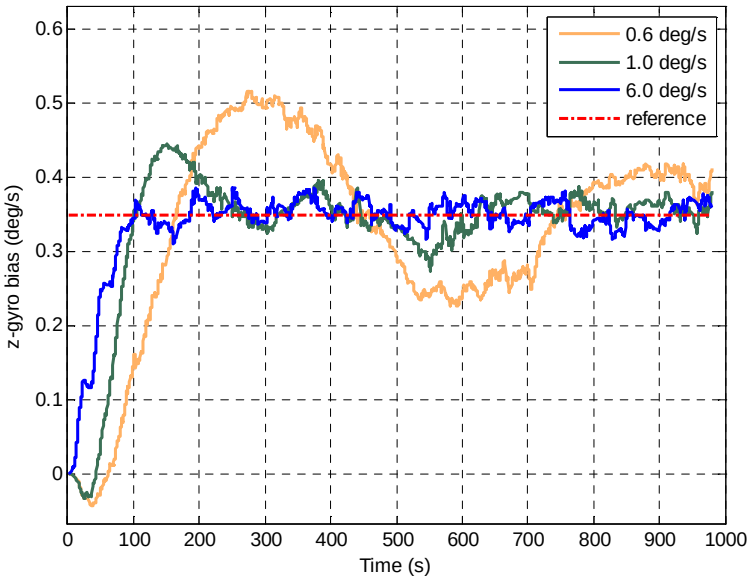

Fig. 7.4 Comparison of z-axis gyro bias when different rotation rates are used

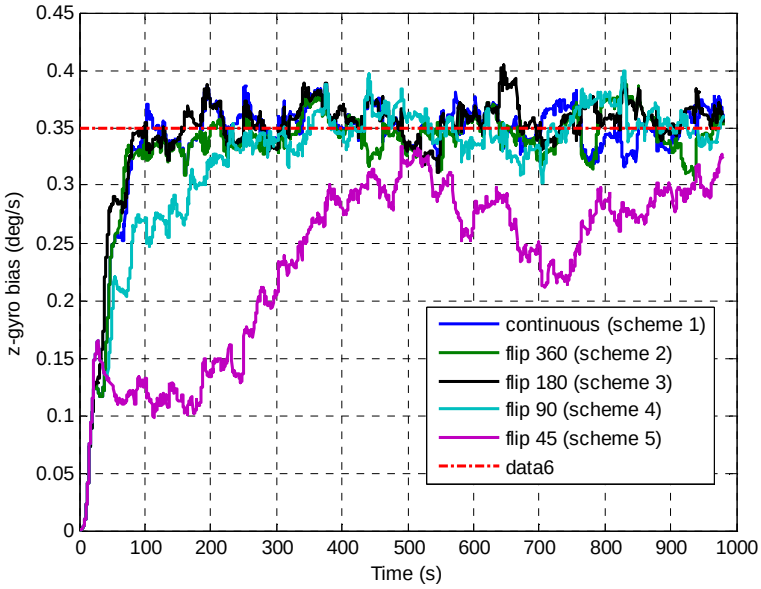

Fig. 7.5: Comparison of z-axis gyro bias when different rotation schemes were used

7.3.1.3 Error Observability

Fig. 7.6 shows two sets of errors that were estimated in the KF when the RIMU was used when stationary (updated also with ZUPTs). They are accelerometer biases (x, y and z-axis) on the left (from top to bottom) and gyro biases (x, y and z-axis) on the right (from top to bottom). The blue line represents the estimated bias when the RIMU was in operation, the green line represents the estimated bias using normal IMU approach (without the RIMU) and the red line represents the simulated truth bias. It is identified that out of 6 biases for gyros and accelerometers to be estimated, 5 have been observed. Only the y-axis gyro bias was not observed as it was the axis of rotation for the RIMU. In contrast, when the RIMU was not used, out of the 6 biases to be estimated, only 2 are observed. Table 7.1 summarizes the observability of these errors based on observation from Fig. 7.6, and its discussion follows in the next paragraph.

The observability result in the table is consistent with the effect of RIMU to the error observability discussed in Section 7.2.2. For the no-RIMU case (as discussed in Section 4.4), the attitude error in the Down axis (which directly correlated with the z-axis gyro bias) was not observable through velocity updates because of the absence of the horizontal acceleration. All the accelerometer biases for the no-RIMU case were also not observable. This is because when stationary (as discussed in Section 7.2.2), the accelerometer error terms appeared in Eq. (7.7) and (7.8) cannot be separated from the attitude errors and therefore cannot be observed (because the equations contain the same terms). That is why manoeuvring is usually required during GPS/INS alignment to separate these two errors.

Table 7.1: IMU errors observability while stationary

Error States	**Observability**	
	RIMU	**No-RIMU**
x-axis gyro bias	Yes	Yes
y-axis gyro bias	Yes	Yes
z-axis gyro bias	Yes	No
x-axis accelerometer bias	Yes	No
y-axis accelerometer bias	No	No
z-axis accelerometer bias	Yes	No

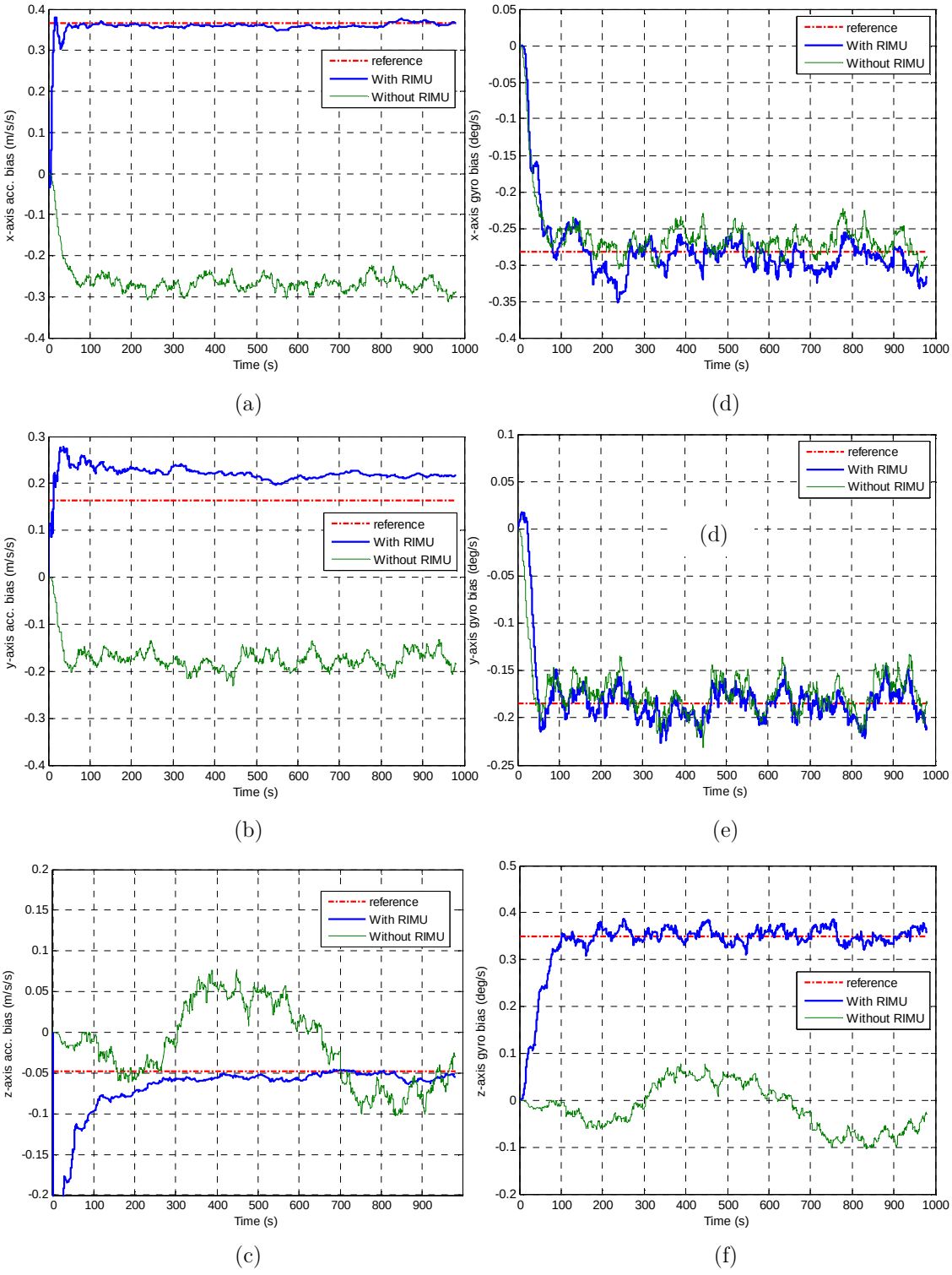

Fig. 7.6: Accelerometer bias for (a) x-axis, (b) y-axis and (c) z-axis, and gyro bias for (d) x-axis, (e) y-axis and (f) z-axis.

It is also observed that there is a slight delay (approximately 100 s) when estimating all the error terms. This is because of the slower rotation rate used, which influenced the convergence rate. It was identified in Section 7.3.1.2 that the faster rotation rate should result in a much quicker convergence rate. This is because less time is required for the RIMU axes to observe forces resulting from gravity in different orientations to separate the true acceleration from the gravity acceleration.

7.3.2 Simulation of Walking RIMU Trial

This section analyzes a simulated walking trial to see the improvement made by the RIMU in mitigating heading drift error.

7.3.2.1 Construction of Walking Trajectory

As mentioned in Chapter 5, the data simulator requires the trajectory data to be in the form of position, velocity and attitude. A straight walking trajectory was chosen simply because it would be easier to analyze the heading drift error and was constructed for 1000 s. Fig. 7.7 shows the created reference trajectory. A simple calculation of total distance divided by time shows that the simulated velocity is approximately 1.4 m/s, which is a typical pedestrian velocity (Fig. 7.8).

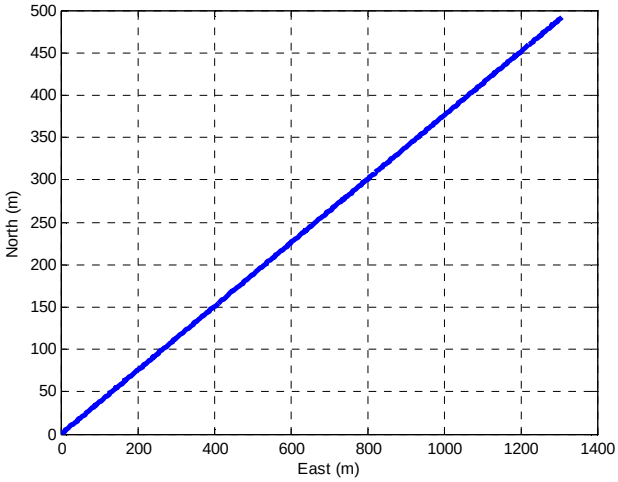

Fig. 7.7: A walking trajectory as a reference.

7.3.2.2 Simulated Walking Velocity

Fig. 7.8 (left) shows a sample of a pedestrian's true walking velocity. The sample was taken from the Chapter 6 trial and was used to recreate a simulated walking velocity for IDS simulation. Fig. 7.8 (right) shows the simulated walking velocity (which started at about 60 s), created using standard Fourier series equation. Although the simulated output does not match exactly the actual sample of walking velocity for a pedestrian, it does give a similar plot to represent a typical walking velocity for a pedestrian.

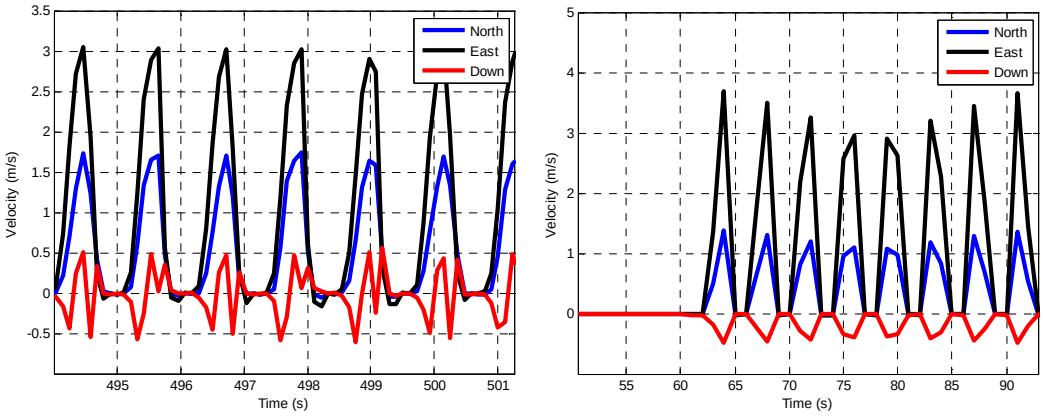

Fig. 7.8: Sample velocity for walking pedestrian (left) true, and (right) simulated.

7.3.2.3 Inertial Sensor Simulated Output

Fig. 7.9 (left) and (right) show the simulated acceleration and the angular rate outputs for the RIMU, generated from IDS using scheme 2, as chosen in the previous section. The scheme was simulated such that the pitch was rotated from 0^0 to 360^0 back and forth. This is visible in Fig. 7.9 (left), where the acceleration on the x- and z-axes resembles a sinusoidal plot. The spikes modulated onto the sinusoidal plot are the simulated walking velocity from Fig. 7.8 (right).

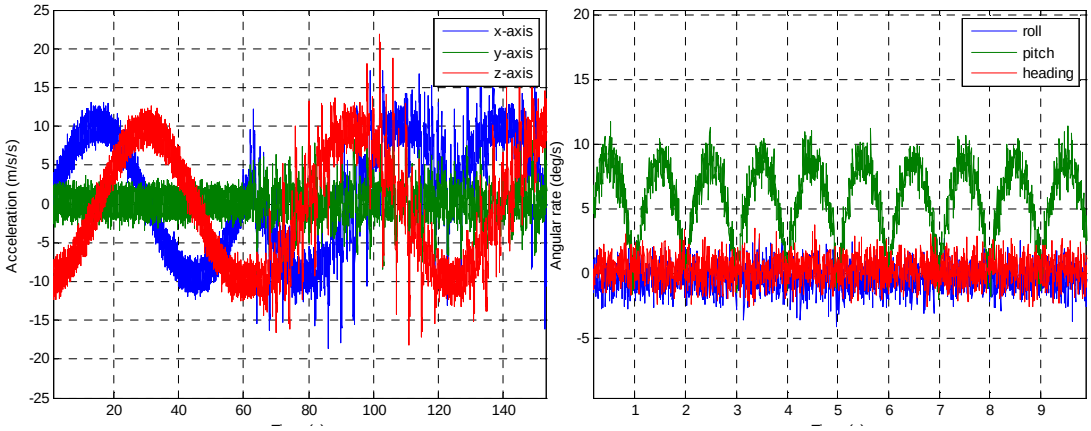

Fig. 7.9: Simulated inertial sensor output in b-frame for (left) acceleration, and (right) angular rate

The sinusoidal plot, for example z-axis acceleration, increased sinusoidally from about -1 g (pointing down) during levelled platform, to about 1 g in the middle of the 180^0 rotation (pointing up), and back to about -1 g at the end of the first rotation (pointing down again) at 60 s ($6^0/s \times 60\ s = 360^0$). The scheme then rotated back from about -1 g to 1 g and finished at about -1 g at the end of the second rotation at 120 s. Acceleration on the y-axis did not undergo a 'flipping' motion as the y-axis was the RIMU rotation axis, therefore it did not measure any 'g's before the walking trial began at 60 s. Fig. 7.9 (right) shows the RIMU rate used, rotating about the y-axis, with a mean of 6 $^0/s$. Note that because the angular rate for the other two axes are close to zero, the simulated walking trial is not as realistic as it should have been for a walking pedestrian, as it only simulates the horizontal acceleration. It is thought nevertheless to be sufficient to understand the effect of the RIMU when used for the low-cost PNS.

7.3.2.4 Analysis of Heading Estimation

Fig. 7.10 shows the estimated heading for the RIMU (blue dots) and non-RIMU (green dots) with two reference headings of 45^0 (reference 1) and 180^0 apart (reference 2). Fig. 7.11 magnified Fig. 7.10 for clearer view. The reference heading of 45^0 (solid red line) was the true heading, while the second reference heading (dashed red line) was the heading when the z-axis was flipped 180^0 because of the RIMU. Note that the accelerometer biases and gyro biases were not shown in this section because similar results (with Section 7.3.1.4) were produced.

It now appears, apart from the sudden change of heading quadrant for the RIMU resulting from the flipping of z-axis, the RIMU heading is now bounded and follows closely the reference heading. In contrast, the heading for non-RIMU appears to be growing. The growth appears to be linear and it was actually resulting from the simulated constant bias in IDS. In reality, the heading drift may be non-linear because of variations in bias (for example, see the result in Section 8.3.4). Therefore, the simulated heading output of non-RIMU is considered valid because it was meant to show that it was drifting, which is a typical output of a low-cost IMU.

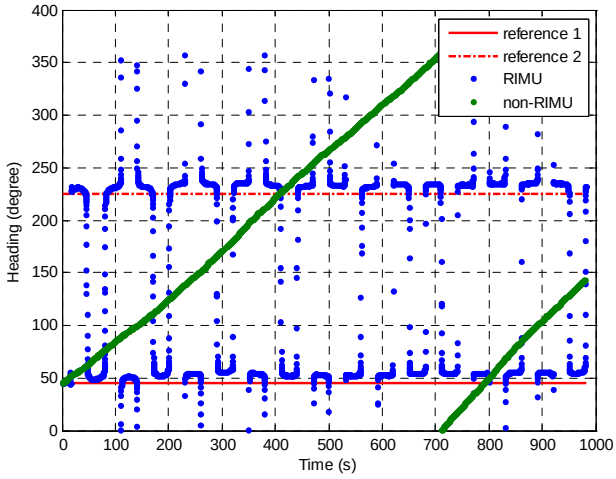

Fig. 7.10: Comparison of heading angle for RIMU and non-RIMU.

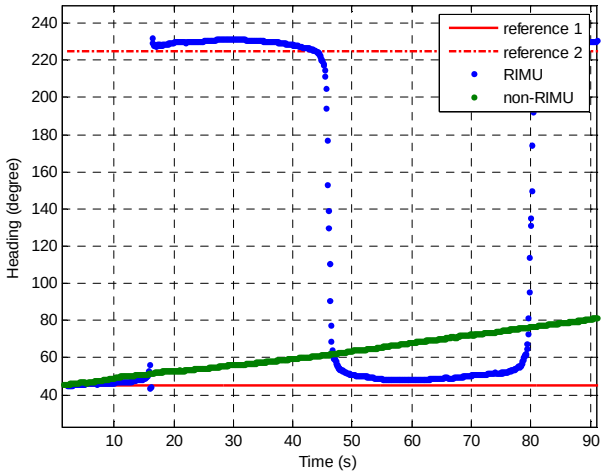

Fig. 7.11: Magnified heading angle from Fig. 7.10

7.3.2.5 Heading Initialization Issue

If the IMU was not rotating, the heading would be drifting (discussed previously). However, when rotating the IMU, the initial heading before the z-axis gyro bias is observable is also drifting. This is plotted in Fig. 7.12. For example, at the beginning of the plot (at $0\ s < t < 15\ s$), the heading was still drifting (increasing). For this trial, the z-axis gyro bias was successfully resolved at about $t = 100\ s$ (similar to the result from the stationary trial before). Therefore, the drift in heading for the RIMU now appears to be reduced only after this time, shown for example in Fig. 7.13 as between $240\ s < t < 260\ s$ and $290\ s < t < 310\ s$, and for the rest of the simulation trajectory.

Therefore, an issue to consider is the initialization of the heading for a 'lowest-cost' IMU (or uncalibrated IMU) when using the RIMU approach. Standard coarse alignment for a strapdown IMU would be to set the IMU initial heading during coarse alignment, based on information from for example the GPS heading or magnetometer. The same approach cannot be applied to the RIMU because of the reason described next.

Suppose the IMU horizontal alignment is performed for $1\ s$ (heading is initialized manually), and the walk is performed after $20\ s$. Suppose also the true

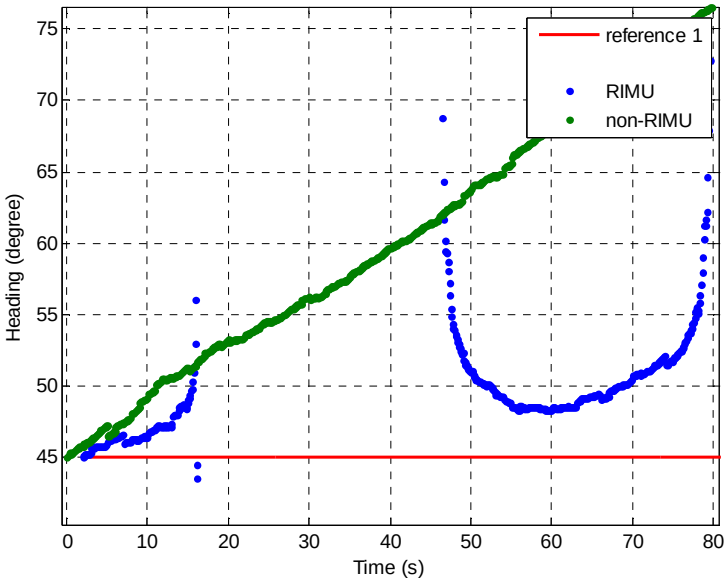

Fig. 7.12: The RIMU initial heading

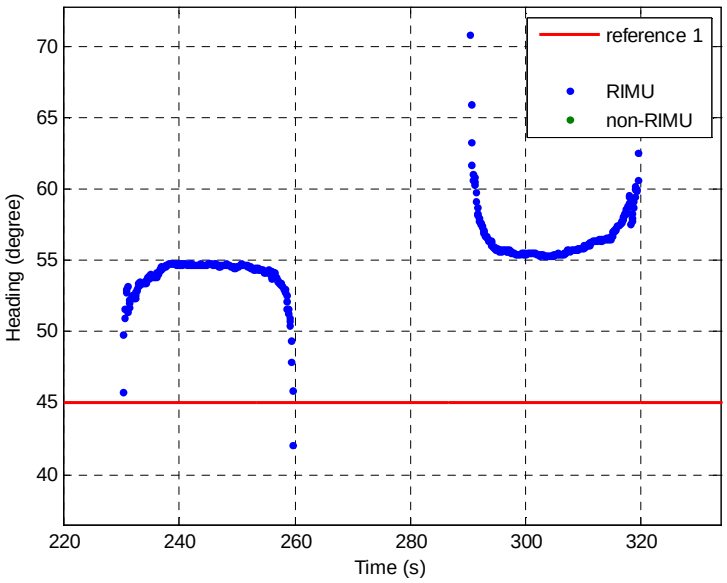

Fig. 7.13: The RIMU heading after resolving the error in Down axis

initial heading is 45^0 and the low-cost RIMU drifts at a rate of 10 $^0/s$. If the RIMU heading is manually set during heading alignment to 45^0, the actual initial heading at the start of the walk (at 20 s) for the RIMU would be different. This is because the RIMU heading will still drift because the z-axis gyro bias will take some time to be observed by the RIMU. After 20 s, the IMU heading would have been 200^0 off from the true heading. This will cause the actual initial heading (used for the IMU mechanization) to have been 245^0, which is wrong. This subsequently affects the position computation (although the heading drift after this period would be reduced because of the RIMU effect).

Nevertheless, this case assumed that the z-axis gyro bias was zeroed during initialization for simulation purpose. Usually in practice, gyro biases were initialized with its average values taken during stationary alignment. This therefore gives some information to the KF when estimating the biases and the heading errors. The only probable dilemma is if the initialized gyro bias value (using its average values during alignment) may not represent the correct estimation of the true values (the uncertainty is too large). For example, the biases might change so much and very rapidly, subsequently affecting the estimation of the heading error even when initialized properly. If this is the case, then the heading initialization issue must be addressed appropriately.

7.3.2.6 Comparison of Position Solution

Fig. 7.14 shows the computed relative position solution for the RIMU (blue), without RIMU (green) and the simulated reference (red). It is clearly shown that without RIMU, the position solution drifted quite significantly. When the RIMU was used, the position solution did not drift as much as without RIMU because the heading error was now observable. Nonetheless, as discussed in the previous section, it appears that because the z-axis gyro bias was not resolved until after 100 s, the RIMU position has drifted slightly during the first 100 s. This, however, was not as bad as it might have been, because of the low drift rate used for the simulation of heading (approximately 0.35 $^0/s$, based on the z-axis gyro bias reference).

Consider this. Heading was initialized manually as 45^0 during coarse alignment for this simulation. It appears that because the drift rate was at about 0.35 $^0/s$, the heading after 100 s into simulation would have been about 35^0 off from the reference (because the z-axis gyro bias was not resolved until after 100 s). However, note that after 15 s or 90^0 rotation (see Fig. 11), the flipping of the z-axis has caused the heading to change its value. Heading is now decreasing after this period (heading is drifting in the opposite direction because of the flipping of the axis). After another flipping at 45 s, the heading was increasing again because heading is drifting again in the opposite direction (note that the heading is still drifting at 0 $s < t <$ 100 s because the z-axis gyro bias has not yet resolved). The drift nevertheless after 15 s and before 100 s was considered to average out thanks to this increasing and decreasing in the heading. Therefore what remains is the drift that had happened for the first 15 s of the simulation as shown in Fig. 7.15, which shows the drift in the initial RIMU heading. This is because the unresolved z-axis gyro bias and the flipping of the axis had not yet happened. As shown in Fig. 7.15, the initial heading has drifted about 5^0 from the reference, which agrees theoretically (i.e 0.35 $^0/s \times 15\ s = 5.25^0$). This therefore signifies the issue of heading initialization as discussed in Section 7.3.2.5.

This does, though, highlight the advantage of the RIMU over a non-RIMU, where the RIMU significantly mitigated heading drift error. When the RIMU was not used, the position trajectory drifted quite significantly against the reference. In contrast, when the RIMU was used, the position trajectory improved and the heading drift was no longer visible, apart from the initial drift in heading resulting from the issue discussed in the previous paragraph.

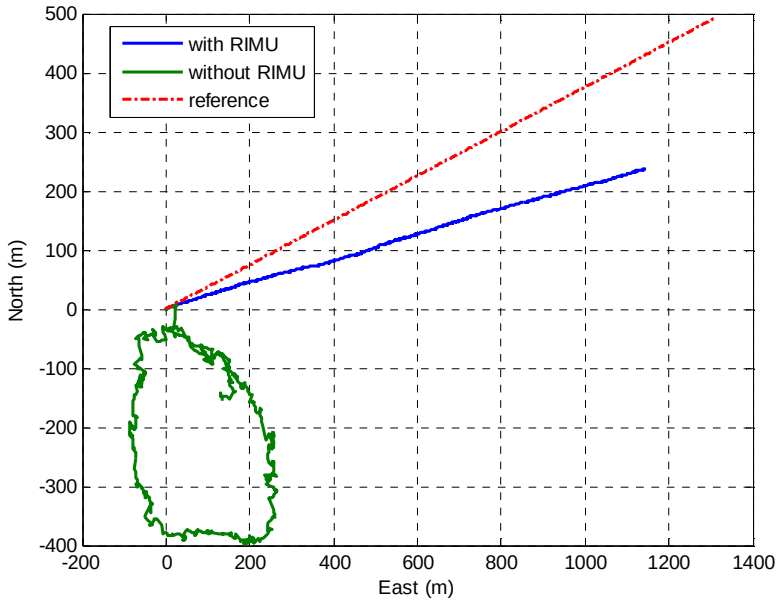

Fig. 7.14: The comparison of the RIMU position with the reference and without-RIMU

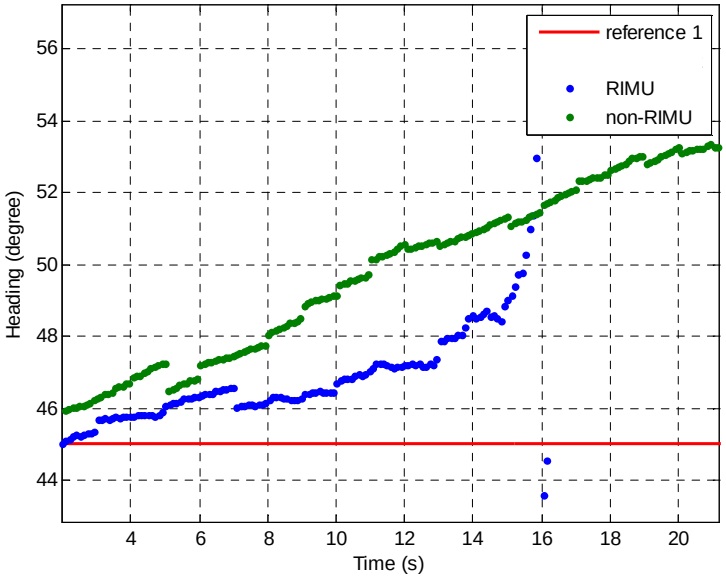

Fig. 7.15: The drifting in the initial RIMU heading

7.4 RIMU Field Trial

To verify the RIMU simulated performance, a field trial was performed using the RIMU prototype, shown in Fig. 7.16, developed by the Geospatial Research Centre New Zealand (GRCNZ). Marker 'A' in Fig. 7.16 (left) shows the platform that was designed to rotate, onto which an IMU was mounted. The IMU was 'strapped' on the platform using a tape as rigid as possible, so that the IMU represented the actual motion of the platform. The IMU used was the same as in Chapter 6, which was powered by a 12V battery carried in a back pack along with the data logger to log the raw IMU data. The black box marked as 'B' in Fig. 7.16 (right) is the RIMU controller and houses two 9V batteries. The platform rotation speed can be increased or decreased from a switch at the side of the controller, although the exact rotation rate is unknown. There is also an ON/OFF switch on the controller to switch on or off the RIMU mode.

Fig. 7.16: RIMU prototype with (left) IMU mounted on a rotating platform, and (right) the RIMU controller

7.4.1 Trial Description

The rotating of the IMU platform was started from the beginning (when powering the device). A user equipped with the RIMU stood on the starting position so that the IMU horizontal alignment could be made for approximately 1 s at the beginning of the walk. He then performed two walks (back to back) around the Nottingham Geospatial Building (NGB) office area. This created a rectangular

trajectory around the office, where the start and the end trajectory is the same, marked by a tape (shown in Fig. 7.17).

The first walk with the RIMU was for 10 rounds. At the end of the 10^{th} round, the RIMU mode was turned off by stopping the platform rotation using the switch, whilst keeping the IMU switched on. The user walked again immediately for the second walk with another 10 rounds on approximately the same trajectory (by following straight features on the floor carpet). The two trials lasted for about 650 *s* each. The reference for comparison of error estimation (discussed more in Section 7.4.2) was created based on the second walk, in which a method developed in Chapter 8 was applied, and for visualisation is plotted manually on top of the NGB floor plan as a green line in Fig. 7.17. The raw acceleration data from the IMU is plotted in Fig. 7.18 to show the RIMU in operation. Both the RIMU and non-RIMU walks started at about 17 *s*. Fig. 7.19 shows an example of the detected ZUPT events for the trial. The POINT software (Chapter 5) was then used to post-process the data, and the outputs are analyzed.

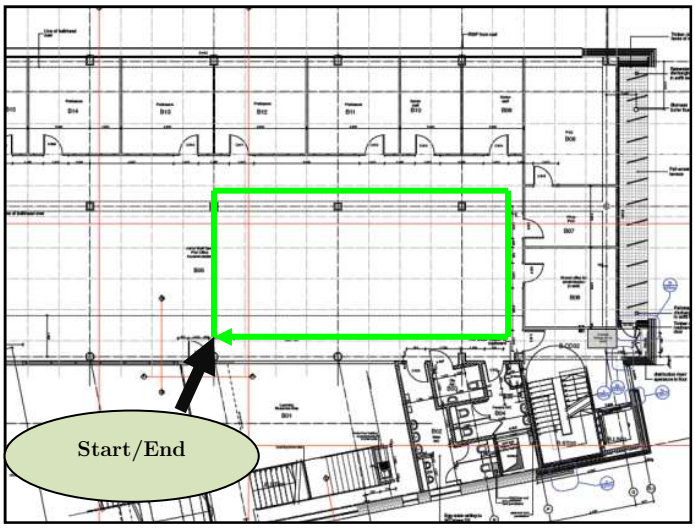

Fig. 7.17: The visualization of the RIMU trajectory

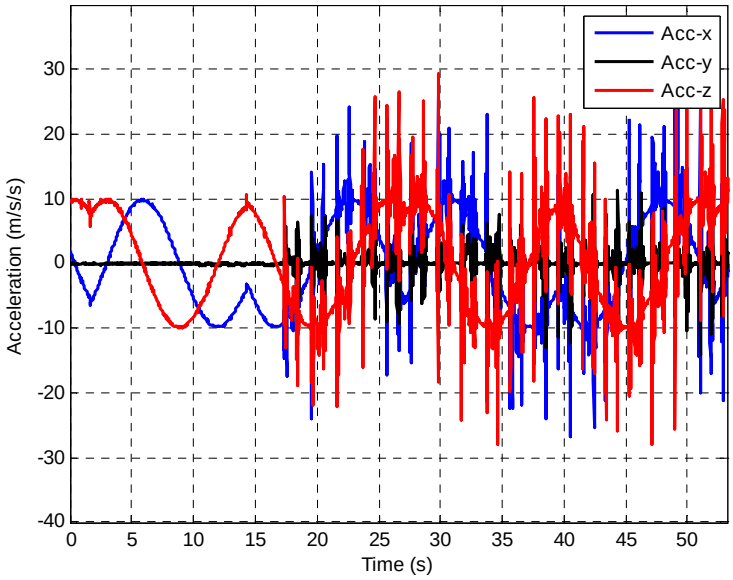

Fig. 7.18: The actual raw IMU acceleration data

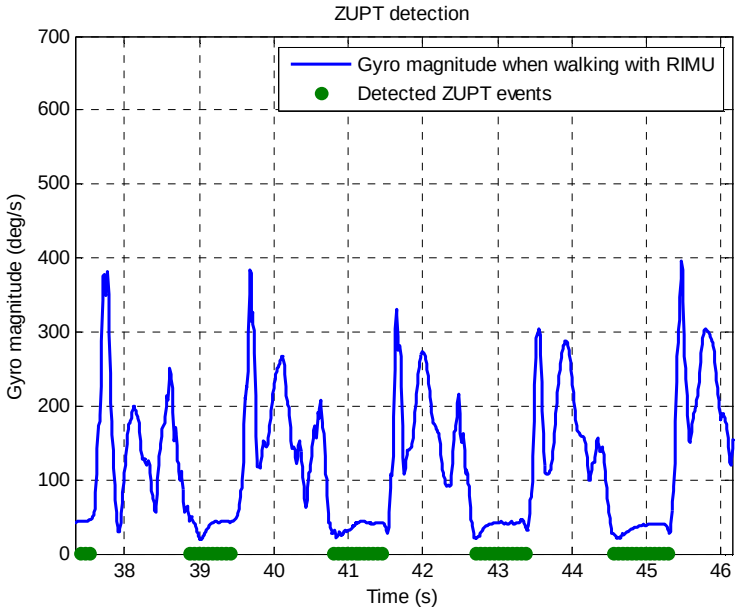

Fig. 7.19: An example of ZUPT detection for the trial.

7.4.2 Analysis Assumptions

Before the IMU error comparison between the two walks could be made, it is worthwhile to highlight that the impact of, for example, temperature dependent bias and turn on bias of the IMU is considered less destructive. This is because the two trials were performed back to back without switching the IMU off. The sensitivity of *'a priori'* process noise initial covariance and measurement noise towards filter convergence (Hide et al., 2003) was also not discussed. Both were, therefore, given the same information to reduce the dependence of process convergence on the initial covariance.

It is impossible to quantify the true IMU errors to be used as a reference for the trials because they are unknown. Therefore for comparison purpose, implementing a method from Chapter 8 should give sufficient information about the best estimate of the IMU errors because the method gives a more accurate position solution. This however is slightly overoptimistic because in reality, there will be always errors resulting from the inaccuracy when modelling the INS error propagation. The error in measured forces by the IMU will affect the estimation of the IMU attitude errors. This subsequently will affect the estimation of the IMU accelerometer errors because of the correlation between error states. Therefore, it is assumed that the estimation of the accelerometer biases and gyro biases from Chapter 8 are adequately estimated. Although only a coarse comparison of IMU errors can be performed, it should give a general idea of the overall improvement made by the RIMU towards errors observability.

The method from Chapter 8 was used as a reference to compare the bias estimation of the RIMU. Note that the IMU used in the reference was not rotated. This is in order that the actual improvement made by the RIMU to mitigate heading drift can be seen when the biases are made to be more observable. Two separate trials with the same trajectory were therefore performed: the actual trial with the RIMU and the reference trial without the RIMU (but aided with the method from Chapter 8). Nevertheless, a difference reference trial was used when comparing the RIMU position solution. The reference trial was constructed from

the same trial performed with the RIMU, but this time aided with the method from Chapter 8. Table 7.2 summarizes the trials and reference used.

Table 7.2: Trials and the reference trials used for two different analyses.

Compare Position Solutions		**Compare IMU Biases**	
Trials	**Reference Trials**	**Trials**	**Reference Trials**
RIMU	RIMU + Chapter 8	RIMU	IMU + Chapter 8
IMU	IMU + Chapter 8		

Furthermore, a precise statistical analysis for the estimation of IMU biases (for RIMU and reference trial (IMU + Chapter 8)) are deemed impossible because of the two following factors:

- The two trials were not performed in exactly the same time, and
- The reference trial was performed in a separate trial.

Unless all the trials are completed in exactly the same period, the two factors will cause possible discrepancies when comparing the estimate of errors (for the RIMU and non-RIMU) with the reference. The effect, however, is assumed to be negligible for analysis purposes. Note also that the results for position solutions' comparison in this chapter show only horizontal positioning accuracy, in relation with the research problem investigated for the low-cost PNS (heading drift problem) presented in Chapter 4. Thus, the vertical positioning accuracy for the low-cost PNS is not presented because it is directly correlated with the estimation of velocity errors on the INS Down axis, which is assumed to be well-estimated by the use of ZUPTs frequently.

7.4.3 Gyro Bias Estimates

Fig. 7.20 shows the z-axis gyro bias estimates for RIMU and non-RIMU, plotted against the reference. Both datasets were initialised with its average bias values during alignment. It can be observed from the figure that the RIMU has a similar plot to the reference, as opposed to non-RIMU. After about 50 s, the RIMU has resolved and stabilized to within 0.05 $^0/s$ from the reference, whilst the non-RIMU has not yet resolved to the reference, even until the end of the trial. This indicates that z-axis gyro bias is made observable through the use of the RIMU (which agrees with Table 7.1 and is discussed in Section 7.2.2) as opposed to the non-RIMU where the z-axis gyro bias converged to a wrong value.

Fig. 7.21 shows the x and y-axis gyro bias estimates for both RIMU and non-RIMU, plotted against the reference. Both x and y-axis gyro biases have been estimated to be well within 0.1 $^0/s$ with the reference throughout the dataset. This indicates that the observability effect of RIMU is not as influential as it is for when estimating z-axis gyro bias previously. This is because both of these errors were observable even when the IMU was not rotated, as shown in Table 7.1. Velocity updates through ZUPTs, which was performed every footstep during walking, has the effect of estimating the correlated attitude errors on x- and y-axis as well through Eq. (7.5) (this was discussed in Section 7.2.2).

The heading initialization issue before IMU errors were fully resolved is not obvious here because the z-axis gyro bias was initialized with its average bias (as discussed in Section 7.3.2.5). As shown in Fig. 7.20, the estimated z-gyro bias for this trial did not deviate too much from its average bias (low uncertainty). This means that by initializing the z-gyro bias using the average bias during alignment, the heading drift is not as severe as it was during the walking simulation, where the bias was initialized from zero. In the simulation, the initial heading was still drifting because it took time for the filter to resolve to the correct bias value. It might be possible, however, that if the bias varies too much in practice (high uncertainty), the issue discussed in Section 7.3.2.5 will be significant to the overall accuracy of the RIMU position solutions.

The heading of the low-cost PNS with the RIMU was not plotted here as similar heading plot was found as in Section 7.3.2.4. The RIMU benefit in mitigating heading drift to the overall low-cost PNS performance is, therefore, assessed using its position solution, presented in Section 7.4.5.

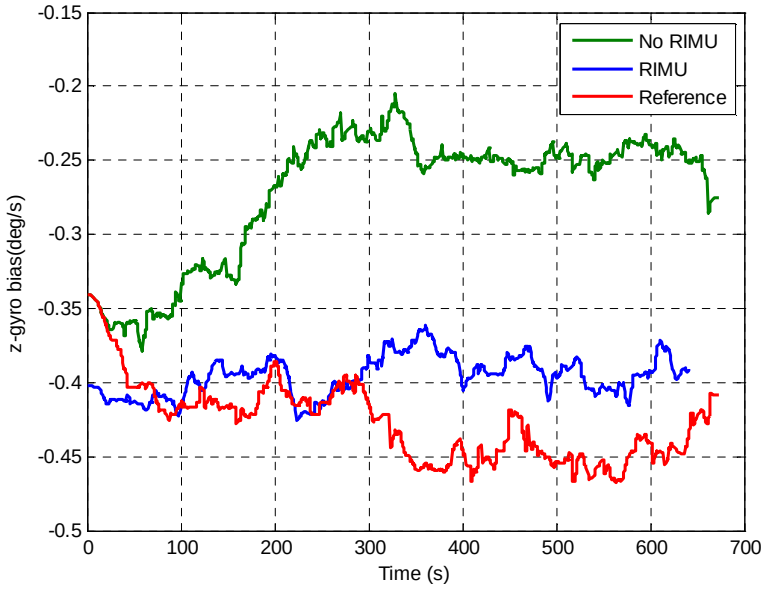

Fig. 7.20: A comparison of z-gyro bias estimation with different approaches

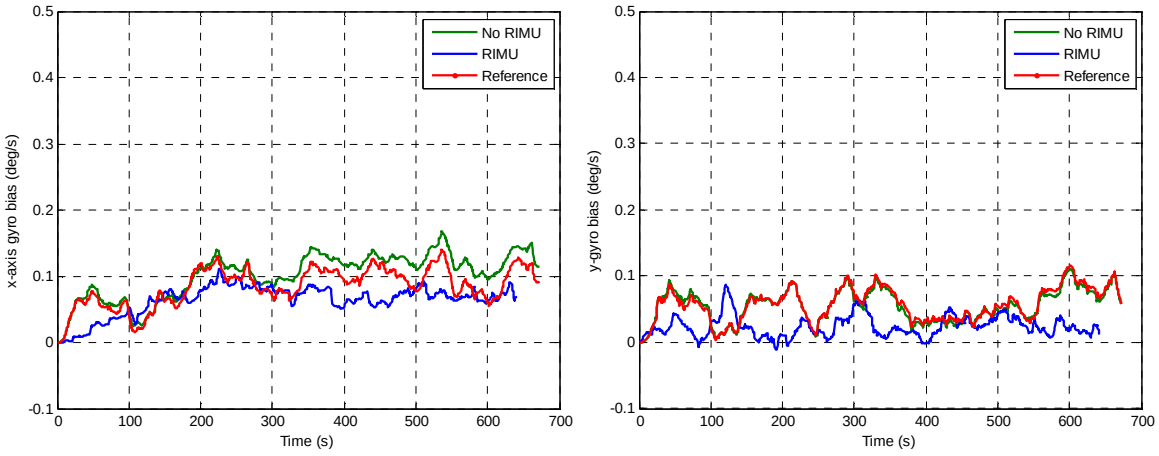

Fig. 7.21: A comparison of (left) x-axis gyro bias, (right) y-axis gyro bias estimation with different approaches

7.4.4 Accelerometer Bias Estimates

Before presenting the accelerometer bias estimation results here, it is reminded about the assumption of the analysis on this error in Section 7.4.2.

Accelerometer biases on x, y and z-axis for both the RIMU and non-RIMU are plotted against the reference in Fig. 7.22. It is observed from the figure that implementing the RIMU in the walking trial had no significant advantage over the non-RIMU when estimating accelerometer biases for all three axes.

With or without the RIMU, the accelerometer biases on x, y and z-axis still resolved to within 0.05 m/s^2 with the reference. This indicates that there is no significant difference from the two cases (with or without RIMU) in the observability of all these errors. Nonetheless, Table 7.1 showed that for the RIMU, y-axis accelerometer bias should have not been observed, which was different from the result obtained. It also showed that accelerometer biases on all axes for the non-RIMU were not observable. The reason for this is that Table 7.1 was tabulated for a non-walking trial, where there was no horizontal acceleration induced by the system in between steps. When walking, accelerometer biases for both RIMU and non-RIMU are therefore well observed through velocity updates because there was a horizontal acceleration. For example, a forward acceleration can separate the pitch error and forward accelerometer bias (see Eq. (7.4)).

A closer look in Fig. 7.22 shows there was a spike at the beginning of the dataset for x and z-axis when the RIMU was implemented. Fig. 7.22 is further enlarged in Fig. 7.23 for further analysis.

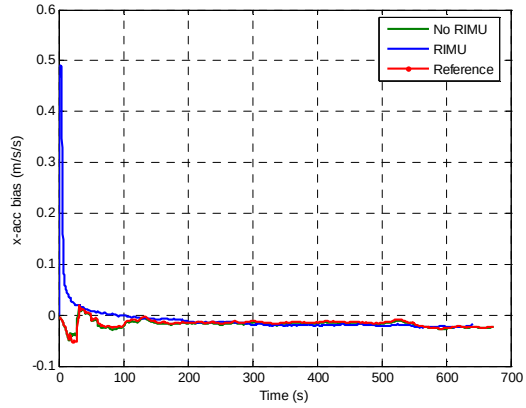

Fig. 7.22: (counter clockwise from top left corner): x-, y- and z-accelerometer bias

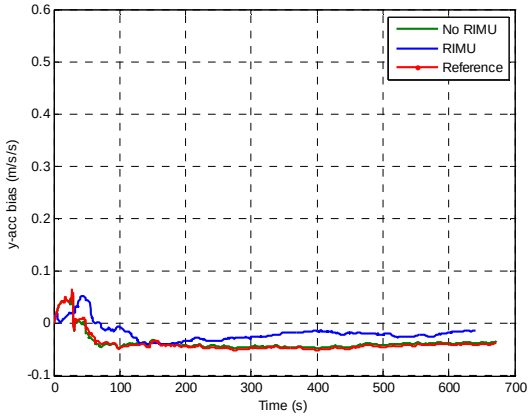

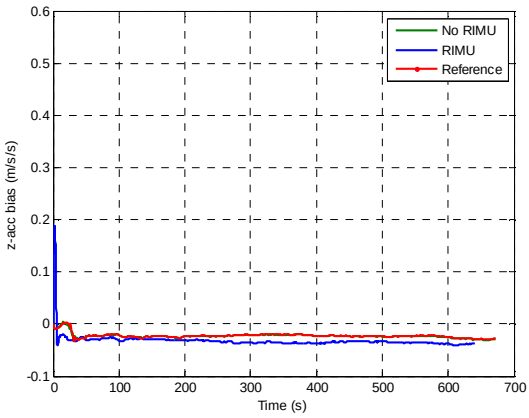

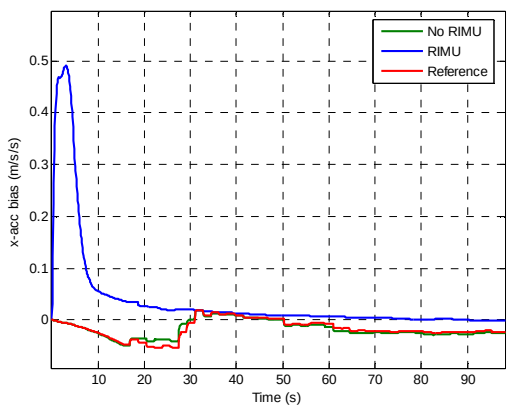

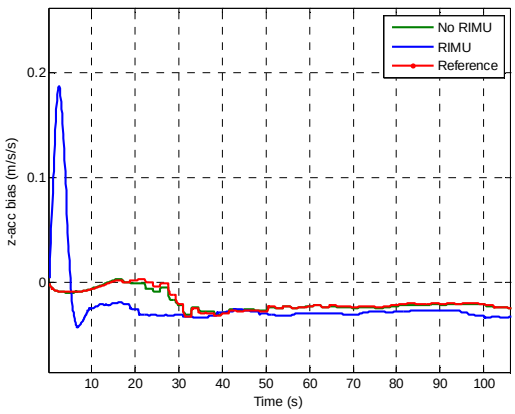

Fig. 7.23: Magnified x-accelerometer bias (left) and z- accelerometer bias (right)

The blue plot in Fig. 7.23 for the RIMU experienced a spike at the beginning of the dataset. Its effect is observed for the x and z-axis accelerometer bias for the first 17 s of the dataset when the RIMU remains stationary, with a maximum of 0.48 m/s^2 and 0.18 m/s^2 respectively. This was caused by the effect of having the RIMU rotate about its y-axis, which in turn caused the x and z-axis to be rotated. As a result, the x and z-axis observed a certain amount of gravity acceleration during this rotation period. The higher uncertainty resulting from the higher initial process noise therefore gives too much weight from the innovation sequence to the bias estimates. However, as the KF gets more information from the velocity updates, it is able to separate the attitude and acceleration error. By setting a lower initial process noise, it actually reduced the spike at the beginning of the dataset, as shown in Fig. 7.24, when a lower initial process noise value was used. The proper initialization and estimation of the stochastic properties of the filter is a challenging task. Please refer, for example, to Hide (2003) and Groves (2008) for more details. Its discussion is beyond the scope of this thesis because it concerns with the convergence rates of the estimated states. This thesis however focuses on the observability of the states (converging to the correct values). This research thus used a tuning approach for the KF as discussed in Section 5.3.1.

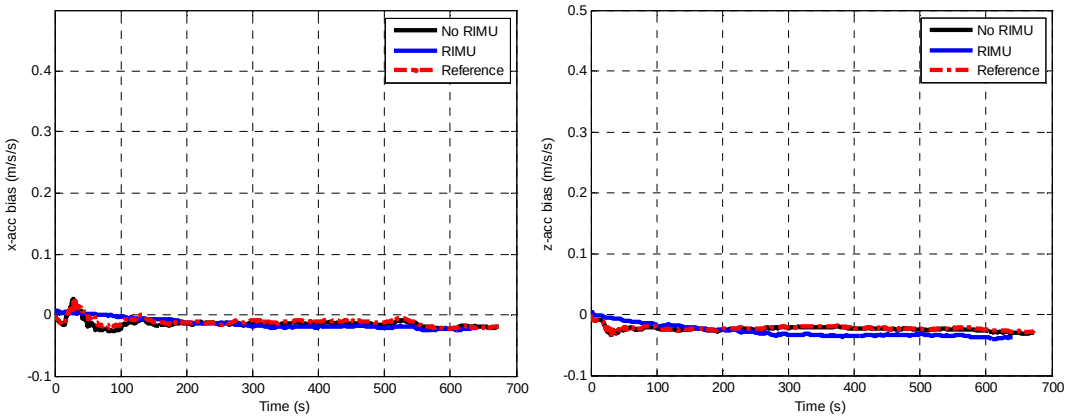

Fig. 7.24: Accelerometer biases for (left) x-axis, and (right) y-axis, with lower initial process noise value.

.

7.4.5 Comparison of Position Solution

Statistical comparison for the position solution in this section is discussed using four criteria: Return Position Error (RPE) in meters, percentage of RPE from the total distance travelled, mean of Horizontal Position Error (HPE) and maximum Position Error (PE) (both in meters).

Fig. 7.25 shows two plots of relative position solutions comparing the non-RIMU with its reference, and the RIMU with its reference. There were two references on which these solutions were based. For the non-RIMU case, the reference was constructed using its own raw data, but aided with a method developed in Chapter 8. This reference was the same with the one used for the error estimations in all previous analysis. For the RIMU case, the best approximation of its position accuracy would be to compare with its own reference, as its position trajectory is not exactly the same as the non-RIMU case. Therefore, the RIMU reference was constructed using its own raw data, aided using the method from Chapter 8.

From Fig. 7.25 (top), when the RIMU was used, the RPE was relatively better with less than 1 m after travelling for an estimated distance of 354.1m. This constitutes less than 0.3 % of RPE from the total distance travelled. On the other hand, from Fig. 7.25 (bottom), it is observed that without the RIMU the position has drifted quite considerably, mainly resulting from heading drift. After walking for about 11 minutes with an estimated distance travelled of 385.3 m, the RPE was computed to be more than 12 m. In percentage, this represents an RPE of more than 3% from the total distance travelled. These position errors however would be much more if the walk were to be performed in a straight line.

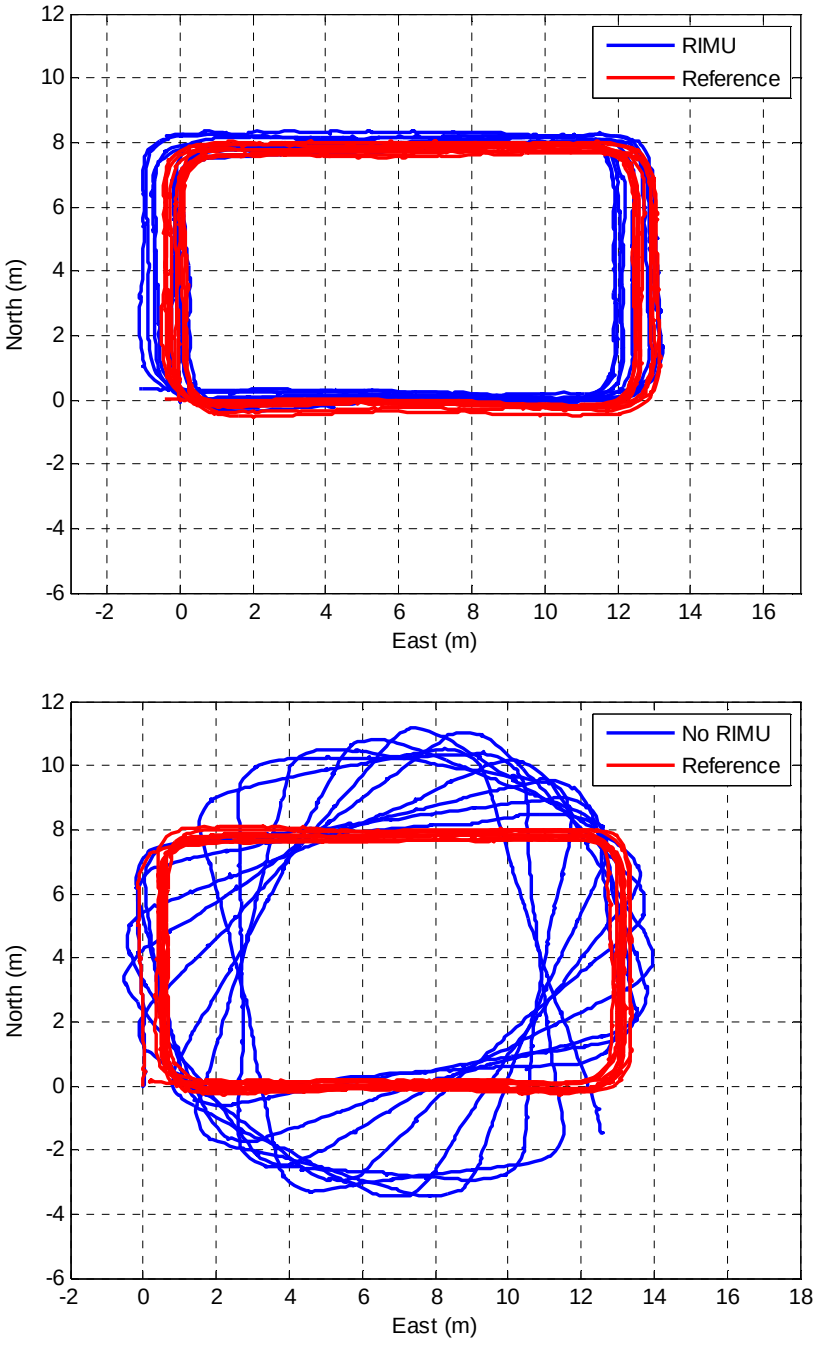

Fig. 7.25: Position solution plotted against reference when (top) with RIMU and (bottom) without RIMU.

To observe the Position Error (PE) after 11 minutes of walking for the trial, Fig. 7.26 is plotted. From the figure, when the RIMU was not used, the maximum PE for North (left figure) and East (right figure) is 10.9 m and 12.4 m respectively. In contrast, implementing the RIMU has reduced the North PE by more than tenfold, where the maximum PE falls to 0.6 m. Likewise, for East PE, implementing RIMU reduces the East PE by about the same amount, with maximum East PE now only 0.7 m.

The mean HPE is computed by taking an average of the HPE, where HPE is represented by the square root of the sum of the squared of North and East PEs. For this trial, the mean HPE was computed to be only 0.4 m when RIMU was implemented, but increases to 4.2 m when RIMU was not implemented.

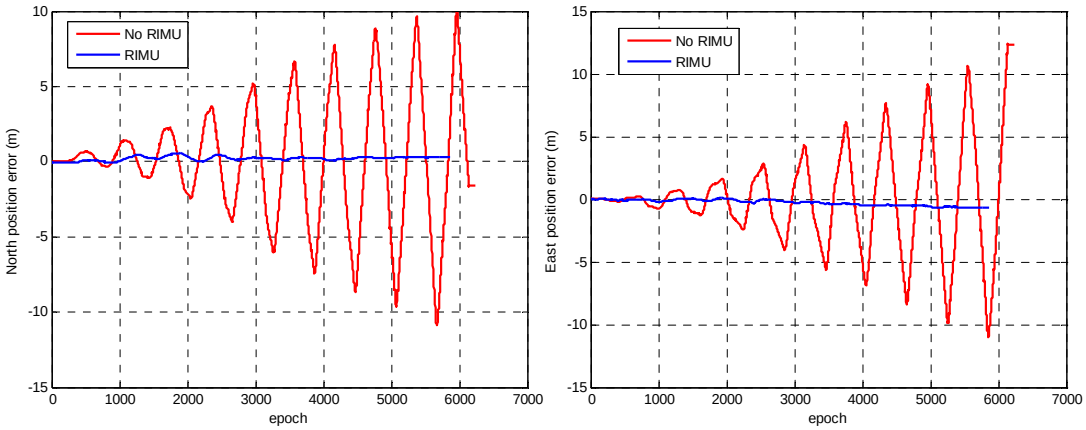

Fig. 7.26: Position error for (left) North and (right) East

7.4.6 Trial Repeatability

Two more real walking trials were performed on a different trajectory to check whether the positioning accuracy result achieved previously can be repeated. Trials 2 and 3 trajectories were constructed from walks inside the same NGB building and contain a few small loops. Table 7.3 summarizes the performance of using the RIMU results from the three indoor trials.

For the RIMU, the three trials lasted for an average duration of 13.4 minutes. The average distance travelled is 458.3 m. From these three RIMU trials, an

average maximum Position Error (PE) for North and East were computed to be only 1.6 m and 1.1 m respectively. The average RPE was also relatively better at only 0.74 m, or only below 0.2% from the total distance travelled.

For the non-RIMU, the three trials lasted for an average duration of 13.5 minutes with an average distance of 469.8 m. In contrast with the RIMU case, an average maximum PE for North and East when the RIMU was not implemented are relatively higher at 9.5 m and 9.1 m respectively. Additionally, the average RPE also increases by tenfold to 7.5 m, or above 1% from the total distance travelled.

Furthermore, the maximum RIMU Horizontal Position Error (HPE) computed from North and East maximum PE, on average was found to be only 1.9 m whilst for the non-RIMU, the maximum HPE was relatively worst at 13.2 m. This, therefore, indicates a significant improvement in position by reducing more than 85% of maximum HPE when the method of rotating the IMU was implemented.

Table 7.3: Position comparison between RIMU and no-RIMU

Trial	**Method**		**Duration (min)**	**Total dist. (m)**	**Max. PE (m)**		**RPE (m)**	**Mean HPE (m)**
					North	**East**		
1	No-RIMU		11.2	385.3	10.9	12.42	12.35	4.59
		RIMU	10.7	354.0	0.6	0.7	0.80	0.42
2	No-RIMU		14.3	475.4	10.7	7.0	3.36	2.68
		RIMU	13.9	475.7	1.3	0.8	0.15	0.6
3	No-RIMU		15.0	548.8	6.8	8.0	6.79	3.14
		RIMU	15.5	545.2	2.9	1.8	1.27	1.93
MEAN		RIMU	13.4	458.3	1.6	1.1	0.74	1.0
		No-RIMU	13.5	469.8	9.5	9.1	7.5	3.5

7.5 Discussion

1. An investigation was made on the observability of the IMU error states after introducing a single axis Rotation IMU approach (RIMU). An IMU was mounted on a platform that rotated about its y-axis and used for the low-cost PNS. Of particular interest was the z-axis gyro bias (which corrupted the INS heading) that was unobservable in a system that had no other external measurement update except ZUPTs. This error was thought to be the main error source contributing to position drift, hence the significance of having a good estimation of this error. The investigation began with a simulation of a static and walking trajectory, followed by real field trials. The results were analyzed in terms of IMU error observability and the low-cost PNS position accuracy.

2. At the beginning of this chapter, it was hypothesized that the RIMU introduced an oscillation effect onto the output of the IMU on the flipping axes. This was supposed to average the measurements, thus cancelling out all the errors perturbing IMU axes. It was found, however, that apart from the averaging effect, the RIMU also improved the IMU error observability.

   Using the RIMU approach, it was shown in a static trial simulation that IMU error observability increased, outperforming the non-RIMU approach. Apart from accelerometer errors on the rotating axis (y-axis), all other error terms converged to the correct reference values. This is quite significant – for example for even lower cost inertial sensors (mostly uncalibrated), where the huge errors and its variations are often very difficult to estimate properly without proper aiding sources. It is thought that because of its observability advantage, an RIMU would be able to 'track' the variations on these huge errors for such cases.

   As a result of improved error observability resulting from the RIMU, the heading drift on both cases, walking simulation and real walking trial, was reduced. This was clearly shown in the comparison of position solution for the

real walking trial, where on an average of 13 minutes of walking, the average maximum HPE was below 2 m when the RIMU was implemented. In contrast, without implementing the RIMU, the maximum HPE was more than 9 m.

3. Nonetheless, more trials are worth performing in order to assess the RIMU's true capability, once a better RIMU prototype is available. This is because at the moment, the RIMU prototype is impractical for mass trials because of its weight and size. Once all the components such as the motor and the platform can be miniaturized, it will be more practical to put them on a foot or shoe. Trials such as a true fire-fighter trial (if possible) can be very useful because of its operating environment with extreme temperature variation. This is thought to be useful to assess the RIMU performance as the RIMU was supposed to estimate better the error terms, regardless of the IMU bias variations that could be caused by, for example, extreme temperature. This ultimately should further improve positioning accuracy for such a case.

7.6 Summary

A new approach of a Rotating the IMU (RIMU) on a y-axis for the low-cost PNS was presented. Its benefit to mitigate heading drift was assessed through simulation and real field trials. Its significance is that it is able to reduce position drift error without the need to have any other external measurements, such as from magnetometer, apart from available ZUPTs. Moreover, it outperformed the normal IMU/ZUPT in terms of error observability. The main limitation however is the need for a physical rotation. Therefore, in a quest to mitigate heading drift and reducing position drift error subsequently for the low-cost PNS without extra cost, another approach is devised in the next chapter.

Chapter 8

Building-Heading Aided

This chapter presents a low-cost IMU-only navigation that is capable of navigating in indoor building for significantly long period of up to 40 minutes, with only below 5 m of horizontal position error. This was very difficult to achieve before, and therefore offers a significant improvement over existing indoor positioning systems, such as the magnetometer-aided system investigated before. This is done by proposing a new approach of aiding low-cost PNS heading measurement using 'building' heading. In light of Chapter 7, the new approach totally eliminates the requirement to have moving mechanical parts. The proposed Cardinal Heading Aided Inertial Navigation (CHAIN) algorithm is a subject of patent application and, together with its sub-algorithms developed herein, has resulted in a few publications (see List of Publications, pp. x).

8.1 Introduction

This chapter begins by describing a Cardinal Heading Aided Inertial Navigation (CHAIN) algorithm in Section 8.2. The underlined idea is explained in detail, verified afterwards by real field trials. CHAIN is further extended by incorporating a few sub-algorithms. These sub-algorithms are presented in the subsequent sections, and are abbreviated as ZIHR (Zero Integrated Heading Rate) in Section 8.3, MPA (Multiple Polygon Area) in Section 8.4 and HH (Heuristic Height) in Section 8.5. Their benefits are discussed using results from real field trials and the chapter ends with a chapter summary.

8.2 CHAIN Algorithm

The following section introduces the algorithm. Its advantages, when used in realistic pedestrian navigation scenarios, will be revealed in the result section.

8.2.1 Introduction

An algorithm is developed that uses simple heading information to restrict the heading drift that occurs when using the low-cost PNS. The heading information in the algorithm can be derived quickly and potentially in an automated manner using free maps or aerial images, and a heading database can then be constructed to aid future navigation. Furthermore, there is no requirement to have high-fidelity maps and detail internal maps of the building to acquire the heading information. This heading information will then form heading measurements to update the Kalman Filter (KF) and the novel use of such measurement in the KF environment will be shown to significantly reduce the position drift of the low-cost PNS (IMU-only pedestrian navigation). Once the system has been initialised, there is no requirement for other measurements, such as from GPS, compasses or visual sensors, to update the KF.

It will be demonstrated that the position accuracy indoors can be maintained below 5 meters for significantly long periods of up to 40 minutes (approximately below 7.5 *meters per hour*). Furthermore, results from multiple field trials provide a low-cost PNS with an average position accuracy of below 0.3% of the total distance travelled. This kind of accuracy, for standalone inertial navigation system, was previously only achievable using high accuracy inertial sensors (Mezentsev et al., 2005). Nonetheless, even these devices still need ZUPT or other sensor measurements to control position drift.

The algorithm is simple to implement and can be easily scaled to large areas even if the map information is derived manually. Furthermore, it will be demonstrated that the algorithm is robust to short periods where the pedestrian walks in directions not consistent with the building. The proposed algorithm is called Cardinal Heading Aided for Inertial Navigation (CHAIN).

8.2.2 The Idea

The sections afterwards develop a novel and effective algorithm for generating heading measurements from a basic knowledge of the orientation of the building that the pedestrian is walking. The idea is based on the assertion that most buildings are constructed with a rectangular shape. Within this shape, most rooms and corridors are constructed of smaller rectangles, which constrain the direction a pedestrian can walk throughout the building to one of four headings. The term 'cardinal heading' is used to describe these four possible headings that the user is likely to walk in most of the time. It is helpful to highlight that building orientation will be consistent with the Course-Over-Ground (COG) direction that the user walks as opposed to heading or yaw which is the true orientation of the IMU x-axis with respect to North.

Although by no means all buildings are constructed in this way, many buildings are. For example, it was surveyed by Ling et al. (2007) that 83.2% of building orientation in Kuala Lumpur, capital city of Malaysia, for high rise building is in a rectangular and square shape. Another good example is Manhattan,

New York where a large number of buildings are aligned in a single direction as in Fig. 8.1, and most of the buildings in this area will have rooms and corridors aligned with a heading of either 29.4^0, 119.4^0, 209.4^0 or 299.4^0. These four headings can be represented by a single angle since the others are simply offset by 90^0. A simple method for deriving this heading is to use the distance and angle measurement tool in the Google Earth application (Butler, 2006). On a smaller scale, Fig. 8.2 shows part of The University of Nottingham campus where most of the buildings are aligned in one of two orientations. Furthermore, when considering buildings on an individual scale, the majority of buildings conform to this concept.

Fig. 8.1: Buildings in Manhattan, New York.

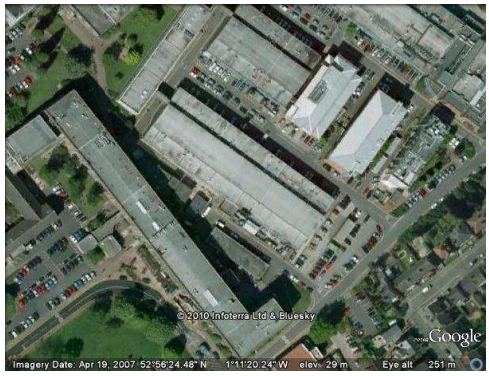

Fig. 8.2: Buildings in the University of Nottingham, UK.

8.2.3 The Algorithm

The developed algorithm is based mainly on standard inertial navigation equations (Chapter 2), with errors controlled through the use of measurements applied using the KF (Chapter 2 and Chapter 5).

The algorithm makes two important assumptions. Firstly, it is assumed that the pedestrian will typically (but not always) walk in a direction that is consistent with the orientation of the outer walls of the building. Secondly, it is assumed that the difference between the Course-Over-Ground (Section 8.2.3.2) and the outer orientation of the building is the result of heading drift plus some uncertainty resulting from the pedestrian not walking in a straight line. This second

assumption is only valid because there is a large acceleration caused by the foot moving through a step. Due to this large acceleration, the heading error is observable through the position difference, as heading is used to determine the orientation of the accelerometer axes. For other applications such as vehicle navigation, it is not possible to use this assumption since the vehicle may be travelling at a constant velocity and therefore heading has no effect on position. The subsequent sections will detail the new CHAIN algorithm, which will be entirely based on a simple diagram drawn in Fig. 8.3.

In essence, the algorithm comprises three stages in sequence:

1. Identification of a step
2. Determination of a Course-Over-Ground (COG)
3. Kalman filter heading measurement update

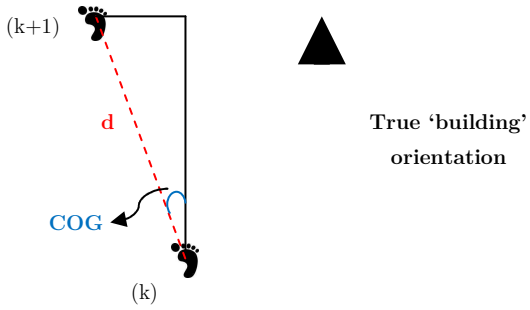

Fig. 8.3: Illustration of heading measurement at each ZUPT epoch

8.2.3.1 Identification of a Step

The algorithm starts by running a check on the system to determine whether a step has been taken or not. This is to identify that indeed a walk has been performed, and is run on every ZUPT epoch. It is performed by computing the step length (or stride length) between the current ZUPT epoch and the previous epoch, assuming that the ZUPT has been detected correctly when the foot is on the

ground. Step length, d, in Fig. 8.3, is computed based on the changes in horizontal position (North and East), dN and dE, where

$$d = \sqrt{(dN^2 + dE^2)} \tag{8.1}$$

and if it falls below a certain threshold, the algorithm continues to the second stage, since the walk has been identified. Otherwise, the algorithm will wait for another ZUPT epoch to start again the identification process. The empirical threshold is chosen using a typical step length of a normal being, by multiple processing of many samples data, knowing that it is possible a step has been taken if the measured step length is more than 0.1 m, and is almost impossible for a normal person to take a step more than 10 m in length (other reasonable values can also be used).

8.2.3.2 Course-Over-Ground (COG)

The algorithm continues by determining the Course-Over-Ground (COG) of the pedestrian, as shown in Fig. 8.3. This stage comprises two steps:

1. Computation of a step heading, $\hat{\psi}_s$
2. Declaration of $\hat{\psi}_s$ as the COG

The first step is the computation of a step heading. The step heading is defined as the angle between two successive steps that signals the walking direction and this is calculated at every ZUPT epoch. In other words, it is defined as the change in heading measurement at current ZUPT epoch (t), from previous ZUPT epoch (t-1). It is conveniently chosen with the assumption that within this epoch, the IMU error remains small. The following equation,

$$\hat{\psi}_s = atan2\left(dE, dN\right) \tag{8.2}$$

is used to calculate step heading by utilizing *atan2* function, where it is just a variation of *atan* (tan^{-1}) function. It is used here because it can resolve the angle in

the right quadrant. $\hat{\psi}_s$ is the measured step heading and dE and dN are the changes in East and North position over one step. This heading measurement is based only on the change in position caused by a single step. Therefore, $\hat{\psi}_s$ not only consists of the true heading plus drift, it also consists of other small unmodelled errors from inertial navigation.

CHAIN will use $\hat{\psi}_s$ for the next stage of the algorithm (Section 8.2.3.3) only if $\hat{\psi}_s$ can be declared as COG. From Fig. 8.3, COG is defined as the angle between steps, which is consistent with the cardinal headings of the building. Therefore, an empirically derived threshold is used to exclude steps that are not consistent with the current building heading, $\hat{\psi}_B$ such as when walking around corners or not walking straight along a corridor:

$$\text{COG} = \begin{cases} \hat{\psi}_s & \text{if } |\hat{\psi}_s - \hat{\psi}_B| \leq \theta_{th} \end{cases} \tag{8.3}$$

The threshold, θ_{th} has to be large enough to accommodate the heading drift of the IMU as well as small variations in COG that are caused by the pedestrian not walking exactly in straight lines. If passes this test, a measurement is added to the KF (Section 8.2.3.3); otherwise no measurement update is applied to the KF.

8.2.3.3 KF Measurement Update

The measurement used for the KF is the difference between COG, calculated from the change in position between steps, and the orientation of the building. A measurement update is applied by forming the observation equation,

$$\delta\psi = \hat{\psi}_B - \text{COG} \tag{8.4}$$

where $\delta\psi$ is the INS heading error and $\hat{\psi}_B$ is the current 'building' orientation. Based on Eq. (2.34), Eq. (8.4) is then used with Eq. (5.17) to update the KF,

$$\delta\psi = \begin{pmatrix} \frac{\partial\psi}{\partial\epsilon_N} & \frac{\partial\psi}{\partial\epsilon_E} & \frac{\partial\psi}{\partial\epsilon_D} \end{pmatrix} \epsilon + n_k \tag{8.5}$$

where n_k is the measurement noise with covariance

$$R_k = E(n_k n_k^T) \tag{8.6}$$

The measurement noise, n_k represents uncertainties when pedestrians do not walk in straight lines with respect to building orientation. Therefore, n_k must be large enough to account for steps that do not follow exactly the building orientation (which is closely related to the threshold value used to determine COG in Section 8.2.3.2). In addition, it is worthy to highlight that the heading error measurement, $\delta\psi$ does not relate directly to the physical attachment of the IMU. This means that the IMU can be mounted in any orientation on the user's shoe. This is significant for realistic application of pedestrian navigation as then, it does not matter if the user is walking sideways, or even backwards, for the algorithm to work.

8.2.4 Trials and Results

Four field trials were undertaken to test the proposed approach. The first trial involves normal walking around a typical football pitch with a Network Real Time Kinematic (NRTK) system to act as a position reference to evaluate the accuracy of the foot mounted IMU. The second trial involved walking along a straight line (next to a straight road). For the third and fourth trials, normal walking and irregular walking were undertaken respectively in a typical indoor environment at the Queens Medical Centre (QMC) hospital, Nottingham within a built up area of about 65 000 m^2. There was no ground reference used in the QMC trial because of the difficulty in having such a reference system inside buildings, hence the result is discussed using Google Earth aerial imagery as a coarse approximation. The total walking distance for all the trials is computed using raw IMU position output.

8.2.4.1 Trials Description

The following sections describe trials that have been conducted to test the new algorithm. The equipment used was described in Section 5.4. The initial position for the IMU was estimated from the GPS position (which in practice would assume that navigation would start in a well received GPS signal area). As discussed in

Section 2.4.3.1, the initial roll and pitch of the IMU was calculated during a short stationary period (1 *s*) by differencing the accelerometer measurements with the local gravity vector. The heading was initialised manually, but it is expected that a one-off magnetometer reading could be sufficient to initialise the algorithm (as performed in Chapter 6), provided that magnetic disturbances can be filtered out reliably. Normal strapdown navigation equations were used to resolve and update the position and attitude of the IMU (Section 2.4.3.2). Once it has been initialised, the system computes its position relative to the initial position. The developed algorithm generated heading measurements for the KF and the measurements were then post-processed using the Nottingham Geospatial Institute's POINT (Position and Orientation Integration) software (Section 5.3), although the algorithm could still be used in real-time. The developed algorithm (Section 8.2.3) is now part of the POINT software.

8.2.4.2 Football Pitch Trial with NRTK Reference

In order to quantify the accuracy for any positioning or navigating system, a comparison of position solution between low accuracy systems such as integrated standalone GPS–INS and more accurate reference systems such as Network Real Time Kinematic (NRTK) (Aponte et al., 2008), is typically performed. This can however only be reliably performed outdoors where NRTK is always available.

In the case of the present low-cost PNS trial, it was not possible to have NRTK reference in an indoor environment for comparison purpose. Therefore the trial was replicated in an outdoor environment, with a clear line of sight to GPS and good network coverage for NRTK corrections, so that a comparison analysis could be performed with a reliable NRTK solution. The NRTK system (using Leica GS10 Geodetic grade receiver) was, therefore, used as a ground reference as it provides a very precise position solution, with a standard deviation of approximately 2 *cm* (figure was given by the Leica receiver) throughout the whole trial.

The outdoor test was conducted with a 40-minute normal walk on a football pitch at the University of Nottingham (Fig. 8.4). The football pitch is approximately 95 m x 55 m in dimension with a typical white boundary line. The user walked ten circuits around the boundary line of the pitch so that the walk was approximately in straight lines, apart from at the corners, emulating a walk around corridors in a building.

Fig. 8.4: Football pitch used for trial environment

Fig. 8.5 shows the comparison of the two trajectories when CHAIN was implemented. The blue trajectory represents the low-cost PNS with CHAIN algorithm while the red trajectory is the reference trajectory from the NRTK solution. It clearly demonstrates the superiority of CHAIN solution, where after significantly long period of time, the position solution is still consistent with the reference solution. In particular is the trajectory heading, where the heading drift is no longer visible. In contrast, Fig. 8.6 shows the trajectory when CHAIN was not implemented (in green), where only ZUPTs were available for measurement update in the KF. It is obvious from the figure that the position has drifted quite significantly with respect to the reference.

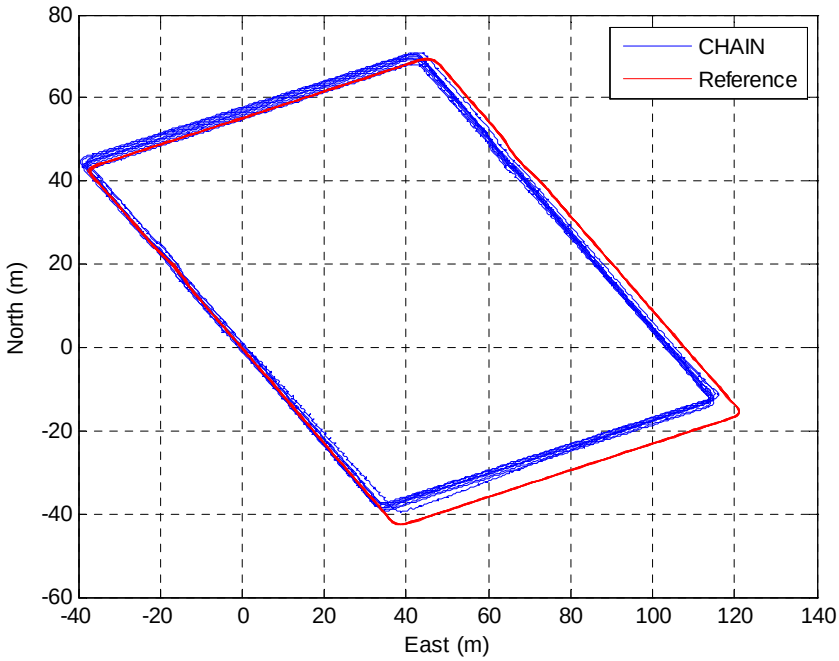

Fig. 8.5: Trajectory of walking on football pitch boundary line when CHAIN was implemented

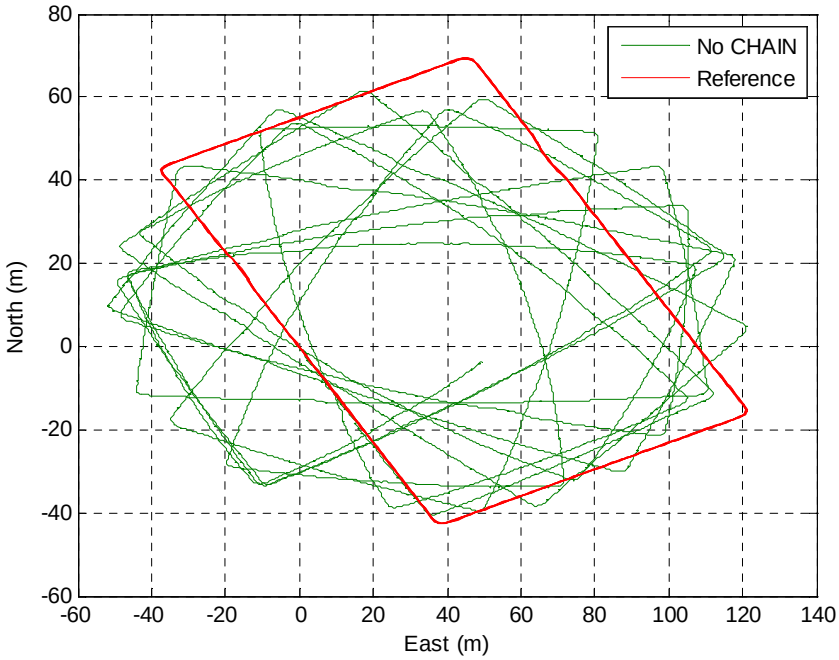

Fig. 8.6: Trajectory of walking on football pitch boundary line when CHAIN was not implemented.

Fig. 8.7 and Fig. 8.8 show the position difference of CHAIN and No-CHAIN solutions respectively, when compared with the NRTK solution. The difference also includes the disjunction error (Section 6.4.2.1.1), where it is the non-constant lever-arm offset of the IMU moving on the user's foot relative to the GPS antenna on the user's back, which is shown by the smaller high frequency oscillations. Similar with Section 7.5.5, comparison will be made in terms of the maximum Position Error (PE) in meters, the Return Position Error (RPE) and the mean of Horizontal Position Error (HPE) (both in meters), and the percentage of RPE from the total distance travelled.

From Fig.8.7, it is observed that the maximum PE for North and East is less than 5 m. For the North and East position errors, the occurrence of big oscillations are the result of a full round of walking (there are 10 peaks which are equivalent to 10 rounds of walking). This appears to be a result of the IMU solution resulting in slightly shorter distance measurements than the NRTK truth. The height error, however, is still prominent with maximum height error of about 25 m after 40 minutes of walking. This will be further addressed in Section 8.5.

After an IMU-only navigation aided with CHAIN for approximately 40 minutes in duration and 3000 m in distance, the absolute RPE was only 4.59 m, or about 0.15% of the total distance travelled. Additionally the maximum HPE was computed to be only 6.50 m, whilst the mean of HPE was 3.68 m. In contrast, when CHAIN was not implemented (Fig. 8.8), the RPE was increased to 29.32 m, the maximum HPE to 106.80 m, and the mean of HPE to 44.16 m. Therefore, in terms of maximum HPE, implementing CHAIN has reduced the error in percentage to about 94%. This represents a significant improvement in the field of low-cost IMU positioning. In fact, such performance is difficult to achieve even with high quality inertial sensors, unless they can be foot-mounted. For example, even navigation grade inertial sensors have a typical drift of approximately 1.5 km/h (Moore et al., 2008), so unless regular measurement updates such as ZUPT can be applied, the performance is deemed to be not comparable to the low-cost IMU solution with CHAIN algorithm.

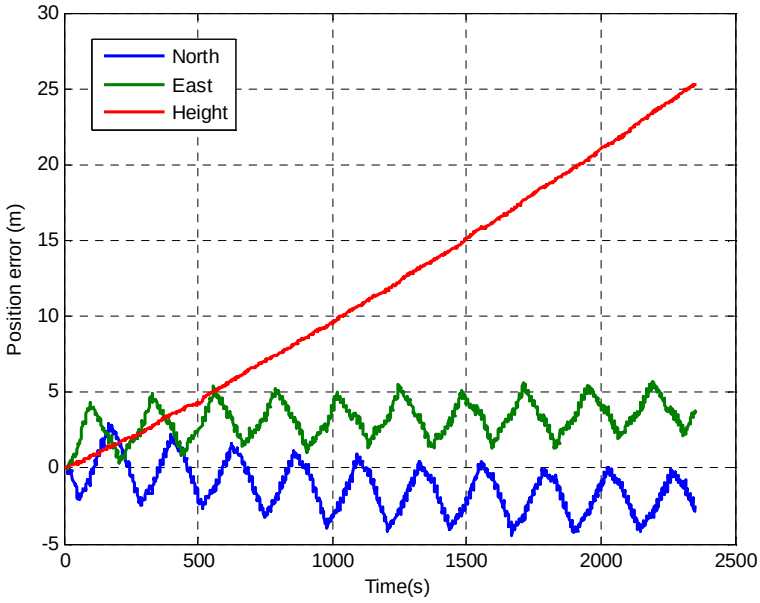

Fig. 8.7: Position difference of CHAIN solution against NRTK solution

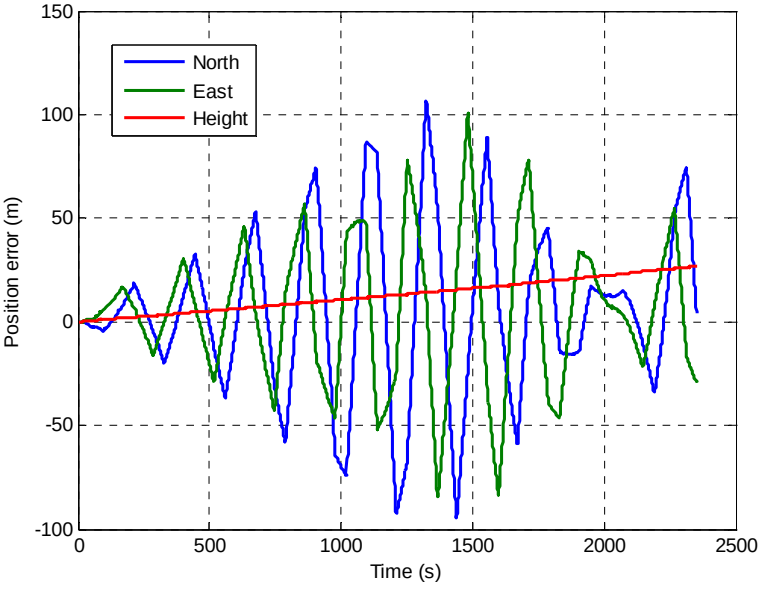

Fig. 8.8: Position difference of no-CHAIN solution against NRTK solution

To demonstrate the application of the heading updates, Fig. 8.9 shows the KF innovation for the heading measurements. The heading innovation is the difference between the INS derived COG and the building heading. The difference comprises the INS heading error, other small INS drift, and also the variation of the user's step in relation to the heading of the building. The standard deviation of heading error is shown to be only 2.1^0 whilst the maximum heading error is 9.7^0 (which correspond to the 10^0 acceptance threshold). The maximum values probably occur as the user walked around corners and the walking in straight line assumption was not correct.

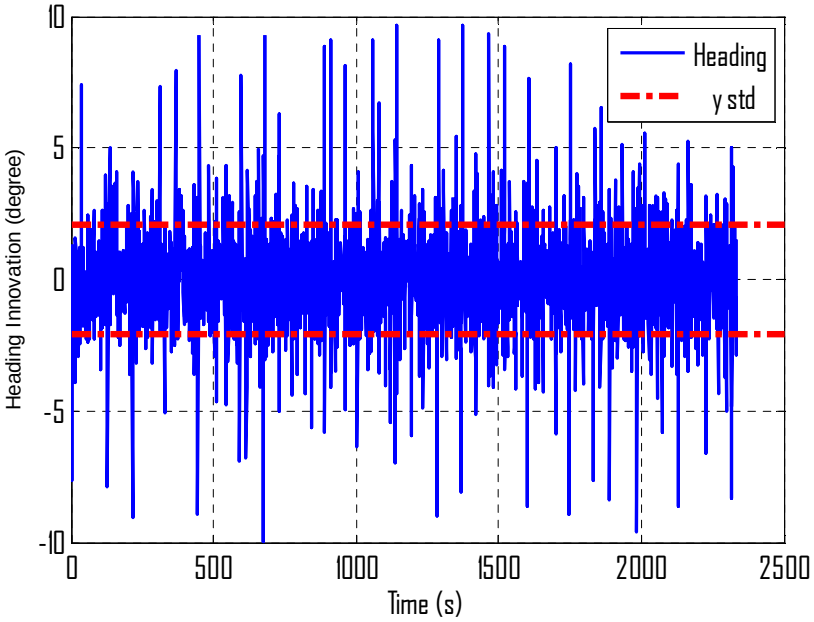

Fig. 8.9: Heading innovation of CHAIN solution

8.2.4.3 Walking Along a Straight Road

Next, the algorithm was tested by walking along a straight line (next to a straight road). Similar with Fig. 8.9, Fig. 8.10 shows the values for $\delta\psi$ that were used in the KF. The standard deviation of the heading difference is only 1.54^0 whilst the

maximum heading difference is 7.58^0 (which again correspond to the 10^0 threshold used).

Fig. 8.11 shows the position error after approximately 3 minutes of walking in a straight line. The blue line represents the position error using the CHAIN algorithm while the black line represents position error without using the algorithm. Using the CHAIN update, the final North position error is only 1.25 m, whereas in contrast the error is 49.77 m if the algorithm was not used. Further results in more realistic situations are described next.

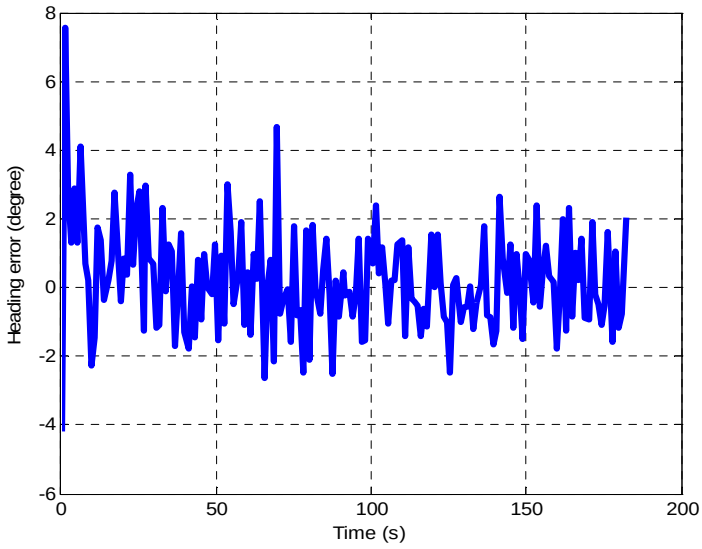

Fig. 8.10: Heading error for walking in a straight walk

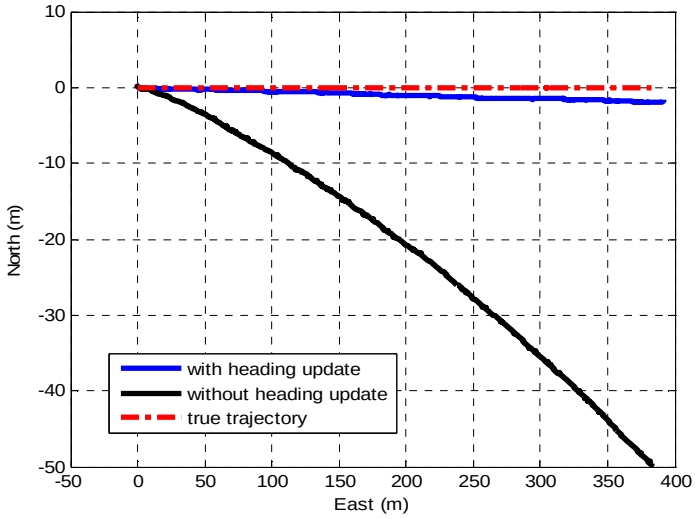

Fig. 8.11: Relative position with and without heading update

8.2.4.4 QMC Hospital Trial with Normal Walking.

Fig. 8.12: Hospital entrance with sign as the start and end location

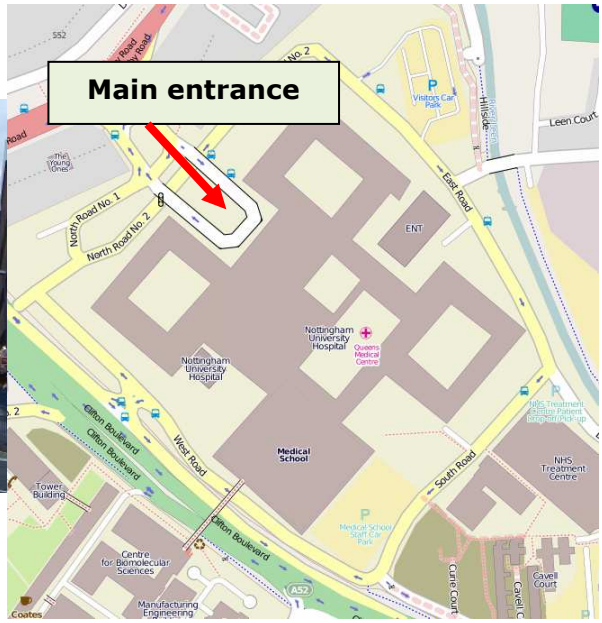

Fig. 8.13: QMC street map view from OpenStreetMap.

A third trial using the low-cost PNS was undertaken at Queens Medical Centre Hospital, Nottingham as shown in Fig. 8.12. This building was selected because it represented a typical building with many straight features. The normal walking trial was done for about 40 minutes with an approximate distance of 2400 m. The trial started and ended at approximately the same location as shown by the junction at the right of Fig. 8.12 (No-Entry sign). The user started walking from outside of the hospital, and walking into the hospital through the main entrance (see Fig. 8.13). After walking was done inside the hospital, the user walked out again through the same entrance, back to the starting position. The reason behind starting and ending at approximately the same position is to ensure that the quantification of the Return Position Error (RPE) (or the start-end position error) can be performed. This is because ideally, starting and ending at exactly the same location should give an RPE value of 0 m. The u-Blox High Sensitivity (HS) GPS receiver was only used for comparison purposes to indicate the performance of a

high sensitivity receiver in this building. Fig. 8.14 shows the trajectory taken during the trial. The green line shows the output of the low-cost PNS implementing CHAIN algorithm and the red dot marker shows the HSGPS output. Although the HSGPS receiver can track more than 4 satellites in some parts of the building (shown by the red markers where position solutions are available), there are no useful comparisons to be made between the HSGPS solution with the proposed CHAIN solution. This is because of the corrupted position measurements and jumps in position solutions (white lines in the figure), which may be caused by the multipath error and the unavailability of the GPS signal in indoor (Section 3.2.1). Coarse analysis using aerial imagery from Google Earth (as shown in the figure), is thus sufficient to indicate that the CHAIN position solution is usually better than 5 m, and typically < 2 m most of the time with respect to the image. Furthermore, as expected, the heading is always consistent with the building.

As mentioned before, there was no ground reference except the freely available aerial imagery of the QMC building; hence only rough approximation of the trajectory analysis can be made using Google Earth. For Fig. 8.15, nonetheless, it provides a useful insight into the effectiveness of a low-cost PNS with CHAIN against a low-cost PNS with ZUPT-only. It is obvious that CHAIN solution (green) overcomes a standard INS–ZUPT solution (red) based on the difference between the two trajectories in the figure. It is clear that the majority of the position drift occurs as a result of heading drift, as highlighted in Chapter 4. The RPE for CHAIN system is about 2.30 m, approximately only 0.1% position error from the total walking distance of 2400 m, which again is a significant improvement in performance. In contrast, for the INS/ZUPT only approach, the RPE is about 220 m, approximately 9% of the total distance and with a significantly corrupted heading solution.

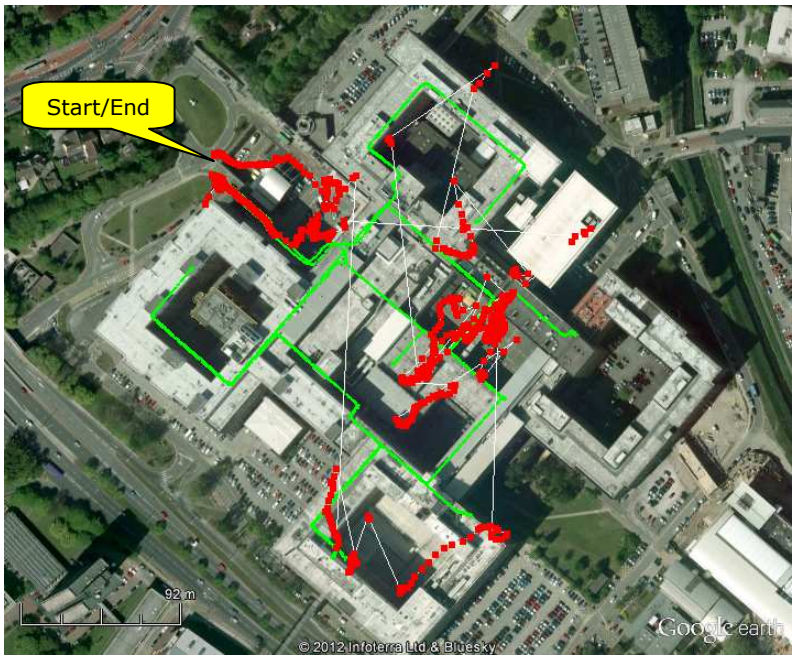

Fig. 8.14: Comparison of CHAIN solution (green) and HSGPS solution (red)

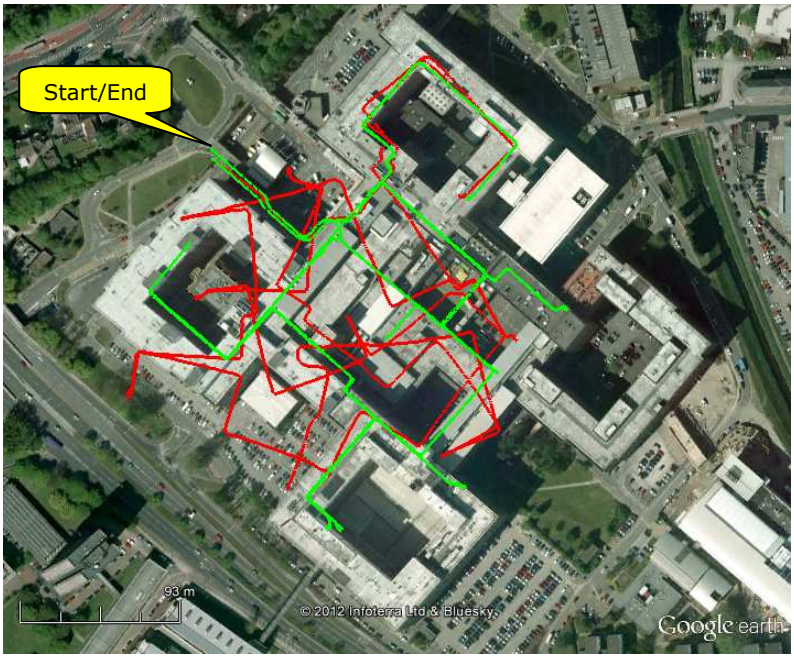

Fig. 8.15: Comparison of CHAIN solution and INS/ZUPT solution.

8.2.4.5 QMC Hospital Trial with Irregular Walking.

A fourth trial for a period of 15 minutes was undertaken to address the irregular walking behaviour for pedestrian, starting and ending at the same location. This is to examine the performance of the algorithm when the 'walking in straight line assumption' within the building does not necessarily hold true. Four different types of walking pattern were analysed and alphabetically depicted in Fig. 8.16 as A, B, C and D, and their descriptions are shown in Fig. 8.17 next.

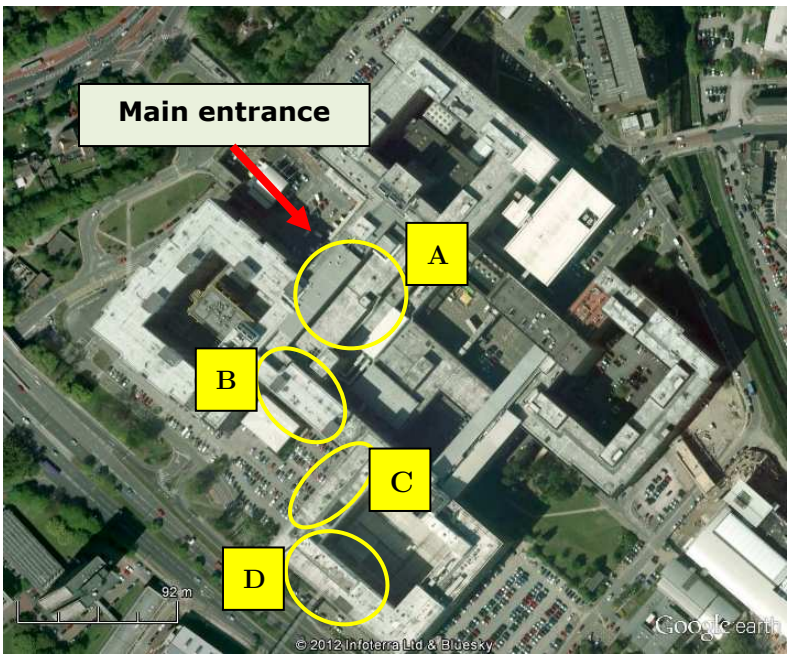

Fig. 8.16: Areas of irregular walking in QMC hospital.

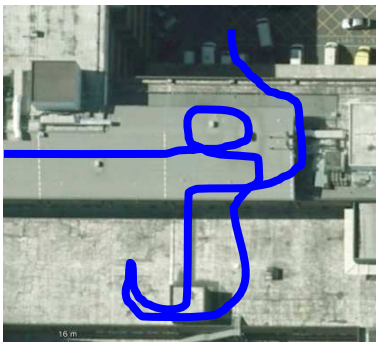

[A] Entering QMC through the main entrance *(from top middle)* to a convenience shop *(bottom middle)*, walking into two aisles before coming out from the shop. Walking into another shop *(middle)*, did one round before coming out and proceeding to stage [B].

[B] After coming out from the shop *(from upper right corner)*, walked straight and cornered to the left. Then, walked in a 'zig-zag' pattern to stage [C].

[C] In this stage, the user walked backwards from the start of the corridor *(right of the picture)* until the end of the corridor *(the left of the picture)*

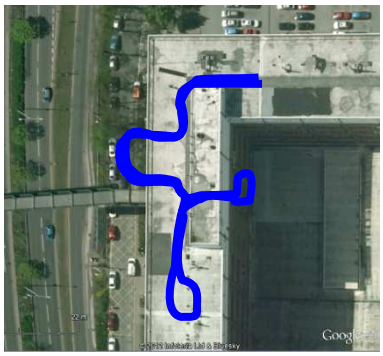

[D] Walked *(from top)* to the spiral stairs, down to the lower floor until the end *(bottom)* and made a small loop around a pillar *(bottom)*. Then walked up to another staircase for three levels *(right)* and then walked down again towards the spiral stairs. Continued walking up the spiral stairs to the start of walk.

Fig. 8.17: Description of each stages [A], [B], [C], and [D] as depicted in Fig. 8.16.

Again there was no ground truth to be used as a reference; instead aerial imagery from Google Earth is used only for visualisation purpose. Fig. 8.18 shows the entire trajectory when CHAIN is used. It was shown that even with irregular walking, CHAIN algorithm still manages to maintain sufficient accuracy to return to the starting position (top of Fig. 8.18).

Likewise, Fig. 8.19 shows the times at which CHAIN heading measurement updates were automatically applied to the system, depicted by the red dots. It was observed that the low-cost PNS using CHAIN showed robustness for short periods when heading measurement is not being updated (period where there is no red dot). This is true for example in the top right corner in Fig. 8.19 when zig-zag walking was performed. With these irregular walking patterns, the RPE was still about 1.25 m, again approximately only 0.1 % of the total walking distance of about 1250 m.

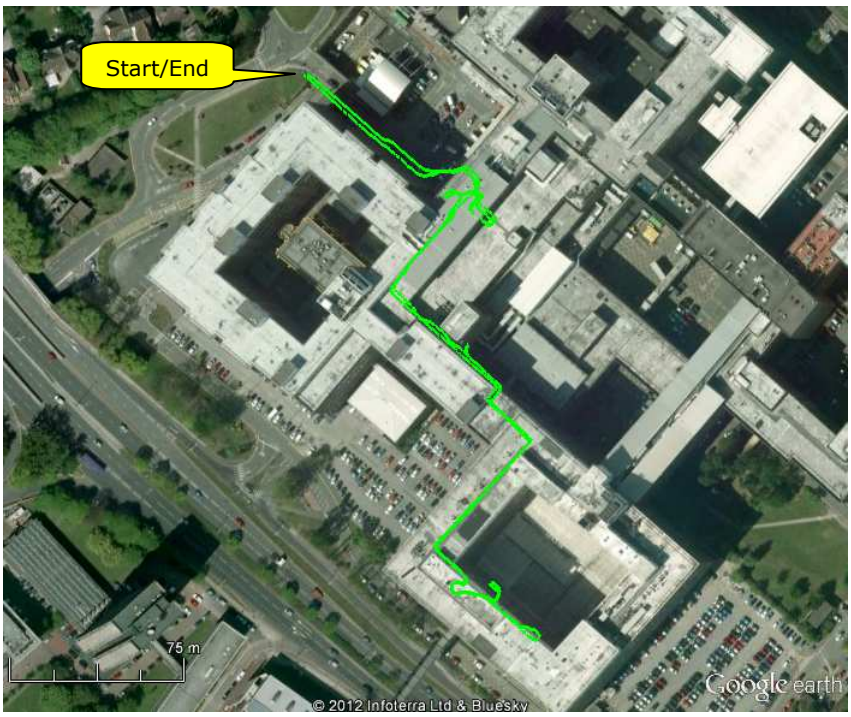

Fig. 8.18: Irregular walking trajectory using CHAIN algorithm.

Fig. 8.19: From left top corner (clockwise) - Trajectory [A],[B],[C] and [D].

8.2.5 Discussion

In this section, the advantage of CHAIN algorithm will be discussed, including possible areas where the algorithm will possibly not work. This is purely based on a theoretical view along with experience of the algorithm already accumulated from multiple field trials.

1. Because of the heading observability issue discussed in Section 4.4 and its relation with the importance of having a dynamic model that precisely describes the propagation of IMU errors, CHAIN method is thought to be

more superior from the previous methods presented so far. This is because, first the method takes into account possibly all the drifts accumulated during swing phases when providing the heading error measurements. These measurements therefore contain all the errors that affect subsequently the error in position solutions. Second is because of the existence of a large acceleration when the foot is moving through a step. As a result, the impact of the attitude error about the Down axis (see Eq. (4.1) & (4.2)) can be seen on the horizontal position errors. The horizontal position errors can thus be mitigated using the knowledge of the attitude error about the INS Down axis when updating the KF.

2. Continuous walking in circles or non-straight lines (curves) for a long period of time is likely to cause a problem for the algorithm. This is because a straight walk check (Section 8.2.3.2) will always return false in the algorithm and as a result, there are no heading measurements available to update the KF. Therefore during this period, the heading will drift. If the drift is so large that the building heading does not remain within the threshold check when the user does start to walk in straight lines again, the algorithm will fail. However, experiences with the algorithm when walking in a circle (in Jubilee Campus library with circular corridor) indicated that there are times when a few heading updates from CHAIN can be expected, even when walking in a circle. This is because, if the circle is big enough, there are times where the circle appears to be in a straight line, and CHAIN can be applied to update the estimation process. This should be enough to keep the heading from drifting much further. Furthermore, as shown in Section 8.2.4.5, the algorithm should be robust to short periods of irregular walking (where there are no heading updates), before the heading drift becomes significant.

3. It is clear that not all buildings conform to the simple geometry of constraining most walking to one of four cardinal directions. In the extreme case, some buildings are built with circular corridors and the algorithm is unlikely to

improve the INS-only solution when prolonged walking in this building is performed. A similar situation will occur when a pedestrian is walking inside a large room where the motion is not constrained to the four cardinal directions. Other less common situations are where a building is constructed with rooms and corridors using more than one possible heading. In this situation, it may be possible to extend the algorithm to include additional headings, although this is likely to reduce the robustness of the algorithm. Another situation is that the internal rooms and corridors may not be aligned with the outside of the building. This would cause a problem since the building heading is extracted using the measurement tool in Google Earth via aerial imagery. If this angle is not the usual angle that people walk inside the building, the algorithm will not work satisfactorily. Nevertheless, it is by far the most common situation that buildings are designed with a simple construction (such as demonstrated in the trials), where the algorithm will work well.

4. The third issue that should be discussed is as the user walks between buildings, the algorithm will need to change the heading that is used. At the moment, the information is extracted from a Google Earth *kml* file that contains polygons which have been manually defined. It is necessary that the position remains accurate when the pedestrian walks between buildings, otherwise the wrong heading may be used, and this will result in an unpredictable heading and position error. This will be highlighted in Section 8.4. Furthermore, by using measurements from other systems such as GPS when it is available, for example in an open area in between buildings, it is expected that position drift can be restricted sufficiently in most situations.

5. Another issue is the pedestrian is assumed to be walking continuously without stopping for any long periods. If the user stops, heading measurements will not be available because the algorithm can only compute heading drift when a user takes a step. During this time the heading drift will be unconstrained, and when the user moves again, the heading may have drifted so much that the

algorithm will not work. In this situation, it is expected that a heading drift restriction algorithm could be applied where the gyro output is threshold-checked, and if the output is within the threshold, a measurement will be used to maintain the heading to the last known heading. This will be addressed properly in Section 8.3 next.

6. Apart from the points discussed earlier, note that using the Kalman Filter (KF) provides an advantage of using other reliable measurements (if they are available) to further improve the navigation solution. This could be from occasional reliable GPS positions, sparse WiFi/RFID 'fingerprinted' positions, or simply a point in a map. This flexibility should provide more integrity and better accuracy to the estimation of the system solution, if the measurements can be used reliably to update the KF. In all the trials presented so far, however, there were no other measurement updates used, except from ZUPTs and CHAIN algorithm. Note also that there is an advantage in using Inertial Navigation System (INS) against the basic Pedestrian Dead Reckoning (PDR) algorithm. The basic PDR (Section 3.2.8.1) assumes that all steps detected are forward walking with fixed stride length (distance), thus side-stepping and backward walking lead to false measurements, whereas INS, conversely, is capable to handle this and measuring stride length simultaneously.

7. Another point to be highlighted is the fact that the IMU and the GPS antenna are not collocated. The IMU was mounted on foot while the antenna was mounted above the head for a better viewing angle. This resulted in an effect called disjunction error (discussed in Section 6.4.2.1.1). This means that the position error in Fig. 8.7 incorporated this position error of about 0.5 m, when the foot swayed back and forth with respect to the antenna.

8. Although not explained explicitly, Appendix D (that relates directly with the CHAIN algorithm) shows that a building heading can be generated automatically (and most importantly it is free) by extracting it from a map.

Likewise, the heading of a building can also be assumed to be known. This is a valid assumption because it is possible for this information to be made known, especially in public buildings. This is not impractical because normally every permanent building can have its own heading surveyed once and stored in a database. This is very convenient from the user's point of view since only one update from this information is needed to navigate in that building. Once the system has worked out its heading, there is no need for a repeated request, unless the user has moved out from the current building to a different building with different building heading. This is very important especially for a future low-cost system, for example one that looks for a real-time solution with low-cost capability (computing power, cost).

9. Although at first instances the approach might be interpreted as a particular case of map-matching, they are actually different (discussion in Section 3.2.6 can be referred). The obvious disadvantage of map-matching is the map itself must be accurate otherwise the accuracy of the computed position solutions will be degraded. The map-matching method therefore relies heavily on the integrity of the map. Furthermore, the map must also be embedded with the position information (coordinates) before it can be used for positioning, which relates with the heavy computational processing required. In contrast, the method presented in this chapter does not set the requirement to use the map. If the information about the building heading is known beforehand, for example from a database, it still can be used with the method (note that only single information about the building heading is sufficient). The method may however make use of the map (if available) to extract the building heading information, but the map does not necessarily need to be accurate, as long as the orientation is correct.

10. Finally, it is worth to mention that a similar idea was apparently developed independently by Borenstein and Ojeda (2010). However, they implemented PDR approach, which does not have the advantage of the INS and the KF

(point 5). Secondly, the true building heading was not used explicitly, which means PDR heading is initialized with 0^0 when aligned with the direction of travel. Walking in any of the dominant direction in a building thus results in the use of the dominant angles (0^0, 90^0, 180^0, 270^0) by the PDR. Recently, Jiménez et al. (2011) implemented the same approach by the author and compared the approach with Borenstein's work. Interestingly, it was shown to improve the position solution over the approach by Borenstein, especially in difficult trajectories such as when walking around corners as presented in Section 8.2.4.5.

8.3 CHAIN with Zero Integrated Heading Rate

The following section describes further improvement made to the CHAIN algorithm. The new CHAIN algorithm was shown previously to be able to control heading drift when the user is walking, but the heading error will still accumulate when the user is stationary. Therefore another measurement, known as Zero Integrated Heading Rate (ZIHR) (Shin, 2005) is used to address this issue.

8.3.1 ZIHR Introduction

Zero Integrated Heading Rate (ZIHR) was first used in a vehicle navigation system by Shin (2005) to stop heading drift when the vehicle stops. To the author's knowledge, ZIHR has never been used before in pedestrian navigation to constrain heading drift during prolonged stop. Most of the results in the literature demonstrate walking without stopping in an extended period of time, which is slightly unusual for pedestrians.

In a stationary situation, roll and pitch errors can be constrained for low-cost PNS by applying ZUPTs, but not the heading error due to its poor observability (Section 4.4). Thus, the heading error will still accumulate during this situation. Applying the CHAIN algorithm unfortunately requires the user to walk, which is

not the case in hand. Therefore, in order to restrict this error accumulation, another measurement is used in the Kalman Filter during prolonged stationary situation ('stop' situation). It uses the knowledge of previous and current heading to constrain the system from accumulating the heading drift error. A simpler approach of using a predetermined threshold to limit the heading drift whenever a 'stop' situation is detected can also be applied. ZIHR, however, has the advantage of modelling the covariance information correctly in the filter (discussed in Section 8.3.5).

8.3.2 ZIHR Algorithm

Based on Eq. (2.34), the ZIHR measurement model is written as follows (Shin, 2005):

$$\frac{\psi_k - \psi_{k-1}}{\Delta t_k} \approx \begin{pmatrix} 0\ , & sec\theta sin\varphi\ , & sec\theta cos\varphi \end{pmatrix} b_g + n_k \qquad \textbf{(8.7)}$$

where ψ_k is the INS heading; roll (φ) and pitch (θ) are considered as constants over the time interval Δt_k; b_g is the vector of body frame gyro biases; n_k is the remaining noise term; and k is the epoch. Due to the term $sec\,\theta$, ZIHR cannot be applied when pitch is close to $\pm 90^0$. The algorithm essentially describes that the change of heading over a certain time interval during stop situation is mainly caused by the gyro bias and noise on the z-axis of the IMU.

8.3.3 ZIHR in Low-cost PNS

Before the ZIHR measurement model can be used in the Kalman Filter (KF), the low-cost PNS needs to satisfy two conditions:

1. ZUPT check
2. Rotating foot check

First, the ZUPT event is checked to ensure that the system is in a stationary situation (pedestrian stops walking). If this event returns true, a second check is done by checking whether the foot is rotating. This is important to highlight a case when a pedestrian stops walking and rotates his foot (effectively the heading) at the same time. If the second check was not introduced in the system, the pedestrian heading will still be maintained due to Eq. (8.7), where it describes that during the stationary situation, the heading should have not been changed (which is wrong). In contrast, because of foot was rotating during the stationary situation, the heading should have been showing a different heading value (which is right) and ZIHR should have not been applied. Therefore, ZIHR is declared to be used to update the KF only when these two conditions are satisfied (return true).

These two conditions test the magnitude of the velocity and the gyros and compare it with an empirically determined threshold, where velocity is the three dimensional velocity of the IMU velocity and gyros is the three dimensional rotations determined by the gyros. The threshold must be set to be larger than the expected total gyro bias and yet small enough to ensure the IMU is not physically rotating. If these conditions are satisfied, then the ZIHR measurement model is used to update the gyro bias estimation in the KF, otherwise, no update is sent to the KF.

8.3.4 Stationary Trial

The stationary trial is conducted by putting the IMU that was initialized with a known heading on a stationary table for 16 minutes. Comparison is then made between using INS–ZUPT only (normal approach) and using INS–ZUPT with ZIHR. Only a stationary trial is conducted because the ZIHR will only be applied during stationary events of the low-cost PNS, which occurs during ZUPT epochs (effectively when stance phase is detected). For full trials implementing ZIHR, the result will be presented in Section 8.7.

Fig. 8.20 shows the heading error when ZIHR was and was not used. The red line in the figure represents INS–ZUPT heading error (ZIHR was not used). It

clearly shows that the heading drifted quite considerably when ZIHR was not used (only INS–ZUPT), but maintained sufficient accuracy when INS–ZUPT with ZIHR was used. When ZIHR was not used, after 200 s, a heading error of 30^0 is observed, which then grows to about 100^0 after 900 s. When ZIHR was used (blue line), it maintained precise heading with a heading error standard deviation of 0.03^0 (shown in Fig. 8.21).

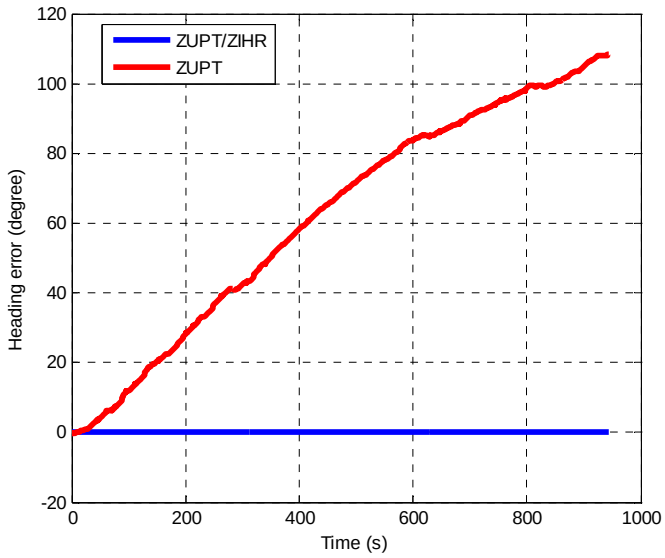

Fig. 8.20: Heading errors using ZUPT only and ZUPT with ZIHR.

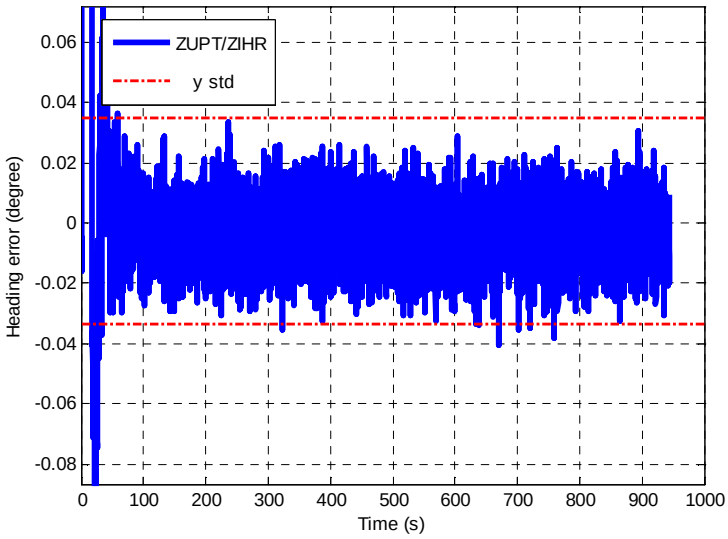

Fig. 8.21: Heading errors of INS/ZUPT with ZIHR.

8.3.5 Discussion

1. An alternative to using ZIHR is to fix the heading whenever conditions in Section 8.3.3 are satisfied (return true). However this will not make a full use of the measurement as achieved using ZIHR, where full correlation between states is exploited. If the heading measurement is used directly, it will result in an over optimistic estimate of the uncertainty of the attitude states. Consider an example where initial heading uncertainty and heading measurement noise are set to 10 degree and 1 degree respectively. Fig. 8.22 shows the standard deviation of the attitude error state about the Down axis, ϵ_D. The standard deviation for fixing-yaw measurement case drops to a small value, which is unrealistic as the measurement is not a true measurement (such as from an external sensor). Instead, it is desirable only to stop the heading error from increasing and at the same time preserving the covariance information in the KF. This means that ZIHR is able to make full use of the measurement while preserving the covariance in the KF.

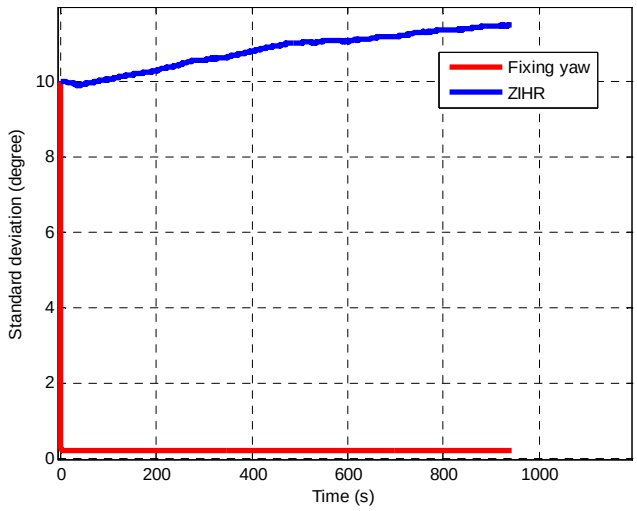

Fig. 8.22: Comparison of attitude error standard deviation on the Down axis for the ZIHR case and 'fixing yaw' case.

2. Another issue is how realistic is the condition of the non-rotating assumption in Section 8.3.3, before ZIHR can be used. Note that the first condition to be

satisfied before using ZIHR is the ZUPT check. This condition is important as it reduces the possibility to have a rotating movement during stationary situation (when ZUPT check holds true). In other words, it is practically hard to rotate the foot whilst simultaneously in a stationary situation. Moreover, in a stationary situation, rotating the foot slowly is quite difficult and can easily violate the small predetermined threshold (note the discussion in Section 8.3.3 where the threshold is determined to be higher than the gyro bias, and yet small enough to ensure the foot is not physically rotating).

8.4 CHAIN with Multiple Polygon Areas

The following section describes a scenario when pedestrian traverses between buildings, and how CHAIN can be further developed to address this using Multiple Polygon Area (MPA) approach.

8.4.1 MPA Introduction

For a case when traversing between buildings with different building heading information, the CHAIN algorithm is extended further to include a construction of Multiple Polygon Areas (MPA). As explained previously, CHAIN algorithm uses heading information of a building in the KF to estimate the INS heading error, thus reducing the effect of heading drift for a low-cost PNS in indoor building. In this section, the heading information is extended to include multiple headings information from multiple buildings that make up the Multiple Polygon Areas (MPA).

8.4.2 MPA Creation

The new multiple headings information is generated using a predefined 'polygon area' that was created to contain heading information, and as the user walks, the system is updated with the new heading information. A simple and well known

algorithm in computer graphics is adopted where a point is tested to be located inside or outside a certain 2D polygon area (written as 'polygon' afterwards). A polygon is generally defined as a set of a finite sequence of straight lines or straight edges that make up a closed path, whilst the points where two edges or lines meet are called polygon's vertices. The test algorithm is widely known as point in polygon test (Taylor, 1994) and is summarized in Appendix E.

After the algorithm has been set up, a set of geodetic points are constructed so that it makes up a polygon area of the trial buildings. Multiple polygon areas are created where each polygon area covers specific trial building and contains heading information for that building. Using a freely available tool in Google Earth, the polygon area is manually constructed for the trial area and it contains four polygon areas that have four different headings. These building headings were derived using a method from Appendix D and stored within the polygon area.

The algorithm works by testing the test points against the constructed polygon area. The test points are represented by each estimated coordinates (latitude and longitude), calculated from the INS mechanization. As the user walks, the current estimated coordinate will be compared to the polygon area coordinates. If the estimated coordinate lies in any of the polygon areas, then that polygon area is chosen. This selected polygon area, which contains specific building heading information for that area, will then be used as the current building heading for INS, and a similar step as in the previous sections will be performed to update the KF.

Fig. 8.23 shows four polygon areas constructed for the trial and are marked as areas A, B, C and D. Area A is represented by a cyan line, B by a blue line, C by a green line and D by a white line. It covers a total area of approximately 2.5 km^2, with multiple buildings that have a common heading (for example polygon C) are put together into one polygon area.

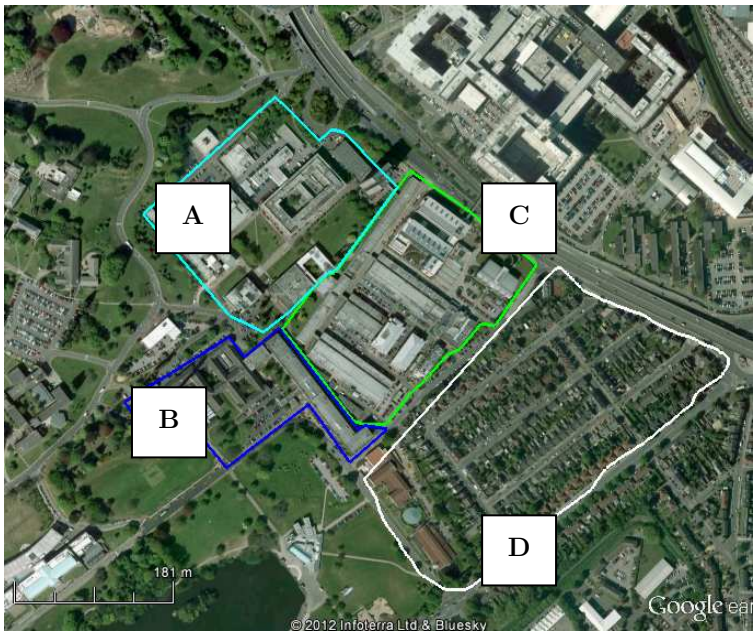

Fig. 8.23: Four constructed polygon areas for the trial.

8.4.3 Trials and Results

The first trial involves walking in the same public hospital (QMC Hospital), as in Section 8.2, which represents a typical public building. The walk started and ended at approximately the same position, lasted for about 30 minutes for a total distance of about 2000 *m*. As there was no ground truth that can be used as a reference, the start and end positions are used as a reference to check the position error. Similar to a previous section, an ideal system would result in a Return Position Error (RPE) value of 0 *m*. Fig. 8.24 shows the trajectory solution of the low-cost PNS without MPA (only with CHAIN and ZIHR) and is depicted by a green line. The blue line represents the INS–ZUPT only solution, while the red dots represent the High Sensitivity GPS (HSGPS) solution.

The RPE was measured by calculating the difference between the start and end positions. For INS–ZUPT only approach (blue line), without using any MPA method the RPE was 299.71 *m*, which is about 15% from the total distance travelled. Conversely, the RPE for the low-cost PNS (green line) was found to be

4.63 *m*, which is about only 0.23% from the total distance travelled. This contributes more than fiftyfold in position improvement. Although there are some parts where the GPS signal can be detected, the reliability of HSGPS solution (red dots) is questionable because of jumps in the solution. Further work should investigate the possibility of using this occasional GPS position update in the KF (but only if it can be shown to be accurate and reliable). Since this trial did not use the MPA approach, the solution at the bridge area (zoomed figure) gives suboptimal result because of the different orientation of the bridge from the main building. Therefore, a second trial is conducted next to highlight the advantage of having an MPA approach.

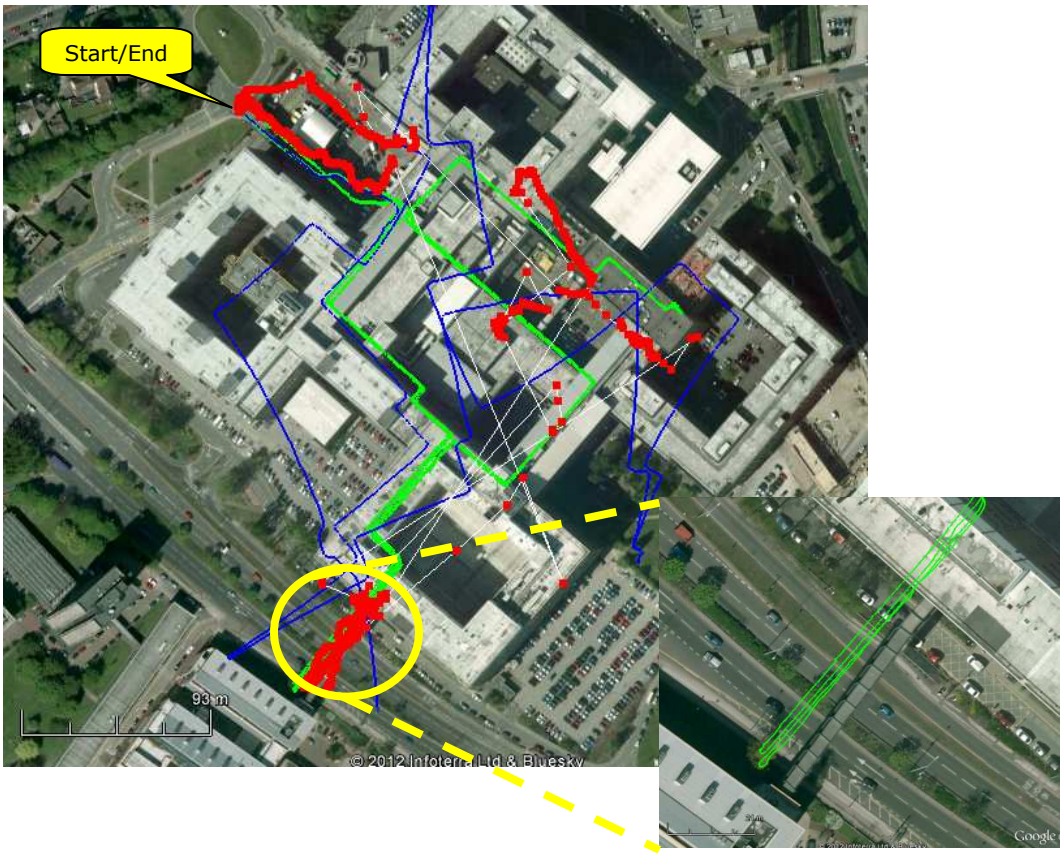

Fig. 8.24: The position solutions of HSGPS (red), low-cost PNS + ZUPT (blue), low-cost PNS + ZUPT + CHAIN (green)

The second trial involves walking in multiple polygon areas created as in Fig. 8.23. The trial lasted for about 43 minutes with a distance of about 3300 m. The area covered is estimated to be about 2.5 km^2. As before, a pedestrian equipped with only the low-cost PNS, started the walk in area C. The walk then moved to area A, after which he walked towards area B, followed by area D and then came back to the start position in area C.

Fig. 8.25 shows the trajectory solution of the low-cost PNS aided by only ZUPTs without MPA and is depicted by a red line, while Fig. 8.26 shows the trajectory with MPA depicted by a green line. Remarkably, the low-cost PNS trajectory in Fig. 8.26 is able to follow the trial path (the trial path was obtained from the knowledge of the trajectory during the trial) right until the end of the trial, as opposed to normal INS–ZUPT approach in Fig. 8.25 (the accuracy throughout the trial is not known as only occasional GPS solutions were available). For this trial, the RPE for the proposed system shown in Fig. 8.26 was 4.28 m, about 0.13% from the total distance travelled. This outperforms the INS–ZUPT-only solution by more than one hundred fold, where the INS–ZUPT solution has a large RPE of 561.35 m.

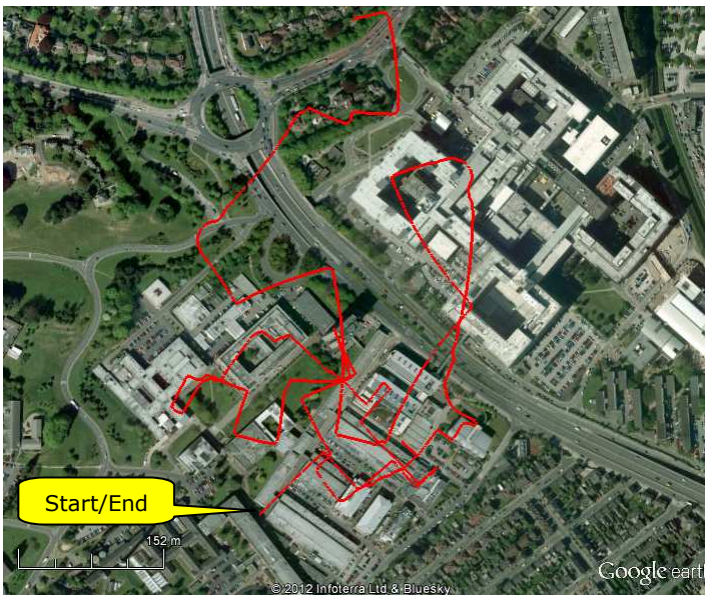

Fig. 8.25: Low-cost PNS/ZUPT solution without MPA trajectory solution

Fig. 8.26: Low-cost PNS/ZUPT with MPA trajectory solution

8.4.4 Discussion

1. This section highlights the case where a user might need to traverse between buildings that have different orientation. The previous CHAIN algorithm has been extended to address such case. An approach of using the Multiple Polygon Area (MPA) was explored and two trials were undertaken to demonstrate its advantage. It resulted in a significant improvement in position accuracy for the low-cost PNS. It has been shown that using only forward KF, the estimated accuracy in position is 4.28 m in 43-minutes walk, about 0.13% of the total distance travelled (total distance travelled was computed from the IMU data). Note that this figure represents the RPE (difference between start and end position), and not the accuracy of the system throughout the trial. However, it did follow the correct trajectory throughout the whole trial.

2. The MPA were created to show the possibility of gathering the heading data for a huge navigation area with different building orientations. This can be very useful for a pedestrian who wants to traverse between these buildings. While the basic CHAIN algorithm requires that each building heading is to be

derived, this section introduced a way to reduce the complexity of having multiple heading data for each building. This is done by working out the same heading area using a polygon that consists of several buildings with the same heading. This does not mean that buildings need to be exactly identical to each other, but more towards having the same orientation to have the same heading value.

3. Although the motivation was to have a self-contained low-cost PNS, it is important to highlight the advantage of having extra measurements to the overall solution accuracy. Due to the assumption of a straight walk for most of the time, there will be a time where this assumption might not valid; for example during long cornering (although the algorithm was shown to work fairly well in a short cornering in Section 8.2.4.5). The uncompensated heading error will build up because of the increase in uncertainty in the KF and will cause a position drift error during this period. Therefore, an occasional absolute position update might be useful for the system to correct its position drift (note that using the KF provides the capability to combine every available measurement).

   This could be done if, for example, one could figure out a reliable position from the degraded GPS signal, or simply by walking into an open space in between buildings, where the GPS can provide a reliable and accurate position solution. Another possible example would be to have a little more information from the map (again not a detailed map) such as having true positions (coordinates) of entrances and exits of a building. This could correct some of the position drifts if a user can be identified to have indeed walked through these entrances or exits.

4. Further work should highlight a point where more accurate boundary detection should be done for polygon area creation when buildings with different heading are not well separated from each other. The results presented herein are only the output of coarse creation of the polygon area. If a more

accurate position solution is sought in an environment where buildings are closely separated, then a better detection and polygon creation should be applied to have the correct heading update.

For example, let's consider an extreme scenario as depicted in Fig. 8.27. Suppose a low-cost PNS has a system accuracy of 5 m, and two buildings with different headings are separated with less than 5 m from each other. Due to the inaccuracy in the low-cost PNS, the position has drifted into the green building (a black arrow). This creates problem because when CHAIN and MPA are applied, wrong position solution will be computed (red arrow).

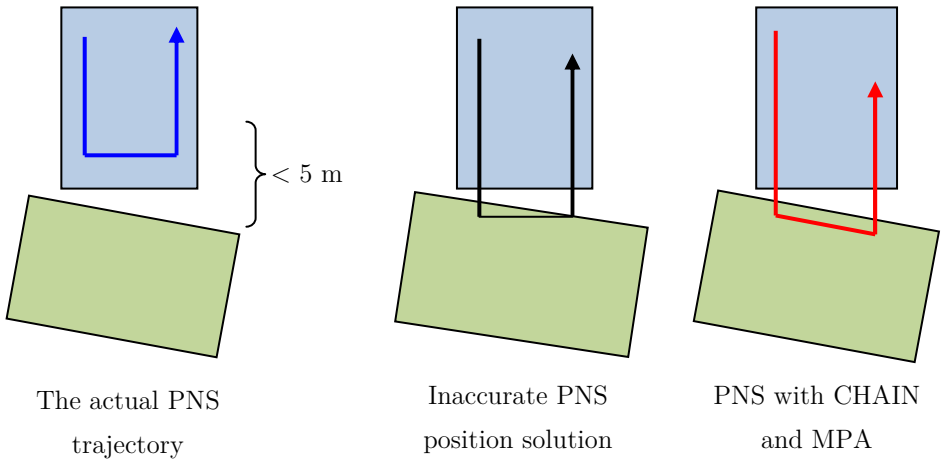

Fig. 8.27: Extreme scenario when MPA causes problem to the overall PNS solution

8.5 CHAIN with Heuristic Height

The following section describes the constraint used heuristically to reduce huge height error for the low-cost PNS.

8.5.1 Heuristic Height Introduction

According to, for example Tanigawa et al. (2008) and as demonstrated in Section 8.2, there is still an inherent vertical drift error for the low-cost PNS solution. This can be due to the remaining small error perturbing the IMU Down-axis, which causes biased measurements on the axis. This translated to an error in the velocity measurement, and subsequently causes an error in the height computation. Furthermore, an inaccurate gravity compensation model used in INS mechanization algorithm can exaggerate the effect, although the effect of gravity variation can be neglected because of the low-cost IMU used and a relatively small area of indoor navigation.

Due to this, the IMU height error is often aided with barometer (pressure sensor), such as in Lammel et al. (2009), Weimann and Hofmann-Wellenhof (2007) and Tanigawa et al. (2008). The change in pressure, which varies according to height, can then be matched with a floor level database to indicate the correct level the user is in. When barometer is supplied with an indication of altitude, it is known as altimeter, such as the one used in for example aircraft. However, barometer measures pressure, which sometimes varies due to other factors as well such as wind, temperature and weather. For instance, Lachapelle et al. (2003) showed there was a different in pressure measurement measured in staircases area, with the one measured in other area at the same level (for his trial area). This translated to a different height for the two areas on the same level, which is wrong.

In the low-cost PNS, therefore, a different approach is taken so as not to use an additional sensor, such as barometer, to give height measurements. An assumption is therefore made that the height change in indoor buildings is only caused by the use of staircases. Therefore a Heuristic Height (HH) method is used

to stop this error from building up to give a good *pseudo-height* solution when the pedestrian is inside the building. The term *pseudo-height* is used to differentiate it from the true geodetic height, where *pseudo* term often means something that is having the appearance of the truth.

8.5.2 Heuristic Height Measurement

A height measurement is therefore introduced for the low-cost PNS to restrict the IMU height drift indoors. Without the availability of height measurements from sensors such as barometer and GPS, the height of the INS solution will drift as a result from the accumulation of errors in the IMU that are not fully removed through ZUPT measurements. Therefore, the knowledge that the floor is level in most indoor buildings is used. It is assumed that the changes in height in indoors would be caused only by walking up or down the staircases.

Since it is reasonable to assume that a pedestrian's foot lies on the floor during every stance phase, a predetermined height threshold that represents step height is created to limit the height error growth (which is updated in every stance phase). The change in height over one step is calculated and if it is below the threshold, the height from a previous epoch calculation is maintained and projected to the next epoch. The changes in height, Δh, between ZUPT epoch is computed as:

$$\Delta h = |h_k - h_{k-1}| \tag{8.8}$$

where epochs k and $k-1$ correspond to different steps at successive ZUPT epochs. For the trial presented in this section, an empirical threshold of 0.05 m was used to decide whether height change has happened. This was based on the height of the steps. If Δh falls below the threshold, then height at the last epoch is preserved to update the position state vector in the KF, otherwise no update is applied.

Using the measurement in this way unfortunately results in an over optimistic covariance of the height resulting from the issues discussed in regard to heading measurements in Section 8.3. Although not strictly rigorous, the benefits of applying the height correction indoors are thought to outweigh any issues caused

by an overoptimistic height covariance estimate. A measurement update is applied by forming the observation using Eq. (5.14), based on Eq. (2.34):

$$\delta h = \begin{pmatrix} 0 & 0 & -1 \end{pmatrix} \delta r^n + n_k \tag{8.9}$$

where δr^n is the IMU position error state vector with measurement noise n_k that is closely related to the threshold value used to determine height change.

8.5.3 Trial and Results

A trial for the Heuristic Height (HH) is carried out by walking down and up a staircase. A pedestrian walked from the top to the bottom of the stairs, then walked up again and stopped at the same starting position. The staircase consists of 42 steps with 16.5 $\pm$ 0.5 *cm* each in height (measured using steel tape and assumed to be the truth), totalling 6.93 *m* in height. Fig. 8.28 shows the low-cost PNS height, with (blue) and without height constraint (red) and Fig. 8.29 shows the period when the height constraint was performed (green dots).

From Fig. 8.28, when the HH is used, the end position error for this trial is 6.6 *cm*, and it correctly identified 42 steps. In contrast, without the HH, the end position error has drifted to 45 *cm*. The start of the data in Fig. 8.28 is further magnified and shown in Fig. 8.29. It clearly shows that when the height constraint is performed (green dots), the height error does not grow as opposed to when height constraint is not used (red plot). It is important to highlight that for height constraint to hold true, changes in height in indoor buildings are assumed to be caused by staircases only. Therefore, the height constraint will not work as expected if other situations are considered, where the height change between epochs might not be big such as when walking on a ramp on the floor.

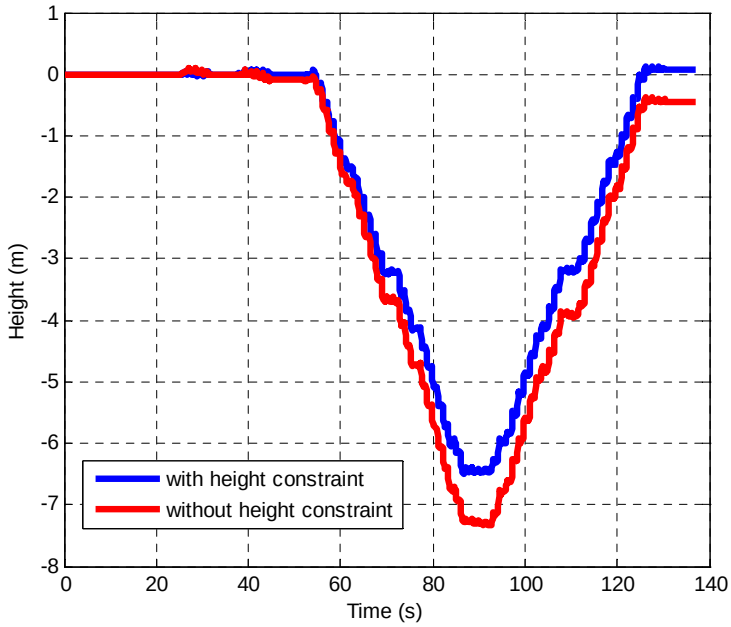

Fig. 8.28: IMU height output with and without Heuristic Height

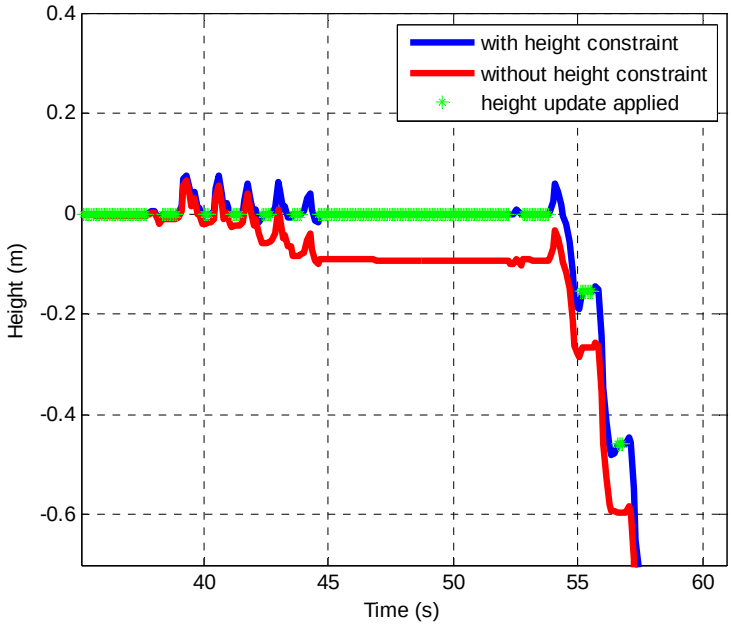

Fig. 8.29: Height constraint is being updated

8.6 Position Comparison between CHAIN and Magnetometer-Aided PNS

To show the significant improvement made by the full CHAIN algorithm over an example of the magnetometer-aided PNS (using the best case with frequent heading updates), the same trial result from Section 6.4.2.1 is compared with when full CHAIN algorithm was implemented. Figure 8.30 shows comparison of the Horizontal Position Error (HPE) between the two cases. It is identified that the maximum HPE for magnetometer-aided is about 14.0 m, whilst reduced significantly for CHAIN-aided to about 5.0 m.

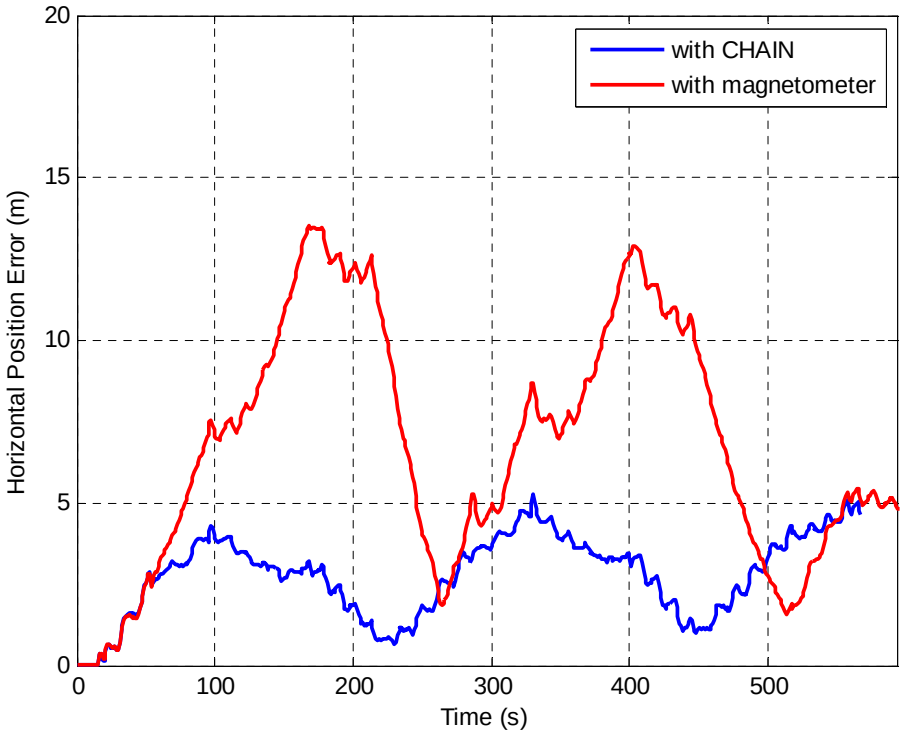

Fig. 8.30: Comparison of position error for CHAIN-aided and magnetometer-aided for the low-cost PNS

8.7 Full Trials Repeatability

Using the full CHAIN algorithm described before (Section 8.2 till Section 8.5), 8 more field trials have been conducted in Nottingham, UK for repeatability purpose. Table 8.1 summarises the output of the walks. Trial 1 until 8 represents: straight road, car park, football pitch, hospital #1, hospital #2, hospital #3, hospital #4, and the Jubilee Campus. The Return Height Error (RHE) represents the difference in height between the start and end positions, while Return Position Error (RPE) represents the difference in position, after returning to the same location. The RPE is tabulated in m and percentage of the total distance, where lower values of these represent a better solution than the one with higher values. The 'CHAIN' column consists of the results when CHAIN and all the sub-algorithms were used, while the 'normal' column represents the results when only ZUPT was used to update the KF.

The results are summarized in Table 8.1. All the trials lasted for a period of at least 10 minutes, with a minimum and maximum distance of about 500 m and 3000 m respectively. From these 8 field trials, it was identified that for an average duration of 23.8 minutes and an average total distance travelled of 1552 m, the average RHE is 0.4 m and the average RPE is 4.7 m. In contrast, the trials that did not implement the CHAIN algorithm have higher average error in the RHE and the RPE of 40.4 m and 153.6 m respectively.

In terms of the RPE and the RHE, using CHAIN has therefore improved the figures on average by over 95% against the normal solutions. Fig. 8.31 shows the visualisation of the three example outputs from the trials tabulated in Table 8.1, where heading drift errors have been reduced significantly. In the figure, the green line shows the position output when CHAIN was used and the red line marks the position output when CHAIN was not used.

Table 8.1: Comparison of errors for proposed system with and without constraints applied

Trial	Dur. (min)	Total dist. (m)	RHE (m)		RPE (m)		RPE of Total Distance (%)	
			CHAIN	Normal	CHAIN	Normal	CHAIN	Normal
1	15.7	496.8	~0.00	5.6	6.3	270.4	1.3	54.4
2	12.7	902.8	~0.00	0.3	4.0	28.6	0.4	3.2
3	40.0	2963.8	~0.00	25.3	4.6	34.5	0.2	1.2
4	30.4	1973.7	1.0	16.2	4.2	109.6	0.2	5.6
5	21.9	1443.9	0.2	0.8	7.6	518.2	0.5	35.9
6	38.8	2665.3	~0.00	26.3	3.1	204.2	0.1	7.7
7	16.0	918.8	0.2	85.1	6.2	38.7	0.7	4.2
8	14.8	1058.4	0.2	117.4	1.2	24.5	0.1	2.3
MEAN	23.8	1552.9	0.4	40.4	4.7	153.6	0.3	9.9

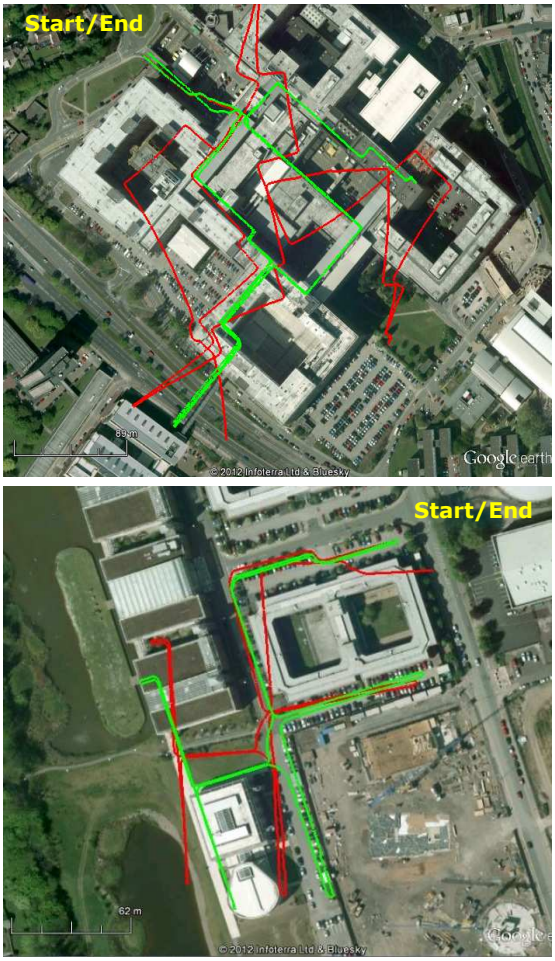

Fig. 8.31: (clockwise from bottom left): Example of position output from trial 8, trial 4 and trial 2 tabulated in Table 1.

8.7 Summary

A new algorithm termed the CHAIN algorithm has been proposed for the low-cost PNS. The algorithm was investigated using real field trials and has shown its capability in mitigating heading drift error significantly. This resulted in a more accurate trajectory for the low-cost PNS. CHAIN has been further developed by including the Zero Integrated Heading Rate (ZIHR) algorithm, which is important to stop the heading drift error when a pedestrian stops walking. Next, the Multiple Polygon Area (MPA) and the Heuristic Height (HH) approaches were also integrated to accommodate navigation in a larger area and to reduce vertical positioning error respectively.

The results have shown notable improvement for indoor pedestrian navigation. For example, previously, a positioning system integrating WiFi, Bluetooth, High-Sensitivity GPS, accelerometer, digital compass and camera by Kuusniemi et al. (2011) achieved maximum Horizontal Position Error (HPE) of about 15 m within 4 minutes of operation. With the developed algorithm presented in this chapter, only a low-cost IMU is needed for a pedestrian to navigate for as long as 40 minutes, with the average position errors being consistently kept below 5 m. The Return Position Error (RPE) was also found to be better than 5 m for most of the trials, with the best recorded to be below 2 m. Pseudo-height error was also kept below 1 m for all of the trials.

.

Chapter 9

Summary and Conclusions

This chapter summarizes the research presented in the thesis and provides conclusions about the results that have been obtained, and what could be done in the future. This leads to a recommendation for a future research in the area of non-GPS integrated indoor pedestrian navigation systems, along with a summary of the contributions to the knowledge achieved from the research.

9.1 Summary

The main aim of the research presented in the thesis was to mitigate the heading drift problem for an autonomous Pedestrian Navigation System (PNS) that uses only a low-cost IMU, aided with only ZUPTs. Heading drift for such a low-cost system has long been regarded as one of the major stumbling blocks for the system to be generally adopted. Improving the heading drift thus creates an opportunity for far more applications for the low-cost IMUs than there are today.

In order to understand this properly, an early investigation must first be conducted. This was presented in Chapter 4 by examining the performance of a low-cost PNS entirely on its own without any heading aiding, which confirmed the severity of the growth of heading error. A literature survey on the other approaches to mitigate the heading drift problem was also briefly reviewed.

The first objective of the research was to assess the performance of the commonly used method in a low-cost PNS to mitigate heading drift error. This was presented in Chapter 6 using an exemplary method of filtering out bad magnetometer heading measurements. A magnetometer was used because its heading measurements do not drift over time, as opposed to the low-cost IMU. Accepted heading measurements were then used to provide reliable absolute heading measurements to the low-cost PNS. It was found that frequent reliable magnetometer heading updates were still required, which is not always the case indoors because of high magnetic disturbances.

The second objective of the research was to propose rotating the IMU mechanically as an alternative to the magnetometer to mitigate the heading drift error. Therefore, the proposal of rotating the low-cost IMU around its y-axis was presented in Chapter 7, and was termed as the Rotating IMU (RIMU) in the thesis. This was initially intended to eliminate the dependence of the low-cost PNS on the additional sensors, such as a magnetometer, to mitigate the heading drift error. The RIMU approach was later become more significant as the research progressed. This is because relying on additional sensors such as the magnetometer to be the

additional heading sensor to mitigate heading drift may not be advantageous. For example, frequent and reliable magnetometer heading measurements may not always possible indoors because of magnetic disturbances.

The third objective of the research was to test the RIMU approach through simulation and real field trials. This was presented in Chapter 7 in the trial sections. Two pedestrian scenarios; in a stationary condition and a walking condition, were simulated using an in-house simulator. The simulated data was then processed using the in-house processing software. The performance was evaluated in terms of the observability of IMU errors and how by improving the IMU error observability can help to mitigate the heading drift of the low-cost PNS. Three field trials were also presented to verify the improvement made by the RIMU proposal. The RIMU was shown to mitigate the heading drift by improving the observability of IMU errors. The RIMU, however, is still largely limited by the need to have a physical rotation of the IMU.

Following this, the fourth and the fifth objectives were set in the research. The fourth objective was to develop a new approach which did not use mechanical moving parts. Subsequently, the fifth objective was to assess the approach using field trials. Therefore, a new method that is much simpler and inexpensive was presented next in Chapter 8. This is so to eliminate the dependence on the extra components required when implementing the RIMU. The method, for the first time, successfully mitigates the heading drift after a long period of autonomous inertial navigation, whilst simultaneously keeping the cost down. This is a result of the simplistic nature of the algorithm used by the method, which means the method may be affordable for real-time purposes and for integration with other similar system. The algorithm was devised to use true building heading information in the Kalman Filter (KF) framework, and was termed as Cardinal Heading AIded Navigation (CHAIN). Several sub-algorithms were also added to account for different possible pedestrian scenarios, which were not given much weight by other related works. To present CHAIN applicability to indoor pedestrian navigation, the full algorithm was tested in several field trials, including inside real buildings. The

performance of the low-cost PNS deployed with the algorithm was presented in terms of the accuracy of heading for the entire trajectory and also the accuracy of the position solution. Chapter 9 then summed up the research presented in the thesis.

The following Section 9.2 contains conclusions drawn from the testing results and is followed by contributions made from the research in Section 9.3. Recommendations for further research are discussed in Section 9.4 and the chapter ends with a summary in Section 9.5.

9.2 Conclusions

This section summarises the results and conclusions from the research presented in the thesis. It will be divided into two sections, which represent the results achieved using data simulation and the results achieved using practical trials.

9.2.1 Data Simulation Results

The RIMU trial using simulated data from NGI's Inertial Data Simulator (IDS) was conducted as part of the research presented in this thesis. It acted as the 'acceptance trial' before the RIMU prototype was built by the GRCNZ for practical trials. The conclusion drawn from the simulated RIMU trials are summarised below.

1. IMU errors are made to be more observable when the RIMU is deployed during stationary condition. In this situation, the coordinate transformation matrix changes due to the RIMU. With the availability of the ZUPT measurements, the RIMU method helped to estimate all accelerometer biases and most of the gyro biases (Section 7.2.2). In the stationary test (Section 7.3.1.4), it was demonstrated that a stationary RIMU aided with ZUPT improved the IMU errors observability. Out of 6 biases for gyros and

accelerometers to be estimated, 5 have been estimated, except the gyro bias on the rotating axis (IMU y-axis) because of the observability problem (Section 7.2.2). In contrast, when the RIMU was not used, the stationary system aided by ZUPT managed to estimate only 2 gyro biases on the x- and y-axis, whilst the remaining 4 biases (z-axis gyro bias and three accelerometer biases) were not observable.

2. In the simulated walking trial, the heading drift for the low-cost PNS appeared to be mitigated (Section 7.3.2.4) due to the RIMU. Because the IMU error observability is improved, the correlated heading drift is also mitigated and resulted in a more accurate position solution (Section 7.3.2.6).

3. The convergence rate to observe the IMU errors can be affected by the rotation rate used for the RIMU. A quicker rotation rate (Section 7.3.1.2) was shown to increase the convergence rate of the error estimation. This is because a quicker rotation rate resulted in a quicker flipping of the rotating axes. This means the KF should have enough information from the ZUPT measurements and the RIMU in a short period of time to estimate the IMU error. Unfortunately, a rotation rate of more than 6 $^{0}/s$ could not be simulated in IDS due to an unknown bug (Section 7.3.1.2). It is, however, not an important issue as the objective of the simulation trial was to gain knowledge on the advantage of the RIMU to mitigate heading drift, and not to quantify the convergence rate for error estimation.

4. The convergence rate can also be affected by the way the rotation is performed. In Section 7.3.1.3, five different ways of doing the rotation with the same rotation rate were examined. All five of them converged to the reference value but with different rate of convergence. It was observed that as long as the rotation caused the axis to be flipping (for example Eq. (7.1) resulted in +ve and –ve values in gyro errors), the convergence rate would be similar.

Otherwise it will take a longer time to converge, as demonstrated by the 90^0 and 45^0 rotations, where the axes were not fully flipped.

9.2.2 Practical Trials Results

Practical trials were presented in this thesis for three principal reasons. Firstly, in the case of the magnetometer aided trial presented in Chapter 6, it was performed to analyze the magnetometer performance in very high magnetic disturbances such as indoors. Secondly, the RIMU trials in Chapter 7 were presented to verify the performance of its simulation, in particular for more realistic walking scenarios. Finally, the trials in Chapter 8 were presented to validate the CHAIN algorithm formulated in the chapter to mitigate the heading drift.

9.2.2.1 Magnetometer Aided Trials

1. Reliable magnetometer heading measurements could be beneficial to aid heading error estimation for a low-cost PNS. In an outdoor trial (Section 6.4.2.1.), it was identified that fewer magnetic disturbances could be expected. As a result, frequent reliable magnetometer heading measurements were easily extracted, and were shown to reduce the heading drift of the low-cost PNS.

2. However, infrequent but reliable magnetometer heading measurements offer little help to mitigate heading drift of a low-cost PNS. Indoors, high magnetic disturbances could be expected (Section 6.4.2.2) that could corrupt magnetometer headings. An indoor trial (manipulated from the outdoor trial data) was presented in Section 6.4.2.2 and resulted in only a few reliable magnetometer heading measurements. The interval between magnetometer heading updates for the KF were thus increased from about 1-2 s to about 20 s. This increased the heading uncertainty between these updates, which caused an increase in the position error. Subsequently, this resulted in an

unrecoverable position drift, even when aided with reliable magnetometer heading measurements afterwards.

9.2.2.2 Rotating IMU Trials

1. The RIMU has made all gyro biases for a low-cost PNS to be more observable when used with ZUPTs, which agreed with its simulated trial (Section 7.4.3). Of particular interest was z-axis gyro bias, which converged to its reference value due to the RIMU, against the non-RIMU (normal IMU) where the z-axis gyro bias did not converge even until the end of the walking trial.

2. The RIMU was not instrumental in estimating accelerometer biases for the low-cost PNS (Section 7.4.4). Without implementing the RIMU, the accelerometer biases still converged to its reference values. The availability of velocity updates through ZUPTs during detected stance phases and forces due to the acceleration when taking a step, were sufficient to update the error estimation in the KF.

3. When implementing the RIMU, the heading drift of the low-cost PNS was mitigated significantly. In terms of the final position accuracy, the RIMU has outperformed the non-RIMU, as presented in Section 7.4.5 and 7.4.6. For the three trials presented, on average the RPE for the RIMU was better than the non-RIMU (below 1 m) whilst for the non-RIMU, the RPE was more than 7 m. Furthermore, the maximum RIMU Horizontal Position Error (HPE), on average, was found to be only 1.9 m whilst for the non-RIMU, the maximum HPE was 13.2 m. This reduces the maximum HPE significantly, in fact by more than 85%. Likewise, in the RIMU trial 1 for example, when the RIMU was implemented the mean for HPE was only 0.42 m, whilst without the RIMU, the mean for HPE increased to 4.6 m.

9.2.2.3 Building-Heading Aided Trials

1. The Cardinal Heading AIded Navigation (CHAIN) algorithm also mitigates significantly heading drift. Using this algorithm, only a low-cost IMU is needed, and there is no requirement to integrate with external sensors. It also does not require the physical rotation of the low-cost IMU as demonstrated by the RIMU approach. A longer period of accurate autonomous navigation using low-cost inertial sensor is therefore possible indoors, with below 7.5 *m/hr* position drift rate. Its effectiveness was presented in Section 8.2.4 and 8.6 using a series of field trials. For example, in the second trial (Section 8.2.4.2), the Return Position Error (RPE) was only 4.6 *m* and the mean of Horizontal Position Error (HPE) was only 3.68 *m* for a period of 40 minutes. In contrast, when the CHAIN was not implemented, the RPE was increased to 29.32 *m* and the mean of HPE to 44.16 *m*. The maximum HPE was 106.8 *m* when the CHAIN was not implemented, but reduced drastically to only 6.497 *m* when the CHAIN was used. This therefore represents a significant improvement by reducing more than 94% of the maximum HPE value (better than the RIMU at 85%).

2. The Zero Integrated Heading Rate (ZIHR) algorithm is deemed to be important and thus, recommended to be used with the CHAIN algorithm. The ZIHR trial was presented in Section 8.3.4 to demonstrate its usefulness when stationary. When the ZIHR was implemented, it maintained precise heading with a standard deviation of below 0.05^0. Conversely, when the ZIHR was not implemented, after 200 *s*, a heading error of 30^0 was observed, which then grew to about 100^0 after 900 *s*.

3. Traversing between buildings with different building headings was made possible with the Multi Polygon Area (MPA) method. Its trial was presented in Section 8.4.3. For this trial, the RPE was 4.28 *m*, only about 0.13% from the total distance travelled after 43 minutes of navigation. This betters the

INS/ZUPT-only solution by more than 500 fold, where the INS/ZUPT solution had a large RPE of 561.35 m.

4. In situations where a 3-dimensional pedestrian navigation is required for a longer period of navigation, Heuristic Height (HH) method (Section 8.5) is capable of reducing the height error. A trial was presented in Section 8.5.3, where it showed that when HH was used, the end position error was only 6.6 cm after about 2 minutes, and it correctly identified 42 steps. In contrast, without HH, the end position error has drifted to 45 cm. Although it seems that the error is small and thus tolerable, the effect was quite pronounced when a longer period of navigation was performed (Section 8.2.4.2).

9.3 Thesis Contributions

The different topics investigated in the research are detailed throughout the thesis. Some of these points have been published in journals and conference proceedings, and have resulted in a patent application. The published papers are mentioned specifically in the respective chapters where necessary – see the List of Publications (page ix) for details. The summary of contributions below is sorted according to its significance, such that the main contribution appears first, followed by the consecutive contributions.

1. **Cardinal Heading Aided Inertial Navigation (CHAIN) algorithm.** The new algorithm has been successfully designed and implemented for a low-cost PNS. This has made autonomous inertial pedestrian navigation in indoor environment possible for an extended period of time. Field trial results have shown that it is possible to navigate within buildings for as long as 40 minutes with below 5.0 m of start-end position error. On average, this is more than an 85% improvement in position error if one were to use standard INS/ZUPT indoor positioning. *This has become the subject of a patent application.*

2. **Zero Integrated Heading Rate (ZIHR).** Following 1, the CHAIN algorithm has been extended to include the ZIHR algorithm. This is a very important approach for an extended period of non-walking (remaining stationary) for pedestrians. To the author's knowledge, it has never been applied in a pedestrian navigation system before. It correctly modelled the covariance information of heading error in the Kalman Filter whilst simultaneously halting the heading error growth. This introduces more stability to the low-cost PNS solutions, resulting in a more reliable system. Its significance is based upon several field trial results, leading to a recommendation for all pedestrian navigation systems to incorporate the ZIHR algorithm.

3. **Multiple Polygon Areas (MPA).** Following 1 and 2, the CHAIN algorithm has been further extended by proposing the integration of an MPA approach, for the purpose of navigating in a larger navigation area. Only a single value of heading information is needed for each area that is identified by a polygon. Thus a cluster of polygons, with heading information embedded in them, make up the MPA. As such, very little information and computing power are needed, which could be useful for real-time systems. This effort has therefore made it possible for a pedestrian to navigate in a larger area that would involve walking across multiple buildings and areas.

4. **Heuristic Height (HH) constraint.** Inside buildings, a heuristic assumption was made to enable the height constraint to be integrated with the CHAIN algorithm to reduce the height error. The height change was heuristically assumed to be caused only by the use of staircases. Therefore, in situations where 3-dimensional pedestrian navigation is required, then the constraint is capable of reducing the height error growth without the use of external sensors such as a barometer.

5. **A single axis Rotated-IMU (RIMU).** An approach to pedestrian navigation, whereby the IMU is rotated mechanically on a single axis (around its y-axis), has been proposed and investigated. The investigation was made through a simulation trial and real field trials. The IMU heading error was made observable through the RIMU and, by also improving the observability of other errors of the IMU, was shown to be capable of reducing position drift for a low-cost PNS. The method is also envisaged to have a significant impact in an extreme scenario, for example during rescuing operation carried out by fire fighters, where the extreme temperature would have caused large variations in IMU errors. This is because RIMU should then be able to 'track' these errors efficiently.

6. **Magnetometer analysis.** The performance of magnetometer measurements used to aid INS heading by providing reliable absolute heading measurements was investigated. Most current literature highlights the advantage of filtering out outliers in magnetometer measurements to get good heading measurements. It does not, however, properly address the impact of long intervals between heading updates, which often happens indoors. Because of this, it was found that in a magnetically-disturbed environment, such as indoors, infrequent magnetometer heading measurements in an estimation filter were not adequate to reduce the heading drift error for low-cost PNS.

9.4 Future Recommendation

The research presented in the thesis has proven the ability of a low-cost IMU to be used alone, for an extended period of up to 40 minutes of unaided pedestrian navigation in an indoor environment with sufficient accuracy, which had previously

been very difficult to achieve before. The following recommendations are made here to continue the research and perhaps make further advancements in the field.

Rotating IMU

1. The results presented in the thesis, examining the RIMU approach for the low-cost PNS, are promising. Further investigations are however required to identify and quantify the impact of different unmodelled system errors such as axis-misalignment and scale factor. Although it is unlikely to improve the position accuracy (as presented in the thesis where even without modelling the errors, position was significantly reduced), it is thought to be useful in understanding the overall benefits of the RIMU.

2. More trials are worth performing to assess the RIMU's true capability, once a better prototype can be made available. For now, the RIMU prototype is impractical for mass trial because of its weight and size. Once all the components such as the motor and the platform can be miniaturized, it will then be more practical to mount them on foot/shoe. For example, deploying several fire-fighters in a real life fire-fighting exercise might be useful to assess the RIMU performance in an extreme temperature condition that might alter the IMU errors unpredictably. This is thought to be useful because the RIMU is supposed to be able to estimate better the error terms as it was shown to increase IMU errors observability.

3. The RIMU approach, and its associated trials presented in Chapter 7, assumed a known initial position and attitude. In reality, however, accurate initialization of heading is difficult. As discussed in Section 7.3.2.5, if the IMU is rotated continuously from the beginning, a correct initialization of heading must be acquired before the user starts to walk. Likewise, the initialization of heading is still required even if the IMU is not rotated from the beginning.

Therefore, further research may be explored to address the heading initialization problem appropriately.

Building Heading Aided

1. Further testing of the CHAIN algorithm in a more challenging environment might need to be performed. Although the results presented in Chapter 8 are very promising, there are still some possible issues which were discussed in Section 8.2.5, 8.3.5 and 8.4.4. These issues thus need to be addressed properly, in terms of having real practical trials to properly quantify the position errors expected when CHAIN operates in such environments. While this research shows that the low-cost PNS with CHAIN is able to navigate in an extended period of navigation of up to 40 minutes inside a building with such an environment, it is necessary to know for how long the low-cost PNS can still produce a useful position solution.

2. For integrity purpose, it might be possible to integrate a magnetometer, which is already built in most of the low-cost IMUs in the market, with CHAIN algorithm. Provided that the issue of magnetic disturbances can be addressed properly, having magnetometer heading may increase the robustness of CHAIN algorithm. For example, currently, the decision making in the algorithm to change its cardinal heading depends entirely on the IMU data. If the magnetometer is integrated together, potentially, its heading may be used to confirm the decision making process. Furthermore, magnetometer measurement can also be used to initialize IMU heading because currently, IMU heading is initialized manually.

3. A MEMS barometer may be also coupled together (again for integrity purpose) with the low-cost IMU to provide height measurement. This could increase the confidence level for the Heuristic Height (HH) algorithm in CHAIN. It might

not necessarily be using the actual height measurement from a barometer, but rather using it to verify the HH algorithm during processing.

4. The algorithm might be further extended using heading information extracted from environmental information or features. These features may comprise elements such as roads, external walls, pedestrian pathways and fences. This is because it is likely that a pedestrian will navigate along these features. This information may be extracted easily and automatically, for example using an existing digital map that incorporates all these elements, as shown in Appendix D.

5. As with the RIMU in the previous section (point 3), the CHAIN algorithm in Chapter 8 and its associated trials assume a known initial position and attitude information. Further research may therefore be explored to investigate the effect of having proper initialization from other available sensors, such as GPS, to the overall position accuracy. For example, recently Pinchin (2011) has initiated the work by comparing the use of HSGPS and NRTK GPS for system initialization.

6. Finally, the research presented throughout the thesis has used only a low-cost IMU from MicroStrain. It is, therefore, interesting to see the comparison of navigation performance when different low-cost IMUs from different manufacturers are used. Furthermore, the system noise statistics for the IMU were chosen empirically during the research. Although some tools can be used to approximate these statistics such as Allan Variance, it may not work well for low-cost sensors and may vary according to temperature change (Shin, 2005). Apart from requiring a large amount of data (for Allan Variance) which might not be so convenient, it may not also provide the overall system noise statistics because the noise statistics can vary according to the dynamics of the systems (Wis and Colomina, 2010). Although some studies have been

conducted on the adaptation of the system noise statistics by using an adaptive filtering approach, it is still considered as an open research area.

9.5 Summary

A summary of the work conducted for the research has been presented. Conclusions were then drawn from the results achieved. Based on these, continuation of the research for improvement was suggested and listed as a recommendation for future work. A summary of contribution to knowledge was also restated. It is hoped that the research presented in this thesis may motivate further research in the field, and can be successfully commercialized in the future.

Appendix A

NSS Control File

```
FILES
 DATSTYLE C:/Simulator/GPS/***.not

 STATION   (Location for kinematic/trajectory file)
  NAME movb118  KINEMATIC
    C:/Simulator/NSS/DataSim/maketraj/straightTrajectoryNSS.out
 END

 EPH
   SP3 sp3/igs12234.sp3
 END

 COMMONERR
   SATCLK    sunb/satclkfile.out
   SAERR     sunb/saerrfile.out
 END

  REPSTYLE
   RECCLK  sunb/***.rclk
   POSREC  sunb/***.rpos
   SATCLK  sunb/***.sclk
   SAERR   sunb/***.SA
   IONO    sunb/***.ION
   TROP    sunb/***.trop
   MULTI   sunb/***.mult
   NOISE   sunb/***.noise
   SLIP    sunb/***.slip
  END

END
PROCOPT
  MODEL
    IONO          1
```

```
    TROPO          1
    SA             0
    MULTIPATH      0
    DOPPLER        1
    SPLINE         1
  END

  PARAMETERS
    STARTTIME   GPS 1223 355000.0
    STOPTIME    GPS 1223 355980.0 !364800
    INTERVAL    1
    SATCLKRANDOMERR  1.0d-12
    RECCLKRANDOMERR  4.0d-07
    DOPPLERERROR     0.001d0
    SIMSATCLK        EPH
    SIMRECCLK        YES
    SASIM            NO
    L1PSEUDO    0.75d0
    L2PSEUDO    0.75d0
    L1CARR      0.001d0
    L2CARR      0.001d0
    ELEVMIN     5.0d0
    OUTPUT      PART !FULL
    SLIP        NO
    NOTT2       1
  END
END

INERTIAL    (Inertial errors to be simulated)
  MODEL
    LEVERARM 0.0d0 0.0d0 0.0d0
    GPSOFFSET 0.0d0 0.0d0 0.0d0
    NGYRO    3
    NACCEL   3
    INSDAT   C:/Simulator/INS/insfileStraight.dat      (IMU output filename)
    INTERVAL 0.005d0    (IMU sampling rate)
    AERONAV  0
    EARTHROT YES
    GRAVITY  1  !0: 9.81  1: Titterton  2: Farrell    (Gravity model)
    SYNCH 0.00 !333333333333333
    TTR 1d-7 !timetag random error
    TEMP 1 0.0d0
  END

  GYROS
    AXI1 1.0 0.0 0.0 (Definition of IMU axes)
    AXI2 0.0 1.0 0.0
    AXI3 0.0 0.0 1.0
    BIAS 0.35d0      (deg/s)
    BIASINST 1e-5 100
    MAXINRUN 0.0
    RUNST 0.0           (deg/s/s)
    NOISE 0.100000028d0      (deg/s)
```

```
    SF1   0.1 1.0      (%)
    TEMP1 0.02       (deg/s/degC)
    TEMP2 0.0
    SATURATION 400  (deg/s)
    QUANTI 0.011    (deg/s)
    MISALIGMENT  0.0172 (deg)
  END

  ACCELEROMETERS
    AXI1 1.0 0.0 0.0
    AXI2 0.0 1.0 0.0
    AXI3 0.0 0.0 1.0
    BIAS  0.294        (m/s/s)
    BIASINST 1e-5 60
    NOISE 0.1      (m/s/s)
    SF1 0.1          (%)
    TEMP1 0.02   (m/s/s/degC)
    TEMP2 0.0  0.0
    SATURATION 176.5179       (m/s/s)
    QUANTI  0.003d    (m/s/s)
    MISALIGMENT 0.0172d0 (deg)
    CROSS 0.0          (%)
  END

END
```

Appendix B

Example of Kinematic Data File

(Week number and seconds of epoch)
1223 354993.0000

Position at epoch (x,y,z) ECEF Units - metres
3851531.965529 -78696.606346 5066401.686044

Velocity at epoch (x,y,z) ECEF Units -metres/second
0.000000 0.000000 0.000000

Attitude at epoch (heading, pitch, roll) Units - degrees
45.000000 0.000000 0.000000

1223 354994.0000
3851531.965529 -78696.606346 5066401.686044
0.000000 0.000000 0.000000
45.000000 1.000000 0.000000

(until the end)

Appendix C

Dynamic Matrix for INS Error States

The state-space form of the INS error equations is shown in Chapter 5 (Eq. (5.11)). The full system dynamic matrix, F with its partial derivates can therefore be reproduced here as:

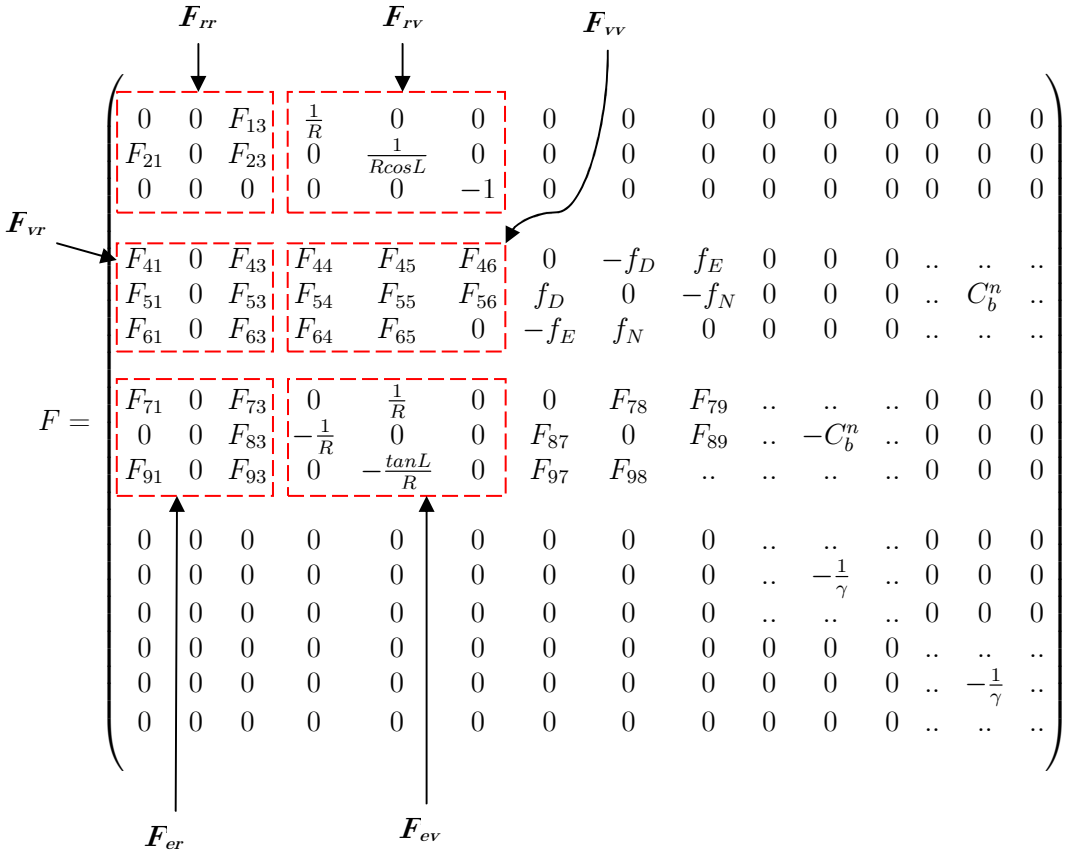

where

$F_{13} = -\frac{v_N}{R_N}$, $F_{21} = \frac{v_E tanL}{R_E cosL}$,$F_{23} = -\frac{v_E}{R_E^2 cosL}$, $F_{41} = -v_E(2\Omega cosL + \frac{v_E}{R_E cos^2 L})$,

$F_{43} = \frac{v_E^2 tanL - v_N v_E}{R_E^2}$, $F_{51} = 2\Omega(v_N cosL - v_D sinL) + \frac{v_N v_E}{R cos^2 L}$,

$F_{53} = \frac{v_E}{R_E^2}(v_N tanL + v_D)$, $F_{61} = 2\Omega v_E sinL$, $F_{63} = \frac{1}{R^2}(v_N^2 + v_E^2)$, $F_{44} = \frac{v_D}{R}$,

$F_{45} = -2(\Omega sinL + \frac{v_E}{R} tanL)$, $F_{46} = \frac{v_N}{R_N}$, $F_{54} = 2\Omega sinL + \frac{v_E}{R_E} tanL$,

$F_{55} = \frac{v_N tanL + v_D}{R_N}$, $F_{56} = 2\Omega cosL + \frac{v_E}{R_E}$, $F_{64} = \frac{-2v_N}{R_N}$, $F_{65} = -2(\Omega cosL + \frac{v_E}{R_E})$,

$F_{71} = \Omega sinL$, $F_{73} = -\frac{v_E}{R_E^2}$, $F_{83} = \frac{v_N}{R_N^2}$, $F_{91} = -\Omega cosL - \frac{v_E}{R_E cos^2 L}$, $F_{93} = \frac{v_E tanL}{R_E^2}$,

$F_{78} = -\Omega sinL - \frac{v_E tanL}{R_E}$, $F_{79} = \frac{v_N}{R_N}$, $F_{87} = \Omega sinL + \frac{v_E}{R_E} tanL$,

$F_{89} = \Omega cosL + \frac{v_E}{R_E}$, $F_{97} = -\frac{v_N}{R_N}$, $F_{98} = -\Omega cosL - \frac{v_E}{R_E}$, $R = \sqrt(R_N R_E)$

$\gamma = 3600$ is the reciprocal of the process correlation time for modelling the bias states as the first order Gauss Markov process.

Appendix D

Building Heading Generation

As discussed in Chapter 8, heading of a building can be possibly derived automatically using a free map available. This section will show an example of how this was done.

Street Level Map

Street level map, among other types of maps such as world map, topographic map and geological map, is very useful for street level navigation. This is because it provides useful street level information to users that include features such as buildings outline and roads, and uses either line map (2D representation) or aerial imagery (3D-like representation). An extra piece of information commonly found from this type of map is that the map is orientated such that North is always pointing straight up, East to the right, West to the left and South is pointing to the bottom of the map. For example, (Schöning et al., 2009) revealed that from his collection of 93 maps in 21 cities (in 8 countries in central Europe and North America), 81% had the correct Northing. This important map information is therefore used, together with classical edge detection algorithm to show the concept of deriving building heading from minimal map information.

There are many methods for edge detection but Canny method is chosen as it is the simplest method and commonly used in digital image processing. It works by looking for the minimum and maximum value in the first derivative of an image pixel values. Points that sit within this threshold will be detected as edge points. For further details, please refer to (Canny, 1987).

After that, Hough Transform (Illingworth and Kittler, 1988) is used to detect straight line features from the building image. This is done primarily because edge detection shows where edges are, but not what they are geometrically such as line or arcs. The idea of Hough Transform is that if certain points satisfy the line equation, then it will be considered as a straight line. The longest detected straight line is then selected for reliability purpose as quite often short straight feature does not present the true building orientation. The start and end point of this line are then stored in terms of pixel values and then the equation below is used:

$$\psi = atan2\left(\delta y, \delta x\right)$$

Where ψ is a derived building heading, δy is the difference between start and end y-pixel value, δx is the difference between start and end x-pixel value and *atan2* function is just a variation of *atan* function, and it is used here because it can resolve the angle in the right quadrant.

The flowchart in Fig. 1 summarizes the heading derivation process which was done automatically in Matlab environment.

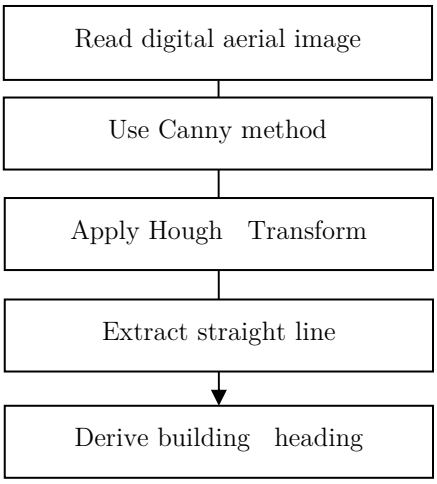

Fig.1: Heading derivation process

Next, Fig. 2 shows the derived heading in degree for one of the trial presented in Chapter 8. The red line is the longest straight line feature detected in the image with a calculated heading to be -49.8^0. After the building heading is acquired, a simple offset of +90^0 is added to the remaining three headings to make up the four derived building headings of 40.2^0, 130.2^0, 220.2^0 and 310.2^0. These 4 headings information can then be used for CHAIN algorithm.

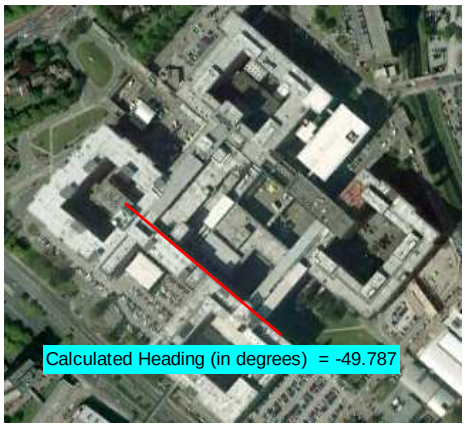

Fig. 2: Test building image with calculated heading

Appendix E

Point in Polygon

Consider a polygon that contains K vertices (x_n,y_n) where n ranges from 1 to K. Now the problem is how to test whether a point (x_p,y_p) is indeed inside this polygon. Imagine a line is extended horizontally from (x_p,y_p). The test begins by checking: if the number of times this line intersects the polygon edges is even, then the point is outside the polygon and if the number of intersections is odd, then the point (x_p,y_p) is inside the polygon. Fig. 3 below shows the extended line for some sample points A, B and C (denoted by dots). It describes more clearly on how the check is run to determine whether a point lies inside or outside the polygon. For point A and B, the extended lines intersect with the edges for odd times (1x and 3x), hence they are considered to be located inside the polygon. On the other hand, point C line intersects with the edges for even time (2x), hence it is considered to be outside the polygon area.

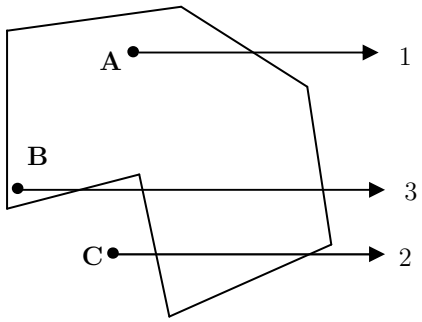

Fig. 3: The point in polygon test

To avoid the problem when an edge of the polygon lies on the same line from (x_p,y_p), the polygon area is constructed such that it is always bigger than the building. By doing this, the position solution from INS will never go beyond polygon boundary; therefore there will be no occasion where the extended line from the test point overlaps horizontally with the edges.

References

Afzal, M. H., Renaudin, V. & Lachapelle, G., 2010. Assessment of indoor magnetic field anomalies using multiple magnetometers. In *Proccedings of ION GNSS 2010.* Oregon, USA, 21-24 September 2010.

Afzal, M. H., Renaudin, V. & Lachapelle, G., 2011. Multi-magnetometer based perturbation mitigation for indoor orientation estimation. *Navigation,* 58, 279-292.

Aggarwal, P., Syed, Z., Niu, X. & El-sheimy, N., 2008. A standard testing and calibration procedure for low cost MEMS inertial sensors and units. *The Journal of Navigation,* 61**,** 323-336.

Aggarwal, P., Syed, Z., Noureldin, A. & El-sheimy, N., 2010. *MEMS-based integrated navigation.* Boston: Artech House.

Aggarwal, P., Thomas, D., Ojeda, L. & Borenstein, J., 2011. Map matching and heuristic elimination of gyro drift for personal navigation systems in GPS-denied conditions. *Measurement Science and Technology,* 22**,** 025205.

Ahmed, E. R., 2006. *Introduction to GPS: The Global Positioning System.* 2nd ed. Boston: Artech House.

Alkan, R., Karaman, H. & Sahin, M., 2005. GPS, GALILEO and GLONASS satellite navigation systems & GPS modernization. In *Proceedings of 2nd International Conference on Recent Advances in Space Technologies.* Istanbul, Turkey, 9-11 June 2005.

Amendolare, V., Cyganski, D., Duckworth, R. J., Makarov, S., Coyne, J., Daempfling, H. & Woodacre, B., 2008. WPI precision personnel locator system: Inertial navigation supplementation. In *Proceedings of IEEE/ION PLANS 2008.* California, USA, 6-8 May 2008.

An, L., Guo-bin, C., Fang-jun, Q. & Hong-wu, L., 2010. Improved precision of strapdown inertial navigation system brought by dual-axis continuous rotation of inertial measurement unit. In *Proceedings of 2nd International Asia Conference on Informatics in Control, Automation and Robotics (CAR), 2010.* Wuhan, China, 6-7 March 2010.

Aponte, J., Meng, X., Dodson, A., Moore, T., Hill, C., Burbidge, M., 2008. Performance assessment of a GPS network RTK service. In *Proceedings of ENC GNSS2008.* Toulouse, France, 23-25 April 2008.

Aponte, J., Meng, X., Hill, C., Moore, T., Burbidge, M. & Dodson, A., 2009. Quality assessment of a network-based RTK GPS service in the UK. *Journal of Applied Geodesy,* 3**,** 25-34.

Arikawa, M., Konomi, S. & Ohnishi, K., 2007. Navitime: Supporting pedestrian navigation in the real world. *Pervasive Computing, IEEE,* 6**,** 21-29.

Ascher, C., Kessler, C., Wankerl, M. & Trommer, G., 2010. Dual IMU Indoor Navigation with particle filter based map-matching on a smartphone. In *Proceedings of Indoor Positioning and Indoor Navigation (IPIN) 2010.* Guimarães, Portugal 15-17 September 2010.

Bachmann, E. R., Yun, X. & Brumfield, A., 2007. Limitations of attitude estimation algorithms for inertial/magnetic sensor modules. *Robotics & Automation Magazine, IEEE,* 14**,** 76-87.

Bancroft, J. B., 2010. *Multiple inertial measurement unit fusion for pedestrian navigation.* Ph.D. University of Calgary.

Beauregard, S., 2007. Omnidirectional Pedestrian Navigation for First Responders. In *Proceedings of 4th Workshop on Positioning, Navigation and Communication (WPNC '07).* Hannover, Germany, 22 March 2007.

Bebek, O., Suster, M. A., Rajgopal, S., Fu, M. J., Xuemei, H., Cavusoglu, M. C., Young, D. J., Mehregany, M., Van den bogert, A. J. & Mastrangelo, C. H., 2010. Personal navigation via high-resolution gait-corrected inertial measurement units. *IEEE Transactions on Instrumentation and Measurement,* 59**,** 3018-3027.

Ben, Y.-Y., Chai, Y.-L., Gao, W. & Sun, F., 2010. Analysis of error for a rotating strapdown inertial navigation system with fibro gyro. *Journal of Marine Science and Application,* 9**,** 419-424.

Bird, J. & Arden, D., 2011. Indoor navigation with foot-mounted strapdown inertial navigation and magnetic sensors. *Wireless Communications, IEEE,* 18**,** 28-35.

Biswas, J. & Veloso, M., 2010. WIFI localization and navigation for autonomous indoor mobile robots. In *Proceedings of International Conference on Robotics and Automation (ICRA) 2010.* Anchorage, Alaska, 3-8 May 2010.

Blake, S., 2008. *Heave compensation using time-differenced carrier observations from low-cost GPS receivers.* Ph.D. The University of Nottingham.

Borenstein, J. & Ojeda, L., 2010. Heuristic drift elimination for personnel tracking systems. *The Journal of Navigation,* 63**,** 591-606.

Boucher, C. & Lensch, R., 2010. *MEMS technology: Nearing the tipping point.* [online] Boucher-Lensch Associate LLC. Available at: < http://www.boucherlensch.com/bla/IMG/pdf/BLA_MEMS_Report_031003.pdf> [Accessed on 11 December 2011].

BGS, 2011. *The International Geomagnetic Reference Field (IGRF).* [online] Available at http://www.geomag.bgs.ac.uk/data_service/models_compass/igrf.html [Accessed on 2 August 2011].

Brown, A. K. & Olson, P., 2006. Urban/indoor navigation using network assisted GPS. In *Proceedings of the 61st Annual Meeting of The Institute of Navigation.* Cambridge, USA, 27-29 June 2005.

Bruce, N., Mccracken, J., Albalak, R., Schei, M., Smith, K. R., Lopez, V. & West, C., 2004. Impact of improved stoves, house construction and child location on levels of indoor air pollution exposure in young Guatemalan children. *Journal of Exposure Science and Environmental Epidemiology,* 14**,** S26-S33.

Butler, D., 2006. Virtual globes: the web-wide world. *Nature,* 439**,** 776-778.

Callmer, J., To, X, Rnqvist, D. & Gustafsson, F., 2010. Probabilistic stand still detection using foot mounted IMU. In Proceedings of the *13th Conference on Information Fusion (FUSION) 2010.* Edinburgh, UK, 26-29 July 2010.

Campbell, W., 2001. *Earth magnetism: A guided tour through magnetic fields.* California: Academic Press.

Canny, J., 1987. A computational approach to edge detection. *IEEE Transaction of Pattern Analysis and Machine Intelligence,* 8(6), 679-698.

Caruso, M., 1998. Applications of magnetoresistive sensors in navigation systems. [online] Honeywell Inc. Available at: < http://www.ssec.honeywell.com/position-sensors/datasheets/sae.pdf> [Accessed on 11 December 2011].

Caruso, M., 2000. Applications of magnetic sensors for low cost compass systems. In *Proceedings of Position, Location and Navigation Symposium (PLANS 2000).* California, USA, 13-16 March 2000.

Chang, B. S., Lee, J. G. & Kang, T. S., 2006. Design and performance test of digital rebalance loop for MEMS gyroscope. *Key Engineering Materials,* 326**,** 249-252.

Chen, W., Fu, Z. Q., Chen, R. Z., Chen, Y. W., Andrei, O., Kroger, T. & Wang, J. Y., 2009. An integrated GPS and multi-sensor pedestrian positioning system for 3D urban navigation. In *Proceedings of Joint Urban Remote Sensing Event 2009.* Shanghai, China, 20-22 May 2009.

Chen, W., Chen, R., Chen, Y., Kuusniemi, H., Fu, Z., & Wang, J., 2010. An adaptive calibration approach for a 2-axis digital compass in a low-cost pedestrian navigation system. In *Proceedings of 2010 Instrumentation and Measurement Technology Conference (I2MTC).* Texas, USA, 3-6 May 2010.

Chiu, D. S. O. K., Kyle P., 2009. Seamless Outdoor-to-lndoor Positioning DGPS + UWB. In *Proceedings of the 21st International Technical Meeting of the Satellite Division of The Institute of Navigation (ION GNSS 2008).* Savannah, USA, September 2008.

Cho, S. Y. & Park, C. G., 2005. MEMS based pedestrian navigation system. *The Journal of Navigation,* 59**,** 135-153.

Choi, W. H., Park, K. H., Yang, W. H., Lee, K. Y., Yoon, C. S., Son, B. S., Jeon, J. M. & Yu, S. D., 2010. Comparison of VOCs personal exposure levels according to time-activity patterns in Korea. *Epidemiology,* 22(1).

Chung, J., Donahoe, M., Schmandt, C., Kim, I. J., Razavai, P. & Wiseman, M., 2011. Indoor location sensing using geo-magnetism. In *Proceedings of the 9th International Conference on Mobile Systems, Applications, and Services.* Washington, USA, 28 June – 1 July 2011.

Collin, J., Mezentsev, O. & Lachapelle, G., 2003. Indoor positioning system using accelerometry and high accuracy heading sensors. In *Proceedings of the 16th International Technical Meeting of ION GPS/GNSS 2003.* Portland, Oregon, 9-12 September 2003.

Curey, R. K., Ash, M. E., Thielman, L. O. & Barker, C. H., 2004. Proposed IEEE inertial systems terminology standard and other inertial sensor standards. In *Proceedings of Position, Location and Navigation Symposium (PLANS 2004).* California, USA, 27-29 April 2004.

Dedes, G. & Dempster, A. G., 2005. Indoor GPS positioning-challenges and opportunities. In *Proceedings of Vehicular Technology Conference.* Stockholm, Sweden, 30 May – 1 June 2005.

Diffey, B., 2011. An overview analysis of the time people spend outdoors. *British Journal of Dermatology,* 164**,** 848-854.

Dovis, F., Lesca, R., Margaria, D., Boiero, G. & Ghinamo, G., 2008. An assisted high-sensitivity acquisition technique for GPS indoor positioning. In *Proceedings of Position, Location and Navigation Symposium (PLANS 2008).* California, USA, 6-8 May 2008.

Dragunas, K. & Borre, K., 2011. Multipath mitigation based on deconvolution. *Journal of Global Positioning Systems,* 10**,** 76-85.

Ekahau, 2011. [Online] Available at: <www.ekahau.com> [Accessed on 9 December 2011].

Ezzati, M., Saleh, H. & Kammen, D. M., 2000. The contributions of emissions and spatial microenvironments to exposure to indoor air pollution from biomass combustion in Kenya. *Environmental Health Perspectives***,** 108(9), 833-839.

Farnell, 2010. [online] Available at: <www.uk.farnell.com> [Accessed on 1 January 2012].

Farrell, J. & Barth, M., 1998. *The Global Positioning System and inertial navigation.* New York: McGraw-Hill Professional.

Farrell, J. & Barth, M., 2008. *Aided navigation: GPS with high rate sensors.* New York: McGraw-Hill Professional.

Faulkner, W. T., Alwood, R., Taylor, D. W. A. & Bohlin, J., 2010. GPS-denied pedestrian tracking in indoor environments using an IMU and magnetic compass. In *Proceedings of the 2010 International Technical Meeting of the Institute of Navigation.* California, USA, 25-27 January 2010.

Feliz, R., Zalama, E. & Gómez, J., 2009. Pedestrian tracking using inertial sensors. *Journal of Physical Agents,* 3(1)**,** 35-43.

Fernández-Prades, C., Presti, L. L. & Falletti, E., 2011. Satellite radiolocalization from GPS to GNSS and beyond: Novel technologies and applications for civil mass market. *Proceedings of the IEEE,* 99(11)**,** 1882-1904.

Finlay, C., Maus, S., Beggan, C., Bondar, T., Chambodut, A., Chernova, T., Chulliat, A., Golovkov, V., Hamilton, B. & Hamoudi, M., 2010. International Geomagnetic Reference Field: the eleventh generation. *Geophysical Journal International*, 183, 1216-1230.

Fischer, C. & Gellersen, H., 2010. Location and navigation support for emergency responders: A survey. *IEEE Pervasive Computing,* 9**,** 38-47.

Foxlin, E., 2005. Pedestrian tracking with shoe-mounted inertial sensors. *IEEE Computer Graphics and Applications,* 25(6), 38-46.

Fu, Q. & Retscher, G., 2009. Another look indoors GPS + RFID. *GPS World.* [online] Available at: <http://www.gpsworld.com/wireless/personal-navigation/gps-rfid-7166> [Accessed on 11 October 2011].

Fuchs, C., 2010. A Survey on Indoor Trackings for Mission Critical Scenarios. *Pervasive and Mobile Computing.* 7(1), 1-15.

Geller, E. S., 1968. Inertial system platform rotation. *IEEE Transactions on Aerospace and Electronic Systems,* AES-4**,** 557-568.

Glanzer, G. & Walder, U., 2010. Self-contained indoor pedestrian navigation by means of human motion analysis and magnetic field mapping. In *Proceedings of the 7th Workshop on Positioning, Navigation and Communication (WPNS 2010).* Dresden, Germany, 11-12 March 2010.

Godha, S. & Lachapelle, G., 2008. Foot mounted inertial system for pedestrian navigation. *Measurement Science and Technology,* 19**,** 075202.

Godha, S., Lachapelle, G. & Cannon, M. E., 2006. Integrated GPS/INS system for pedestrian navigation in a signal degraded environment. In *Proceedings of the ION GNSS 2006.* Texas, USA, 26-29 September 2006.

GPS Wing, 2010. *IS-GPS-200E GPS Interface Control Document: Navstar GPS Space Segment / User Segment Interfaces.* [online] Available at: < http://www.gps.gov/technical/icwg/IS-GPS-200E.pdf> [Accessed on 2 September 2011].

Grejner-brzezinska, D., Toth, C. & Moafipoor, S., 2008. Performance assessment of a multi-sensor personal navigator supported by an adaptive knowledge based system. *The International Archives of the Photogrammetry, Remote Sensing and Spatial Information Science, XXXVII (B5),* 857-867.

Grejner-brzezinska, D., Toth, C. K., Markiel, J. N., Moafipoor, S. & Czarnecka, K., 2009. Personal navigation: Extending mobile mapping technologies into indoor environments. *Boletim De Ciencias Geodesicas,* 15(5)**,** 790-806.

Grejner-brzezinska, D., Yi, Y. & Toth, C. K., 2001. Bridging GPS gaps in urban canyons: The benefits of ZUPTs. *The Journal of Navigation,* 48**,** 217-225.

Grewal, M. S. & Andrews, A. P., 2008. *Kalman filtering: theory and practice using MATLAB.* 3rd ed. New York: Wiley.

Groves, P., Pulford, G., Littlefield, C., Nash, D. & Mather, C., 2007. Inertial navigation versus pedestrian dead reckoning: Optimizing the integration. In *Proceedings of ION GNSS 2007.* Texas, USA, 25-28 September 2007.

Groves, P. D., 2008. *Principles of GNSS, inertial, and multi-sensor Integrated Navigation Systems.* Boston: Artech House.

Guo, P. F., Qiu, H. T., Yang, Y. C. & Ren, Z., 2008. The soft iron and hard iron calibration method using extended kalman filter for attitude and heading reference system. In *Proceedings of IEEE/ION PLANS 2008.* California, USA, 6-8 May 2008.

Haverinen, J. & Kemppainen, A., 2009. Global indoor self-localization based on the ambient magnetic field. *Robotics and Autonomous Systems,* 57**,** 1028-1035.

Hide, C., 2003. *Integration of GPS and low cost INS measurements.* Ph.D. The University of Nottingham.

Hide, C., 2009. *Algorithm documentation for POINT software,* Geospatial Research Centre, New Zealand.

Hide, C., Botterill, T. & Andreotti, M., 2009. An Integrated IMU, GNSS and Image Recognition Sensor for Pedestrian Navigation. *Proceedings of International Technical Meeting of The Satellite Division of the Institute of Navigation (ION GNSS 2009).* Savannah, USA, 22-25 September 2009.

Hide, C., Moore, T. & Hill, C., 2007a. A multi-sensor navigation filter for high accuracy positioning in all environments. *The Journal of Navigation,* 60**,** 409-425.

Hide, C., Moore, T. & Smith, M., 2003. Adaptive Kalman filtering for low-cost INS/GPS. *The Journal of Navigation,* 56**,** 143-152.

Hide, C., Pinchin, J. & Park, D., 2007b. Development of a Low Cost Multiple GPS Antenna Attitude System. *Proceedings of the IONGNSS 2007.* Texas, USA, 25-28 September 2007.

Huang, C., Liao, Z., & Zhao, L., 2010. Synergism of INS and PDR in self-contained pedestrian tracking with a miniature sensor module. *IEEE Sensors Journal,* 10 (8)**,** 1349-1359.

Illingworth, J. & Kittler, J., 1988. A survey of the Hough transform. *Computer Vision, Graphics, and Image Processing,* 44**,** 87-116.

Intersense, 2011. [Online] Available at: <www.intersense.com> [Accessed on 2 December 2011].

Invense, 2010. *ITG-3200 Product Specification.* [online] Available at: <www.invensense.com/mems/gyro/itg3200.html> [Accessed on 2 December 2011].

Ishibashi, S., Tsukioka, S., Yoshida, H., Hyakudome, T., Sawa, T., Tahara, J., Aoki, T. & Ishikawa, A., 2007. Accuracy improvement of an inertial navigation system brought about by the rotational motion. In *Proceedings of OCEANS 2007-Europe.* Aberdeen, Scotland, 18-21 June 2007.

Jadaliha, M., Shahri, A.M. & Mobed, M., 2008. A new pedestrian navigation system based on a low-cost IMU. In *Proceedings of the 5th International*

Conference on Ubiquitous Robots and Ambient Intelligence (URAI 2008). Seoul, Korea, 20-22 November 2008.

Jadaliha, M., 2007. A high-performance, low-cost INS for autonomous mobile robots. In *Proceedings of the 4th International Conference on Ubiquitous Robots and Ambient Intelligence (URAI 2007).* Pohang, Korea, 14-16 November 2007.

Januszewski, J., 2010. Assisted-GNSS, Why, Where and for Whom? In *Proceedings of the 10th Conference on Transport Systems Telematics.* Ustron, Poland, 20-23 October.

Ji, S., Chen, W., Ding, X., Chen, Y., Zhao, C. & Hu, C., 2010. Potential benefits of GPS/GLONASS/GALILEO integration in an urban canyon - Hong Kong. *The Journal of Navigation,* 63**,** 681-693.

Jiménez, A., Seco, F., Prieto, J. & Guevara, J., 2010. Indoor Pedestrian Navigation using an INS/EKF framework for Yaw Drift Reduction and a Foot-mounted IMU. In *Proceedings of the 7th Workshop on Positioning, Navigation and Communication (WPNC 2010).* Dresden, Germany, 11-12 March 2010.

Jiménez, A., Seco, F., Zampella, F., Prieto, J. & Guevara, J., 2011. Improved Heuristic Drift Elimination (iHDE) for pedestrian navigation in complex buildings. In *Proceedings of the International Conference on Indoor Positioning and Indoor Navigation (IPIN 2011).* Guimarães, Portugal, 21-23 September 2011.

Jones, E. S. & Soatto, S., 2011. Visual-inertial navigation, mapping and localization: A scalable real-time causal approach. *The International Journal of Robotics Research,* 30(4)**,** 407-430.

Kalman, R. E., 1960. A new approach to linear filtering and prediction problems. *Journal of Basic Engineering,* 82**,** 35-45.

Kaniewski, P. & Kazubek, J., 2009. Integrated system for heading determination. *Acta Physica Polonica A,* 116(3)**,** 325-330.

Karimi, H. A., Roongpiboonsopit, D. & Kasemsuppakorn, P., 2011. Uncertainty in personal navigation services. *The Journal of Navigation,* 64**,** 341-356.

Kealy, A., LI, B., Gallagher, T. & Dempster, A., 2010a. Evaluation of WIFI technologies for indoor positioning applications. In *Proceedings of Surveying and Spatial Sciences (SSC 2009).* Adelaide, Australia, 28 September – 2 October 2010.

Kealy, A., Roberts, G. & Retscher, G., 2010b. Evaluating the performance of low cost MEMS inertial sensors for seamless indoor/outdoor navigation. In *Proceedings of IEEE/ION Position Location and Navigation Symposium (PLANS 2010).* California, USA, 3-6 May 2010.

Kemppi, P., Pajunen, J. & Rautiainen, T., 2010. Use of artificial magnetic anomalies in indoor pedestrian navigation. In *Proceedings of IEEE Vehicular Technology Conference.* Ottawa, Canada, 6-9 September 2010.

Kietlinski-zaleski, J., Yamazato, T. & Katayama, M., 2010. TDoA UWB positioning with three receivers using known indoor features. In *Proceedings of IEEE International Conference on Ultra-Wideband (ICUWB 2010).* Nanjing, China, 20-23 September 2010.

Kijewski-correa, T. & Kochly, M., 2007. Monitoring the wind-induced response of tall buildings: GPS performance and the issue of multipath effects. *Journal of Wind Engineering and Industrial Aerodynamics,* 95**,** 1176-1198.

Kjærgaard, M., Blunck, H., Godsk, T., Toftkjær, T., Christensen, D. & Grønbæk, K., 2010. Indoor positioning using GPS revisited. In *Proceedings of the International Conference on Pervasive Computing*, Helsinki, Finland, 17-20 May 2010.

Klepeis, N. E., Nelson, W. C., Ott, W. R., Robinson, J. P., Tsang, A. M., Switzer, P., Behar, J. V., Hern, S. C. & Engelmann, W. H., 2001. The National Human Activity Pattern Survey (NHAPS): a resource for assessing exposure to environmental pollutants. *Journal of Exposure Analysis and Environmental Epidemiology,* 11**,** 231-252.

Kourepenis, A., Borenstein, J., Connelly, J., Elliott, R., Ward, P. & Weinberg, M., 1998. Performance of MEMS inertial sensors. In Proceedings of *Position Location and Navigation Symposium (PLANS 1998).* California, USA, 20-23 April 1998.

Krach, B. & Robertson, P., 2008. Integration of foot-mounted inertial sensors into a Bayesian location estimation framework. In *Proceedings of the 5th Workshop on Positioning, Navigation and Communication (WPNC 2008).* Hannover, Germany, 27 March 2008.

Kuusniemi, H., Liang, C., Ruotsalainen, L., Ling, P., Yuwei, C. & Ruizhi, C., 2011. Multi-sensor multi-network seamless positioning with visual aiding. In *Proceedings of the 2011 International Conference on* of *Localization and GNSS (ICL-GNSS).* Tampere, Finland, 29-30 June 2011.

Lachapelle, G., 2004. GNSS indoor location technologies. *Journal of Global Positioning Systems*, 3, 2-11.

Lachapelle, G., 2007. Pedestrian navigation with high sensitivity GPS receivers and MEMS. *Personal and Ubiquitous Computing,* 11**,** 481-488.

Lachapelle, G., Godha, S. & Cannon, M. E., 2006. Performance of integrated HSGPS-IMU technology for pedestrian navigation under signal masking. In *Proceedings of European Navigation Conference (ENC-GNSS 06).* Manchester, UK, 7-10 May 2006.

Lachapelle, G., Kuusniemi, H., Dao, D. T. H., Macgougan, G. & Cannon, M. E., 2004. HSGPS signal analysis and performance under various indoor conditions. *Navigation,* 51(1), 29-44.

Lachapelle, G., Mezentsev, O., Collin, J. & Macgougan, G., 2003. Pedestrian and vehicular navigation under signal masking using integrated HSGPS and self contained sensor technologies. In *Proceedings of the 11th IAIN World*

Congress, Smart Navigation - Systems and Services. Berlin, Germany, 21-24 October 2003.

Lai, Y. C., Jan, S. S. & Hsiao, F. B., 2010. Development of a low-cost attitude and heading reference system using a three-axis rotating platform. *Sensors,* 10**,** 2472-2491.

Lammel, G., Gutmann, J., Marti, L. & Dobler, M., 2009. Indoor navigation with MEMS sensors. *Procedia Chemistry,* 1, 532-535.

Lane, N. D., Miluzzo, E., Lu, H., Peebles, D., Choudhury, T. & Campbell, A. T., 2010. A survey of mobile phone sensing. *IEEE Communications Magazine,* 48**,** 140-150.

Legat, K. & Lechner, W., 2000. Navigation systems for pedestrians - a basis for various value-added services. In *Proceedings of ION GPS 2000.* Utah, USA, 19-22 September 2000.

Leondes, C. T. & Apostolyuk, V., 2006. Theory and Design of Micromechanical Vibratory Gyroscopes. In: *MEMS/NEMS Handbook: Techniques and Applications.* USA: Springer. Ch.6.

Lin, C. H., Liu, Y. S., Chen, C. H., Lin, B. Y. & Lo, C. C., 2011. A real-time campus guidance system based on energy efficient location determination method. *Advanced Materials Research,* 211**,** 485-489.

Ling, C., Ahmad, M. & Ossen, D., 2007. The effect of geometric shape and building orientation on minimising solar insolation on high-rise buildings in hot humid climate. *Journal of Construction in Developing Countries,* 12**,** 27-38.

Liu, H., Darabi, H., Banerjee, P. & Liu, J., 2007. Survey of Wireless Indoor Positioning Techniques and Systems. *IEEE Transactions on Systems Man and Cybernetics, Part C Applications and Reviews,* 37(6)**,** 1067-1080.

Liu, S., Zhang, Z. & Hung, J. C., 1989. A high accuracy magnetic heading system composed of fluxgate magnetometers and a microcomputer. In *Proceedings of the IEEE 1989 National Aerospace and Electronics Conference, 1989.* Dayton, USA, 22-26 May 1989.

Lobo, J. & Dias, J., 2007. An introduction to inertial and visual sensing. *The International Journal of Robotics Research,* 26**,** 519-535.

Lukianto, C., Ho, X, Nniger, C. & Sternberg, H., 2010. Pedestrian smartphone-based indoor navigation using ultra portable sensory equipment. In *Proceedings of the 2010 International Conference on Indoor Positioning and Indoor Navigation (IPIN 10).* Guimarães, Portugal, 15-17 September 2010.

Mather, C. J., Groves, P. D. & Carter, M. R., 2006. A Man Motion Navigation System Using High Sensitivity GPS, MEMS IMU and Auxiliary Sensors. In *Proceedings of the 19th International Technical Meeting of the Satellite Division of the Institute of Navigation (ION GNSS 2006).* Texas, USA, 26-29 September 2006.

Maybeck, P. S., 1979. *Stochastic Models, Estimation and Control Vol 1.* London: Academic Press.

Mezentsev, O., 2005. *Sensor aiding of HSGPS pedestrian navigation.* Ph.D. University of Calgary.

Mezentsev, O., Collin, J. & Lachapelle, G., 2003. Vehicular navigation in urban canyons using a high sensitivity GPS receiver augmented with a medium-grade IMU. In *Proceedings of 10th Saint Petersburg Conference on Integrated Navigation System.* St. Petersburg, Russia, 26-28 May 2003.

Mezentsev, O., Lachapelle, G. & Collin, J., 2005. Pedestrian dead reckoning – a solution to navigation in GPS signal degraded areas. *Geomatica,* 59**,** 175-182.

Microstrain, 2011a. *3DM-GX3-25: Miniature Attitude Heading Reference System (AHRS).* [online] Available at: <http://www.microstrain.com/inertial/3dm-gx3-25> [Accessed on 9 November 2011].

Microstrain, 2011b. [Online] Available at: <www.microstrain.com> [Accessed on 2 December 2011].

Molina, P., Colomina, I., Troger, M., Hofmann-wellenhof, B. & Aguilera, C., 2011. Qualitative motion analysis INS/GNSS in care-giving applications. *GPS World.* [online] Available at: < http://www.gpsworld.com/wireless/personal-navigation/qualitative-motion-analysis-10885> [Accessed on 10 January 2012].

Moore, T., Hill, C., Norris, A., Hide, C., Park, D. & Ward, N., 2008. The potential impact of GNSS/INS integration on maritime navigation. *The Journal of Navigation,* 61**,** 221-237.

Nam, Y., 2011. Map-based indoor people localization using an inertial measurement unit. *Journal of Information Science and Engineering,* 27**,** 1233-1248.

National Geophysical Data Centre, 2011. *World Magnetic Model.* [online] Available at: < http://www.ngdc.noaa.gov/geomag/WMM/DoDWMM.shtml> [Accessed on 10 December 2011].

Ni, L. M., Dian, Z. & Souryal, M. R., 2011. RFID-based localization and tracking technologies. *IEEE Wireless Communications,* 18**,** 45-51.

O'driscoll, C., Lachapelle, G. & Tamazin, M., 2011. Combined GPS/GLONASS receivers in urban environments. *GPS World.* [online] Available at: < http://www.gpsworld.com/transportation/road/dynamic-duo-10902> [Accessed on 23 September 2011].

O'Reilly, R., & Weinberg, H., 2010. The five motion senses: MEMS inertial sensing to transform applications. *Sensors.* [online] Available at: < http://www.sensorsmag.com/sensors/acceleration-vibration/the-five-motion-senses-mems-inertial-sensing-transform-appli-6533> [Accessed on 12 December 2011].

OSM, 2012. [Online] Available at: <www.openstreetmap.org> [Accessed on 12 March 2012].

Pang, G. & Liu, H., 2001. Evaluation of a low-cost MEMS accelerometer for distance measurement. *Journal of Intelligent and Robotic Systems,* 30**,** 249-265.

Park, M. & Gao, Y., 2006. Error analysis and stochastic modeling of low-cost MEMS accelerometer. *Journal of Intelligent and Robotic Systems,* 46**,** 27-41.

Peshekhonov, V., 2011. Gyroscopic navigation systems: Current status and prospects. *Gyroscopy and Navigation,* 2**,** 111-118.

Peshekhonov, V. G., Nekrasov, Y. A., Pfluger, P., Kergueris, C., Haddara, H. & Elsayed, A., 2011. Test results of an RR-type micromechanical gyroscope. *IEEE Aerospace and Electronic Systems Magazine,* 26**,** 14-21.

Petovello, M., 2003. *Real-time integration of a tactical grade IMU and GPS for high accuracy positioning and navigation.* Ph.D. University of Calgary.

Petovello, M., Mezentsev, O., Lachapelle, G. & Cannon, M. E., 2003. High sensitivity GPS velocity updates for personal indoor navigation using inertial navigation systems. In *Proceedings of ION GPS/GNSS 2003,* Oregon, USA, 9-12 September 2003.

Pinchin, J., Hide, C., Abdulrahim, K., Moore, T., Hill, C., 2011. Integration of heading-aided MEMS IMU with GPS for pedestrian navigation. In *Proceedings of ION GNSS 2011.* Oregon, USA, 19-23 September 2011.

Pittet, S., Renaudin, V., Merminod, B. & Kasser, M., 2008. UWB and MEMS based indoor navigation. *The Journal of Navigation,* 61**,** 369-384.

Pozzobon, O., 2011. Keeping the Spoofs Out: Signal authentication services for future GNSS. *InsideGNSS.* [online] Available at: < http://www.insidegnss.com/auto/mayjune11-Pozzobon.pdf> [Accessed on 20 October 2011].

Qi, N., Xiaoying, G. & Zhun, L., 2009. Research on accuracy improvement of INS with continuous rotation. In *Proceedings of the 2009 International Conference on Information and Automation (ICIA '09).* Zuhai, China, 22-25 June 2009.

Rajagopal, S., 2008. *Personal dead reckoning system with shoe mounted inertial sensors.* Msc. Stockholm Royal Institute of Technology.

Reissman, D. B. & Howard, J., 2008. Responder safety and health: preparing for future disasters. *Mount Sinai Journal of Medicine: A Journal of Translational and Personalized Medicine,* 75**,** 135-141.

Renaudin, V., Afzal, M. & Lachapelle, G., 2010. New method for magnetometers based orientation estimation. In *Proceedings of ION/IEEE PLANS 2010.* California, USA, 4-6 May 2010.

Renaudin, V., Yalak, O., Tomé, P. & Merminod, B., 2007. Indoor navigation of emergency agents. *European Journal of Navigation,* 5**,** 36–45.

Retscher, G., 2007. Test and integration of location sensors for a multi-sensor personal navigator. *The Journal of Navigation,* 60**,** 107-117.

Robertson, P., Angermann, M. & Krach, B., 2009. Simultaneous localization and mapping for pedestrians using only foot-mounted inertial sensors. In

Proceedings of the 11th ACM International Conference on Ubiquitous Computing (Ubicomp 2009). Orlando, Florida, 30 September – 3 October 2009.

Robertson, P., Angermann, M., Krach, B. & Khider, M., 2010. SLAM dance: inertial-based joint mapping and positioning for pedestrian navigation. *InsideGNSS.* [online] Available at: < http://www.insidegnss.com/auto/may10-Robertson.pdf> [Accessed on 20 September 2011].

Ruotsalainen, L., Kuusniemi, H. & Chen, R., 2011. Visual-aided two-dimensional pedestrian indoor navigation with a smartphone. *Journal of Global Positioning Systems,* 10**,** 11-18.

Sabatini, A. M., 2008. Adaptive filtering algorithms enhance the accuray of low-cost inertial/ magnetic sensing in pedestrian navigation systems. *International Journal of Computational Intelligence and Applications,* 7**,** 351-361.

Schon, S. & Bielenberg, O., 2008. On the capability of high sensitivity GPS for precise indoor positioning. In *Procedings of the 5th Workshop on Positioning, Navigation and Communication (WPNC 2008).* Hannover, Germany, 27 March 2008.

Schöning, J., Krüger, A., Cheverst, K., Rohs, M., Löchtefeld, M. & Taher, F., 2009. PhotoMap: using spontaneously taken images of public maps for pedestrian navigation tasks on mobile devices. In *Proceedings of the 11th international Conference on Human-Computer Interaction with Mobile Devices and Services.* Bonn, Germany, 15-18 September 2009.

Schwieger, V., 2007. High-sensitivity GPS-the low sost future of GNSS. In *Proceedings of FIG Working Week.* Hong Kong, SAR. 13-17 May 2007.

Seco, F., Plagemann, C., Jiménez, A. R. & Burgard, W., 2010. Improving RFID-based indoor positioning accuracy using Gaussian processes. In *Proceedings of International Conference on Indoor Positioning and Indoor Navigation (IPIN 2010).* Zurich, Switzerland, 15-17 September 2010.

Seung-Hyun, K., 2011. Statistical analysis of urban GPS multipaths and pseudo-range measurement errors. *IEEE Transactions on Aerospace and Electronic Systems,* 47**,** 1101-1113.

Shin, E. H., 2005. *Estimation techniques for low cost inertial navigation.* Ph.D. University of Calgary.

Shin, E. H., 2001. *Accuracy improvement of low-cost INS/GPS for land applications.* Msc. University of Calgary.

Shin, S. H., Park, C. G. & Choi, S., 2010. New map-matching algorithm using virtual track for pedestrian dead reckoning. *ETRI Journal,* 32(6), 891-900.

Skog, I. & Handel, P., 2006. Calibration of a MEMS inertial measurement unit. In *Proceedings of XVII IMEKO World Congress.* Rio de Janeiro, Brazil, 17-22 September 2006.

Skog, I. & Handel, P., 2009. In-car positioning and navigation technologies–a survey. *IEEE Transactions on Intelligent Transportation Systems*, 10(1), 4-21.

Skog, I., Händel, P., Nilsson, J. & Rantakokko, J., 2010a. Zero-velocity detection---an algorithm evaluation. *IEEE Transactions on Biomedical Engineering,* 57(11), 2657-2666.

Skog, I., Nilsson, J.-O. & Händel, P., 2010b. Evaluation of zero-velocity detectors for foot-mounted inertial navigation systems. In *Proceedings of International Conference on Indoor Positioning and Indoor Navigation (IPIN 2010).* Zurich, Switzerland,15-17 September 2010.

Skvortzov, V. Y., Lee, H. K., Bang, S. W. & Lee, Y. B., 2007. Application of electronic compass for mobile robot in an indoor environment. In *Proceedings of the 2007 IEEE International Conference on Robotics and Automation.* Roma, Italy, 10-14 April 2007.

Skyhook, 2011. [Online] Available at:<www.skyhookwireless.com> [Accessed on 9 December 2011].

Smith, M. J., Moore, T., Hill, C. J., Noakes, C. J. & Hide, C., 2003. Simulation of GNSS/IMU measurements. In *Proceedings of International Society for Photogrammetry and Remote Sensing, Theory, Tehcnology and Realities of Inertial/GPS Sensor Orientation.* Castelldefels, Spain, 22-23 September 2003.

Soloviev, A. & Dickman, J., 2011. Extending GPS carrier phase availability indoors with a deeply integrated receiver architecture. *IEEE Wireless Communications,* 18**,** 36-44.

Sparkfun, 2010. [Online] Available at: <www.sparkfun.com> [Accessed on 9 December 2011].

Stirling, R., Collin, J., Fyfe, K. & Lachapelle, G., 2003. An Innovative Shoe-Mounted Pedestrian Navigation System. In *Proceedings of European Navigation Conference GNSS 2003.* Graz, Austria, 22-25 April 2003.

Stirling, R., Fyfe, K. & Lachapelle, G., 2005. Evaluation of a new method of heading estimation for pedestrian dead reckoning using shoe mounted sensors. *The Journal of Navigation,* 58**,** 31-45.

Stirling, R.. & Edmonton, A., 2003. *Development of a pedestrian navigation system using shoe mounted sensors.* Msc. University of Alberta.

STMicroelectronics, 2010. *LIS3LV02DL: MEMS inertial sensor.* [online] Available at: <www.st.com/stonline/stappl/productcatalog/app?...LIS3LV02DL> [Accessed on 9 December 2011].

Stockwell, W., n.d. *Angle Random Walk.* [Online] Available at: <www.xbow.com/pdf/AngleRandomWalkAppNote.pdf> [Accessed on 9 November 2011].

Storms, W. F. & Raquet, J. F., 2009. Magnetic Field Aided Indoor Navigation. In *Proceedings of European Navigation Conference (ENC-GNSS 09).* Naples, Italy, 3-6 May 2009.

Storms, W. F., Raquet, J. F. & Shockley, J. A., 2010. Magnetic Field Navigation in an Indoor Environment. In *Proceedings of Ubiquitous Positioning, Indoor Navigation and Location Based Services (UPIN LBS 2010).* Helsinki, Finland, 14-15 October 2010.

Sun, F., Chai, Y., Ben, Y. & Gao, W., 2009. Azimuth rotation experiment and analysis for fiber-optic gyroscope strapdown system. In *Proceedings of International Conference on Information Technology and Computer Science*. Kiev, Ukraine, 25-26 July 2009.

Sun, G., Chen, J., Guo, W. & Liu, K. J. R., 2005. Signal processing techniques in network-aided positioning: a survey of state-of-the-art positioning designs. *IEEE Signal Processing Magazine,* 22**,** 12-23.

Syed, Z., Aggarwal, P., Goodall, C., Niu, X. & El-sheimy, N., 2007. A new multi-position calibration method for MEMS inertial navigation systems. *Measurement Science and Technology,* 18**,** 1897-1907.

Tan, K. M. & Law, C. L., 2007. GPS and UWB Integration for indoor positioning. In *Proceedings of 6th International Conference on Information, Communications and Signal Processing*. Singapore, 10-13 December 2007.

Tanigawa, M., Luinge, H., Schipper, L. & Slycke, P., 2008. Drift-free dynamic height sensor using MEMS IMU aided by MEMS pressure sensor. In *Proceedings of the 5th Workshop on Positioning, Navigation and Communication*. Hannover, Germany, 27 March 2008.

Taylor, G., 1994. Point in polygon test. *Journal of Survey Review,* 32**,** 479-484.

Ting, S., Kwok, S. K., Tsang, A. H. C. & Ho, T., 2011. The study on using passive RFID Tags. *International Journal of Engineering,* 3**,** 9-15.

Titterton, D. H. & Weston, J. L., 2004. *Strapdown inertial navigation technology.* 2nd ed. Herts: The IEE.

Torres-solis, J. & Chau, T., 2010. Wearable indoor pedestrian dead reckoning system. *Pervasive and Mobile Computing,* 6(3), 351-361.

Uliana, M., Andreucci, F. & Papalia, B., 1997. The navigation system of an autonomous underwater vehicle for Antarctic exploration. In *Proceedings of OCEANS '97.* Nova Scotia, Canada ,6-9 October 1997.

Van diggelen, F. & Abraham, C., 2001a. Indoor GPS Technology. In *CTIA Wireless-Agenda.* Dallas, USA, 14-18 May 2001.

Van diggelen, F. & Abraham, C., 2001b. Indoor GPS: The no-chip challenge. *GPS World.* [online] Available at: <http://www.gpsworld.com/lbs/indoor-positioning/indoor-gps-the-no-chip-challenge-1823> [Accessed on 5 May 2011].

Vossiek, M., Wiebking, L., Gulden, P., Wieghardt, J., Hoffmann, C. & Heide, P., 2003. Wireless local positioning. *IEEE Microwave Magazine,* 4**,** 77-86.

Waldmann, J., 2007. Feedforward ins aiding: an investigation of maneuvers for in-flight alignment. *Sba: Controle & Automação Sociedade Brasileira de Automatica,* 18**,** 459-470.

Walther-franks, B. & Malaka, R., 2008. Evaluation of an augmented photograph-based pedestrian navigation system. In *Proceedings of the 9th International Symposium on Smart Graphics.* Salamanca, Spain, 28-30 May 2008.

Wan, S. & Foxlin, E., 2010. Improved pedestrian navigation based on drift-reduced MEMS IMU chip. In *Proceedings of the 2010 International Technical Meeting of the Institute of Navigation - Itm 2010.* California, USA, 25-27 January 2010.

Watson, R., Lachapelle, G., Klukas, R., Turunen, S., Pietila, S. & Halivaara, I., 2006. Investigating GPS signals indoors with extreme high-sensitivity detection techniques. *Navigation,* 52(4), 199-213.

Weimann, F. & Hofmann-wellenhof, B., 2007. *Development of a pedestrian navigation system for urban and indoor environments.* [online] Available at:<http://citeseerx.ist.psu.edu/viewdoc/download?doi=10.1.1.133.441&rep=rep1&type=pdf> [Accessed on 15 September 2011].

Weinberg, M. S. & Kourepenis, A., 2006. Error sources in in-plane silicon tuning-fork MEMS gyroscopes. *Journal of Microelectromechanical Systems,* 15, 479-491.

Widyawan, M. & Beauregard, S., 2008. A backtracking particle filter for fusing building plans with PDR displacement estimates. In *Proceedings of the 5th Workshop on Positioning, Navigation and Communication.* Hannover, Germany, 27 March 2008.

Wis, M. & Colomina, I., 2010. Dynamic dependent IMU stochastic modeling for enhanced INS/GNSS navigation. In *Proceedings of the 5th ESA workshop on Satellite Navigation Technologies and European Workshop on GNSS Signals and Signal Processing.* Noordwijk, Netherlands, 8-10 December 2010.

Woodman, O. & Harle, R., 2008. Pedestrian localisation for indoor environments. In *Proceedings of International Conference on Ubiquitous Computing.* Seoul, Korea. 21-24 September 2008.

Woodman, O. J., 2007. *Technical Report - Introduction to Inertial Navigation System.* [online] Available at:<http://www.cl.cam.ac.uk/techreports/UCAM-CL-TR-696.pdf> [Accessed on 5 May 2010].

Xsens, 2011. [Online] Available at: <www.xsens.com> [Accessed on 2 December 2011].

Yang, Y. & Miao, L., 2004. Fiber-optic strapdown inertial system with sensing cluster continuous rotation. *IEEE Transactions on Aerospace and Electronic Systems,* 40, 1173.

Yi, T. H., Li, H. N. & Gu, M., 2011. Characterization and extraction of global positioning system multipath signals using an improved particle-filtering algorithm. *Measurement Science and Technology,* 22, 075101.

Zandbergen, P. A. & Barbeau, S. J., 2011. Positional accuracy of assisted GPS Data from high-sensitivity GPS-enabled mobile phones. *The Journal of Navigation,* 64**,** 381-399.

Zha, F., Xu, J., Hu, B. & Qin, F., 2010. Error analysis for SINS with different IMU rotation scheme. In *Proceedings of 2nd International Asia Conference on Informatics in Control, Automation and Robotics*. Wuhan, China, 6-7 March 2010.

Zhang, J., Li, B., Dempster, A. G. & Rizos, C., 2010. Evaluation of High Sensitivity GPS Receivers. *Coordinates.* [online] Available at: < http://mycoordinates.org/evaluation-of-high-sensitivity-gps-receivers/all/1/> [Accessed on 1 October 2011].

Zhang, L., Lian, J., Wu, M. & Zheng, Z., 2009. Research on Auto compensation technique of strap-down inertial navigation systems. In *Proceedings of the International Asia Conference on Informatics in Control, Automation and Robotics*. Bangkok, Thailand, 1-2 February 2009.

Zhao, L., Wang, X.-Z., Huang, C. & Cheng, J.-H., 2009. The research on rotation self-compensation scheme of strapdown inertial system. In *Proceedings of the 2009 International Conference on Mechatronics and Automation (ICMA 2009).* Jilin, China, 9-12 August 2009.